



HAL
open science

Topology Optimization of High Efficiency Heat Exchangers using the Level Set Method and Anisotropic Mesh Adaptation

Wassim Abdel Nour

► **To cite this version:**

Wassim Abdel Nour. Topology Optimization of High Efficiency Heat Exchangers using the Level Set Method and Anisotropic Mesh Adaptation. Mechanics of materials [physics.class-ph]. Université Paris sciences et lettres, 2023. English. NNT : 2023UPSLM072 . tel-04581386

HAL Id: tel-04581386

<https://pastel.hal.science/tel-04581386>

Submitted on 21 May 2024

HAL is a multi-disciplinary open access archive for the deposit and dissemination of scientific research documents, whether they are published or not. The documents may come from teaching and research institutions in France or abroad, or from public or private research centers.

L'archive ouverte pluridisciplinaire **HAL**, est destinée au dépôt et à la diffusion de documents scientifiques de niveau recherche, publiés ou non, émanant des établissements d'enseignement et de recherche français ou étrangers, des laboratoires publics ou privés.



THÈSE DE DOCTORAT

DE L'UNIVERSITÉ PSL

Préparée à Mines Paris - PSL

**Topology Optimization of High Efficiency Heat Exchangers
using the Level Set Method and Anisotropic Mesh
Adaptation**

**Optimisation Topologique des Echangeurs de Chaleur à
Haute Efficacité par la Méthode Level-Set et l'Adaptation
Anisotropique de Maillage**

Soutenue par

Wassim ABDEL NOUR

Le 23 Novembre 2023

École doctorale n°364

**Sciences fondamentales et
appliquées**

Spécialité

**Mathématiques Numériques,
Calcul Intensif et Données**

Composition du jury :

Delphine LABOUREUR Associate Professor, VKI	<i>Présidente</i>
Anca BELME Doctor, Sorbonne Université	<i>Rapporteuse</i>
Talib DBOUK Professor, Université de Rouen	<i>Rapporteur</i>
Philippe MELIGA Doctor, Mines Paris	<i>Examineur</i>
Elie HACHEM Professor, Mines Paris	<i>Directeur de thèse</i>

To my Family ...

Acknowledgements

I am immensely grateful to all those who have supported me throughout this journey, without whom this achievement would not have been possible. This endeavor has been a labor of passion and dedication, and I extend my heartfelt gratitude to:

My Supervisors

Your guidance, expertise, and unwavering support have been instrumental in shaping the direction of my research and helping me overcome numerous challenges. Your mentorship has been a source of inspiration, and I am thankful for the valuable insights you provided at every stage of my PhD.

My Family

To my family, for their unwavering love, encouragement, and understanding during the ups and downs of this journey. Your support has been my rock, and I am grateful for your sacrifices that allowed me to pursue this endeavor wholeheartedly.

Friends and Peers

I extend my appreciation to my friends and fellow PhD candidates for being my pillars of strength. Your camaraderie, shared experiences, and stimulating discussions have made this academic pursuit enjoyable and fulfilling.

Institutional Support

I acknowledge the resources, facilities, and institutional support provided by CEMEF, Mines Paris. These resources have been crucial in enabling me to conduct my research effectively.

Funding Organizations

I am grateful for the financial support provided by Clean Sky 2, through Temisth. Your contributions have played a pivotal role in facilitating my research and academic growth.

Everyone I Might Have Missed

I apologize if I have inadvertently missed acknowledging anyone who played a role in

shaping my journey. Your contributions have not gone unnoticed or unappreciated.

Each of the above-mentioned has left an indelible mark on my academic and personal growth. Thank you for being a part of this transformative chapter in my life.

Sincerely,
wassim

Contents

Contents	i
List of Figures	iv
List of Tables	xii
1 General Introduction	1
1.1 Aircrafts' Cooling System	2
1.2 Motivations	2
1.3 Objectives of the thesis	3
1.4 Optimization in Computational Fluid Dynamics	6
1.4.1 Problem Formulation	6
1.4.2 Optimization Techniques	7
1.4.3 Topology Optimization Methods	8
1.4.4 Sensitivity Analysis	10
1.5 Work Environment	11
1.6 Author's contribution during the PhD	12
1.6.1 Journal Articles	12
1.6.2 Communications	12
1.7 Layout of the thesis	12
1.8 Résumé du chapitre en français	13
2 General Framework for Topology Optimization	14
2.1 Introduction	15
2.2 General model for fluid flow topology optimization	15
2.3 State Equations	15
2.4 Adjoint Based Sensitivity Analysis	16
2.5 Immersed Volume Method	18
2.6 Level Set Representation of the Interface	19
2.7 Anisotropic Mesh Adaptation	21
2.7.1 Construction of an anisotropic mesh	21

2.7.2	Edge error estimate	22
2.7.3	Metric construction	23
2.7.4	Summary	23
2.7.5	Level set-based adaptation criteria	24
2.8	Variational Multi-Scale Modeling	26
2.8.1	Navier–Stokes Equations	27
2.8.2	Adjoint Navier–Stokes Equations	28
2.8.3	Interface Update Scheme	29
2.9	Conclusion	30
2.10	Résumé du chapitre en français	30
3	Topology Optimization Framework Designed for 2D Incompressible Fluid Flows	32
3.1	Introduction	33
3.2	Numerical Implementation	34
3.2.1	Geometrical Constraints	34
3.2.2	Steepest Descent Update Rule	35
3.2.3	Descent Factor	36
3.3	General Algorithm	37
3.4	Numerical Benchmarks	37
3.4.1	Preliminaries	37
3.4.2	Design of a pipe bend	40
3.4.3	Design of a four terminal device	41
3.4.4	Design of a double pipe	44
3.5	Discussion	48
3.5.1	Computational efficiency	48
3.5.2	Convergence and mesh dependency	48
3.6	Résumé du chapitre en français	56
4	Topology Optimization Framework : Extension to Parallel 3D Resolution with Anisotropic Meshing	57
4.1	Introduction	58
4.2	Parallel Computational Framework	59
4.2.1	Parallel Resolution	60
4.2.2	Parallel adaptive remeshing	60
4.2.3	Dynamic load balancing	62
4.3	Numerical Benchmarks	62
4.3.1	Single inlet/single outlet duct flow	64
4.3.2	Single inlet/multiple outlets duct flow	70
4.3.3	Multiple inlets/multiple outlets duct flow	74
4.3.4	Discussion	78

4.4	Résumé du chapitre en français	81
5	Topology Optimization Framework : Design of Conjugate Heat Transfer Systems	82
5.1	Introduction	83
5.2	Governing Equations	84
5.3	Adjoint Based Sensitivity Analysis	86
5.4	Multi-Objective Optimization	89
5.5	Numerical Resolution	90
5.5.1	Heat Equation	91
5.5.2	Adjoint Heat Equation	91
5.5.3	Adjoint Navier–Stokes	92
5.6	Numerical Benchmark	93
5.6.1	Preliminaries	93
5.6.2	Two-dimensional single pipe with heated walls	95
5.6.3	Three-dimensional single pipe with heated walls	104
5.7	Résumé du chapitre en français	108
6	Industrial Application	112
6.1	Introduction	113
6.2	PFHE Simplified Header	114
6.3	PFHE Modified geometry	114
6.4	Collector Optimization	121
6.5	Résumé du chapitre en français	124
7	Conclusions and Perspectives	125
7.1	Conclusion	126
7.2	Perspectives	128
A	Brief Overview of Temisth	131
B	Generalities about Heat Exchangers	133
B.1	Definition	133
B.2	Classification of Heat Exchangers	133
B.2.1	Architecture	134
B.2.2	Fluids Involved	136
B.3	Multiphase Heat Exchangers	136
B.4	Plate and Fin Heat Exchangers	138
B.5	Flow Distribution	139
	Bibliography	141

List of Figures

1.1	Diagram of a Vapor Cycle System of an Aircraft Cooling System [2]	2
1.2	GWP Values for some Refrigerants [6]	3
1.3	Solid (in red) and fluid (in blue) regions of a converged solution of an optimization problem computed on a (54×81) rectangular elements mesh. The solid-fluid interface showcases the staircase effect induced by the coarse grid mesh.	4
1.4	(to the left) the solid-fluid interface for a converged solution of a topology optimization problem undergoing AMR, (to the right) image of the mesh corresponding to the region wrapping the interface.	5
1.5	Explanatory Drawing for Comparison between Size, Shape and Topology Optimization. Dark gray represents the solid region while light gray represents the fluid one. Hashed Area represents the obstacle. (a) Initial Design. (b) Example of Size Optimization. (c) Example of Shape Optimization. (d) Degrees of Freedom for Shape Optimization. (e) Example of Topology Optimization. (f) Degrees of Freedom for Topology Optimization	9
1.6	Representative scheme of the derivation phase of the discrete form of the adjoint system [58]	11
2.1	Schematic representation of the design variable β	16
2.2	Schematic representation of the level set function for multi-domain problems.	20
2.3	Left: basic level set function. Right: truncated level set function.	21
2.4	Three immersed solid objects inside a squared cavity filled with fluid. (a) Mesh and zero iso-value of the level set function for a structured mesh with 500 nodes. (b) Same as (a) for an anisotropic mesh with 500 nodes, adapted using the level set filtered with $E = 2 \times 10^{-3}$ (c-h) Same as (a-b) for (c-d) 1000 nodes with $E = 10^{-3}$, (e-f) 2500 nodes with $E = 5 \times 10^{-4}$, and (g-h) 5000 nodes with $E = 10^{-4}$. The red and blue hues correspond to the solid and fluid domains, respectively.	25

3.1	Flowchart of performance topology optimization procedure.	38
3.2	Set-up of the pipe bend problem. The light gray shade denotes parts of the boundary where solid boundary conditions are appended to level set auto-reinitialization equation.	41
3.3	Designs of a pipe bend sampled over the course of optimization using the parameters given in Tab. 3.1. (a) Anisotropic adapted mesh. (b) Zero iso-value of the level set function. (c) Norm of the velocity vector. The optimal pipe bend is shown at the bottom.	42
3.4	(a) Anisotropic adapted mesh of the optimal pipe bend. (b) Successive close-ups.	43
3.5	Optimal designs for the Bend Pipe problem of [79] showcasing the staircase effect. The computation was performed on regular grid type meshes of respectively 2500 (to the left) and 10000 (to the right) elements.	43
3.6	Set-up of the four terminal device problem. The light gray shade denotes parts of the boundary where solid boundary conditions are appended to level set auto-reinitialization equation.	44
3.7	Designs of a four terminal device sampled over the course of optimization using the parameters given in Tab. 3.1. (a) Anisotropic adapted mesh. (b) Zero iso-value of the level set function. (c) Norm of the velocity vector. The optimal four terminal device is shown at the bottom.	45
3.8	(a) Anisotropic adapted mesh of the optimal four terminal device. (b) Successive close-ups.	46
3.9	Set-up of the double pipe problem. The light gray shade denotes parts of the boundary where solid boundary conditions are appended to level set auto-reinitialization equation.	46
3.10	Designs of a double pipe sampled over the course of optimization using the parameters given in Tab. 3.1. (a) Anisotropic adapted mesh. (b) Zero iso-value of the level set function. (c) Norm of the velocity vector. The optimal double pipe is shown at the bottom.	47
3.11	(a) Anisotropic adapted mesh of the optimal double pipe. (b) Successive close-ups.	48
3.12	Computational cost of the implemented algorithm, as obtained averaging 300 update steps of the pipe bend, double pipe, and four terminal device problems (100 steps for each) using the simulation parameters provided in Tab. 3.1. All results normalized to achieve unit average time per iteration. The LS and LSF labels stand for level set (LS) and filtered level set (LSF), respectively.	49

3.13	(a) Interface surface area computed over the first 200 iterations for the bend pipe (solid line), four terminal device (dashed line) and double pipe (dash-dotted line) problems, using the parameters given in Tab. 3.1. (b) Convergence history for the bend pipe problem with 60000 (in black), 20000 (dashed line), 40000 (dash-dotted line) and 80000 (dash-dot-dotted line) mesh elements. The circle symbols mark the random iterations sampled in Figs. 3.3-3.14. (c) Same as (b) for the four terminal device problem. The circle symbols mark the random iterations sampled in Figs. 3.7-3.15. (d) Same as (b) for the double pipe problem with 80000 (in black), 25000 (dashed line), 55000 (dash-dotted line) and 10500 (dash-dot-dotted line) mesh elements. The circle symbols mark the random iterations sampled in Figs. 3.10-3.16. The ellipses at the bottom indicate the transition from the double-ended wrench to the single-ended wrench minimizer. All cost function values made non dimensional using the inlet width and mean inlet velocity (equivalently, using $\rho q_i^3 / e_i^2$ as reference cost functional value).	51
3.14	Anisotropic meshes of a pipe bend sampled over the course of optimization, using (a) 80000, (b) 40000 and (c) 20000 mesh elements.	52
3.15	Anisotropic meshes of a four terminal device sampled over the course of optimization, using (a) 80000, (b) 40000 and (c) 20000 mesh elements.	53
3.16	Anisotropic meshes of a double pipe sampled over the course of optimization, using (a) 105000, (b) 55000 and (c) 25000 mesh elements.	54
4.1	Illustration of the iterative parallel remeshing steps on a model 2-D distributed mesh.	61
4.2	(a) Before and (b) after load balancing for the same model 2-D distributed mesh as in Fig. 4.1.	62
4.3	Problem set-up for the (a) single inlet/single outlet (b-c) single inlet/multiple outlets and (d) multiple inlets/multiple outlets examples.	65
4.4	Optimization of the single inlet/single outlet duct flow presented in Fig. 4.3(a). The zero iso-value of the level set function and associated anisotropic adapted meshes are sampled at intermediate iterations 1, 402, 548, 700 and 900 (from top to bottom) using the parameters given in Tab. 4.2. The associated volumes of fluid are 77.0%, 40.8%, 27.5%, 13.7% and 3.94%, respectively.	66
4.5	Convergence history for the 3-D bend pipe problem with $5M$ elements. All cost function values made non dimensional using the inlet diameter and maximum inlet velocity (equivalently, using $\rho u_i^3 e_i^2$ as reference cost functional value). The dashed line shows the decrease in the target volume.	68

4.6	Illustration of mesh partitioning for the three dimensional, single inlet/single outlet duct flow. The colors in these plots represent the 64 subdomains generated by the graph/mesh partitioning/repartitioning for the same iterations sampled in Fig. 4.4.	69
4.7	Optimization of the single inlet/multiple outlet duct flow presented in Fig. 4.3(b). The zero iso-value of the level set function and associated anisotropic adapted meshes are sampled at intermediate iterations 1, 505, 624, 750 and 1050 (from top to bottom) using the parameters given in Tab. 4.3. The associated volumes of fluid are 75.6%, 37.8%, 28.9%, 19.5% and 15.0%, respectively.	71
4.8	Optimization of the single inlet/multiple outlet duct flow presented in Fig. 4.3(c). The zero iso-value of the level set function and associated anisotropic adapted meshes are sampled at intermediate iterations 1, 60, 110, 180 and 300 (from top to bottom) using the parameters given in Tab. 4.3. The associated volumes of fluid are 36.2%, 30.0%, 24.8%, 17.5% and 9.9%, respectively.	72
4.9	Comparison between optimal designs of the problem in Fig. 4.3 (b) (to the left) and its counterpart in [82] (to the right).	74
4.10	Optimization of the multiple inlet/multiple outlet duct flow presented in Fig. 4.3(d). The zero iso-value of the level set function and associated anisotropic adapted meshes are sampled at intermediate iterations 1, 201, 283, 400 and 550 (from top to bottom) using the parameters given in Tab. 4.2. The associated volumes of fluid are 72.8%, 45.9%, 34.8%, 18.9% and 4.9%, respectively.	75
4.11	Optimization of the multiple inlet/multiple outlet duct flow presented in Fig. 4.3(d). The zero iso-value of the level set function and associated anisotropic adapted meshes are sampled at intermediate iterations 700, 800, 830, 850 and 1000 (from top to bottom) using the parameters given in Tab. 4.2. The associated volume of fluid of all samples matches the target (5%) within the desired tolerance.	76
4.12	(a) Computational cost of the implemented algorithm, as obtained averaging 50 update steps of the 3-D single inlet/single duct flow presented in Fig. 4.3(a). (b) Same as (a) for the single inlet/multiple outlet duct flow presented in Fig. 4.3(b), (c) single inlet/multiple outlet duct flow presented in Fig. 4.3(c), and (d) multiple inlet/multiple outlet duct flow presented in Fig. 4.3(d). All simulation parameters are those provided in Tabs. 4.1-4.4. The LS and LSF labels stand for level set (LS) and filtered level set (LSF), respectively.	79
4.13	Average run time per iteration for the various cases documented in Fig. 4.12.	80

5.1	Schematic of the inputs/outputs of the computational models and their coupling.	90
5.2	Set-up of the two-dimensional single pipe problem with heated walls. The orange and light gray shade denote hot isothermal and adiabatic walls, respectively.	95
5.3	Optimal designs sorted by weighting ω for the two-dimensional single pipe device with heated walls presented in Fig. 5.2. (a) Low and intermediated thermal weights. The dashed lines denote the results obtained at large thermal weights, further presented by the close-ups in (b-c) for (b) symmetric and (c) asymmetric designs.	98
5.4	Multi-objective optimization of the two-dimensional single pipe device with heated walls presented in Fig. 5.2. From top to bottom: the zero iso-value of the level set function and associated anisotropic adapted meshes are sampled over the course of optimization using the parameters given in Tab. 5.2. (a) Straight pipe solution with $\omega = 0.4$. (b) Solid core solution with $\omega = 0.7$. (c) Fragmented core solution with $\omega = 0.987$	99
5.5	Multi-objective optimization of the two-dimensional single pipe device with heated walls presented in Fig. 5.2. From top to bottom: the zero iso-value of the level set function and associated anisotropic adapted meshes are sampled over the course of optimization using the parameters given in Tab. 5.2. (a) Bent pipe solution with $\omega = 0.85$. (b) Z pipe solution with $\omega = 0.97$. (c) Fragmented Z pipe solution with $\omega = 0.998$	100
5.6	Fragmented core solutions computed under various initial designs under thermal weigh $\omega = 0.987$	101
5.7	Comparison of similiar architectures encountered in [116] (on the top) and in the current study (on the bottom). Optimal designs were taken at different thermal weights, for intence on the top, and from left to right, $\omega = 0, 0.6, 0.8, \text{ and } 1.0$, where for the current study (also from left to right) $\omega = 0, 0.8, 0.97, \text{ and } 1.0$	101
5.8	Pareto frontier for bi-objective topology optimization of the single pipe device with heated walls. The red symbols are the near-optimal design for which both the dissipated power and the recoverable thermal power approach their single objective optimization value.	102
5.9	Set-up of the three-dimensional single pipe problem with heated walls: one single hot stripe. The orange and light gray shade denote hot isothermal and adiabatic walls, respectively.	104

5.10	Multi-objective optimization of the three-dimensional single pipe device with heated walls (one single hot stripe) presented in Fig. 5.9. The zero iso-value of the level set function and associated anisotropic adapted meshes are sampled over the course of optimization using the parameters given in Tab. 5.3. The associated volume of fluid (from top to below) is as follows: 90%, 42.9%, 20.6%, 20.5% and 20.4%, respectively.	105
5.11	Optimal design of the three-dimensional single pipe device with heated walls (one single hot stripe) presented in Fig. 5.9, together with stream-wise and cross-wise cuts at positions shown by the gray planes. The colors hue corresponds to the temperature profile.	107
5.12	Set-up of the three-dimensional single pipe problem with heated walls: one single upstream hot stripe vs. two hot stripes. The orange and light gray shade denote hot isothermal and adiabatic walls, respectively.	108
5.13	Multi-objective optimization of the three-dimensional single pipe device with heated walls (one single upstream hot stripe) presented in Fig. 5.12(a). The zero iso-value of the level set function and associated anisotropic adapted meshes are sampled over the course of optimization using the parameters given in Tab. 5.3. The associated volume of fluid (from top to below) is as follows: 90%, 43.0%, 20.4%, 20.5% and 20.4%, respectively.	109
5.14	Multi-objective optimization of the three-dimensional single pipe device with heated walls (two hot stripes) presented in Fig. 5.12(b). The zero iso-value of the level set function and associated anisotropic adapted meshes are sampled over the course of optimization using the parameters given in Tab. 5.3. The associated volume of fluid (from top to below) is as follows: 90%, 54.4%, 31.9%, 20.6% and 20.3%, respectively.	110
5.15	(a) Optimal design of the three-dimensional single pipe device with heated walls (one single upstream hot stripe) presented in Fig. 5.12(a), together with stream-wise and cross-wise cuts at positions shown by the gray planes. (b) Same as (a) for the device with heated walls (two hot stripes) presented in Fig. 5.12(b). The colors hue corresponds to the temperature profile.	111
6.1	PFHE actually in service shown from different perspectives.	113
6.2	Problem set-up for the simplified PFHE distributor.	114

6.3	Optimization of the plate fin heat exchanger distributor presented in Fig. 6.2. The zero iso-value of the level set function is sampled at intermediate iterations 1, 70, 100, 110, 140, 160 and 400 (from top to bottom, left to right) using the parameters given in Tab. 6.1. The associated volumes of fluid are 50%, 28.8%, 26.3%, 25.5%, 23.1%, 21.4% and 17.6%, respectively. The red color highlights the leads, here representing the inlets and outlets of the system.	115
6.4	Base Geometry for Topology Optimization [121]	117
6.5	Problem setup for the manifold with (a) inlet to the left and (b) inlet at the top center of the manifold	117
6.6	Optimization of the first configuration of the exchanger’s manifold (with the inlet positioned on the center left of the box) presented in Fig 6.4(a). The zero iso-value of the level set function is sampled at intermediate iterations 1, 70, 180, 230, 320, 440 and 700 (from top to bottom, and from left to right) using the parameters given in Tab 6.2. The associated volumes of fluid are 57.0%, 49.0%, 23.5% and 8%, respectively. The red color highlights the leads, here representing the inlets and outlets of the system.	119
6.7	Optimization of the first configuration of the exchanger’s manifold (with the inlet positioned on the top center of the box) presented in Fig 6.4(b). The zero iso-value of the level set function is sampled at intermediate iterations 1, 50, 120, 180, 230, 380 and 700 (from top to bottom, and from left to right) using the parameters given in Tab 6.2. The associated volumes of fluid are 56.8%, 53.8%, 47.0%, 40.8%, 35.0%, 20.5% and 8%, respectively. The red color highlights the leads, here representing the inlets and outlets of the system.	120
6.8	Problem setup for the collector.	121
6.9	Optimization of the exchanger’s collector presented in Fig 6.4(a). The zero iso-value of the level set function is sampled at intermediate iterations 1, 80, 250 and 700 (from top to bottom, and from left to right) using the parameters given in Tab 6.3. The associated volumes of fluid are 57.0%, 49.2%, 32.5% and 8%, respectively. The red color highlights the leads, here representing the inlets and outlets of the system.	123
B.1	Classification of Heat Exchangers with respect to their Architecture [134].	134
B.2	Schematic representation of several types of flow arrangement [136].	135
B.3	Typical assembly and cross-flow arrangement of plate-fin PFHE: (a) plate-fin exchanger assembly; (b) cross-flow arrangement [143].	137
B.4	Schematic diagrams of different geometries of fin surfaces encountered in PFHEs [146].	138

B.5 Impact factors on flow distribution over multi-channel heat exchangers [147]. 139

List of Tables

1.1	Classification of Sensitivity Analysis Methods into Gradient-Based or Gradient-Free Algorithms	10
3.1	Numerical parameters for the pipe bend, four terminal device and double pipe topology optimization problems.	39
3.2	Convergence data for the pipe bend, four terminal device and double pipe topology optimization problems. All cost function values made non dimensional using the inlet width and mean inlet velocity (equivalently, using $\rho q_i^3/e_i^2$ as reference cost functional value).	50
4.1	Algorithmic parameters.	63
4.2	Numerical parameters for the single inlet/single outlet duct flow problem.	67
4.3	Numerical parameters for the single inlet/multiple outlets duct flow problems.	70
4.4	Numerical parameters for the multiple inlet/multiple outlets duct flow problem.	77
4.5	Run times for the various cases documented in Fig. 4.12.	81
5.1	Algorithmic parameters.	93
5.2	Numerical parameters for the two-dimensional single pipe problem with heated walls.	96
5.3	Numerical parameters for the three-dimensional single pipe problem with heated walls.	106
6.1	Numerical parameters for the plate fin heat exchanger distributor problem.	116
6.2	Numerical parameters for the two possible configurations of the distributor of the heat exchanger.	118
6.3	Numerical parameters for the collector of the heat exchanger.	122

Chapter 1

General Introduction

Contents

1.1	Aircrafts' Cooling System	2
1.2	Motivations	2
1.3	Objectives of the thesis	3
1.4	Optimization in Computational Fluid Dynamics	6
1.4.1	Problem Formulation	6
1.4.2	Optimization Techniques	7
1.4.3	Topology Optimization Methods	8
1.4.4	Sensitivity Analysis	10
1.5	Work Environment	11
1.6	Author's contribution during the PhD	12
1.6.1	Journal Articles	12
1.6.2	Communications	12
1.7	Layout of the thesis	12
1.8	Résumé du chapitre en français	13

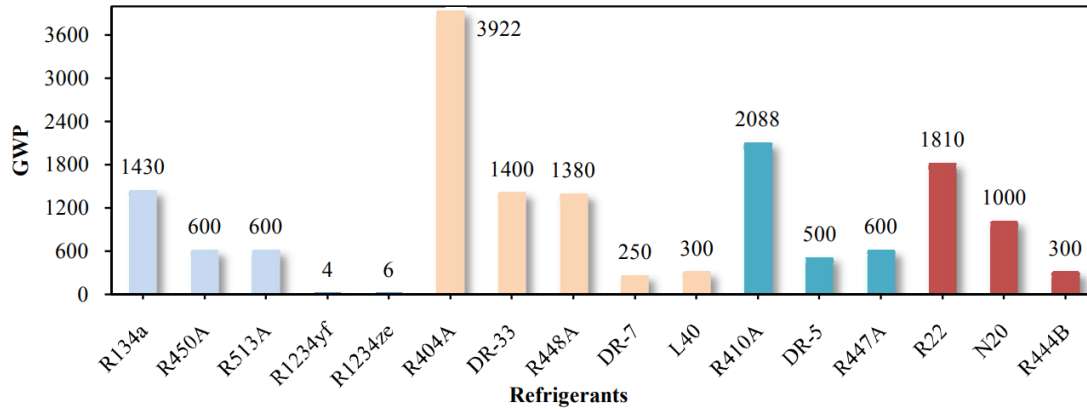


Figure 1.2: GWP Values for some Refrigerants [6]

The substitution of these refrigerants with alternatives that have a lower GWP often leads to a decrease in the heat exchanger’s performance. From here arises the need of an innovative methodology that generates a change in the heat exchanger’s architecture to use a low GWP coolant (ideally R1234ze) while improving the heat dissipation rate and reducing the energy required to drive the thermal system.

This matter piqued the interest of Liebherr-Aerospace who raised the issue with the European Commission (EC) through its research and innovation program Horizon 2020. Consequently, the Panther project was initiated with funding from clean-sky 2, a European public-private partnership dedicated to advancing research and development programs in line with the EU’s ambition of achieving climate neutrality by 2050. The final objective of the Panther project was to design a new generation plate and fin heat exchanger that operates with R1234ze refrigerant but still meets the requirements of the VCS. The project encompassed three main components: (i) numerical design of the heat exchanger core; (ii) numerical design of the upstream and downstream sections of the heat exchanger; and (iii) experimental characterization of the newly designed heat exchanger. The present PhD research addresses the second part of the project by pushing the envelope with cutting-edge optimization techniques to advance the design of the specified parts to their maximum potential.

1.3 Objectives of the thesis

The objective of this thesis is to develop a topology optimization framework to optimize the manifold design of the newly designed heat exchanger. The norm in topology optimization is to employ fixed finite element meshes with uniform (or close-to-uniform) element size, small enough that all relevant physical phenomena are reliably captured, but not so small that the cost of performing the optimiza-

tion becomes unaffordable. Lately, this approach showed effectiveness in validating sensitivity computations and gaining insight into optimal architectures. However, it also posed several drawbacks, as the resulting designs were far from being manufacturable. A notable issue is illustrated in Fig. 1.3, which depicts the staircase effect frequently observed when optimization takes place on a fixed mesh.

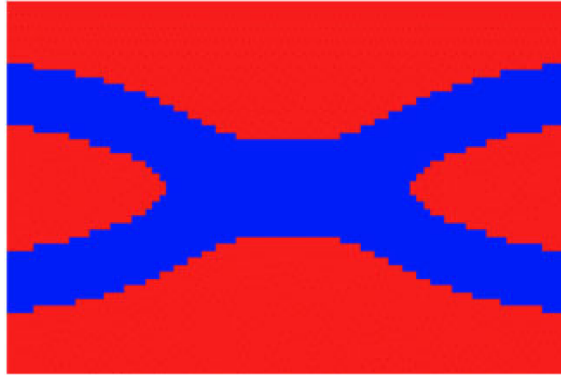


Figure 1.3: Solid (in red) and fluid (in blue) regions of a converged solution of an optimization problem computed on a (54×81) rectangular elements mesh. The solid-fluid interface showcases the staircase effect induced by the coarse grid mesh.

A recent trend has been to use adaptive remeshing techniques to maintain a competitive computational cost. Such an approach consists in generating a coarse base grid, then in adding recursively finer and finer subgrids in the regions requiring higher resolution, either until a maximum level of refinement is reached, or until the local truncation error drops below a certain tolerance (for more sophisticated implementations endowed with error estimation routines). Within the context of fluid flow problems, particular emphasis has been put on (but not limited to) adaptive meshing refinement (AMR) schemes, using both density [7, 8] and level set methods [9, 10]¹. Although significant improvements were observed, the final result, even at its best, presented impurities even for simple geometries, as illustrated in Fig. 1.4.

There is still ample room for progress, though, as almost all adaptive algorithms applied so far to fluid flow topology optimization support only isotropic size maps. Fluid dynamics conversely involves convection dominated phenomena for which anisotropic meshes are highly desirable [15], especially in the vicinity of the solid boundaries, where the fluid velocity exhibits steep gradients in the wall-normal direction and skin-friction plays a defining role. The premise of this study is that

¹see also [11] for an application to phase field methods and [12, 13, 14] for recent efforts applying a different remeshing scheme to a combination of level set functions and adaptive body-conforming meshes.

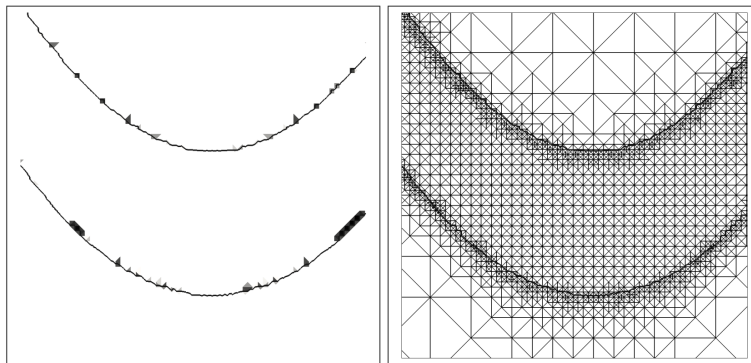


Figure 1.4: (to the left) the solid-fluid interface for a converged solution of a topology optimization problem undergoing AMR, (to the right) image of the mesh corresponding to the region wrapping the interface.

the ability to generate highly stretched elements in boundary layer regions can substantially increase the accuracy of the geometric representation (compared to what is often seen in topology optimization of flow problems) and naturally convey said accuracy to the numerical solution without sophisticated interpolation or discretization techniques. We note that this is all perfectly in line with the recommendations made in [16] to improve upon the current state-of-the-art; Nonetheless, our literature review did not reveal any other study combining anisotropic mesh adaptation and fluid flow topology optimization, besides the density-based optimization of Stokes flow in Ref. [8], possibly because the notorious difficulty of finding spatial discretization schemes that meet the level of robustness required by automatic anisotropic mesh adaptation.

This research intends to fill the gap by introducing a novel numerical framework for topology optimization of Navier–Stokes flows, coupled or not with thermal transfer; The latter combines level set methods and anisotropic mesh adaptation to handle arbitrary geometries immersed in an unstructured mesh. All quantities of interest, including the sensitivity needed to evolve the level set function, are computed by a variational multiscale (VMS) stabilized finite element method supporting elements of aspect ratio up to the order of 1000:1 [17]. The metric map providing both the size and the stretching of mesh elements in a very condensed information data is derived from the level set. A posteriori anisotropic error estimator is then used to minimize the interpolation error under the constraint of a prescribed number of nodes in the mesh. The latter can be adjusted over the course of optimization, meaning that the base grid can be either refined or coarsened on demand (in contrast with AMR, whose total number of mesh elements cannot be controlled, and whose mesh cannot be coarsened further than its base configuration). This is expected to achieve further speed-ups (by reducing the cost of modeling the solid

material away from the interface) and also to help improve manufacturability of the optimal design, which remains an issue as most classical topology optimization methods render organic designs that can be difficult to translate into computer-aided design models. By employing topology optimization techniques, the goal is to achieve a non-conventional design that minimizes pressure drop, and maximizes heat transfer performance by optimizing the fluid distribution [18, 19, 20] on the different compartments of the plates and fin heat exchanger.

1.4 Optimization in Computational Fluid Dynamics

Optimization in computational fluid dynamics has emerged as a powerful tool in today's industrial landscape, revolutionizing the design and analysis of fluid flow systems. By combining the principles of numerical simulations and optimization techniques, CFD optimization offers unprecedented opportunities to enhance system performances, reduce costs, and accelerate product development cycles. From aerospace and automotive engineering to energy production and biomedical applications, CFD optimization has become an indispensable asset for industries seeking to stay competitive in a rapidly evolving environment [21].

1.4.1 Problem Formulation

Typically, any optimization problem can be formulated using three key elements: a cost function, a set of constraints, and a design variable [22, 23].

- A cost function [24], also known as an objective function, is a mathematical function that quantifies the performance or quality of a system in relation to a set of parameters or variables. It provides a measure of how well a particular solution or set of parameters satisfies the desired objectives of a problem. It is typically defined based on the specific problem's goals. It represents the objective to be minimized or maximized during the optimization process.
- set of constraints, divided between equality and inequality constraints.
 - Equality constraints [25], also known as state equations, refer to the equations that describe the dynamics or behavior of the system being optimized. They are partial differential equations derived from the underlying physical laws that govern the behavior of the system. Ideally, these equations must be exactly the same as the ones used for industrial validation. Sadly, this is not always the case (mainly in topology optimization) due to purely numerical reasons.

- Inequality constraints [26], could be bounded or not. They impose limitations, restrictions, or requirements on the decision variables of the optimization problem. Mostly being -but not limited to, geometrical constraints, they mainly emerge from the limitations of manufacturing processes, or are the result of space/weight restrictions.
- A design variable [27], usually a vector. It combines the inputs that affect, either directly or indirectly, the evolution of the cost function. The choice of the design variable and the number of degrees of freedom of the system depend largely on the type of optimization's algorithm [28]. Several types will thus be discussed in the following sections.

The objective would then be to find the value of the design variable that minimizes the cost function while respecting the constraints of the problem.

1.4.2 Optimization Techniques

Optimization techniques can be splitted into three main categories: parametric, shape and topology optimization.

1.4.2.1 Parametric Optimization

Parametric optimization is an optimization technique used to determine the optimal size or dimensions of a design variable or component. In parametric optimization, the design variables should be dimensions whose values are adjusted to achieve the desired outcomes [29]. Thus, the original topology or architecture is conserved, as are the geometrical shapes. Only changes in dimensions are observed. This is represented in figure 1.5 (b) where only the spatial position of the turning point for the fluid has been modified.

In computational fluid dynamics, size optimization would be more relevant if combined with optimization algorithms such as Genetic or Evolutionary Algorithms [30]. It has also been found to be very valuable when combined with Design of Experiment [31] or Design Exploration [32] techniques. Indeed, by exploring different design alternatives, these techniques lead to the construction of a response surface or surrogate model. This model approximates the relationship between the design variables and the corresponding performance measures. Optimal designs can finally be interpolated on the response surface.

1.4.2.2 Shape Optimization

Shape optimization technique is used to find the optimal shape or geometry of a component. It aims to improve the performance of the design by altering its

external contours [33]. Shape optimization can be applied to various parameters, such as cross-sectional profiles, curvature, or specific regions of the optimization domain. Figures 1.5 (c) and (d) show, respectively, a representative example of shape optimization and its assigned design variables.

This method found success in aerodynamic applications, where the layout of the external surface is deterministic for the system's performance [34]. From drag and lift coefficients, to stability control and noise reduction [35], being all solely dependent on the curvature of the component, they became prominent in shape optimization.

The successful implementation of shape optimization algorithms can be greatly enhanced if one can efficiently manipulate the computational mesh. In this regard, shape optimization is usually combined with mesh morphing techniques [36] for the enabling of seamless deformation of the mesh geometry to align with the changing shape without affecting the topology of the system [37, 38].

1.4.2.3 Topology Optimization

Topology optimization goes a step further than its two precedents by allowing for the exploration and determination of the optimal distribution of material within a given design space [28, 39]. In opposite to size and shape optimization, topology optimization algorithms imperatively use numerical methods [40] to iteratively remove or add material to improve fluid flow behavior.

When it was combined with steepest descent algorithms, topology optimization became a game changer in engineering design. It contributed to reducing the time, cost, and effort involved in the design process. Instead of relying on trial and error, we can avoid unnecessary iterations, while achieving significantly innovative and non-trivial results.

In summary, Fig. 1.5 shows a comparative example of size, shape, and topology optimization with their respective design variables.

1.4.3 Topology Optimization Methods

Leaving aside explicit boundary methods, that represent the fluid-solid interface by edges or faces of a body-fitted mesh, and have limited flexibility to handle complicated topological changes, the prevalent classes of methods for topology optimization are the Density Methods and the Level Set Methods.

Density methods rely on a Brinkman penalization of the solid domain, where the flow is modeled as a fictitious porous material with very low permeability [41, 42, 43]. They manage drastic topological changes, as the gradient information (or sensitivity) is distributed over a large part of the domain, but can lead to spurious or leaking

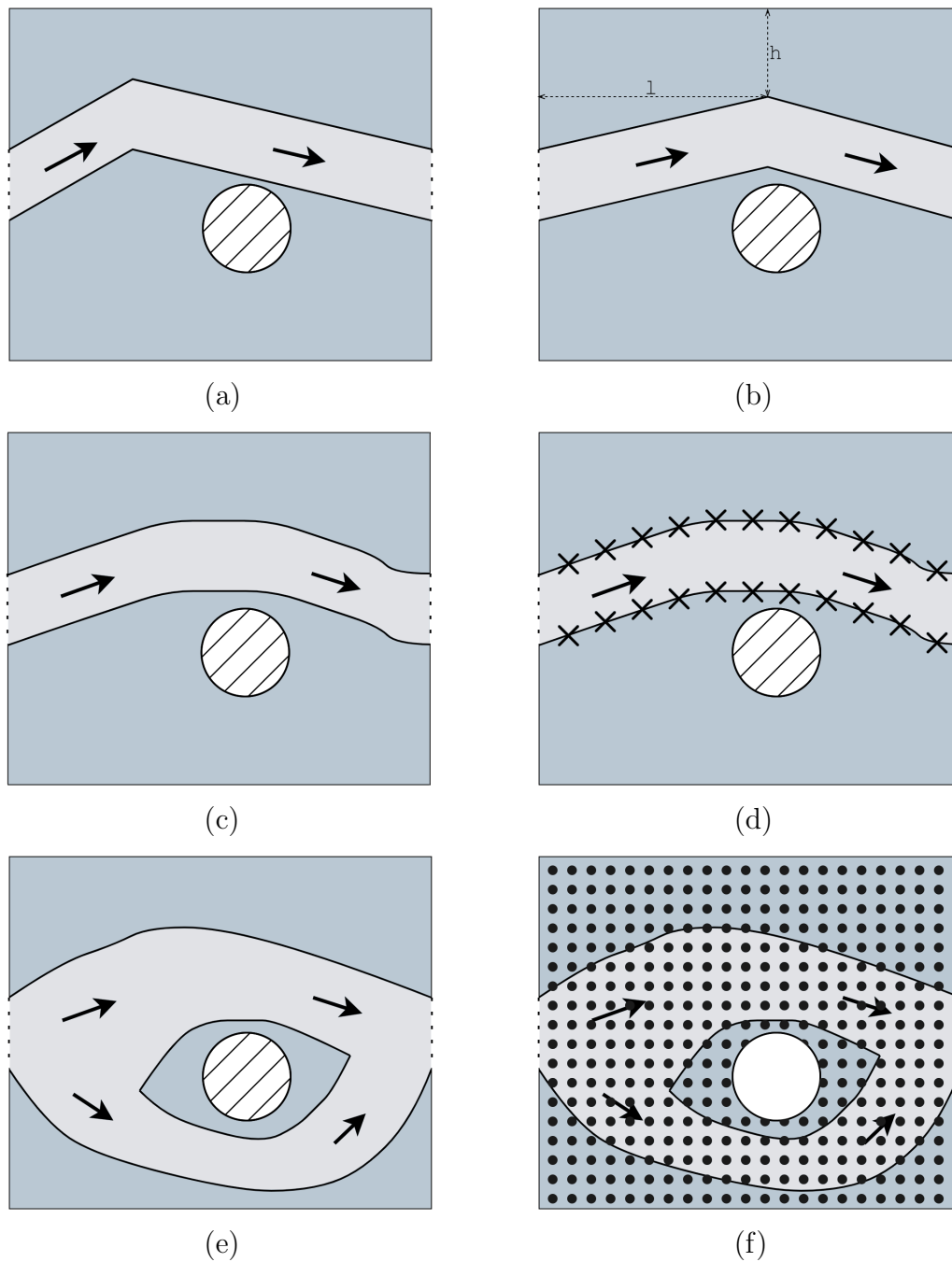


Figure 1.5: Explanatory Drawing for Comparison between Size, Shape and Topology Optimization. Dark gray represents the solid region while light gray represents the fluid one. Hashed Area represents the obstacle. (a) Initial Design. (b) Example of Size Optimization. (c) Example of Shape Optimization. (d) Degrees of Freedom for Shape Optimization. (e) Example of Topology Optimization. (f) Degrees of Freedom for Topology Optimization

flows if the penalization factor is not well-calibrated, since the velocity and pressure fields are computed in the entire domain (both the solid and fluid regions).

Level set methods conversely model the solid boundaries by iso-contours of a level set function [44, 45, 46]. They lack a nucleation mechanism to create new holes, due to the sensitivities being located only at the solid-fluid interface (which is often relieved using initial designs with many holes), but easily handle complicated topological changes (e.g., merging or cancellation of holes), and allow for well defined, crisp interface representations while avoiding the intermediate material phases (grayscale) and mesh-dependent spatial oscillations of the interface geometry (stair-casing) often encountered in density methods [47].

As mentioned previously, we use here the level-set method because it enables a more accurate definition of interfaces (an essential point to address the industrial problem, as it eases the manufacturability of the optimal part) and eases the enforcement of geometric constraints. Additionally, the distance function is more suitable for mesh adaptation, especially for highly stretched anisotropic elements in the interface direction.

1.4.4 Sensitivity Analysis

Topology optimization algorithms can also be classified with respect to the method they use to decide for the optimal direction of design update between two consecutive iterations. From here emerges the classification of the methods into two large families of optimization methods: gradient-based and gradient-free methods [48]. Table 1.1 shows a non-exhaustive list of different approaches for sensitivity computation. While gradient-based algorithms, on one hand, rely on the gradient of the objective

Gradient-Based	Gradient-Free
Adjoint Method [25]	Genetic Algorithms [49]
Moving Asymptotes Method [50]	Evolutionary Method [40]
Optimality Criteria Method [51]	Particle Swarm Optimization [52]
Sequential Programming Method [53, 54]	Simulated Annealing [55]

Table 1.1: Classification of Sensitivity Analysis Methods into Gradient-Based or Gradient-Free Algorithms

function with respect to the design variables, gradient-free algorithms, on the other hand, explore the design space by evaluating the objective function at different design points without explicitly calculating or utilizing gradients.

In the following chapters of this present work, only adjoint based methods will be considered for their ability to efficiently compute the gradients or sensitivities of an objective function with respect to a large number of design variables[56].

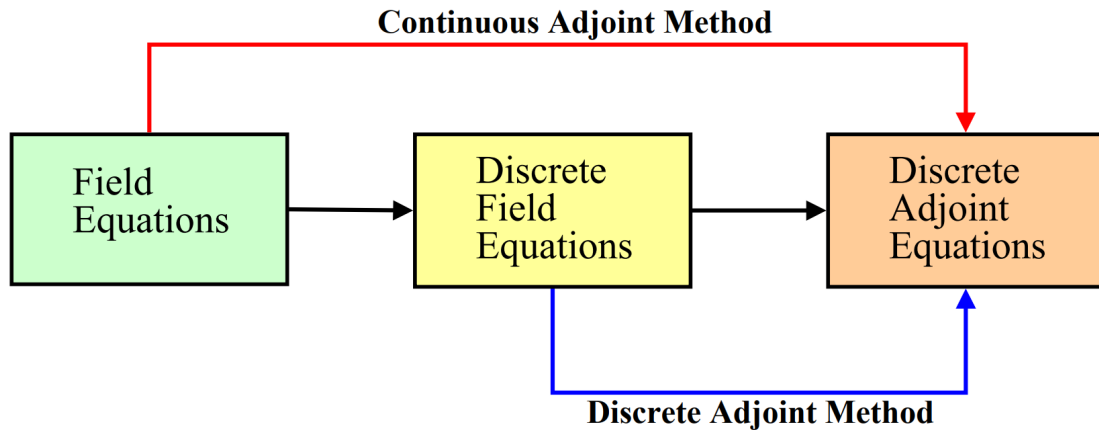


Figure 1.6: Representative scheme of the derivation phase of the discrete form of the adjoint system [58]

Adjoint methods can again be classified as continuous or discrete. As shown in Fig. 1.6, the difference between them resides in whether the adjoint system has been calculated based on the continuous or discrete form of the primary system [57]. Theoretically, both methods should lead to similar results [59]. But in the present work, we favored the continuous method because its adjoint system is simpler to derive [59]. For more information about other sensitivity computation methods, interested readers are referred to [25, 40, 49, 50, 51, 52, 53, 54, 55].

1.5 Work Environment

This thesis was in collaboration with Temisth. It took part of the PANTTHER project, that has received funding from the Clean Sky2 Joint Undertaking (JU) under grant agreement No 886698. The JU receives support from the European Union’s Horizon 2020 research and innovation program and the Clean Sky 2 JU members other than the Union. It reflects only the authors’ view and the JU is not responsible for any use that may be made of the information it contains.

All the developments and numerical implementation were carried out using the finite element library Cimlib-CFD. It is developed by the CFL team. This scientific library represents an Object Oriented Program and a fully parallel code written in C++.

1.6 Author's contribution during the PhD

1.6.1 Journal Articles

- Abdel Nour, Jabbour, Serret, Meliga & Hachem. A Stabilized Finite Element Framework for Anisotropic Adaptive Topology Optimization of Incompressible Fluid Flows. Published in *Fluids* 2023, 8, 232. <https://doi.org/10.3390/fluids8080232>
- Abdel Nour, Larcher, Serret, Meliga & Hachem. Topology optimization of conjugate heat transfer systems using anisotropic adaptive parallel finite element framework. Submitted to *Applied Thermal Engineering*, 2022.
- Abdel Nour, Larcher, Serret, Meliga & Hachem. Large-scale parallel topology optimization of three-dimensional incompressible fluid flows in a level set, anisotropic mesh adaptation framework. Published in *Computer Methods in Applied Mechanics and Engineering* 2023, 416, 116335. <https://doi.org/10.1016/j.cma.2023.116335>

1.6.2 Communications

- International Conference on Fluid Flow, Heat and Mass Transfer (FFHMT'22)
- Computational Fluid Conference (CFC 2023)
- U.S. National Congress on Computational Mechanics (USNCCM17)
- 12th-13th and 14th Symposium of Von Karman Institute for Fluid Dynamics PhD Research
- Colloquium of Doctoral Students 2022

1.7 Layout of the thesis

The structure of this thesis is organized as follows: Chapter 2 presents the general methodology employed in this research. Chapters 3, 4, and 5 showcase the specific methodologies for Navier-Stokes optimization with and without thermal coupling, both providing numerical implementation and analysis. Chapter 6 presents the results of an industrial application for which this framework was primarily developed. Finally, chapter 7 summarizes the findings, draws conclusions, and discusses potential future research directions.

1.8 **Résumé du chapitre en français**

Ce chapitre a fourni une introduction générale au système à cycle de vapeur (VCS) du système de climatisation de la cabine d'un avion. Il a mis en évidence les effets néfastes des réfrigérants actuellement utilisés. La simple substitution du fluide réfrigérant par un autre moins polluant conduira sans doute à la dégradation des performances de l'échangeur de chaleur du cycle. Ainsi, des techniques d'optimisation avancées sont nécessaires pour décider de la nouvelle conception de l'échangeur de chaleur afin de fonctionner avec un réfrigérant moins polluant tout en maintenant/améliorant l'efficacité thermique du système, en laissant les autres conditions de fonctionnement inchangées. Ce chapitre a également fourni un aperçu rapide des techniques d'optimisation disponibles, en mettant l'accent sur la méthode adjointe continue pour l'optimisation topologique, qui a servi de base à l'algorithme d'optimisation de l'étude détaillée dans les chapitres suivant.

Chapter 2

General Framework for Topology Optimization

Contents

2.1	Introduction	15
2.2	General model for fluid flow topology optimization	15
2.3	State Equations	15
2.4	Adjoint Based Sensitivity Analysis	16
2.5	Immersed Volume Method	18
2.6	Level Set Representation of the Interface	19
2.7	Anisotropic Mesh Adaptation	21
2.7.1	Construction of an anisotropic mesh	21
2.7.2	Edge error estimate	22
2.7.3	Metric construction	23
2.7.4	Summary	23
2.7.5	Level set-based adaptation criteria	24
2.8	Variational Multi-Scale Modeling	26
2.8.1	Navier–Stokes Equations	27
2.8.2	Adjoint Navier–Stokes Equations	28
2.8.3	Interface Update Scheme	29
2.9	Conclusion	30
2.10	Résumé du chapitre en français	30

2.1 Introduction

This first chapter serves as the foundation for achieving the objectives outlined in the introduction. Its primary focus is to provide a detailed explanation of the key numerical components within the general formalism employed to optimize single phase incompressible fluid flows in the laminar regime. The chapter will start by establishing the problem setup, then afterwards dive into the stabilized finite element numerical framework used to compute all solutions of interest on anisotropic adapted meshes and perform the design update steps. The continuous adjoint method for sensitivity analysis will be thoroughly examined, followed by a detailed account of the level set method employed for tracking and updating the interface position. Finally, the chapter will provide a comprehensive overview of the numerical computational methods implemented for all the aforementioned models.

2.2 General model for fluid flow topology optimization

In the following, we denote by Ω a fixed, open bounded domain in \mathbb{R}^d (with d the space dimension), with boundary $\partial\Omega$ oriented with inward-pointing normal vector \mathbf{n} . Throughout this study, $\Omega = \Omega_f \cup \Omega_s$ is the disjoint reunion of two domains Ω_f and Ω_s (for simplicity, we refer to Ω_f as the fluid domain, and to Ω_s as the solid domain, although we also fill Ω_s with a fluid for numerical convenience, as further explained in the following). The two domains are separated by an interface $\Gamma = \Omega_f \cap \Omega_s$, whose position we seek to optimize with respect to a certain measure of performance, here a cost function J to be minimized, that we assume can be formulated as a surface integral over the boundary of the fluid domain rather than over its interior, i.e.,

$$J = \int_{\partial\Omega_f} J_s \, ds \tag{2.1}$$

2.3 State Equations

Physically, the solid domain Ω_s is treated as a rigid body at rest, while the flow field in the fluid domain Ω_f is modeled after the steady incompressible Navier–Stokes equations:

$$\rho_f \mathbf{u} \cdot \nabla \mathbf{u} = -\nabla p + \nabla \cdot (2\mu_f \boldsymbol{\varepsilon}(\mathbf{u})) \quad \text{in } \Omega_f \tag{2.2}$$

$$\nabla \cdot \mathbf{u} = 0 \quad \text{in } \Omega_f \tag{2.3}$$

where \mathbf{u} is the velocity, p is the pressure, $\boldsymbol{\varepsilon}(\mathbf{u}) = (\nabla \mathbf{u} + \nabla \mathbf{u}^T)/2$ is the rate of deformation tensor, and we assume constant fluid density ρ and dynamic viscosity

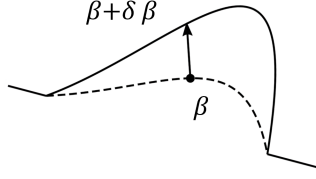


Figure 2.1: Schematic representation of the design variable β

μ . Open flow boundary conditions are appended under the form of a prescribed velocity at the inlet, zero velocity at the wall:

$$\mathbf{u} = \mathbf{u}_i \quad \text{on } \Gamma_i \quad (2.4)$$

$$\mathbf{u} = \mathbf{0} \quad \text{on } \Gamma \quad (2.5)$$

and a convenient outflow condition at the outlet, either a prescribed velocity:

$$\mathbf{u} = \mathbf{u}_o \quad \text{on } \Gamma_o \quad (2.6)$$

adjusted to ensure mass conservation, or a more natural zero pressure/zero viscous stress condition:

$$p\mathbf{n} = \mu_f \boldsymbol{\varepsilon}(\mathbf{u}) \cdot \mathbf{n} = \mathbf{0} \quad \text{on } \Gamma_o \quad (2.7)$$

2.4 Adjoint Based Sensitivity Analysis

The problem of minimizing the cost function subject to Navier–Stokes as state equations is tackled using the continuous adjoint method, to find the cost function sensitivity to variations of a design variable β physically representing deformations of the interface under the form of local surface normal displacements. A schematic representation of the design variable is presented in Fig. 2.1.

Without going into the technicalities of the method (for which the interested reader is referred to [60]), one first forms the Lagrangian:

$$\mathcal{L} = \int_{\partial\Omega_f} J_s ds - \int_{\Omega_f} \tilde{p} \nabla \cdot \mathbf{u} dv - \int_{\Omega_f} \tilde{\mathbf{u}} \cdot (\rho_f \mathbf{u} \cdot \nabla \mathbf{u} + \nabla p - \nabla \cdot (2\mu_f \boldsymbol{\varepsilon}(\mathbf{u}))) dv \quad (2.8)$$

featuring the adjoint velocity $\tilde{\mathbf{u}}$ as the Lagrange multiplier for the momentum equations (2.2) and the adjoint pressure \tilde{p} as the Lagrange multiplier for the continuity equation (2.3), then seeks to decompose the variation of \mathcal{L} due to a change in the interface position into individual variations with respect to the adjoint, state and design variables. The variation with respect to the adjoint variables

$$\delta_{(\tilde{\mathbf{u}}, \tilde{p})} \mathcal{L} = - \int_{\Omega_f} \delta \tilde{p} \nabla \cdot \mathbf{u} dv - \int_{\Omega_f} \delta \tilde{\mathbf{u}} \cdot (\rho_f \mathbf{u} \cdot \nabla \mathbf{u} + \nabla p - \nabla \cdot (2\mu_f \boldsymbol{\varepsilon}(\mathbf{u}))) dv \quad (2.9)$$

is trivially zero as long as (\mathbf{u}, p) is solution to the above Navier–Stokes equations, in which case $\mathcal{L} = J$. After integrating by parts, the variation with respect to the state variables is:

$$\begin{aligned} \delta_{(\mathbf{u}, p)} \mathcal{L} &= \int_{\Omega_f} (\nabla \cdot \tilde{\mathbf{u}}) \delta p \, dv \\ &+ \int_{\Omega_f} (-\rho_f \mathbf{u} \cdot \nabla \tilde{\mathbf{u}} + \rho_f \nabla \mathbf{u}^T \cdot \tilde{\mathbf{u}} - \nabla \tilde{p} - \nabla \cdot (2\mu_f \boldsymbol{\varepsilon}(\tilde{\mathbf{u}}))) \cdot \delta \mathbf{u} \, dv \\ &+ \int_{\partial\Omega_f} (\tilde{p} \mathbf{n} + 2\mu_f \boldsymbol{\varepsilon}(\tilde{\mathbf{u}}) \cdot \mathbf{n} + \rho_f (\mathbf{u} \cdot \mathbf{n}) \tilde{\mathbf{u}} + \partial_{\mathbf{u}} J_s) \cdot \delta \mathbf{u} \, ds \\ &- \int_{\partial\Omega_f} (\tilde{\mathbf{u}} + \partial_p J_s \mathbf{n}) \cdot (-\delta p \mathbf{n} + 2\mu_f \boldsymbol{\varepsilon}(\delta \mathbf{u}) \cdot \mathbf{n}) \, ds \quad (2.10) \end{aligned}$$

on behalf of the viscous stress being purely tangential in incompressible flows. At this stage, adjoint equations and boundary conditions are designed to ensure $\delta_{(\mathbf{u}, p)} \mathcal{L} = 0$, which requires the domain and boundary integrals to vanish individually in (2.10). Keeping in mind that we work here under the assumption of a fixed interface (since the design variable is constant), and that typical cost functions in topology optimization do not depend on the flow quantities on the wall, but are rather formulated as integrals over all or any part of inlet and/or outlet, i.e.,

$$J = \int_{\Gamma_i \cup \Gamma_o} J_s \, ds \quad (2.11)$$

we obtain the linear, homogeneous problem:

$$-\rho_f \mathbf{u} \cdot \nabla \tilde{\mathbf{u}} + \rho_f \nabla \mathbf{u}^T \cdot \tilde{\mathbf{u}} = \nabla \tilde{p} + \nabla \cdot (2\mu_f \boldsymbol{\varepsilon}(\tilde{\mathbf{u}})) \quad \text{in } \Omega_f \quad (2.12)$$

$$\nabla \cdot \tilde{\mathbf{u}} = 0 \quad \text{in } \Omega_f \quad (2.13)$$

driven by the non-homogeneous inlet/wall boundary conditions:

$$\tilde{\mathbf{u}} = -\partial_p J_s \mathbf{n} \quad \text{on } \Gamma_i \quad (2.14)$$

$$\tilde{p} \mathbf{n} + 2\mu_f \boldsymbol{\varepsilon}(\tilde{\mathbf{u}}) \cdot \mathbf{n} + \rho_f (\mathbf{u} \cdot \mathbf{n}) \tilde{\mathbf{u}} = -\partial_{\mathbf{u}} J_s \quad \text{on } \Gamma_o \quad (2.15)$$

$$\tilde{\mathbf{u}} = \mathbf{0} \quad \text{on } \Gamma \quad (2.16)$$

associated to (2.4)-(2.5), with adjoint outflow condition:

$$\tilde{\mathbf{u}} = -\partial_p J_s \mathbf{n} \quad \text{on } \Gamma_o \quad (2.17)$$

if the prescribed velocity outflow condition (2.6) is used, or:

$$\tilde{p} \mathbf{n} + 2\mu_f \boldsymbol{\varepsilon}(\tilde{\mathbf{u}}) \cdot \mathbf{n} + \rho_f (\mathbf{u} \cdot \mathbf{n}) \tilde{\mathbf{u}} = -\partial_{\mathbf{u}} J_s \quad \text{on } \Gamma_o \quad (2.18)$$

if the zero pressure/zero viscous stress outflow condition (2.7) is used.

Note the minus sign ahead of the first term of the adjoint momentum equation (2.12), that reflects the reversal in directionality due to the non-normality of the linearized evolution operator [61]. Expressing the interface normal deformation after [62] as

$$\delta \mathbf{u} = \beta \nabla \mathbf{u} \cdot \mathbf{n} \quad (2.19)$$

the variation with respect to the design variable (now encompassing the domain deformation) is ultimately computed as

$$\begin{aligned} \delta_\beta \mathcal{L} = \delta \mathcal{L} &= \int_\Gamma \beta (\tilde{p} \mathbf{n} + 2\mu_f \boldsymbol{\varepsilon}(\tilde{\mathbf{u}}) \cdot \mathbf{n}) \cdot (\nabla \mathbf{u} \cdot \mathbf{n}) \, ds \\ &= \int_\Gamma \beta \mu_f (\nabla \tilde{\mathbf{u}} \cdot \mathbf{n}) \cdot (\nabla \mathbf{u} \cdot \mathbf{n}) \, ds \end{aligned} \quad (2.20)$$

where the second equality stems from the incompressibility of the state and adjoint solutions [60]. This enables efficient design update schemes via first-order gradient descent methods, as the second term in the integrand is the desired sensitivity to a displacement β at some specific point of the interface. For instance the simplest steepest-descent algorithm implemented herein moves down the cost function, in the direction of the steepest slope using

$$\beta = -\mu_f (\nabla \tilde{\mathbf{u}} \cdot \mathbf{n}) \cdot (\nabla \mathbf{u} \cdot \mathbf{n}) \quad (2.21)$$

up to a positive multiplicative factor to control the step taken in the gradient direction.

2.5 Immersed Volume Method

The immersed volume method (IVM) is used to combine the fluid and solid phases of the problem into a single fluid with variable material properties. Simply put, we solve state equations formally identical to (2.3)-(2.2) and adjoint equations formally identical to (2.13)-(2.12) on a unique mesh of the domain Ω (that encompasses the design domain) in which the fluid and solid domains Ω_f and Ω_s are immersed. Using the level set function (2.27) as criterion for anisotropic mesh adaptation ensures that individual material properties can be distributed accurately and smoothly as possible over the smallest possible thickness around the interface (classically by linear interpolation between the fluid and solid values, using a smooth Heaviside function computed from the level set to avoid discontinuities by creating an interface transition with a thickness of a few elements). Such an approach is especially relevant to thermal coupling problems, as having composite conductivity and specific heat means that the amount of heat exchanged at the interface then proceeds solely from

the individual material properties on either side of it. For the uncoupled problems, tackled here though, it suffices to use constant density and viscosity (equal to the fluid values) and to set the velocity to zero at all grid nodes located inside the solid domain Ω_s . This can be seen as a hard penalty preventing the fluid from leaking across the immersed interface, that holds numerically because anisotropic mesh adaptation ensures that the interface does not intersect arbitrarily the mesh elements (it precisely aims at aligning the mesh element edges along the interface), which may otherwise compromise the accuracy of the finite element approach.

Following this method, both the fluid and solid phases are combined into a single fluid with variable material properties. It thus solves Navier–Stokes equations as

$$\nabla \cdot \mathbf{u} = 0 \quad \text{in } \Omega \quad (2.22)$$

$$\rho \mathbf{u} \cdot \nabla \mathbf{u} = -\nabla p + \nabla \cdot (2\mu \boldsymbol{\varepsilon}(\mathbf{u})) \quad \text{in } \Omega \quad (2.23)$$

and for the adjoint Navier–Stokes equations as

$$\nabla \cdot \tilde{\mathbf{u}} = 0 \quad \text{in } \Omega \quad (2.24)$$

$$-\rho \mathbf{u} \cdot \nabla \tilde{\mathbf{u}} + \rho \nabla \mathbf{u}^T \cdot \tilde{\mathbf{u}} = \nabla \tilde{p} + \nabla \cdot (2\mu \boldsymbol{\varepsilon}(\tilde{\mathbf{u}})) \quad \text{in } \Omega \quad (2.25)$$

respectively identical to (2.3)-(2.2) and (2.13)-(2.12), but with variable (mixed fluid/solid) density ρ , and viscosity μ . Finally, the sensitivity associated with this IVM framework deduces as

$$\beta = -\mu(\nabla \tilde{\mathbf{u}} \cdot \mathbf{n}) \cdot (\nabla \mathbf{u} \cdot \mathbf{n}) \quad (2.26)$$

2.6 Level Set Representation of the Interface

The level set method is used here to localize and capture the interface between the fluid and solid domains from the zero iso-value of a smooth level set function, classically the signed distance function defined as

$$\varphi(\mathbf{x}) = \begin{cases} -\text{dist}(\mathbf{x}, \Gamma) & \text{if } \mathbf{x} \in \Omega_f \\ 0 & \text{if } \mathbf{x} \in \Gamma \\ \text{dist}(\mathbf{x}, \Gamma) & \text{if } \mathbf{x} \in \Omega_s \end{cases} \quad (2.27)$$

with the convention that $\varphi < 0$ in the fluid domain. A schematic representation of the level set function on a 3D spherical solid object is presented in Fig. 2.2. Once the sensitivity analysis has output a displacement β in the direction of the steepest slope, the position of the level set is updated solving a transport equation with normal velocity $\beta \mathbf{n} / \Delta \tau$, where $\Delta \tau$ is a pseudo-time step to convert from displacement to velocity (of no physical relevance since we are not concerned by the absolute displacement of a given point on the interface, only by its relative displacement with

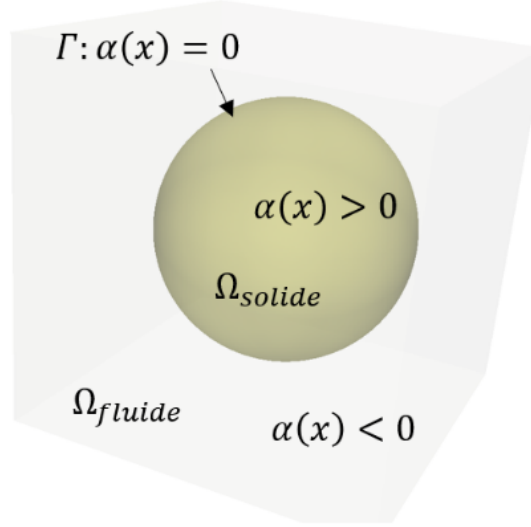


Figure 2.2: Schematic representation of the level set function for multi-domain problems.

respect to its neighbors). The main problem with this approach is that the level set after transport is generally no longer a distance function, which is especially problematic when a specific remeshing strategy depending on the distance property is used at the interface (as is the case in this study). As a result, the distance function needs to be reinitialized, which is done here using a coupled convection-reinitialization method wherein the level set function is automatically reinitialized during the resolution of the transport equation. In practice, the signed distance function is cut off using a hyperbolic tangent filter, as defined by

$$\phi = E \tanh\left(\frac{\varphi}{E}\right) \quad (2.28)$$

with E the cut-off thickness (so the metric property is asymptotically satisfied in the vicinity of the zero iso-value). Fig. 2.3, shows an example of the filtering of the level set function. This filtered level set is then evolved solving the auto-reinitialization equation:

$$\partial_\tau \phi + \mathbf{a}_\tau \cdot \nabla \phi = S \quad (2.29)$$

where we note

$$\mathbf{a}_\tau = \frac{\beta}{\Delta\tau} \mathbf{n} + \frac{\lambda}{\Delta\tau} \operatorname{sgn}(\phi) \frac{\nabla \phi}{\|\nabla \phi\|}, \quad S = \frac{\lambda}{\Delta\tau} \operatorname{sgn}(\phi) \left(1 - \left(\frac{\phi}{E}\right)^2\right) \quad (2.30)$$

and λ is a parameter homogeneous to a length, set to the mesh size h_\perp in the direction normal to the interface. Such an approach is shown in [63, 64, 65] to reduce the computational cost and to ensure a better mass conservation compared to the

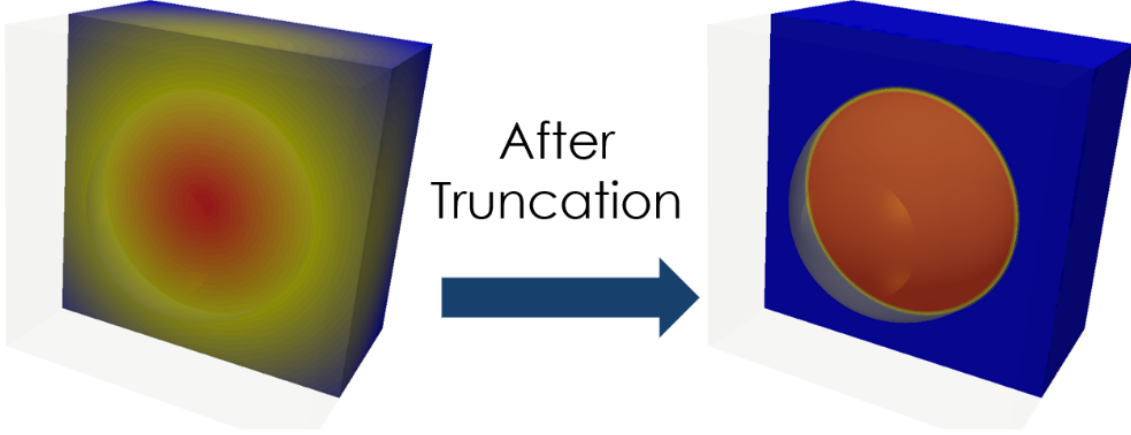


Figure 2.3: Left: basic level set function. Right: truncated level set function.

classical Hamilton–Jacobi method in which both steps are performed in succession). Moreover, since the filtered level set defined in (2.28) is bounded, Dirichlet boundary conditions $\phi = \pm E$ are easily appended to Eq. (2.29) to explicitly design fluid and solid sub-regions of $\partial\Omega$.

2.7 Anisotropic Mesh Adaptation

The implementation of a mesh adaptation algorithm in the context of fluid flow topology optimization makes for the main novelty of this study.

2.7.1 Construction of an anisotropic mesh

The main idea of anisotropic, metric-based mesh adaptation is to generate a uniform mesh (with unit length edges and regular elements) in a prescribed Riemannian metric space, but anisotropic and well adapted (with highly stretched elements) in the Euclidean space. Assuming that, in the context of metric-based adaptation methods, controlling the interpolation error suffices to master the global approximation error, the objective can be formulated as finding the mesh, made up of at most N_n nodes, that minimizes the linear interpolation error in the L^1 norm. Following the lines of [66, 67], an edge-based error estimator combined to a gradient recovery procedure is used to compute, for each node, a metric tensor that prescribes a set of anisotropic directions and stretching factors along these directions, without any direct information from the elements, nor any underlying interpolation. The optimal stretching factor field is obtained by solving an optimization problem using the equi-distribution principle under the constraint of a fixed number of nodes in the mesh, after which a new mesh is generated using the procedure described in [68],

based on a topological representation of the computational domain.

2.7.2 Edge error estimate

Given a mesh Ω_h of the domain Ω , we denote by \mathbf{x}^{ij} the edge connecting a given node \mathbf{x}^i to $\mathbf{x}^j \in \Sigma(i)$, where $\Sigma(i)$ is the set of nodes connected to \mathbf{x}^i , and the number of such nodes is noted as $|\Sigma(i)|$. Also, given a regular analytical (scalar) function ψ defined on Ω , and its P1 finite element approximation ψ_h computed on Ω_h , we follow [66] and estimate the interpolation error along the edge \mathbf{x}^{ij} as the projection along the edge of the second derivative of ψ . This is obtained projecting along the edge a Taylor expansion of the gradient of ψ at \mathbf{x}^j to give

$$\varepsilon_{ij} = |\mathbf{g}^{ij} \cdot \mathbf{x}^{ij}| \quad (2.31)$$

where the i and j superscripts indicate nodal values at nodes \mathbf{x}^i and \mathbf{x}^j , respectively, $\mathbf{g}^i = \nabla\psi(\mathbf{x}^i)$ is the exact value of the gradient at \mathbf{x}^i , and $\mathbf{g}^{ij} = \mathbf{g}^j - \mathbf{g}^i$ is the variation of the gradient along the edge. Although Eq. (2.31) involves only values of the gradient at the edge extremities and can thus be evaluated without resorting to resource expensive Hessian reconstruction methods, this however requires the gradient of ψ to be known and continuous at the nodes, which in turn requires full knowledge of ψ . Meanwhile, only the linear interpolate ψ_h is known in practice, whose gradient is piecewise constant and discontinuous from element to element (although its projection along the edges is continuous since it depends only on the nodal values of the field).

A recovery procedure is thus used to build a continuous gradient estimator defined directly at the nodes. It is shown in [66] that a suitable error estimate preserving second-order accuracy is obtained substituting the reconstructed gradient for the exact gradient in (2.31), to give

$$\varepsilon_{ij} = |\bar{\mathbf{g}}^{ij} \cdot \mathbf{x}^{ij}| \quad (2.32)$$

where $\bar{\mathbf{g}}^{ij} = \bar{\mathbf{g}}^j - \bar{\mathbf{g}}^i$ and we denote by $\bar{\mathbf{g}}^i$ the recovered gradient of ψ_h at node \mathbf{x}^i . The latter is defined in a least-square sense as

$$\bar{\mathbf{g}}^i = \operatorname{argmin}_{\mathbf{g} \in \mathbb{R}^d} \sum_{j \in \Sigma(i)} |(\mathbf{g} - \nabla\psi_h) \cdot \mathbf{x}^{ij}|^2 \quad (2.33)$$

for which an approximate solution using the nodal values as sole input is shown in [66] to be

$$\bar{\mathbf{g}}^i = (\mathbf{X}^i)^{-1} \cdot \sum_{j \in \Sigma(i)} (\psi_h(\mathbf{x}^j) - \psi_h(\mathbf{x}^i)) \mathbf{x}^{ij} \quad (2.34)$$

where \mathbf{X}^i is the length distribution tensor defined as

$$\mathbf{X}^i = \frac{1}{|\Sigma(i)|} \sum_{j \in \Sigma(i)} \mathbf{x}^{ij} \otimes \mathbf{x}^{ij} \quad (2.35)$$

that gives an average representation of the distribution of the edges sharing an extremity.

2.7.3 Metric construction

In order to relate the error indicator ε_{ij} defined in (2.32) to a metric suitable for mesh adaptation purposes, we introduce the stretching factor s_{ij} as the ratio between the length of the edge \mathbf{x}^{ij} after and before the adaptation. The metric at node \mathbf{x}^i is sought to generate unit stretched edge length in the metric space, that is,

$$(s_{ij}\mathbf{x}^{ij})^T \cdot \mathbf{M}^i \cdot (s_{ij}\mathbf{x}^{ij}) = 1, \quad \forall j \in \Sigma(i) \quad (2.36)$$

for which an approximate least-square solution is shown in [66] to be

$$\mathbf{M}^i = \left(\frac{d}{|\Sigma(i)|} \sum_{j \in \Sigma(i)} s_{ij}^2 \mathbf{x}^{ij} \otimes \mathbf{x}^{ij} \right)^{-1} \quad (2.37)$$

provided the nodes in $\Sigma(i)$ form at least d non co-linear edges with \mathbf{x}^i (which is the case if the mesh is valid). The metric solution of (2.37) is ultimately computed setting a target total number of nodes N_n . Assuming a total error equi-distributed among all edges, the stretching factor is shown in [67] to be

$$s_{ij} = \left(\frac{\sum_i N_i(1)}{N_n} \right)^{\frac{2}{d}} \varepsilon_{ij}^{-1/2} \quad (2.38)$$

where $N_i(1)$ is the number of nodes generated in the vicinity of node \mathbf{x}^i for a unit error, given by

$$N_i(1) = \left(\det \left(\frac{d}{|\Sigma(i)|} \sum_{j \in \Sigma(i)} \varepsilon_{ij}^{1/2} \frac{\mathbf{x}^{ij}}{|\mathbf{x}^{ij}|} \otimes \frac{\mathbf{x}^{ij}}{|\mathbf{x}^{ij}|} \right) \right)^{-1/2} \quad (2.39)$$

2.7.4 Summary

In order to simplify and clarify the presentation, the main steps needed for metric construction at the nodes is summarized in the following algorithm: where classical linear interpolation from one mesh to another is applied.

Algorithm 1 Anisotropic mesh adaptation algorithm**Require:** Anisotropic adapted mesh.

- 1: Set number of nodes N_n
- 2: Compute ψ_h on current mesh
- 3: **for** each node \mathbf{x}^i **do**
- 4: Compute length distribution tensor \mathbf{X}^i using (2.35)
- 5: Compute nodal recovered gradient $\bar{\mathbf{g}}^i$ using (2.34)
- 6: **for** all edges \mathbf{x}^{ij} **do**
- 7: Compute edge recovered gradient $\bar{\mathbf{g}}^{ij}$
- 8: Compute edge-based error ε_{ij} using (2.32)
- 9: Compute stretching factor s_{ij} using (2.38)
- 10: Compute metric \mathbf{M}^i using (2.37)
- 11: Generate new mesh by local improvement in the neighborhood of the nodes and edges [68]
- 12: Interpolate ψ_h on new mesh

2.7.5 Level set-based adaptation criteria

In practice, the variable used for error estimation purpose is the filtered level set defined in (2.28), as it satisfies the metric property in a thin layer around the interface (in particular it preserves the zero iso-value of φ , which is the only relevant information for mesh adaptation purposes), but avoids unnecessary adaptation of the mesh further away from the interface (where the zero interpolation error is close-to-zero, due to $\|\nabla\phi\| \sim 0$). In practice, this means that the criterion for mesh adaptation is purely geometric and that the same mesh is pre-adapted around the fluid-solid interface, then used to compute all quantities needed to perform the next design update step. The flexibility of the proposed mesh adaptation technique is illustrated in Fig. 2.4, where three solid objects defined by level set functions (a circle, a square and a regular pentagram) have been immersed close to the boundary of a square cavity filled with fluid, to assess the capability to handle different features (angles, singular points, curvatures) even under drastic conditions. Four meshes made up of 500, 1000, 2500 and 5000 nodes are considered, each of which comes in two flavors, one structured and the other anisotropic, adapted to the level set. On the one hand, the adapted meshes exhibit the expected orientation and deformation of the mesh elements, whose longest edges are parallel to the solid boundaries. On the other hand, they are naturally and automatically coarsened in smooth regions (where the filtered level set is constant) while extremely refined near the interface. Also, the transition is finer with an anisotropic adaptive mesh, which allows maintaining a very good accuracy even for a low number of nodes, as evidenced in Fig. 2.4 by the zero iso-value of the level sets (more quantitative results are available in [69], where

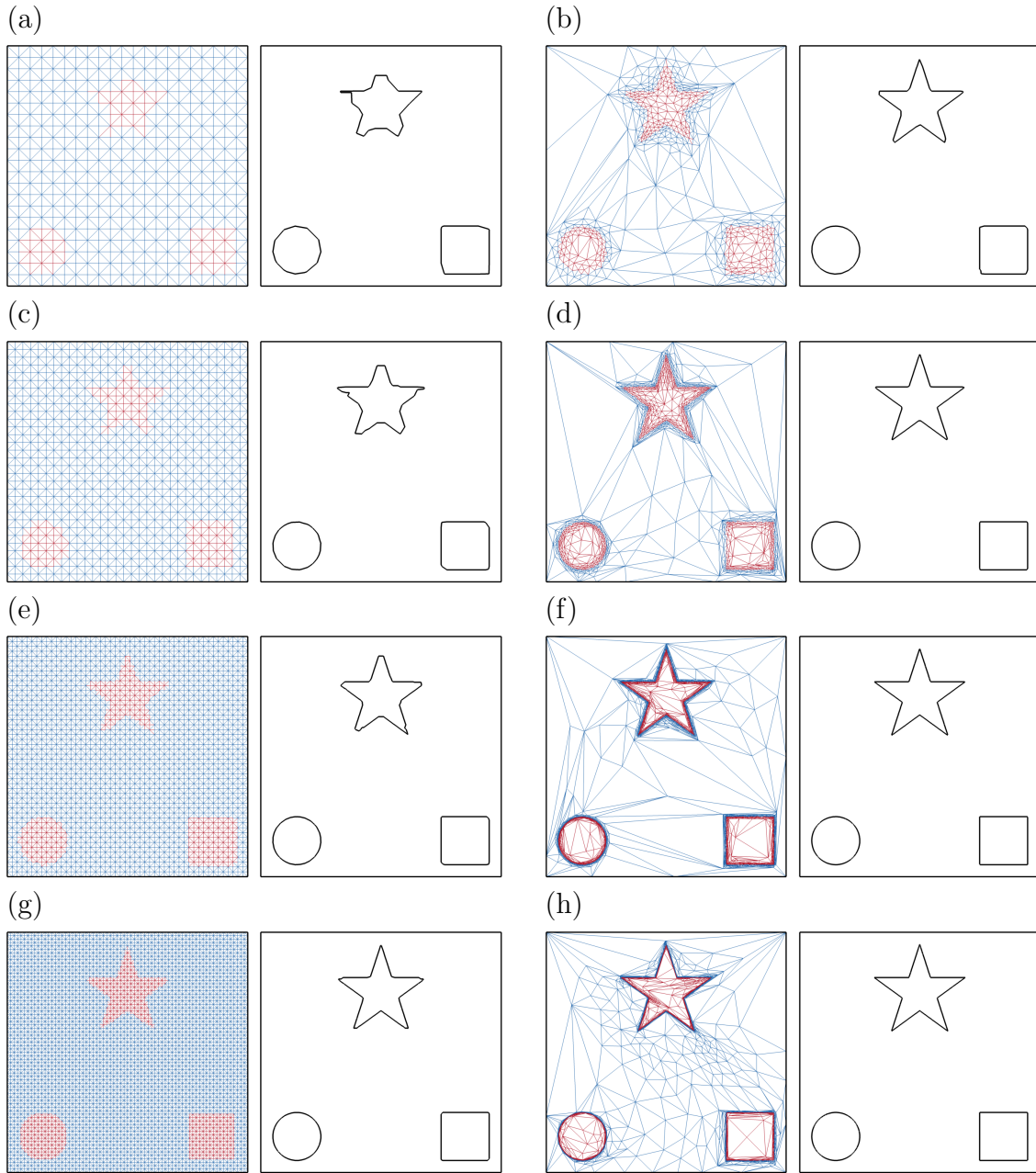


Figure 2.4: Three immersed solid objects inside a squared cavity filled with fluid. (a) Mesh and zero iso-value of the level set function for a structured mesh with 500 nodes. (b) Same as (a) for an anisotropic mesh with 500 nodes, adapted using the level set filtered with $E = 2 \times 10^{-3}$ (c-h) Same as (a-b) for (c-d) 1000 nodes with $E = 10^{-3}$, (e-f) 2500 nodes with $E = 5 \times 10^{-4}$, and (g-h) 5000 nodes with $E = 10^{-4}$. The red and blue hues correspond to the solid and fluid domains, respectively.

it is shown that at least ten times more elements are required in a structured mesh to achieve the same accuracy, as measured computing the total perimeter and area of the three immersed objects).

Nonetheless, it is worth mentioning that the approach also supports more complex adaptation criteria featuring physical quantities, thus providing the ability to dynamically adapt the mesh during the simulations. The common method to adapt a mesh to several variables is to combine the metrics corresponding to each individual variable using metric intersection algorithms, which is known to incur a relatively high computational cost and to have potentially non-unique, suboptimal outcome. Conversely, the present approach allows building directly a unique metric from a multi-component error vector combining level set and any relevant flow quantity of interest, as definition (2.32) is easily extended to account for several sources of error [70]. Indeed, if we consider $\boldsymbol{\psi} = (\psi_1, \psi_2, \dots, \psi_p)$ a vector consisting of p scalar variables, it comes out straightforwardly that the error is now a vector $\boldsymbol{\varepsilon}_{ij} = (\varepsilon_{ij,1}, \varepsilon_{ij,2}, \dots, \varepsilon_{ij,p})$, whose L^2 norm can serve as simple error value for the edge from which to compute the stretching factor (2.38) and ultimately, the metric solution of (2.37). For instance, the $2d + 3$ sized nodal vector field defined as

$$\boldsymbol{\psi}_h(\mathbf{x}^i) = \left(\frac{\phi_h^i}{\max_{j \in \Sigma(i)} \phi_h^j}, \frac{u_{h_k \in \{1 \dots d\}}^i}{\|\mathbf{u}_h^i\|}, \frac{\|\mathbf{u}_h^i\|}{\max_{j \in \Sigma(i)} \|\mathbf{u}_h^j\|}, \frac{\tilde{u}_{h_k \in \{1 \dots d\}}^i}{\|\tilde{\mathbf{u}}_h^i\|}, \frac{\|\tilde{\mathbf{u}}_h^i\|}{\max_{j \in \Sigma(i)} \|\tilde{\mathbf{u}}_h^j\|} \right) \quad (2.40)$$

can be used to combine adaptivity with respect to the norm and direction of the state and adjoint velocity vectors, in addition to the level set. Because all fields are normalized by their respective global maximum, a field much larger in magnitude cannot dominate the error estimator, meaning that the variations of all variables are fairly taken into account. This benefits problems involving more complex physics (e.g., turbulence, heat transfer, fluid-structure interaction, multiple phases, possibly in interaction with one another), all the more so in the context of topology optimization, as the difference in the spatial supports of the state and adjoint quantities (due to the non-normality of the linearized evolution operator [71]) may otherwise yield conflicting requirements in terms of the regions of the computational domain most in need of refinement.

2.8 Variational Multi-Scale Modeling

For the sake of simplicity in the notations (and as long as it does not lead to ambiguity), we omit in what follows the distinction between all continuous variables (e.g., domains, solutions, operators) and their discrete finite element counterparts, as well as the dependency of all variables on the iteration of the optimization process. The convective terms in the incompressible Navier-Stokes and Level-Set transport

equations may cause spurious node-to-node velocity oscillations. Furthermore, the equal order linear/linear approximations used for the velocity and pressure variables, albeit very desirable due to its simplicity of implementation and affordable computing cost (especially for 3D applications), may give rise to spurious pressure oscillations. To prevent these numerical instabilities, we solve here stabilized formulations cast in the Variational Multiscale (VMS) framework, that enhance the stability of the Galerkin method via a series of additional integrals over element interior. The basic idea is to split all quantities into coarse and fine scale components, corresponding to different levels of resolution, and to approximate the effect of the fine scale (that cannot be resolved by the finite element mesh) onto the coarse scale via consistently derived residual based terms.

2.8.1 Navier–Stokes Equations

In practice, the state solution is computed by time-stepping the unsteady Navier–Stokes equations with large time steps to accelerate convergence towards a steady state (the stopping criterion being here for two consecutive time steps to differ by less than 10^{-6} in L^∞ norm). In order to deal with the time-dependency and non-linearity of the momentum equation, the transport time of the time scale is assumed much smaller than that of the coarse scale. In return, the fine scale contribution to the transport velocity is neglected, and the fine scale is not tracked in time (although it is driven by the coarse-scale, time-dependent residuals and therefore does vary in time in a quasi-static manner). In-depth technical and mathematical details together with extensive discussions regarding the relevance of the approximations can be found in [72]. Ultimately, the coarse scale variational problem is formulated as

$$\begin{aligned} & \int_{\Omega} (\rho \partial_t \mathbf{u} + \rho \mathbf{u} \cdot \nabla \mathbf{u}) \cdot \mathbf{w} \, dv + \int_{\Omega} 2\mu \boldsymbol{\varepsilon}(\mathbf{u}) : \boldsymbol{\varepsilon}(\mathbf{w}) \, dv - \int_{\Omega} p(\nabla \cdot \mathbf{w}) \, dv + \int_{\Omega} (\nabla \cdot \mathbf{u}) q \, dv \\ & - \sum_{k=1}^{N_e} \int_{\Omega_k} \tau_1 \mathbf{r}_1 \cdot (\rho \mathbf{u} \cdot \nabla \mathbf{w}) \, dv - \sum_{k=1}^{N_e} \int_{\Omega_k} \tau_1 \mathbf{r}_1 \cdot \nabla q \, dv - \sum_{k=1}^{N_e} \int_{\Omega_k} \tau_2 r_2 (\nabla \cdot \mathbf{w}) \, dv \\ & = 0 \end{aligned} \quad (2.41)$$

where we have considered a discretization of Ω into N_e non-overlapping elements (triangles or tetrahedrons), Ω_k is the domain occupied by the k th element, \mathbf{r}_1 and r_2 are the momentum and continuity residuals

$$-\mathbf{r}_1 = \rho \partial_t \mathbf{u} + \rho \mathbf{u} \cdot \nabla \mathbf{u} + \nabla p, \quad -r_2 = \nabla \cdot \mathbf{u} \quad (2.42)$$

whose second derivatives vanish since we use linear interpolation functions. Finally, τ_1 and τ_2 are ad-hoc stabilization coefficients, computed on each element after [73, 74]

as

$$\tau_1 = \frac{1}{\rho(\tau_t^2(u) + \tau_d^2)^{1/2}}, \quad \tau_2 = \frac{h^2}{\tau_1} \quad (2.43)$$

with convection (transport) and diffusion-dominated limits defined as

$$\tau_t(u) = c_t \frac{u}{h}, \quad \tau_d = c_d \frac{\mu}{\rho h^2} \quad (2.44)$$

Here, u is a characteristic norm of the velocity on the element, computed as the average L^2 norm of the nodal element velocities, h is the element size, computed as its diameter in the direction of the velocity (to support using anisotropic meshes with highly stretched elements [75]), and $c_{t,d}$ are algorithmic constants taken as $c_t = 2$ and $c_d = 4$ for linear elements [73]. Equation (2.41) is discretized with a first-order-accurate time-integration scheme combining semi-implicit treatment of the convection term, implicit treatment of the viscous, pressure and divergence terms, and explicit treatment of the stabilization coefficients. All linear systems are preconditioned with a block Jacobi method supplemented by an incomplete LU factorization, and solved with the GMRES iterative algorithm, with tolerance threshold set to 10^{-6} .

2.8.2 Adjoint Navier–Stokes Equations

Application of the stabilized formulation, as described above, to the adjoint Navier–Stokes equations yields the following coarse scale variational problem:

$$\begin{aligned} & \int_{\Omega} (-\rho \mathbf{u} \cdot \nabla \tilde{\mathbf{u}} + \rho \nabla \mathbf{u}^T \cdot \tilde{\mathbf{u}}) \cdot \mathbf{w} \, dv + \int_{\Omega} 2\mu \boldsymbol{\varepsilon}(\tilde{\mathbf{u}}) : \boldsymbol{\varepsilon}(\mathbf{w}) \, dv + \int_{\Omega} \tilde{p}(\nabla \cdot \mathbf{w}) \, dv + \int_{\Omega} (\nabla \cdot \tilde{\mathbf{u}}) q \, dv \\ & - \sum_{k=1}^{N_e} \int_{\Omega_k} \tilde{\tau}_1 \tilde{\mathbf{r}}_1 \cdot (-\rho \mathbf{u} \cdot \nabla \mathbf{w}) \, dv - \sum_{k=1}^{N_e} \int_{\Omega_k} \tilde{\tau}_1 \tilde{\mathbf{r}}_1 \cdot \nabla q \, dv - \sum_{k=1}^{N_e} \int_{\Omega_k} \tilde{\tau}_2 \tilde{r}_2 (\nabla \cdot \mathbf{w}) \, dv \\ & - \int_{\Gamma_o} \rho(\mathbf{u} \cdot \mathbf{n})(\tilde{\mathbf{u}} \cdot \mathbf{w}) \, ds = \int_{\Gamma_o} \partial_{\mathbf{u}} J_s \cdot \mathbf{w} \, ds \quad (2.45) \end{aligned}$$

The associated momentum and continuity residuals read:

$$-\tilde{\mathbf{r}}_1 = -\rho \mathbf{u} \cdot \nabla \tilde{\mathbf{u}} + \rho \nabla \mathbf{u}^T \cdot \tilde{\mathbf{u}} - \nabla \tilde{p}, \quad -\tilde{r}_2 = \nabla \cdot \tilde{\mathbf{u}} \quad (2.46)$$

and the stabilization coefficients are computed on each element after [76] as:

$$\tilde{\tau}_1 = \frac{1}{(\tau_t^2(u) + \tau_d^2 + \tau_r^2)^{1/2}}, \quad \tilde{\tau}_2 = \tau_2 \quad (2.47)$$

with additional component corresponding to the reaction-dominated limit (which stems from the $\rho \nabla \mathbf{u}^T \cdot \tilde{\mathbf{u}}$ term describing the production of adjoint perturbations) defined as:

$$\tau_r = \rho \nabla u \quad (2.48)$$

where ∇u is a characteristic norm of $\nabla \mathbf{u}$ on the element, computed as the average L^2 norm of the nodal velocity gradients. It is important to note that the adjoint stabilization coefficients depend solely on \mathbf{u} , not $\tilde{\mathbf{u}}$, which is because the adjoint flow field is transported at (minus) the state velocity. Note also, Eq. (2.45) features boundary terms evaluated at the outlet, which is because the integration by part of the pressure and viscous terms unveils a boundary term

$$\int_{\partial\Omega} (\tilde{p}\mathbf{n} + 2\mu\boldsymbol{\varepsilon}(\tilde{\mathbf{u}}) \cdot \mathbf{n}) \cdot \mathbf{w} \, ds = - \int_{\Gamma_o} (\rho(\mathbf{u} \cdot \mathbf{n})\tilde{\mathbf{u}} + \partial_{\mathbf{u}} J_s) \cdot \mathbf{w} \, ds \quad (2.49)$$

due to the adjoint boundary condition (2.15). Eq. (2.45) is fully implicitly integrated, except the outflow boundary term that needs be treated explicitly for implementation convenience. Even though the last computed adjoint solution (hence pertaining to the previous design) is used to evaluate the boundary term, this simple scheme has been found to converge to identical shapes and cost function minimum, compared to solving iteratively with relaxed sub-iterations. Due to the linearity of Eqs. (2.13)-(2.12), this in turn cuts down the numerical effort, as only one single linear system needs be solved at each update step, for which we use a BCGS iterative algorithm with tolerance threshold set to 10^{-12} and LU factorization as preconditioner.

2.8.3 Interface Update Scheme

The auto-reinitialization level set problem (2.29) is solved with an SUPG method, whose stabilization proceeds from that of the ubiquitous convection-diffusion-reaction equation [77, 78]. The associated variational problem is formulated as

$$\int_{\Omega} (\partial_{\tau}\phi + \mathbf{a}_{\tau} \cdot \nabla\phi)\xi \, dv - \int_{\Omega_k} \tau_3 r_3 \mathbf{a}_{\tau} \cdot \nabla\xi \, dv = \int_{\Omega} S\xi \, dv \quad (2.50)$$

with residual

$$-r_3 = \partial_{\tau}\phi + \mathbf{a}_{\tau} \cdot \nabla\phi - S \quad (2.51)$$

and stabilization coefficient

$$\tau_3 = \frac{1}{\tau_t(a_{\tau})} \quad (2.52)$$

It is easily checked that all terms scale as $1/\Delta\tau$, so we can set $\Delta\tau = 1$ without any loss of generality because the solution is ultimately independent on the pseudo-time step value. Equation (2.50) is solved with semi-implicit treatment of the convection

term (as the convection velocity \mathbf{a}_τ depends on main unknown ϕ) and explicit treatment of the source term and stabilization coefficients. All linear systems are solved using the GMRES algorithm with incomplete LU factorization as preconditioner, and tolerance threshold set to 10^{-8} .

2.9 Conclusion

In conclusion, a primitive pseudo-code of the procedure for solving a topology optimization problem is provided in the following algorithm:

Algorithm 2 Simplified update scheme

Require: Anisotropic mesh adapted to initial level set function

- 1: **loop**
 - 2: Compute state
 - 3: Compute adjoint
 - 4: Compute cost function sensitivity
 - 5: Set displacement in the direction of steepest slope
 - 6: Update level set
 - 7: Generate anisotropic mesh adapted to new level set
-

to repeat until a maximum number of iterations or a convergence threshold has been reached. In a nutshell, this is done here using a finite element immersed numerical framework combining implicit representation of the different domains, level set description of the interface, and anisotropic remeshing capabilities. In this chapter we went through the steps 2 to 6 of Alg. 2 and reviewed the various problems involved and the numerical methods for solving them. We presented the state and adjoint equations with interface capturing and advected level set method for interface update. Finally, the IMV and VMS were introduced to stabilization of the partial differential equations. For the sake of readability, step 7 will be disserted in the following chapter. And dedicated chapters will be granted to some topology optimization applications, and to the extension of the following chapter towards large-scale problems and thermo-fluidic systems.

2.10 Résumé du chapitre en français

Ce chapitre a fourni une description détaillée des modèles numériques utilisés dans l'algorithme général d'optimisation des écoulements gouvernés par les équations de Navier-Stokes laminaires incompressibles et pilotés par des fonctions objectif formulées sur les bords du domaine de conception. Les équations d'état ont été introduites et la dérivation du système adjoint continu pour le calcul de sensibilité

par l'approche lagrangienne a été détaillée. La méthode Level-Set pour la capture d'interface a été utilisée, et son transport a été par la méthode Advected Level Set, choisie pour ses particularités de réinitialisation intégrée et de filtrage de domaine, ce qui réduit significativement les coûts de calcul. L' Immerssed Volume Method (IVM) a ensuite été introduite pour pénaliser les régions solides tout en résolvant les équations gouvernantes dans la totalité du domaine de calcul. Dans le cadre des méthodes numériques, la Variarional Multiscale Method (VMS) a été choisie pour éviter les instabilités numériques. Sa formulation variationnelle à grande échelle a été dérivée pour les équations primaires et adjointes, tout comme pour le schéma de transport d'interface. Enfin, certaines considérations numériques ont été détaillées pour des raisons pratiques liées à l'optimisation topologiques. Celles-ci incluent des contraintes géométriques (pour éviter les deux cas extrêmes où le domaine solide obstrue l'ensemble du domaine de conception ou disparaît complètement) et le filtrage et la normalisation de la sensibilité (pour garantir un déplacement maximal de l'interface par itération).

Chapter 3

Topology Optimization Framework Designed for 2D Incompressible Fluid Flows

Contents

3.1	Introduction	33
3.2	Numerical Implementation	34
3.2.1	Geometrical Constraints	34
3.2.2	Steepest Descent Update Rule	35
3.2.3	Descent Factor	36
3.3	General Algorithm	37
3.4	Numerical Benchmarks	37
3.4.1	Preliminaries	37
3.4.2	Design of a pipe bend	40
3.4.3	Design of a four terminal device	41
3.4.4	Design of a double pipe	44
3.5	Discussion	48
3.5.1	Computational efficiency	48
3.5.2	Convergence and mesh dependency	48
3.6	Résumé du chapitre en français	56

3.1 Introduction

In this chapter, we will integrate the numerical methods presented separately in Chaps. 2 into a well-structured algorithm. The primary goal of this algorithm is to achieve optimal designs for pressure drop minimization in incompressible laminar flows. Mathematically, the flow is modeled after the Navier–Stokes equations of Sec. 2.3 i.e.,

$$\begin{aligned} \rho \mathbf{u} \cdot \nabla \mathbf{u} &= -\nabla p + \nabla \cdot (2\mu \boldsymbol{\varepsilon}(\mathbf{u})) && \text{in } \Omega_f \\ \nabla \cdot \mathbf{u} &= 0 && \text{in } \Omega_f \end{aligned}$$

with the open flow boundary conditions:

$$\mathbf{u} = \mathbf{u}_i \quad \text{on } \Gamma_i, \quad p\mathbf{n} = \mu \boldsymbol{\varepsilon}(\mathbf{u}) \cdot \mathbf{n} = \mathbf{0} \quad \text{on } \Gamma_o, \quad \mathbf{u} = \mathbf{0} \quad \text{on } \Gamma$$

These equations serve as the state (or constraint equations) of the optimization problem. The cost function J_s to minimize is the net inward flux of total pressure through the boundaries, taken as a measure of the total power dissipated by a fluid dynamic device. Since the orientation of the normal \mathbf{n} yields $\mathbf{u} \cdot \mathbf{n}|_{\Gamma_i} > 0$ and $\mathbf{u} \cdot \mathbf{n}|_{\Gamma_o} < 0$, this can be expressed in the form of (2.11) using:

$$J_s = p_{tot}(\mathbf{u} \cdot \mathbf{n}) = \left(p + \frac{1}{2}\rho(\mathbf{u} \cdot \mathbf{u})\right)(\mathbf{u} \cdot \mathbf{n}) \quad (3.1)$$

The adjoint system derived from the state equations with respect to the design variables to minimize the upmentioned cost function, is then recalled from Sec. 2.4 as:

$$\begin{aligned} -\rho \mathbf{u} \cdot \nabla \tilde{\mathbf{u}} + \rho \nabla \mathbf{u}^T \cdot \tilde{\mathbf{u}} &= \nabla \tilde{p} + \nabla \cdot (2\mu \boldsymbol{\varepsilon}(\tilde{\mathbf{u}})) && \text{in } \Omega_f \\ \nabla \cdot \tilde{\mathbf{u}} &= 0 && \text{in } \Omega_f \end{aligned}$$

with the following boundary conditions:

$$\begin{aligned} \tilde{\mathbf{u}} &= -\partial_p J_s \mathbf{n} && \text{on } \Gamma_i \\ \tilde{p}\mathbf{n} + 2\mu \boldsymbol{\varepsilon}(\tilde{\mathbf{u}}) \cdot \mathbf{n} + \rho(\mathbf{u} \cdot \mathbf{n})\tilde{\mathbf{u}} &= -\partial_{\mathbf{u}} J_s && \text{on } \Gamma_o \\ \tilde{\mathbf{u}} &= \mathbf{0} && \text{on } \Gamma \end{aligned}$$

The derivatives of (3.1) needed to complete the derivation of the adjoint boundary conditions deduce as:

$$\partial_p J_s = \mathbf{u} \cdot \mathbf{n}, \quad \partial_{\mathbf{u}} J_s = p_{tot}\mathbf{n} + \rho(\mathbf{u} \cdot \mathbf{n})\mathbf{u} \quad (3.2)$$

The state and adjoint solutions are then used to compute the sensitivity of the cost function with respect to the design variable via first-order gradient descent methods,

for instance the simplest steepest-descent algorithm implemented herein moves down the cost function, in the direction of the steepest slope using:

$$\beta = -\mu(\nabla\tilde{\mathbf{u}} \cdot \mathbf{n}) \cdot (\nabla\mathbf{u} \cdot \mathbf{n})$$

Finally, this displacement is included in the transport equation of the interface (detailed in Sec. 2.6), we recall Eq. (2.29):

$$\partial_\tau\phi + \mathbf{a}_\tau \cdot \nabla\phi = S$$

The optimization problems addressed in this chapter are all inspired by problems previously investigated in the literature. By doing so, we aim to evaluate the capabilities of the proposed method and emphasize its advantages over existing methods. The benchmark for this evaluation will consist of the design of a bend pipe, a four-terminal device, and a double pipe. Finally, we will conclude with a discussion and comparison of the obtained results.

3.2 Numerical Implementation

Prior to tackling complete optimization problems, some numerical considerations should be accounted for practical reasons linked to topology optimization. These numerical considerations and their corresponding reasons are elaborated in the following.

3.2.1 Geometrical Constraints

Fluid flow topology optimization is generally performed under geometrical constraints, typically, constant or upper bounded surfaces and/or volumes to avoid the two extreme cases of the solid domain clogging the entire design domain (as in pressure drop minimization problems), or disappearing altogether (as in drag minimization problems). This is usually done adding penalty terms to the Lagrangian (each of which consists of an empirical penalty parameter multiplied by a measure of violation of the constraint), whose variations with respect to the state and design variables snowballs into the derivation of the adjoint problem and of the cost function sensitivity. Here, the constraint of a constant volume of fluid V_{target} is applied a posteriori, i.e., we solve the unconstrained problem presented in Sec. 2.3 (in the sense that no penalty term is added to the Lagrangian, although the optimization remains subject to Navier–Stokes as state equations). Once the convective level set method presented in Sec. 2.6 has updated the interface position, a first pass of anisotropic mesh adaptation is performed, after which the volume of the fluid domain is computed as

$$V_\varphi = \int_\Omega H_\epsilon(\varphi) dv \tag{3.3}$$

where H_ϵ is the smoothed Heaviside function on the fluid domain defined as

$$H_\epsilon(\varphi) = \begin{cases} 1 & \text{if } \varphi < -\epsilon \\ \frac{1}{2} \left(1 - \frac{\varphi}{\epsilon} - \frac{1}{\pi} \sin \left(\pi \frac{\varphi}{\epsilon} \right) \right) & \text{if } |\varphi| \leq \epsilon \\ 0 & \text{if } \varphi > \epsilon \end{cases} \quad (3.4)$$

ϵ is a regularization parameter set to $2h_\perp$. A simple dichotomy approach is then used to optimize a constant deformation $\delta\varphi$ meant to enlarge ($\delta\varphi < 0$) or shrink ($\delta\varphi > 0$) the fluid domain, until the difference $|V_{\varphi+\delta\varphi} - V_{target}|$ between the actual and target volumes drops below a certain tolerance, at which point we cut off $\varphi + \delta\varphi$ and perform a second pass of mesh adaptation. Two points are worth mentioning: first, because each offset changes the min-max values of the truncation, the above procedure requires knowledge of the level set φ (not just the filtered level set ϕ). A brute force algorithm therefore performs beforehand a complete reconstruction of the distance function from the zero iso-value of ϕ , as only the filtered level set (not the level set) is evolved during the convection-reinitialization step. Second, only small deformations are considered so that no intermediate mesh adaptation passes are required. By doing so, the total cost is essentially that of performing the second pass of mesh adaptation, as further discussed in the following.

3.2.2 Steepest Descent Update Rule

In practice, the displacement used to perform the update step is defined as

$$\beta = -\theta \frac{\mu(\nabla \tilde{\mathbf{u}} \cdot \mathbf{n}) \cdot (\nabla \mathbf{u} \cdot \mathbf{n}) \chi_\Gamma(\mathbf{x})}{\max_{\Omega} \mu(\nabla \tilde{\mathbf{u}} \cdot \mathbf{n}) \cdot (\nabla \mathbf{u} \cdot \mathbf{n}) \chi_\Gamma(\mathbf{x}) \prod_l \zeta(\|\mathbf{x} - \mathbf{x}_s^l\|)} \quad (3.5)$$

where $\theta > 0$ is a descent factor controlling the step taken in the gradient direction, and χ_Γ and ζ are activation functions between 0 and 1 ensuring that the design is fittingly updated only in relevant regions of the computational domain. More details are as follows:

- χ_Γ is a binary filter returning a value of 1 only at nodes within a distance E of the interface. This is because the normal vector in a level set framework is computed as $\mathbf{n} = \nabla\phi/|\nabla\phi|$, so the displacement is non-zero in the whole fluid domain, even far from the interface where \mathbf{n} has unit norm because $|\nabla\phi|$ only tends asymptotically to zero. In return, the update step can break down numerically at nodes nearly equidistant from two subparts of the interfaces (for instance the centerline of a channel).

- ζ is a smooth filter assigning 0 value to a position $\mathbf{x}_s \in \partial\Omega$ singled out prior to optimization, because the flow there may be driven to a singularity, and ill-defined velocity gradients may cause large, unphysical displacements. Such singularities can be dealt with numerically by appending fluid/solid Dirichlet boundary conditions to the level set convection-reinitialization problem. Nonetheless, they must not be included in the normalization step to avoid forcing excessively small displacements along the remaining part of the interface, and thereby considerably slowing down the convergence rate of the iterative optimization process. We use here hyperbolic tangent filters

$$\zeta(r) = \frac{1}{2} + \frac{1}{2} \tanh \left(\alpha_s \tan \left(-\frac{\pi}{2} + \frac{\pi}{2} \frac{r}{r_s + \epsilon_{s1}} + \epsilon_{s2} \right) \right) \quad (3.6)$$

increasing from 0 to 1 within a distance of $2r_s$ from the singularity, with r_s a transition radius such that

$$4r_s < \min_{l,m} \|\mathbf{x}_s^l - \mathbf{x}_s^m\| \quad (3.7)$$

to prevent overlaps, α_s a steepness parameter controlling the sharpness of the transition, and $\epsilon_{s1,2}$ small regularization parameters to avoid local discontinuities.

Ultimately, the above filtering and normalization steps ensure that the level set is updated using a displacement that is non-zero only in a thin layer of thickness E about the interface, minus a certain number of spheres of radius r_s centered on the singularities.

3.2.3 Descent Factor

It follows from Eq. (3.5) that the descent factor θ physically represents the maximum displacement amplitude over the update region of interest. In practice, though, the actual numerical displacement (estimated from the difference between zero iso-value of the filtered level set before and after transport) has been found to be well below its theoretical value. This is because the state and adjoint velocities are forced to zero in the solid domain, so the displacement (driven by the velocity gradients) is also zero everywhere in the solid, except in a very narrow region about the interface, typically a couple of elements thick. As a result, it is not possible to explicitly control the displacement achieved numerically at each iteration. A simple scheme to do so would have been to repeatedly evolve the interface with a small descent factor until the difference between the cumulated and target displacement drops below a certain tolerance, but the interface can be evolved only once per update step, as the gradient information is lost if the displacement happens to be in the

direction of the solid (for the same reason mentioned above). We thus tune the descent factor manually on a case by case basis, for the achieved displacement to be slightly smaller than the cut-off thickness. This has been found to be a satisfactory trade-off between accuracy and numerical effort, as the number of iterations required for convergence remains very affordable, and the position of the evolved interface is accurately tracked (displacements larger than the cut off thickness conversely move the level set into regions of the computational domain lacking the proper mesh refinement, which has been found to ultimately affect the accuracy of the interface representation).

3.3 General Algorithm

Figure 3.1 shows the flowchart of the implemented topology optimization algorithm, in which anisotropic mesh adaptation is key to capture the interface with the highest precision possible. Note, as a consequence of the level set-based technique used to enforce the volume of fluid constraint, convergence is achieved not when the displacement is identically zero (as would be the case using a penalized Lagrangian approach), but when the displacement is uniform along the interface. This is not easily assessed on the fly, though, so we rather iterate until a maximum number of iterations has been reached and assess convergence a posteriori; see Sec. 3.5.

3.4 Numerical Benchmarks

This section assesses the accuracy and efficiency of the numerical framework through three examples of two-dimensional ($d = 2$) topology optimization problems recently considered in the fluid mechanics literature. It is thus worth insisting that the novelty lies not in the associated optimal designs themselves, but in the accuracy to which the optimal interfaces are captured in the simulation model.

3.4.1 Preliminaries

All examples feature either a single inlet or multiple identical inlets of width e_i , and either a single outlet, or multiple identical outlets of width e_o . Parabolic flow profiles normal to the boundary are prescribed at all inlets, as defined by

$$\mathbf{u}_i = \frac{3q_i}{2e_i} \left(1 - \left(\frac{2r}{e_i} \right)^2 \right) \mathbf{n} \quad (3.8)$$

where q_i is the injected volumetric flow rate (the same for all inlets), and r is the distance from the inlet centerline. For each case, the sole control parameter is the

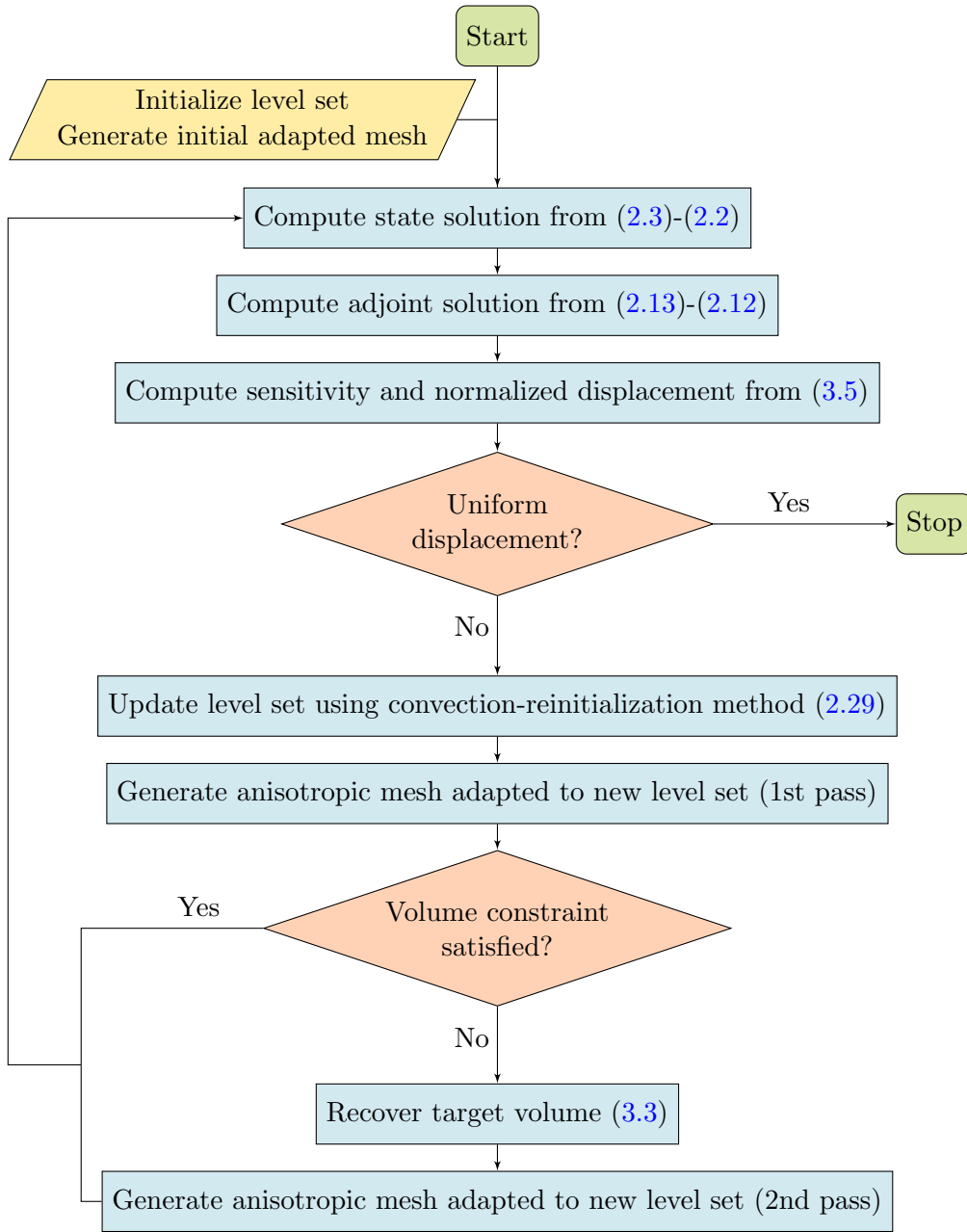


Figure 3.1: Flowchart of performance topology optimization procedure.

Reynolds number defined as $Re = \rho q_i / \mu$ (which amounts to using the inlet width and mean inlet velocity as reference length and velocity scales).

The remainder of the practical implementation details are as follows:

- All design domains are initialized with spherical solid inclusions coming in

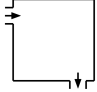
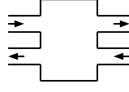

			
$\Omega = [0; 1] \times [0; 1]$	$[0; 0.7] \times [0; 1]$	$[0; 1.5] \times [0; 1]$	Design domain
$V_{target} = 0.25$	0.28	0.5	Target volume of fluid
$Re = 2$	\gg	\gg	Reynolds number
$q_i = 0.0266$	\gg	0.0222	Injected volumetric flow rate
$e_i = 0.2$	\gg	0.166	Inlet width
$e_o = 0.2$	\gg	0.166	Outlet width
$l_c = 0.1$	\gg	\gg	Conveying pipes length
$N_n = 30000$	\gg	40000	Nb. mesh nodes
$N_{el} = 60000$	\gg	80000	Nb. mesh elements
$h_{\perp} = 0.0001$	\gg	\gg	Min. interface normal mesh size
$\Delta t = 0.1$	\gg	\gg	CFD Numerical time step
$E = 0.005$	\gg	\gg	Level set cut off thickness
$ \delta\varphi = 0.001$	\gg	\gg	Initial volume recovery offset
$r_s = 0.0125$	\gg	\gg	Transition radius
$\alpha_s = 2.1$	\gg	\gg	Sharpness parameter
$(\epsilon_{s1}, \epsilon_{s2}) = (0.0005, 0.005)$	\gg	\gg	Regularization parameters

Table 3.1: Numerical parameters for the pipe bend, four terminal device and double pipe topology optimization problems.

various sizes, adjusted for the initial volume¹ of fluid to match the target within the desired tolerance (which essentially removes the need to create new holes by a dedicated nucleation mechanism). The admissible error on the target volume is set to 1%.

- Leads of width l_c appended normal to the boundary are used to systematically convey the fluid into and out from the design domain. This is for numerical consistence, as the exact problem formulation may vary depending on the case, the reference and the problem dimensionality, and it is not always clear whether such leads are included in the design domain (which they are here, although they are not considered in the volume constraint, neither in definition of the target volume nor in the computation of the volume of fluid).
- Since the reference design domains (without the leads) consist of square and rectangular cavities, the singular points excluded from the displacement nor-

¹Actually cross-sectional area or volume per unit length in the third dimension since $d = 2$, but we choose to keep the volume terminology for the sake of generality

malization step are the sharp intersections between the leads and the boundary of the cavities and the leads (without it being a consequence of explicitly representing the leads, as the exact same procedure has been found suitable without such appendage).

- The leads are excluded from the displacement normalization step, for which we simply add to the max argument of (3.5) a binary filter returning a value of 0 at all nodes located inside the pipes. This is again to avoid slowing down the convergence rate of the iterative optimization process, as the maximum displacement is otherwise located in the leads (because the easiest way to minimize the dissipated power is to suppress the flow by having the solid entirely clogging the leads).
- Boundary conditions are appended to the auto-reinitialization level set equation, under the form of fluid at the inlet and outlet, and solid everywhere else.

Finally, all meshes have been checked to have an element-to-node ratio close to 2 (as should be for denser mesh made up of triangular elements). The mesh information is thus documented in the following in terms of its equivalent number of elements $N_{el} = 2N_n$ to ease the comparison with the available literature.

3.4.2 Design of a pipe bend

We consider first the design of a pipe bend, a standard example for topology optimization in fluid dynamics [79, 80, 81, 82, 7, 10] used to provide a first verification and characterization of the method. All relevant problem parameters are given in Tab. 3.1. The design domain is a square cavity of unit length, that has one inlet (left side) and one outlet (bottom side); see Fig. 3.2. The aim is to determine the optimal design of the pipe bend that connects the inlet to the outlet and minimizes the dissipated power subject to the constraint that the fluid must occupy 25% percent of the cavity (the same volume as a quarter torus fitting exactly to the inlet and outlet).

A total of 400 iterations has been run with 60000 mesh elements, as illustrated in Fig. 3.3 by the anisotropic adapted mesh, zero iso-value of the level set function and velocity norm of a selected sample. The method is found to easily handle the multiple topological changes (e.g., merging or cancellation of holes) occurring over the course of optimization. Also, consistently with the results in Sec. 2.7, all meshes exhibit the expected refinement and deformation, with coarse and regular elements away from the interface between solid and fluid (all the more so in the solid domain, where only a few ten elements are used), but fine, extremely stretched elements on either side of the interface (for the velocity to smoothly transition to zero across the boundary

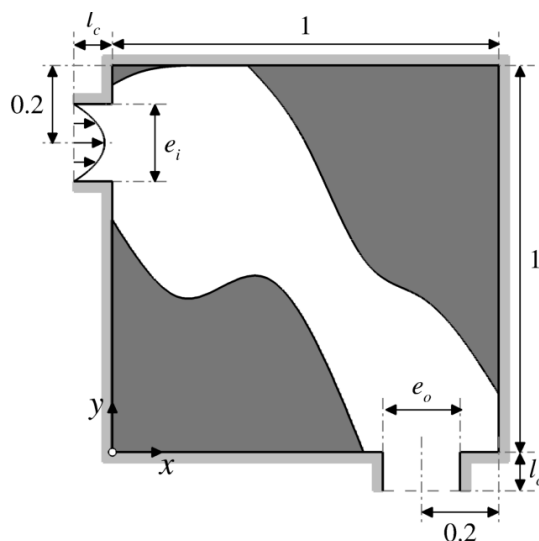


Figure 3.2: Set-up of the pipe bend problem. The light gray shade denotes parts of the boundary where solid boundary conditions are appended to level set auto-reinitialization equation.

layer); see the close-up in Fig. 3.4. In return, the interfaces are sharply captured, not only at optimality but during all stages of the optimization. This represents a major improvement in accuracy of the geometric representation with respect to the available recent literature, as even traditional (isotropic) adaptive mesh refinement techniques have been shown to yield quality issues (staircase effects) in smoothly curved regions. Ultimately, we obtain an almost straight channel nearly identical to that documented in [79] (albeit with a higher resolution as it can be seen in Fig. 3.5), which is because most energy is dissipated by shear at low Reynolds numbers, so an optimal flow pipe is preferably as short and wide as possible. The obtained results are further discussed in Sec. 3.5, with particular emphasis on the convergence rate and sensitivity of the optimal (and the optimization path) to the number of nodes.

3.4.3 Design of a four terminal device

Our second numerical example deals with minimization of the power dissipation in a four-terminal device [83]. This is a follow-up to the previous bend pipe problem, in which the cavity features a rectangular cavity of unit height and aspect ratio 0.7:1, together with two inlets and two outlets distributed antisymmetrically on the left and right sides to level up the complexity; see Fig. 3.6 for a sketch of configuration and Tab. 3.1 for the remaining problem parameters. The aim is to determine the optimal design that connects the inlets to the outlets, subject to the constraint that the fluid must occupy 40% percent of the cavity (the same volume as two straight

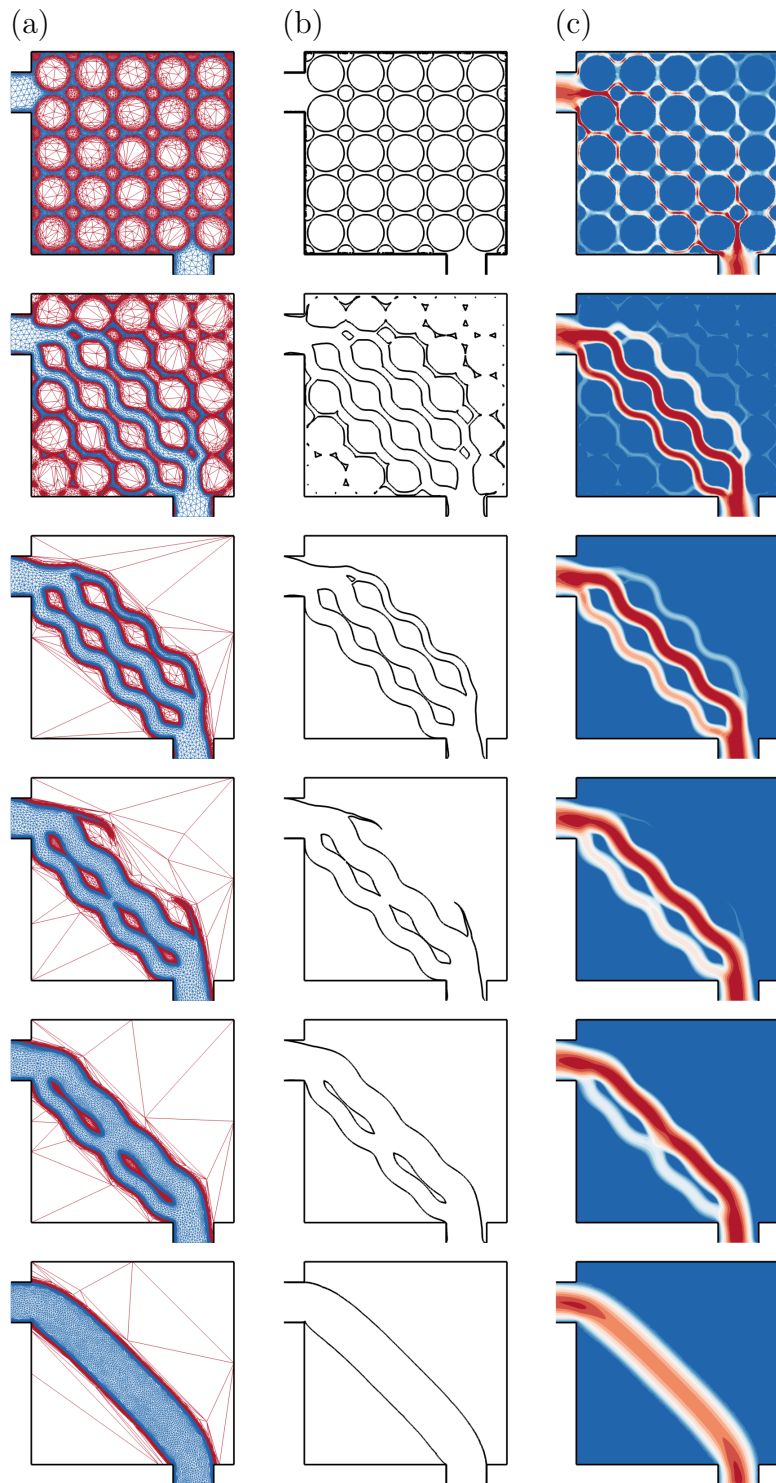


Figure 3.3: Designs of a pipe bend sampled over the course of optimization using the parameters given in Tab. 3.1. (a) Anisotropic adapted mesh. (b) Zero iso-value of the level set function. (c) Norm of the velocity vector. The optimal pipe bend is shown at the bottom.

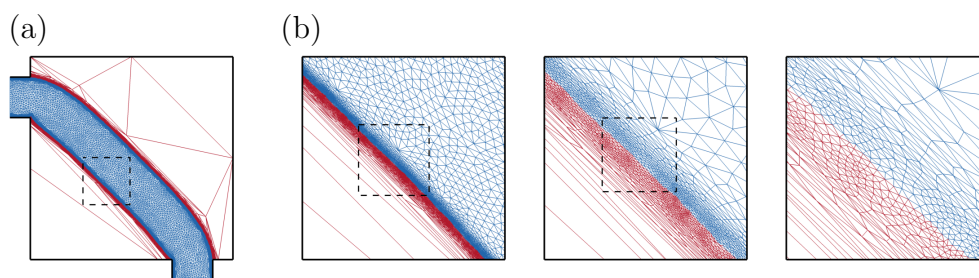


Figure 3.4: (a) Anisotropic adapted mesh of the optimal pipe bend. (b) Successive close-ups.



Figure 3.5: Optimal designs for the Bend Pipe problem of [79] showcasing the staircase effect. The computation was performed on regular grid type meshes of respectively 2500 (to the left) and 10000 (to the right) elements.

parallel pipes fitting the upper and lower pairs of inlet/outlet).

A total of 300 iterations has been run with 60000 mesh elements; see Fig. 3.7 showing the anisotropic adapted mesh, zero iso-value of the level set function and velocity norm of a selected sample collected over the course of optimization. All adapted meshes are especially reminiscent of their bend pipe counterparts, with coarse, regular elements away from the interface and fine, elongated elements on either side of the interface; see Fig. 3.8, and allow accurately representing the boundary layers at all stages of the optimization (even in the leads). Ultimately, we obtain a pair of U-turns connecting each inlet to the outlet on the same side of the design domain. This is consistent with literature results showing that the U-turn solution is favored over the simpler parallel channels solution at aspect ratios larger than 0.6:1 [83, 7, 10], only the present solution is captured with superior accuracy. This is again because optimal pipes at low Reynolds numbers are preferably short and wide, and the cost of bending the fluid stream is low as that most fluid flows in the (shorter) inner region.

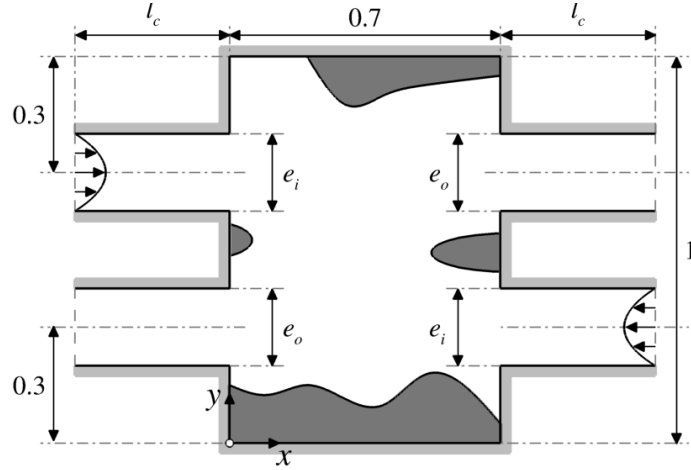


Figure 3.6: Set-up of the four terminal device problem. The light gray shade denotes parts of the boundary where solid boundary conditions are appended to level set auto-reinitialization equation.

3.4.4 Design of a double pipe

In the third numerical example, we consider the double pipe problem, another benchmark for fluid topology optimization [79, 84, 82, 85], whose parameters are provided in Tab. 3.1. The design domain is a rectangular cavity of unit height and aspect ratio 3:2, that has two inlets (left side) and two outlets (right side); see Fig. 3.9. The aim is to determine the optimal design of the double pipe that connects the inlets to the outlets and minimizes the dissipated power subject to the constraint that the fluid must occupy 33.3% percent of the cavity (the same volume as two straight parallel pipes fitting the upper and lower pairs of inlet/outlet).

A total of 3000 iterations has been run with 80000 mesh elements (due to the larger design domain), during which the design goes through several complex stages all accurately represented on anisotropic adapted meshes, as evidenced by the selected sample shown in Fig. 3.10-3.11. Ultimately, the optimal design resembles a single-ended wrench, with the two inlet pipes connecting to a wider pipe in the center of the domain, that itself connects to a single outlet (either the upper or the lower outlet since the setup has horizontal reflectional symmetry). Since the optimal flow pipe at low Reynolds numbers is preferably short and wide, this represents the better trade-off between transporting fluid the shortest way, and transporting it in the widest possible pipe. Note, the obtained solution differs from the double-ended wrench documented in [79, 84, 82], in which the center pipe ultimately connects to the two outlet. This is because the authors prescribe parabolic flow profiles at both the inlets and the outlets. The flow is thus forced to exit via both outlets, while

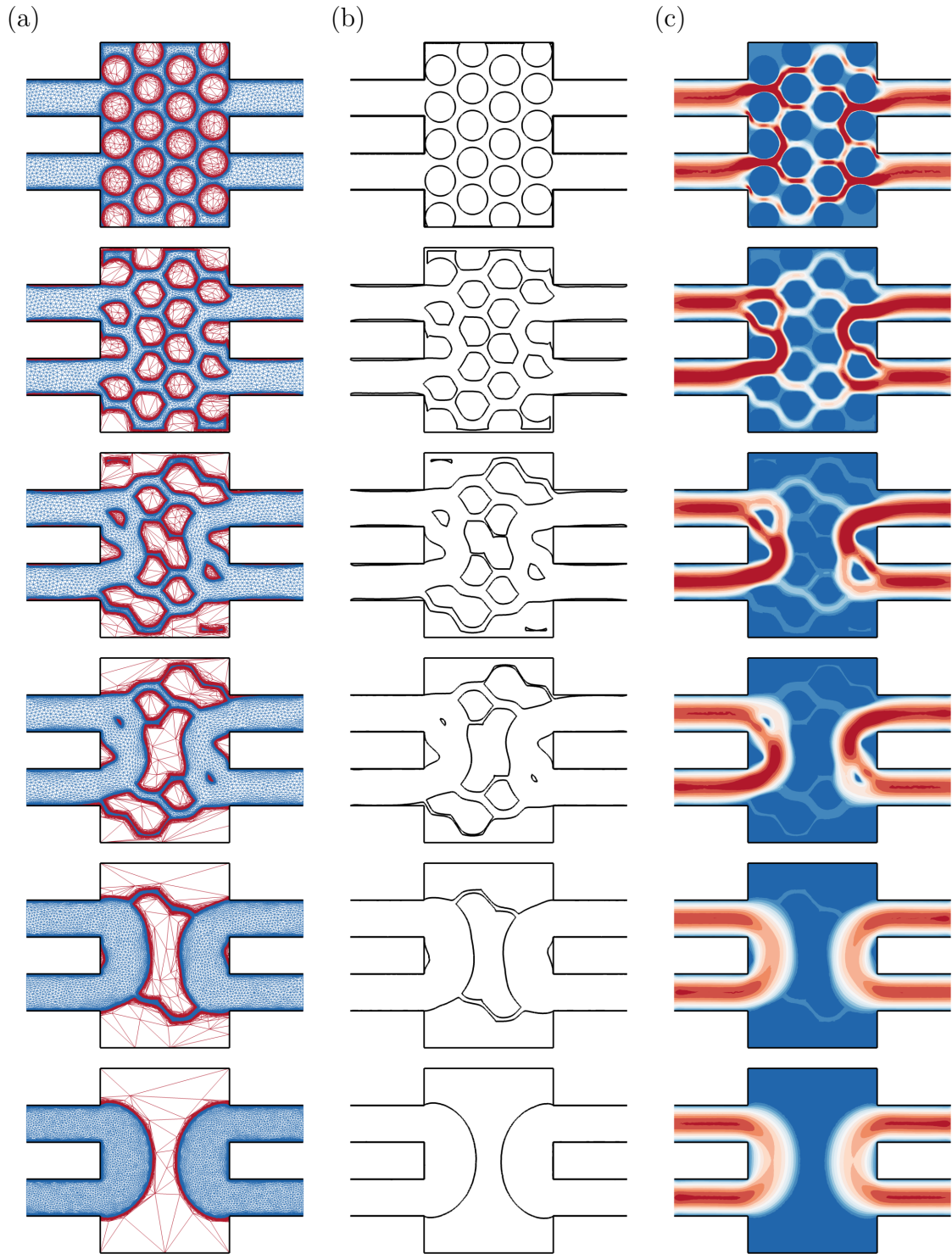


Figure 3.7: Designs of a four terminal device sampled over the course of optimization using the parameters given in Tab. 3.1. (a) Anisotropic adapted mesh. (b) Zero iso-value of the level set function. (c) Norm of the velocity vector. The optimal four terminal device is shown at the bottom.

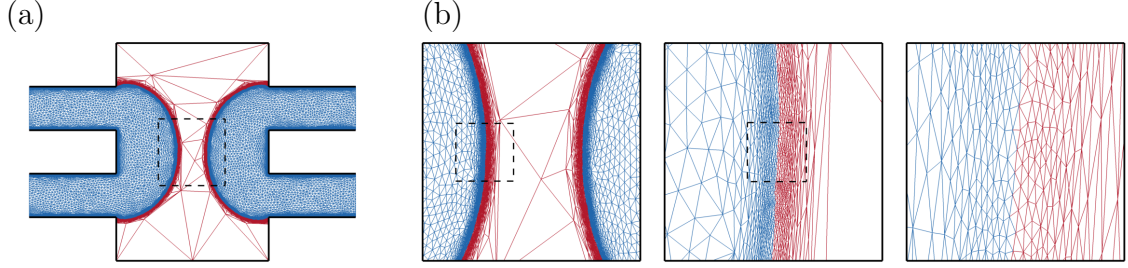


Figure 3.8: (a) Anisotropic adapted mesh of the optimal four terminal device. (b) Successive close-ups.

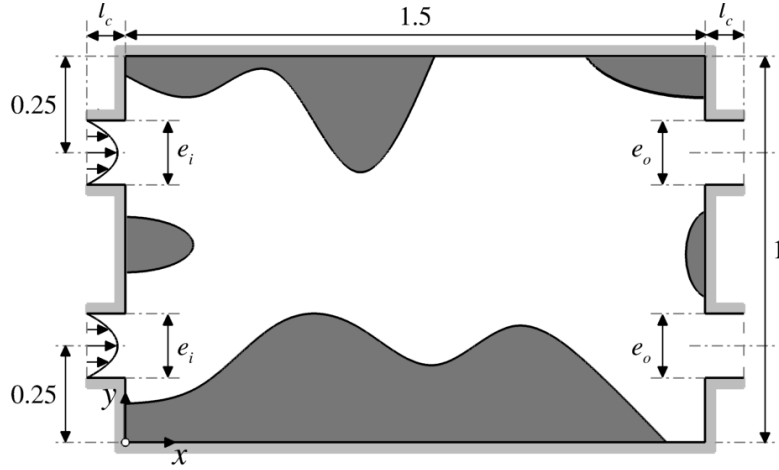


Figure 3.9: Set-up of the double pipe problem. The light gray shade denotes parts of the boundary where solid boundary conditions are appended to level set auto-reinitialization equation.

it can exit via a single outlet under the more physical zero pressure/zero viscous stress condition used here, which allows saving the cost of pipe splitting [85]. The number of iterations run for this case (larger by one order of magnitude compared to the pipe bend and four terminal problems) is easily explained by the fact that the optimization must bypass the basin of attraction of the double-ended wrench, that keeps being a local minimizer. This is all the more difficult because the cost function of both minimizers differs by only 10%, but we show in Sec 3.5 that this particular feature is ultimately very sensitive to the number of nodes used to perform the mesh adaptation.

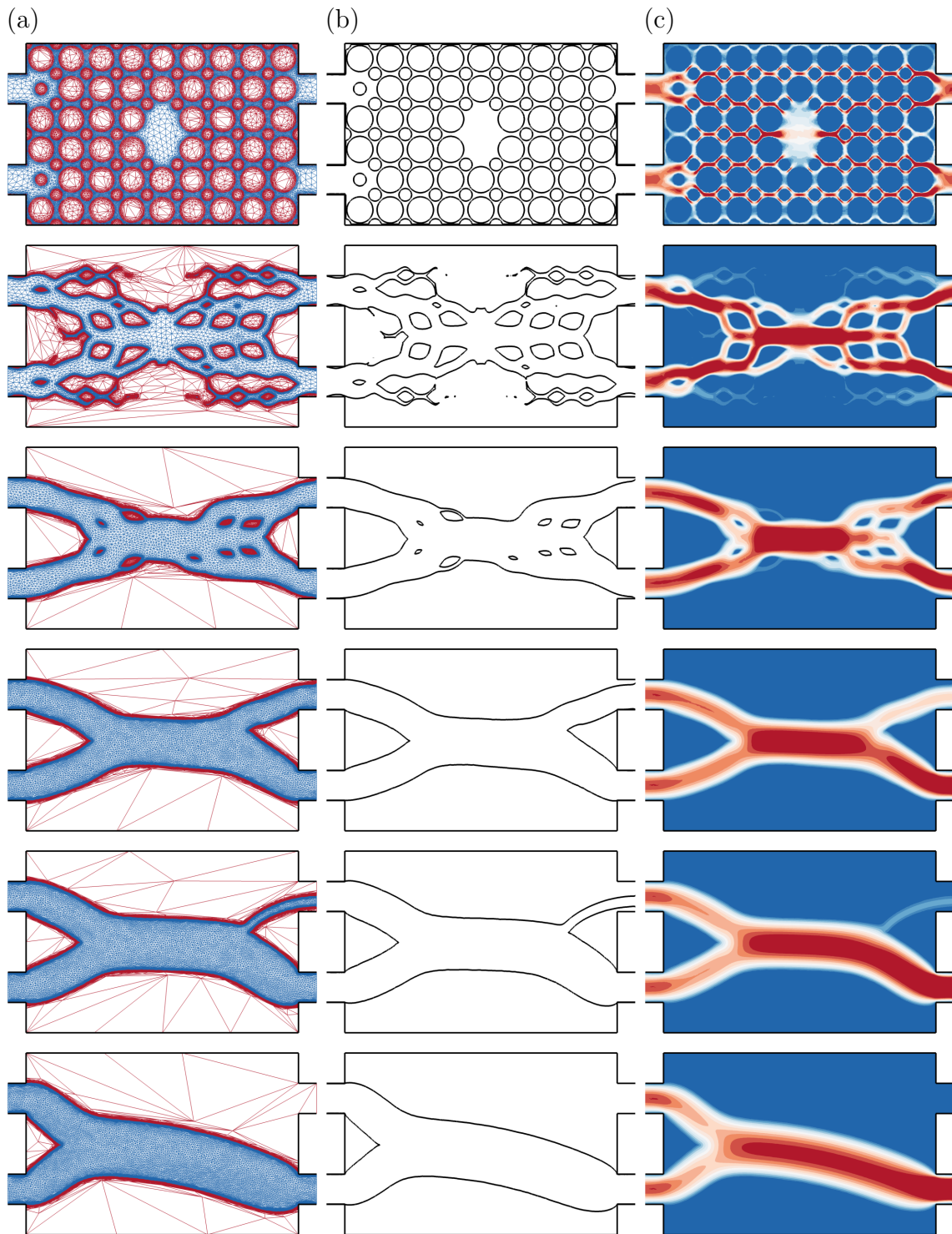


Figure 3.10: Designs of a double pipe sampled over the course of optimization using the parameters given in Tab. 3.1. (a) Anisotropic adapted mesh. (b) Zero iso-value of the level set function. (c) Norm of the velocity vector. The optimal double pipe is shown at the bottom.

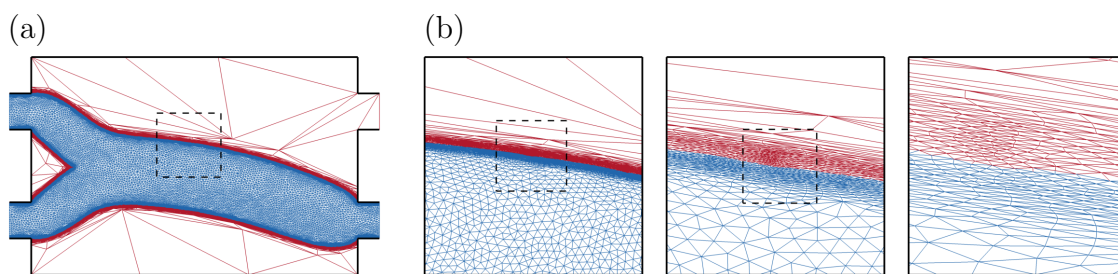


Figure 3.11: (a) Anisotropic adapted mesh of the optimal double pipe. (b) Successive close-ups.

3.5 Discussion

3.5.1 Computational efficiency

Figure 3.12 presents detailed timing results obtained by averaging 300 dedicated update steps (100 for each case presented in Secs 3.4.2-3.4.4) performed with the parameters compiled in Tab. 3.1. As could have been expected, the cost of an iteration is dominated by that of computing the state solution (about 10 Navier–Stokes iterations representing 40% of the total cost, which can be scaled down substantially in the context of steady-state problems using an iterative Newton-like method), and otherwise by that of performing the two passes of mesh adaptation (also about a cumulative 40% of the total cost). Meanwhile, the cost of both geometrically reinitializing the signed distance function level set and of optimizing the volume constraint offset is very affordable (less than 1% in total, with 4-5 dichotomy iterations needed to reach the desired accuracy of 1%). Such conclusions presumably carry over to any other problem of same dimensionality, tackled with comparable parameters.

3.5.2 Convergence and mesh dependency

Since we perform here a fixed number of iterations, convergence is assumed here when the sliding average over the 10 latest cost functional values is less than a prescribed error set to 2% of the cost functional average over the 50 final iterations. This is because (i) the cost function keeps varying even after convergence because the mesh slightly changes between consecutive iterations (and so does the volume of fluid as long as the deviation from the target does not exceed the admissible error), and (ii) assuming convergence simply when the relative difference between two successive cost functional values is less than a prescribed error has been found to yield premature convergence to the double-ended wrench local minimizer of the double pipe problem. Note, all data discussed in the following pertain to a single optimization run. Rigorously speaking, convergence is best assessed by averaging

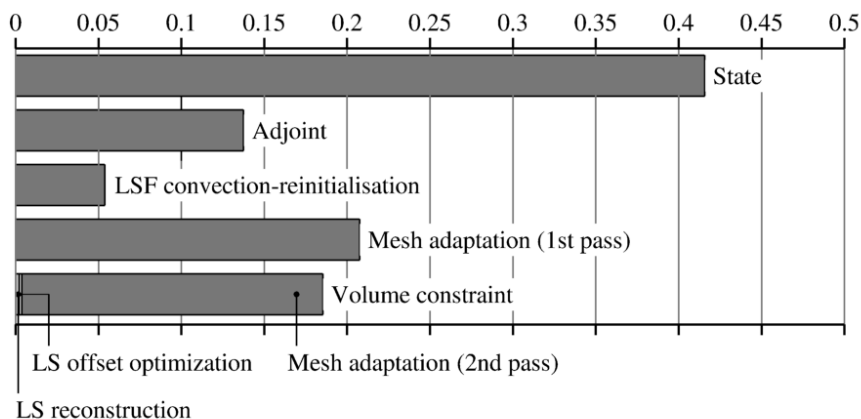


Figure 3.12: Computational cost of the implemented algorithm, as obtained averaging 300 update steps of the pipe bend, double pipe, and four terminal device problems (100 steps for each) using the simulation parameters provided in Tab. 3.1. All results normalized to achieve unit average time per iteration. The LS and LSF labels stand for level set (LS) and filtered level set (LSF), respectively.

results over multiple independent runs, as mesh adaptation procedure is not a deterministic process (the outcome depends on the processors and number of processors used, and any initial difference propagates over the course of optimization because the meshes keep being adapted at each iteration), but we have found very little variability by doing so.

Exhaustive convergence data are provided in Tab. 3.2 for all three cases reported above. Putting the obtained results in a broader context is uneasy because convergence is rarely documented in the literature, and even when it is, the key factors explicitly affecting convergence (e.g., initial shape, convergence criterion and threshold) are not. In practice, our literature review did not reveal any other study putting all these levels of information together. Here, the bend pipe problem converges within 306 iterations, which is well above the convergence iteration reported in the seminal paper by Borrvall & Peterson [79] that lies in a range from 64 (using 2500 mesh elements) to 85 (using 10000 mesh elements). A first explanation is that all designs in the aforementioned reference are evaluated on the same isotropic mesh, hence the descent factor is not constrained by the thickness of the level set, and larger values can be used to speed up convergence. Another possibility further discussed below is that most studies in the literature rely on a limited number of elements in a range from 5000 to 20000, while we use a much larger value (which is on purposes to equally assess all steps of the optimization) that ultimately slows down the convergence rate.

A first important point is that such a large number of nodes is mostly useful during the early stage of optimization, where the many solid inclusions dramatically

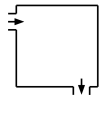
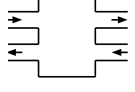
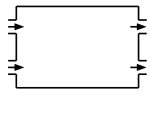
Convergence iter.	Cost function	Nb. mesh elements	
295	33.1	80000	
306	32.7	60000	
212	32.9	40000	
148	32.1	20000	
153	68.9	80000	
129	69.1	60000	
104	69.0	40000	
68	68.6	20000	
2460	68.6	105000	
1750	67.6	80000	
2130	68.2	55000	
1594	67.0	25000	

Table 3.2: Convergence data for the pipe bend, four terminal device and double pipe topology optimization problems. All cost function values made non dimensional using the inlet width and mean inlet velocity (equivalently, using $\rho q_i^3 / e_i^2$ as reference cost functional value).

increase the surface of the interfaces that needs be captured. In practice, the latter has been found to decrease significantly after the first dozens of iterations (by a factor of 3-10 depending on the case); see Fig. 3.13(a) showing the surface area computed over the first 200 iterations as

$$S_\varphi = \int_{\Omega} \delta_\epsilon(\varphi) \, dv \quad (3.9)$$

where δ_ϵ is the Dirac function

$$\delta_\epsilon(\varphi) = \begin{cases} \frac{1}{2\epsilon} \left(1 + \cos \left(\pi \frac{\varphi}{\epsilon} \right) \right) & \text{if } |\varphi| \leq \epsilon \\ 0 & \text{if } |\varphi| > \epsilon \end{cases} \quad (3.10)$$

smoothed with the same regularization parameter ϵ as the Heaviside function (3.4). A second important point is that the anisotropic mesh adaptation algorithm refines the mesh in hierarchical importance of the level set gradient. If new geometrical features appear in the solution (associated with high gradients), the mesh is automatically coarsened in regions with lower gradient and refined near the newly emerging features. If the number of nodes is large (as has been the case so far), the decrease in the interface surface area allows resolving finer, more complex patterns

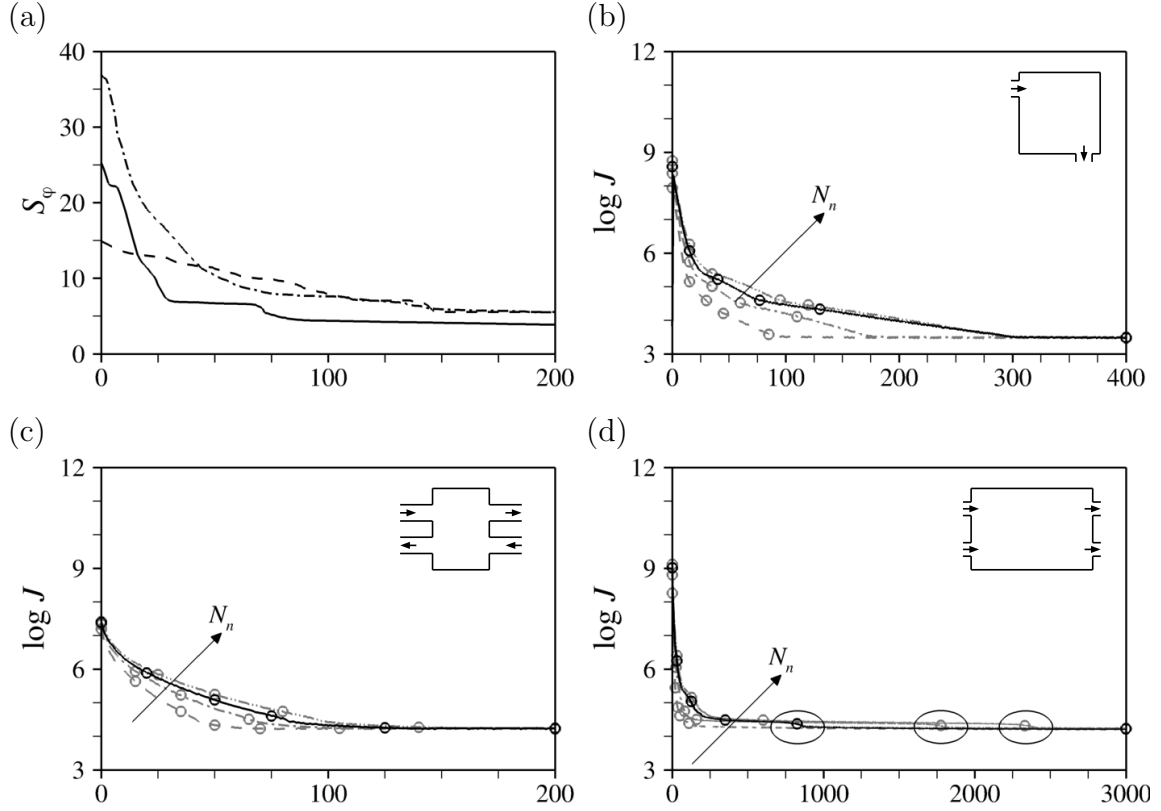


Figure 3.13: (a) Interface surface area computed over the first 200 iterations for the bend pipe (solid line), four terminal device (dashed line) and double pipe (dash-dotted line) problems, using the parameters given in Tab. 3.1. (b) Convergence history for the bend pipe problem with 60000 (in black), 20000 (dashed line), 40000 (dash-dotted line) and 80000 (dash-dot-dotted line) mesh elements. The circle symbols mark the random iterations sampled in Figs. 3.3-3.14. (c) Same as (b) for the four terminal device problem. The circle symbols mark the random iterations sampled in Figs. 3.7-3.15. (d) Same as (b) for the double pipe problem with 80000 (in black), 25000 (dashed line), 55000 (dash-dotted line) and 10500 (dash-dot-dotted line) mesh elements. The circle symbols mark the random iterations sampled in Figs. 3.10-3.16. The ellipses at the bottom indicate the transition from the double-ended wrench to the single-ended wrench minimizer. All cost function values made non dimensional using the inlet width and mean inlet velocity (equivalently, using $\rho q_i^3 / \epsilon_i^2$ as reference cost functional value).

without degrading the accuracy in other parts of the design domain, because the coarsened regions are actually over-resolved. This shows through the progressive mesh refinement in the fluid domain in Figs. 3.3-3.10, as more and more elements

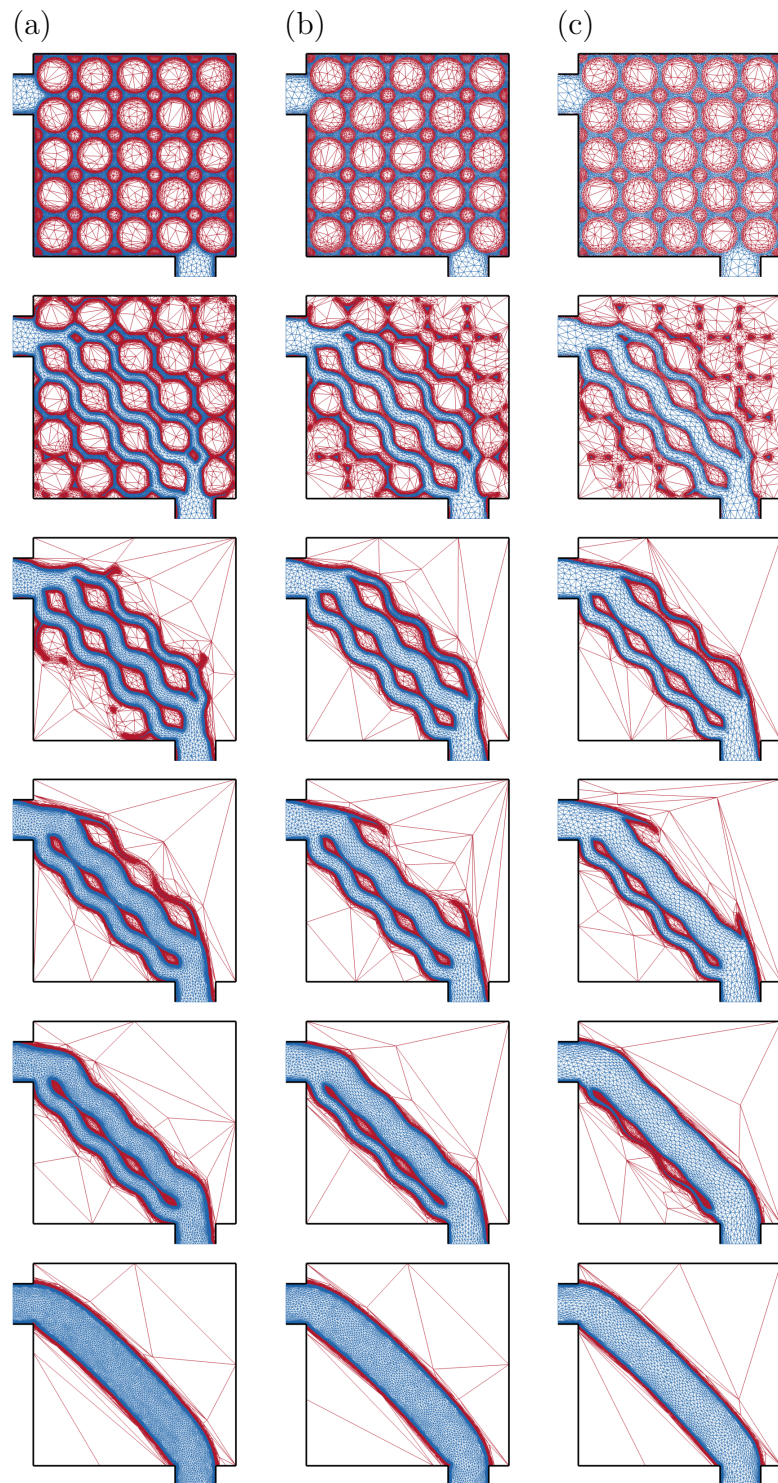


Figure 3.14: Anisotropic meshes of a pipe bend sampled over the course of optimization, using (a) 80000, (b) 40000 and (c) 20000 mesh elements.

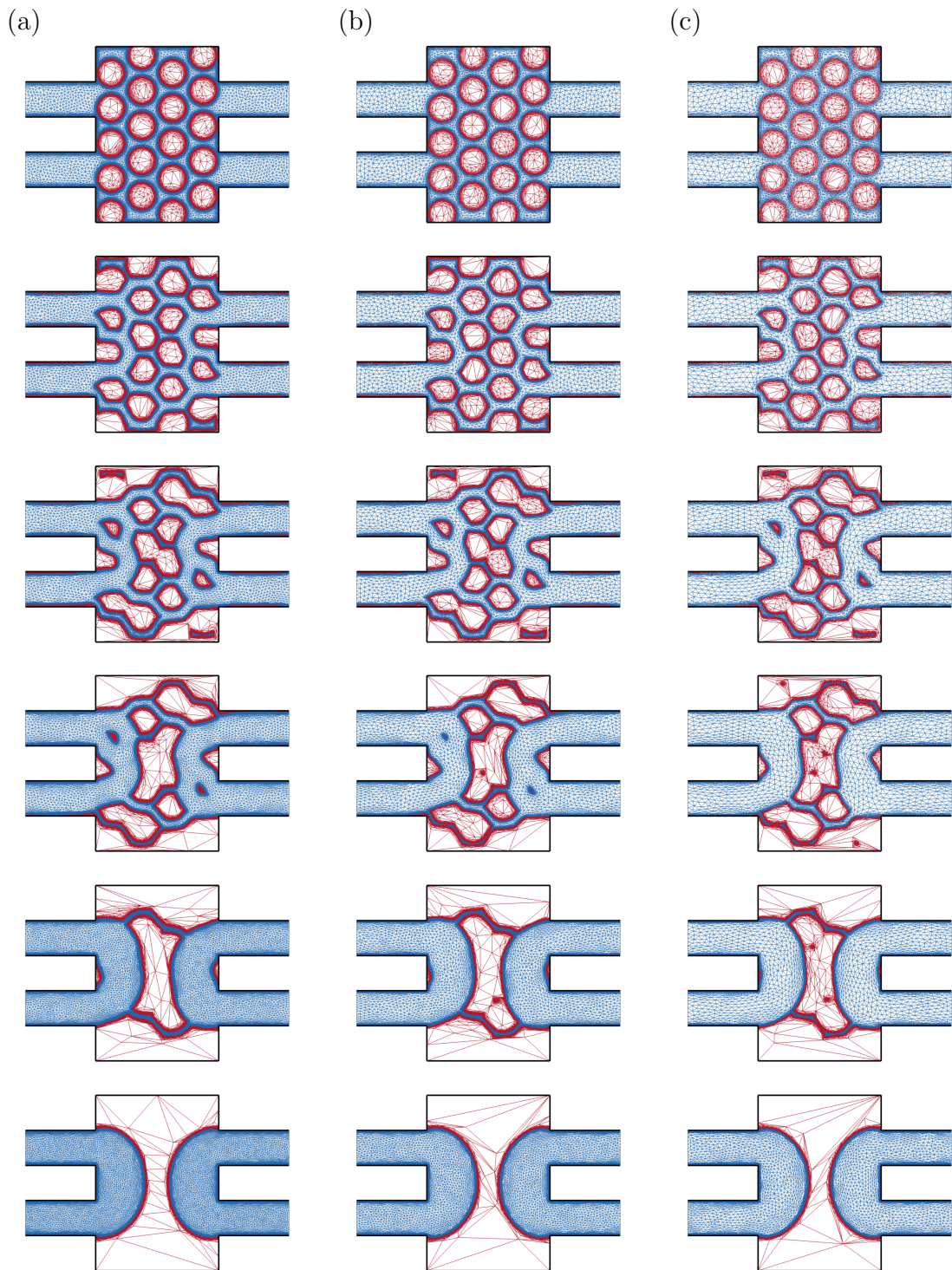


Figure 3.15: Anisotropic meshes of a four terminal device sampled over the course of optimization, using (a) 80000, (b) 40000 and (c) 20000 mesh elements.

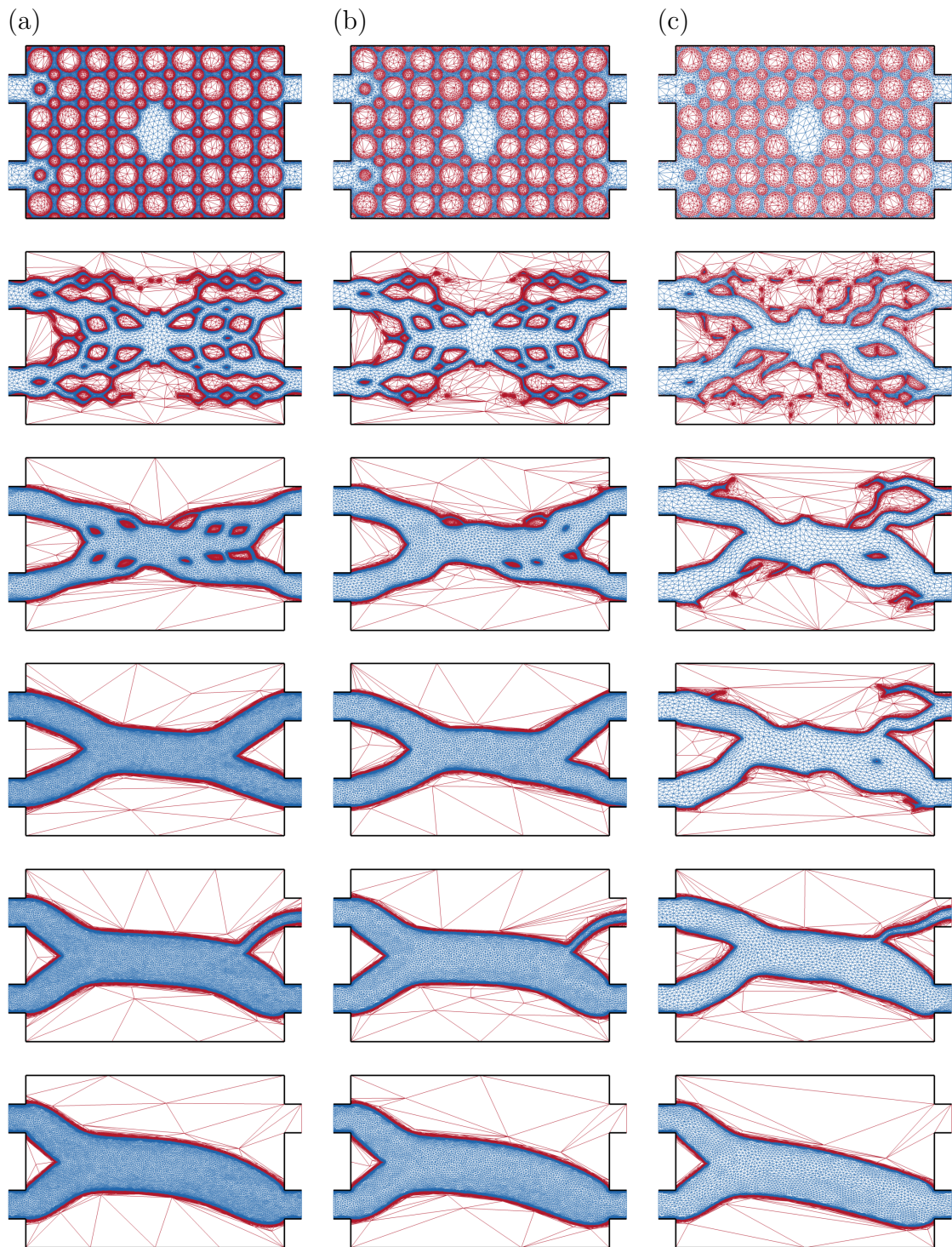


Figure 3.16: Anisotropic meshes of a double pipe sampled over the course of optimization, using (a) 105000, (b) 55000 and (c) 25000 mesh elements..

become available to improve the mesh in other regions of the domain. If the number of nodes is small, all essential features of the solution will remain well captured (albeit to a slightly lower accuracy), but the finest, most intricate topologies will be smoothed out, which is expected to yield faster convergence because the sensitivity will have less overshoots and the displacement will be more homogeneously distributed over the interface.

Confirmation comes from additional runs performed on both denser and coarser meshes. The look-alike design samples documented in Figs. 3.14-3.16 indicate that all runs follow the same optimization path, with smaller details being captured as the number of elements increases. Just as important is the fact all optimal solutions are independent of the mesh size. This means that the ability of the method to represent smaller and smaller features does not result in smaller and smaller features being represented in the optimal designs (as can occur in stiffness optimization of mechanical structures [86]; see also [79] for proof that total power dissipation minimization is well posed in this respect). For the bend pipe and four terminal devices, the expected behavior is observed, as coarser-mesh runs converge substantially faster, for instance the bend pipe with 20000 elements converges within 165 iterations, which is lower by about 45% compared to using 60000 elements. If a less restrictive convergence threshold of 5%, is enforced, this drops to 102, which is only a tad above the 85 iterations of [79]. The improvement carries over to the four terminal device problem, whose run with 20000 elements converges within 68 iterations, which is lower by about 50% compared to using 60000 elements (this further drops to 61 using a convergence threshold of 5%). Note, in both cases, coarser does not equate coarse, as the convergence information compiled in Tab. 3.2 shows that the coarsest meshes actually resolve the optimal interface to an excellent accuracy.

Meanwhile, convergence for the double pipe ends up being almost arbitrary and the algorithm has difficulties in finding the optimal topology due to the characteristics of the cost function landscape. The convergence history in Fig. 3.13(d) shows that the run with 55000 elements does indeed converge faster to the double-ended wrench solution minimizer but then needs more iterations to ultimately reach the single-ended wrench global minimizer, so convergence is ultimately slower than using 80000 elements. Meanwhile, the run with 25000 elements successfully bypasses the local minimizer (because the lack of elements does not allow representing the complexity prevailing in the early stage of the optimization, which ends up quickly breaking the horizontal reflectional symmetry), but the convergence rate ultimately remains comparable to that with 80000 elements, which raises the possibility that the wrench solutions are actually flat minimizers.

3.6 Résumé du chapitre en français

Ce chapitre combine les méthodes numériques précédemment décrites pour former un algorithme bien structuré pour l'optimisation de la topologie des écoulements laminaire incompressibles. Plusieurs problèmes d'optimisation ont été abordés : la conception d'un coude de tuyau, d'un systèmes à quatres terminaux et d'un double tuyau. Les résultats présentés ont mis en évidence la supériorité de la méthode par rapport à ses prédécesseurs en éliminant les effets d'escaliers et les régions grises, tout en maintenant un coût de calcul relativement faible. Une discussion sur le temps de calcul et la dépendance au maillage a également été élaborée.

Chapter 4

Topology Optimization Framework : Extension to Parallel 3D Resolution with Anisotropic Meshing

Contents

4.1	Introduction	58
4.2	Parallel Computational Framework	59
4.2.1	Parallel Resolution	60
4.2.2	Parallel adaptive remeshing	60
4.2.3	Dynamic load balancing	62
4.3	Numerical Benchmarks	62
4.3.1	Single inlet/single outlet duct flow	64
4.3.2	Single inlet/multiple outlets duct flow	70
4.3.3	Multiple inlets/multiple outlets duct flow	74
4.3.4	Discussion	78
4.4	Résumé du chapitre en français	81

4.1 Introduction

This chapter serves as an extension of Chap. 3, where we will offer fundamental verifications of the framework described earlier for topology optimization of large-scale, three-dimensional (3-D) problems. In recent years, an increasing number of studies have dealt with efficient large-scale topology optimization, to which the reader is referred to for further information regarding the use of parallel programming using the message parsing interface (MPI) and parallel resolution of partial differential equations with scalable and high performance algorithms [87, 88, 89, 90, 91]. Particular emphasis is thus put here on the parallel resolution, load balancing, and parallel adaptive meshing technique. The latter combines local remeshing performed independently on each subdomain with fixed interfaces, and constrained repartitioning to move the interfaces between subdomains in an optimal way, both iterated until a satisfying mesh and partition are obtained. The metric map providing both the size and the stretching of mesh elements in a very condensed information data is derived from the level set. A posteriori anisotropic error estimator is then used to minimize the interpolation error under the constraint of a prescribed number of nodes in the mesh. The latter can be adjusted over the course of optimization, meaning that the base grid can be either refined or coarsened on demand: this is expected to achieve further speed-ups, as it reduces the cost of modelling the solid material away from the interface, and also to help improve manufacturability of the optimal design, which remains an issue as most classical topology optimization methods render organic designs that can be difficult to translate into computer-aided design models. The cost function remains the same as of Sec. 3.1:

$$J_s = p_{tot}(\mathbf{u} \cdot \mathbf{n}) = \left(p + \frac{1}{2}\rho(\mathbf{u} \cdot \mathbf{u})\right)(\mathbf{u} \cdot \mathbf{n}) \quad (4.1)$$

as are the functional derivatives:

$$\partial_p J_s = \mathbf{u} \cdot \mathbf{n}, \quad \partial_{\mathbf{u}} J_s = p_{tot} \mathbf{n} + \rho(\mathbf{u} \cdot \mathbf{n}) \mathbf{u} \quad (4.2)$$

The state and adjoint equations also remain unchanged but will be implemented in a massively parallel environment to be able to handle effectively problems with millions of degrees of freedom. They can be recalled from Chap. 2 as:

$$\rho \mathbf{u} \cdot \nabla \mathbf{u} = -\nabla p + \nabla \cdot (2\mu \boldsymbol{\varepsilon}(\mathbf{u})) \quad \text{in } \Omega_f \quad (4.3)$$

$$\nabla \cdot \mathbf{u} = 0 \quad \text{in } \Omega_f \quad (4.4)$$

for the Navier–Stokes equations. And as:

$$-\rho \mathbf{u} \cdot \nabla \tilde{\mathbf{u}} + \rho \nabla \mathbf{u}^T \cdot \tilde{\mathbf{u}} = \nabla \tilde{p} + \nabla \cdot (2\mu \boldsymbol{\varepsilon}(\tilde{\mathbf{u}})) \quad \text{in } \Omega_f \quad (4.5)$$

$$\nabla \cdot \tilde{\mathbf{u}} = 0 \quad \text{in } \Omega_f \quad (4.6)$$

for their adjoint counterparts. A subtlety here lies in the boundary condition on the outlet, where we alter between conditions (2.6) prescribing a specific velocity and (2.7) imposing a zero pressure/zero stress condition. The adjoint outflow boundary conditions would then comply to Eqs. (2.17) and (2.18) respectively. The choice of the outflow condition will depend on whether we intend to enforce the conservation of all outlets in the system or not, as explained in Sec. 3.4.4. The specific condition will be specified for each case and discussed in more detail in the subsequent sections.

In the following work, we will particularly emphasize on the parallel adaptive meshing technique which combines local remeshing performed independently on each subdomain with fixed interfaces, and constrained repartitioning to move the interfaces between subdomains in an optimal way, both iterated until a satisfying mesh and partition are obtained. In the subsequent sections, a numerical benchmark comprising four optimization problems will be tackled. Finally, we will conclude with a detailed discussion and comparison, focusing on the framework's robustness and the reduction in computational costs achieved through its implementation.

4.2 Parallel Computational Framework

The numerical resolution framework relies on the in-house, parallel, finite element library CimLIB.CFD [70], whose organization relies on fundamental choices allowing an efficient implementation of high-level parallel algorithms. We discuss below the efficient tools to generate and adapt the meshes, and to solve the large-scale linear systems arising from the finite element discretization, steps where most computational time is spent. Another key aspect of the method is the ability of the stabilized finite element formulations to support using anisotropic adapted meshes in both the fluid and solid domains, regardless of the problem dimensionality. On the one hand, using linear approximations for all variables drastically reduces the size of the systems that need be solved. To give a taste, the meshes used herein are made up of about 5 million elements yielding a total of 3.5 million degrees of freedom, but 20 million degrees of freedom using quadratic approximations for the velocities, hence a reduction by nearly 80%. On the other hand, using anisotropic meshes decreases the cost of improving the numerical precision, as the number of nodes needs be increased only in the direction of interest. This makes a huge difference in 3-D calculations, as the accuracy can be improved by a factor of 2 (in the best case scenario) using only 2 times as many nodes, instead of 8.

4.2.1 Parallel Resolution

Computing the numerical solutions to the governing Navier–Stokes, adjoint Navier–Stokes and level-set advection equations considered herein requires solving large-scale linear systems (or non-linear systems that may lead to the resolution of several linear systems if an implicit discretization scheme is used). To this end, the resolution step makes a clear distinction between those large-scale systems that need be stored and solved, and their local contributions at the element levels. Namely, all finite element formulations are only implemented sequentially at the element level, then assembled and solved in parallel using the PETSc library [92], that offers a wide range of parallel data structures (linear and non-linear solvers as well as preconditioners) and can be run on large computing clusters. Here, only semi-implicit and explicit discretization schemes are used; see 2.8), and the associated linear systems are sufficiently well conditioned to be solved by iterative methods. We thus use the Generalized Minimal Residual algorithm with block Jacobi incomplete LU preconditioning, and consider the solutions to be converged if the absolute residuals are less than 10^{-6} .

4.2.2 Parallel adaptive remeshing

Although most numerical solvers have embraced parallel computing as a way to continue to improve performance, it is less common to see massively parallel computation using anisotropic adapted unstructured meshes, let alone if the mesh is dynamically adapted to track the interface deformations. An original parallelization strategy is used here for the mesh adaptation step, based on an independent subdomain remeshing under the constraint of blocked interfaces. An initial mesh is partitioned into several submeshes using a parallel graph/mesh partitioning/repartitioning algorithm that allows to balance well the number of mesh entities (vertices or elements) per processor [93, 94, 95]. Remeshing operations are then performed with a sequential mesh adaptator on each subdomain with an extra treatment of the interfaces, using the procedure described in [68], based on a topological representation of the computational domain. In practice, a level-set based error estimate is computed for each subdomain. An iterative approach is used, in which remeshing is performed concurrently on each processor while the interfaces between sub-domains are locked to avoid any communication between processors. Then, to obtain a satisfactory final mesh regarding the quality function, a repartitioning step is performed to move the interface inside the domain in order to enable re-meshing in a next phase. As illustrated in Figure 4.1, the algorithm iterates until all items have been re-meshed. Finally, the new mesh is repartitioned over the allocated CPUs to take into account for the changes of mesh topology in the computational loads distribution. Note, the constraint on the number of mesh elements could be considered as local to each

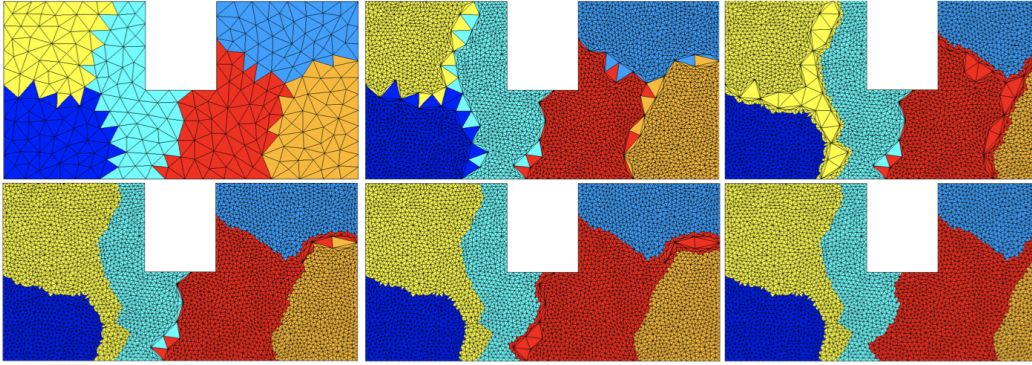


Figure 4.1: Illustration of the iterative parallel remeshing steps on a model 2-D distributed mesh.

subdomain. In this case, solving the error estimate problem is straightforward, as all computations are local and there is no need to exchange data between the processors. The local constraint on the number of elements implies the generation of a new mesh with the same number of elements per processor. This allows avoiding heavy load balancing cost after each mesh adaptation, but tends towards an overestimate of the mesh density on subdomains where flow activity is almost neglected. From a scaling point of view, such an approach leads to a weak scalability model for which the problem size grows linearly with respect to the number of processors. To derive a hard scalability model with good parallel performances, the constraint on the number of elements for the new generated mesh is thus handled globally, with the global number of elements over the entire domain distributed with respect to the mesh density prescribed by the error estimator. In doing so, the parallel behavior of the mesh adaptation is very close to the serial one and the error analysis is still the same, although reload balancing is required after each mesh adaptation stage.

Because the parallel remesher is made of nested iterations between remeshing and repartitioning, the metric map providing both the size and the stretching of mesh elements needs to be transported after each repartitioning step. Indeed, it is given as a nodal field, hence one scalar value per node, and must be updated after each migration or renumbering. The parallel adaptive remeshing is thus the combination of three iteratively nested steps: (i) independent adaptive remeshing per subdomain, (ii) constrained repartitioning and (iii) updating the metric map. Depending on the problem dimensionality, three to five iterations of remeshing and repartitioning are typically needed to build the optimal mesh, but the time spent per iteration decreases drastically as fewer and fewer elements and nodes need to be moved and migrated across processors, as we only need to move bad quality zones inside the domain in order to remesh them. For several test cases in two and three dimensions, this simple approach is shown in [96] to yield close-to-optimal parallel

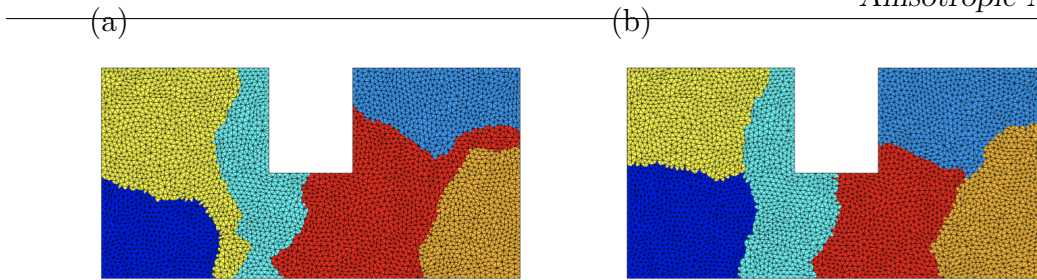


Figure 4.2: (a) Before and (b) after load balancing for the same model 2-D distributed mesh as in Fig. 4.1.

remeshing speed-up up to 32 cores.

4.2.3 Dynamic load balancing

In this work, we follow the same load balancing strategy than in Ref. [93], to which the interested reader is referred for technical details. A cost function is defined and takes into account the theoretical computation and communication time of the allocated resources. Then, the load balancing process is realized using two major steps: (i) forming disjoint pairs of processors that are susceptible to minimize the cost function, and (ii) optimizing the cartography on each pair. This optimization is done by transferring mesh nodes or mesh cells from a processor to the other using the notion of strip migration. These two steps are repeated as long as the global cost of the partition can be optimized. The results from [103] show that the use of this method on various system architectures allows accelerating the mesh partitioning process. In terms of scalability, a linear behavior is observed. An example of load balancing is given in Fig. 4.2 for the same example than in Fig. 4.1 after the parallel remeshing procedure. One notices that the partition in Fig. 4.2(a) is not optimal, as the size of the interfaces is too large, which could have a damaging impact on the communication costs. The cost function is thus optimized using the previously described load balancing procedure by transferring nodes from one processor to the other, in order to obtain the final optimal partition presented on the right side of Fig. 4.2(b).

4.3 Numerical Benchmarks

This section assesses the accuracy and efficiency of the numerical framework through a series of topology optimization problems, for which the novelty lies not necessarily in the associated optimal designs themselves, but in the accuracy to which the optimal interfaces are captured in the simulation model. Each problem is tackled on 64 cores of a cluster of AMD Rome EPYC 7502 bi-processors. All examples aim

$h_{\perp} = 0.0001$	Min. interface normal mesh size
$\Delta t = 0.1$	CFD Numerical time step
$E = 0.005$	Level set cut off thickness
$ \delta\varphi = 0.0005$	Initial volume recovery offset
$r_s = 0.0125$	Transition radius
$\alpha_s = 2.1$	Sharpness parameter
$(\epsilon_{s1}, \epsilon_{s2}) = (0.0005, 0.005)$	Regularization parameters

Table 4.1: Algorithmic parameters.

at finding the best path for a fluid to flow in a reference design domains under the form of cubic or cuboid (parallelepipedic) cavities, with either a single or multiple identical inlets, and a single or multiple identical outlets, all cylindrical. For each case, the sole control parameter is the Reynolds number, built here on inlet diameter and maximum inlet velocity (the same for all inlets).

The remainder of the practical implementation details are as follows:

- All design domains are initialized with solid inclusions coming in various shapes and sizes. No new holes are created over the course of optimization, in the absence of a dedicated mechanism for seeding solid occlusions, but from experience, all problems tackled in the following are essentially insensitive to the initial design provided a sufficiently large number of inclusions is used.
- The admissible error on the target volume is set to 1% in two dimensions, and 5% in three dimensions. In the latter case, we restore the target volume to an accuracy of 0.5%, which has been found suitable to space out the frequency of consecutive corrections, which substantially decreases the computational cost.
- The fluid is systematically conveyed into and out of the design domain using leads of length l_i (the same at all inlets) and l_o (the same at all outlets) appended normal to the boundary. This is for numerical consistency, as the exact problem formulation in the literature may vary depending on the case, and it is not always clear whether such leads should be included in the design domain. This is the case here, although the leads are not considered in the volume constraint, neither in definition of the target volume nor in the computation of the volume of fluid.
- The singular subsets excluded from the displacement normalization step are the sharp intersections between the leads and the boundary of the cavities, hence each smooth filter ζ transitions from 0 to 1 over either a torus of minor

radius $2r_s$ (for all inlets and cylindrical outlets) or a set of intersecting cylinders of radius $2r_s$ (for all rectangular outlets). Note, this is not a consequence of explicitly representing the leads, as the exact same procedure has been found suitable without such appendage.

- The leads are excluded from the displacement normalization step, for which we simply add to the max argument of (3.5) a binary filter returning a value of 0 at all nodes located inside the pipes. This is again to avoid slowing down the convergence rate of the iterative optimization process, as the maximum displacement is otherwise located in the leads, because the easiest way to minimize the dissipated power is to suppress the flow by having the solid entirely clogging the leads.
- Without seeking to optimize the performance, all optimization runs have been found to converge within a few hundreds iterations, which is essentially the number of steps used to fulfill the fluid volume constraint while ensuring that the displacement achieved at each iteration remains below the level set cut-off thickness (more details in the following).
- All 3-D meshes have been checked to have an element-to-node ratio close to 5, as should be for dense meshes made up of tetrahedral elements. In order to ease the comparison with the available literature, the mesh information is thus documented in the following in terms of its equivalent number of elements, defined as $N_{el} = 5N_n$.

Finally, all systems considered in the following have from 1 up to 3 reflectional symmetries. Nonetheless, we do not reduce the computational cost by modeling only a half (or a quarter/eighth) of the domain together with symmetry boundary conditions, which is feasible [97] but would somehow contradict the objective of assessing the method in the context of large-scale CFD systems. The entire domain is thus discretized, and we let symmetry arise as a result of the optimization process, even though this likely increases the number of iterations needed to achieve convergence.

4.3.1 Single inlet/single outlet duct flow

We optimize first the single inlet / single outlet duct flow whose setup is shown in Fig. 4.3(a). The design domain is a cubic cavity of unit length, that has one circular inlet on the left side, one circular outlet at the bottom, and reflectional symmetry with respect to the inlet/outlet plane. The aim is to determine the optimal design of the pipe bend that connects the inlet to the outlet and minimizes the dissipated power subject to the constraint that the fluid must occupy a given fraction of the total volume. The boundary conditions for this case consist of a

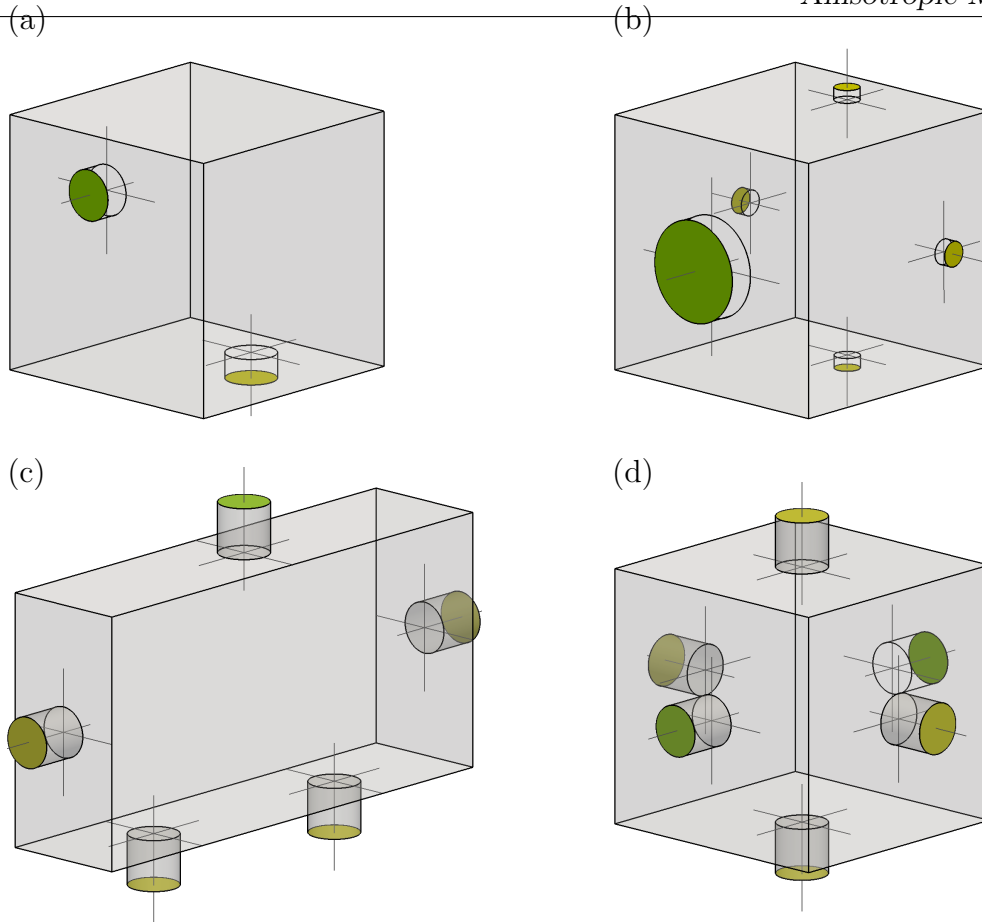


Figure 4.3: Problem set-up for the (a) single inlet/single outlet (b-c) single inlet/multiple outlets and (d) multiple inlets/multiple outlets examples.

normal to the boundary, parabolic inlet velocity profile and a zero pressure/zero viscous stress condition; see Sec. 2.3. This is a classical benchmark for the 2-D topology optimization problem studied in Sec. 3.4.2 and in [79, 80, 81, 82, 7, 10], but the extension of the analysis in three dimensions is less common [82, 97].

The entire cubic cavity discretized into 5000000 (5M) mesh elements. The fluid is now set to occupy 3.9% of the cavity, which is the same as the quarter torus fitting exactly to the inlet and outlet. All other numerical parameters are documented in Tab. 4.2. The initial design in Fig. 4.4 consists of spherical occlusions occupying about 24% of the cavity. The volume of fluid therefore initially fills about 76% of the cavity, in violation of the volume constraint. This is because many more smaller inclusions are needed to recover the proper volume, which in turn would either dramatically increase the surface of the interfaces that needs be captured (and thus the number of mesh elements needed to maintain the numerical accuracy), or

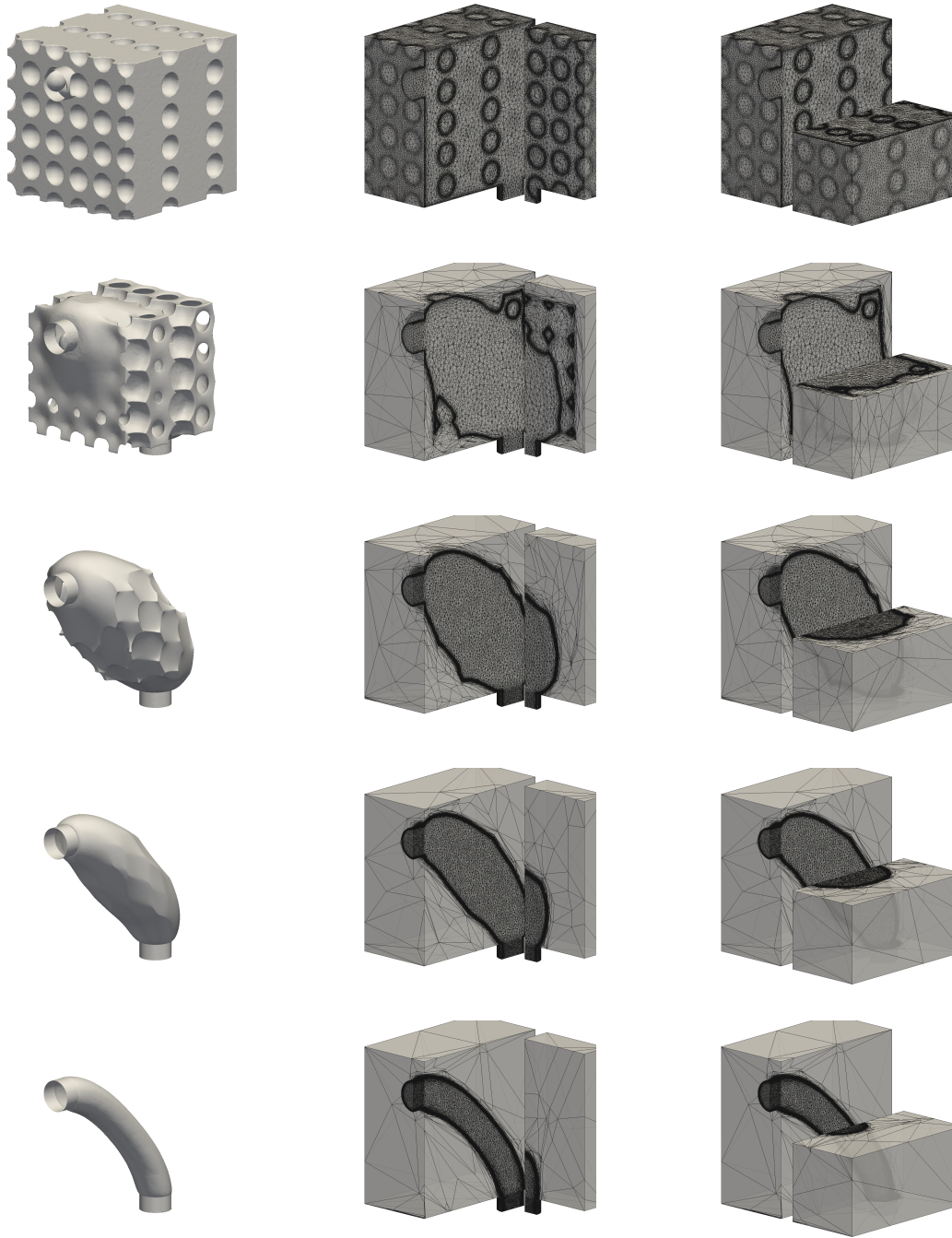
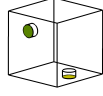


Figure 4.4: Optimization of the single inlet/single outlet duct flow presented in Fig. 4.3(a). The zero iso-value of the level set function and associated anisotropic adapted meshes are sampled at intermediate iterations 1, 402, 548, 700 and 900 (from top to bottom) using the parameters given in Tab. 4.2. The associated volumes of fluid are 77.0%, 40.8%, 27.5%, 13.7% and 3.94%, respectively.



$\Omega = [0; 1] \times [0; 1] \times [0; 1]$	Design domain
$d = 3$	Problem dimensionality
$V_{target} = 0.039$	Target volume of fluid
$V_{\varphi,0} = 0.76$	Initial volume of fluid
$Re = 2$	Reynolds number
$\mathbf{x}_i = (-0.1, 0.8, 0.5)$	Inlet center coordinates
$u_i = 0.2$	Inlet centerline velocity
$e_i = 0.2$	Inlet diameter
$l_i = 0.1$	Inlet leads length
$\mathbf{x}_o = (0.8, 0.5, -0.1)$	Outlet center coordinates
$e_o = 0.2$	Outlet diameter
$l_o = 0.1$	Outlet leads length
$N_n = 1M$	Nb. mesh nodes
$N_{el} = 5M$	Nb. mesh elements

Table 4.2: Numerical parameters for the single inlet/single outlet duct flow problem.

risk clogging the fluid path due to insufficient mesh refinement. As shown in the convergence history presented in Fig. 4.5, there is thus an initial transient during which the cost function, albeit low, has little physical meaning, as the constraint value is decreased up to the point where it reaches the target within the desired tolerance. Once the constraint is satisfied, the cost function adjusts until a feasible minimum is found, that corresponds to the almost straight pipe shown in Fig. 4.4, that closely resembles that in [82], but with vastly superior accuracy. To give a taste, the element size is about 6×10^{-4} at the interface and 0.01 in the fluid domain, with up to 40-50 elements distributed across a pipe diameter. In comparison, the problem in the aforementioned reference is tackled with a uniform grid made up of 162000 tetrahedral elements, hence an element size of about 0.0375, which is insufficient to claim accuracy of the numerical solutions since only 5-6 grid points can be distributed across a pipe diameter. Again, the method handles well the various topological changes occurring over the course of optimization, and all adapted meshes exhibit extremely stretched elements regardless of the interface complexity, that allow sharply representing the fluid and solid domains and accurately computing the fluid solutions during all stages of optimization.

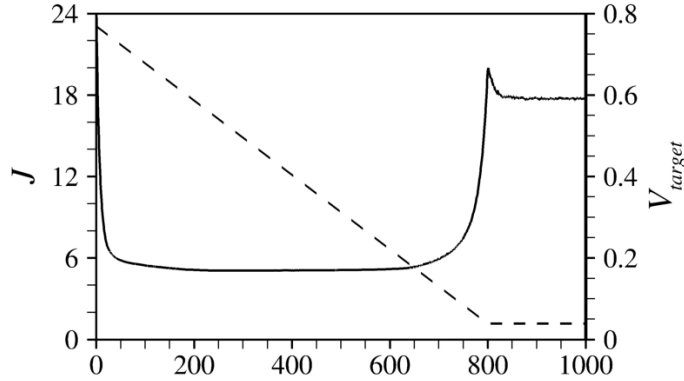


Figure 4.5: Convergence history for the 3-D bend pipe problem with 5M elements. All cost function values made non dimensional using the inlet diameter and maximum inlet velocity (equivalently, using $\rho u_i^3 e_i^2$ as reference cost functional value). The dashed line shows the decrease in the target volume.

4.3.1.1 Discussion

The parallel remeshing strategy for the 3-D case is illustrated in Fig. 4.6 showing for the same iterations already sampled in Fig. 4.4 the 64 submeshes generated by the graph/mesh partitioning/repartitioning algorithm, each shown by a different color and handled sequentially by a different processor. The various submeshes are initially uniformly distributed in the whole domain, due to the presence of the multiple solid occlusions. Nonetheless, they quickly reorganize to cover the vicinity of the interface, where the mesh refinement is maximum, with only a handful of submeshes needed to handle the coarse solid domains, meaning that the load is well balanced between the processors.

It is worth noticing that the large number of nodes used here is mostly useful during the early stage of optimization. This is because the surface of the interfaces (perimeter in two dimensions) that needs to be captured is initially dramatically large to the many solid inclusions, then decreases substantially after the first dozens of iterations, as has been found computing the surface area using Eq. (3.10). Also, the anisotropic mesh adaptation algorithm refines the mesh in hierarchical importance of the level set gradient. If new geometrical features associated with high gradients appear in the solution, the mesh is automatically coarsened in regions with lower gradient and refined near the newly emerging features. If the number of nodes is large, as has been the case so far, the decrease in the interface surface area allows resolving finer, more complex patterns without degrading the accuracy in other parts of the design domain, because the coarsened regions are actually over-resolved. This shows through the progressive mesh refinement in the fluid domain

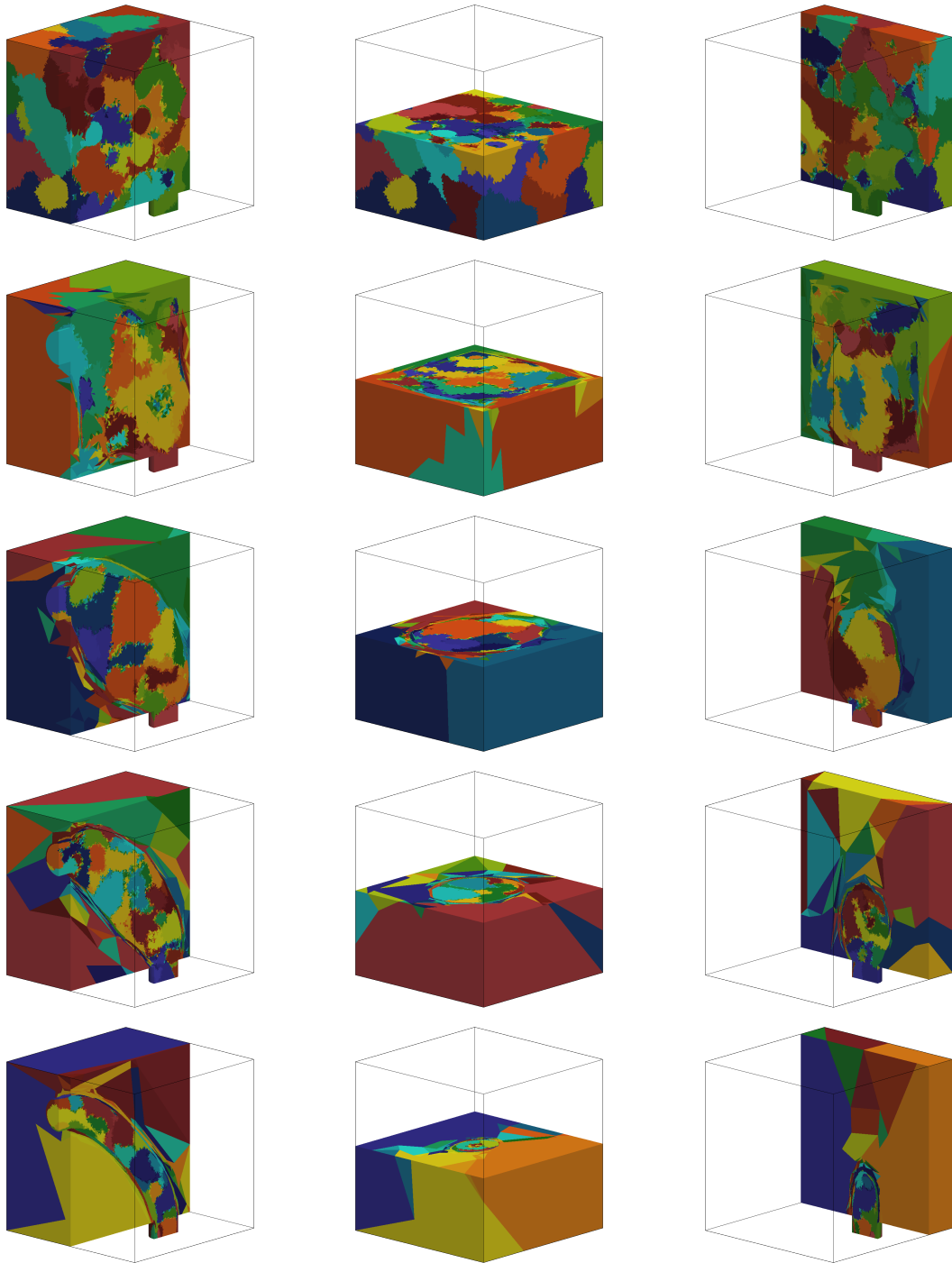


Figure 4.6: Illustration of mesh partitioning for the three dimensional, single inlet/single outlet duct flow. The colors in these plots represent the 64 subdomains generated by the graph/mesh partitioning/repartitioning for the same iterations sampled in Fig. 4.4.


		
$\Omega = [0; 1] \times [0; 1] \times [0; 1]$	$[0; 2] \times [0; 1] \times [0; 0.5]$	Design domain
$d = 3$	3	Problem dimensionality
$V_{target} = 0.15$	0.10	Target volume of fluid
$V_{\varphi,0} = 0.76$	0.37	Initial volume of fluid
$Re = 2$	2	Reynolds number
$u_i = 0.2$	1	Inlet centerline velocity
$e_i = 0.4$	0.2	Inlet diameter
$l_i = 0.1$	0.2	Inlet leads length
$\mathbf{x}_i = (-0.1, 0.5, 0.5)$	$(1, 1.2, 0.25)$	Inlet center coordinates
$u_{o1} = 0.8$	0.1667	Outlet 1 centerline velocity
$u_{o2} = 0.8$	0.1667	Outlet 2 centerline velocity
$u_{o3} = 0.8$	0.3333	Outlet 3 centerline velocity
$u_{o4} = 0.8$	0.3333	Outlet 4 centerline velocity
$e_o = 0.1$	0.2	Outlet diameter
$l_o = 0.05$	0.2	Outlet leads length
$\mathbf{x}_{o1} = (0.75, 0.5, -0.05)$	$(-0.2, 0.5, 0.25)$	Outlet 1 center coordinates
$\mathbf{x}_{o2} = (0.75, 0.5, 1.05)$	$(2.2, 0.5, 0.25)$	Outlet 2 center coordinates
$\mathbf{x}_{o3} = (0.75, -0.05, 0.5)$	$(0.5, -0.2, 0.25)$	Outlet 3 center coordinates
$\mathbf{x}_{o4} = (0.75, 1.05, 0.5)$	$(1.5, -0.2, 0.25)$	Outlet 4 center coordinates
$N_n = 1M$	\gg	Nb. mesh nodes
$N_{el} = 5M$	\gg	Nb. mesh elements

Table 4.3: Numerical parameters for the single inlet/multiple outlets duct flow problems.

in Fig. 4.4, as more and more elements become available to improve the mesh in other regions of the domain.

4.3.2 Single inlet/multiple outlets duct flow

This section is devoted to a series of more complex duct flow problems with one inlet and multiple outlets. All cases are tackled with boundary normal, parabolic velocity profiles prescribed at the inlets and the outlets, with outlet centerline velocities adjusted for the the total amount of mass flow exiting through the outlets to match exactly that entering through the inlet; see Sec. 2.4. The objective for doing so is twofold: first, it forces the inlet to connect to all the outlets, and thereby emphasizes the ability of the numerical framework to engineer complex designs, as a more natural

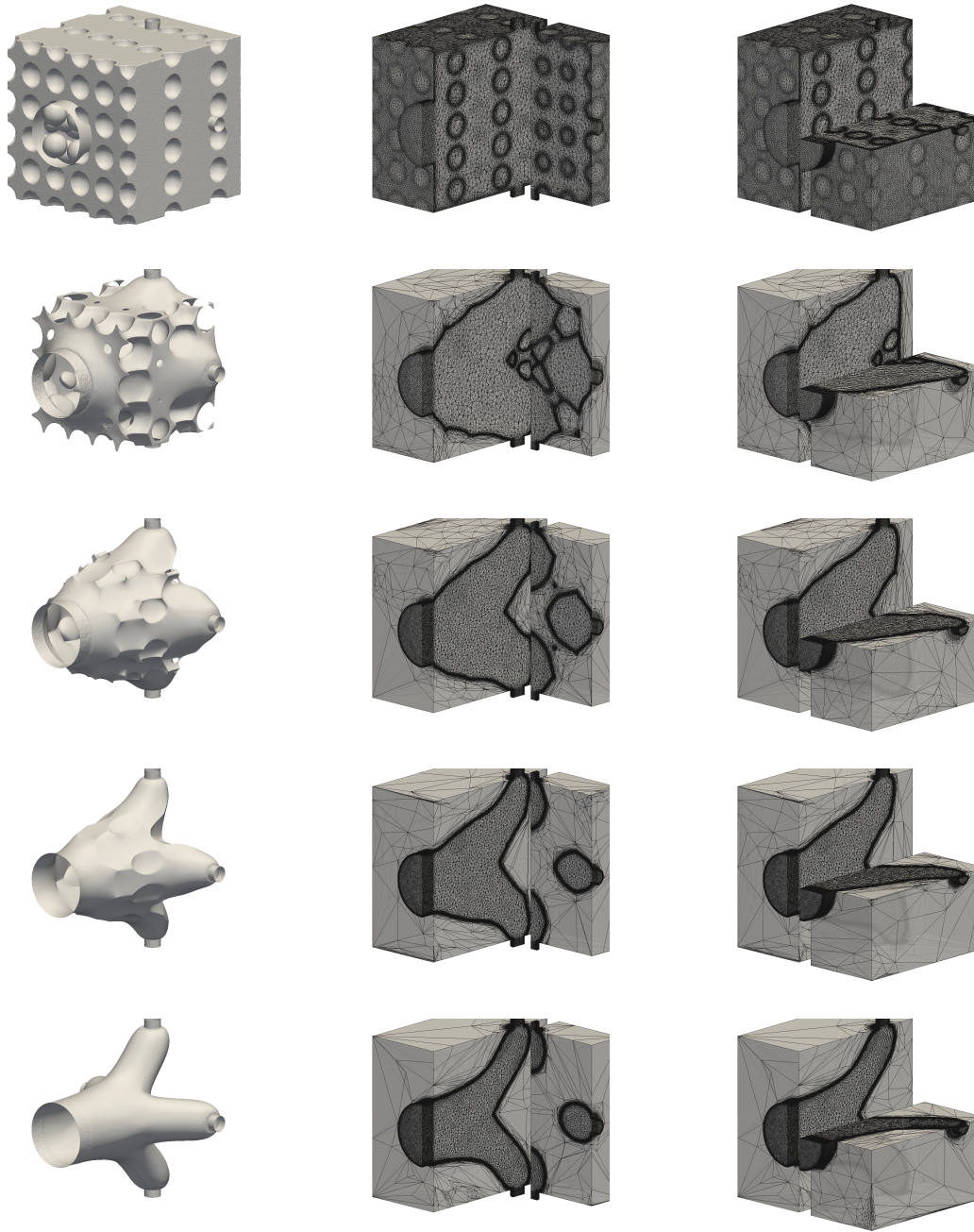


Figure 4.7: Optimization of the single inlet/multiple outlet duct flow presented in Fig. 4.3(b). The zero iso-value of the level set function and associated anisotropic adapted meshes are sampled at intermediate iterations 1, 505, 624, 750 and 1050 (from top to bottom) using the parameters given in Tab. 4.3. The associated volumes of fluid are 75.6%, 37.8%, 28.9%, 19.5% and 15.0%, respectively.

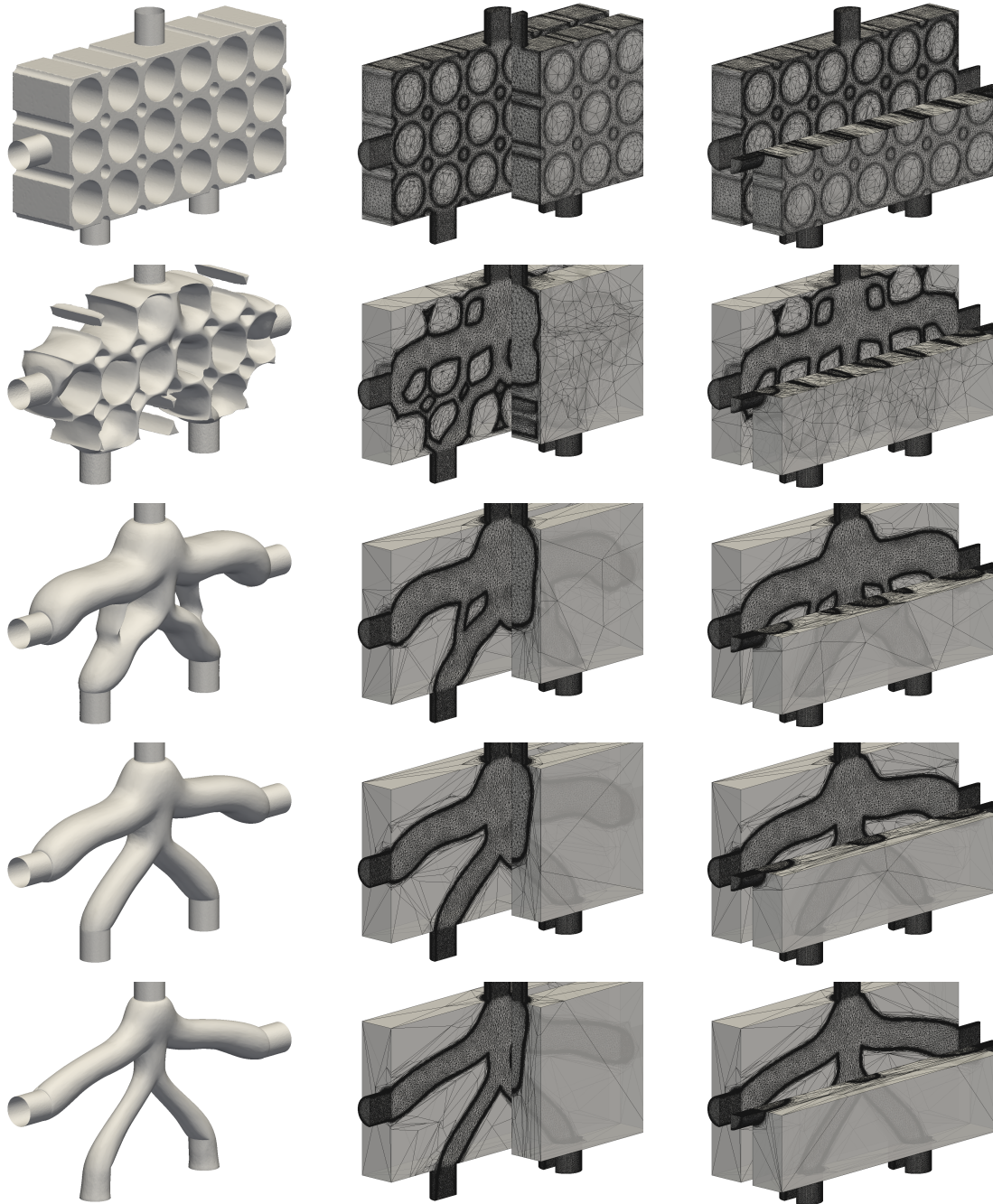


Figure 4.8: Optimization of the single inlet/multiple outlet duct flow presented in Fig. 4.3(c). The zero iso-value of the level set function and associated anisotropic adapted meshes are sampled at intermediate iterations 1, 60, 110, 180 and 300 (from top to bottom) using the parameters given in Tab. 4.3. The associated volumes of fluid are 36.2%, 30.0%, 24.8%, 17.5% and 9.9%, respectively.

zero pressure/viscous stress condition may allow the flow to exit via a single outlet to save the cost of pipe splitting. Second, it reduces the computational cost, as the possibility of having different number of pipes connect to an outlet may give existence to multiple local minimizers, whose basin of attraction can slow down the convergence; see for instance Ref. [85] for an example of competition between the single and double-ended wrench minimizers to the 2-D double pipe problem. In practice, our literature review did not reveal any study tackling multiple outlets 3-D topology optimization problems with zero pressure/viscous stress or zero stress conditions, except for a few cases in Ref. [97] adding mass flow rate constraints to the Lagrangian to similarly force the flow to exit via all outlets.

For the first example whose setup is shown in Fig. 4.3(b), the design domain is a cubic cavity of unit length, that has one inlet on the left side and four identical outlets at the top/bottom and on the front/back sides, each having 1/4 of the fluid flow entering through the inlet. For the second example whose setup is presented in Fig. 4.3(c), the design domain is a cuboid cavity of unit height and aspect ratio 2:1:0.5, that has one inlet at the top, and four identical outlets: two on the left and right sides, each having 1/3 of the fluid flow entering through the inlet, and two at the bottom, each having 1/6 of the inflow. Both domains have two reflectional symmetries with respect to the two inlet/outlet planes, but are discretized in their entirety using 5M mesh elements. For the first case, the initial design in Fig. 4.7 is made up of spherical solid occlusions occupying about 24% of the cavity. For the second case, we take advantage of the fact that all inlet and outlets are in the same plane and initialize the design with cylindrical solid occlusions filling about 63% of the cavity. The volume of fluid in each case is thus initially about 76% (first case) and 37% (second case), and decreases over the course of optimization until it reaches the target within the desired tolerance. The latter is set low to 15% in the first case, and 10% in the second case, to avoid trivial solutions and promote the formation of separate fluid channels.

For both cases, the optimization goes through several complex stages all accurately represented on anisotropic adapted meshes, as evidenced by the selected samples shown in Figs. 4.7-4.8. Similarly to what could be observed in the bend case, all mesh elements are coarse and regular away from the interface but fine and elongated on either side of the interface, to allow accurately representing the boundary layers regardless of topology complexity, even in the leads. The optimal duct for the first case is a wide pipe splitting at mid length into four identical, thinner pipes, each connecting to an outlet. This layout stands as the better trade-off between transporting fluid the shortest way, and transporting it in the widest possible pipe, and is thus consistent with the results documented in [82], although the optimal shapes therein exhibit quality issues (staircase effects), as illustrated in Fig. 4.9 and anisotropic mesh adaptation represents a tremendous improvement in this regards.

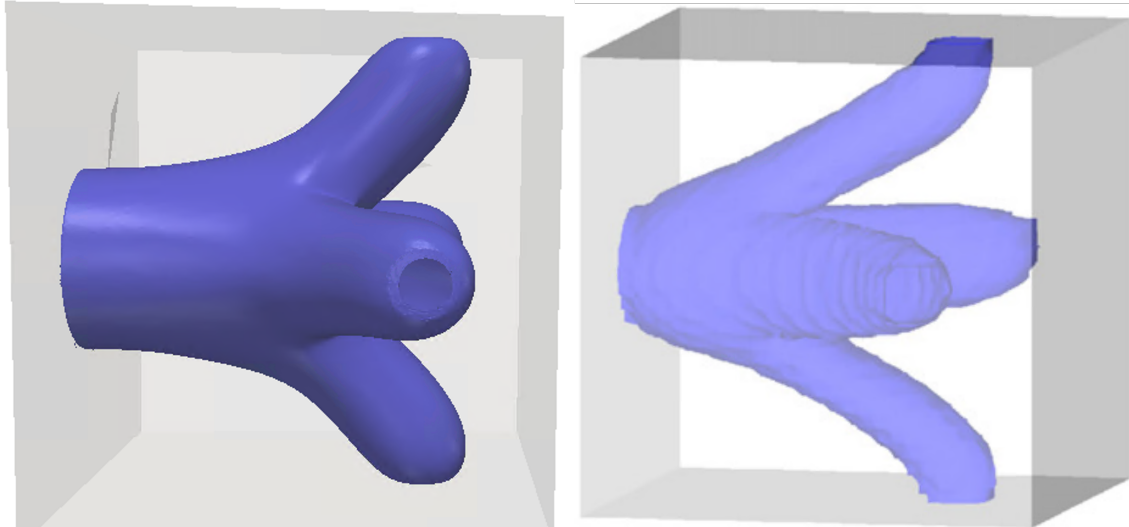


Figure 4.9: Comparison between optimal designs of the problem in Fig. 4.3 (b) (to the left) and its counterpart in [82] (to the right).

For the second case, the optimal duct comprises a wide pipe immediately splitting into three pipes: two symmetrical pipes connecting to the lateral outlets, and a central pipe quickly splitting into two symmetrical pipes connecting to the bottom outlets. All pipes are reasonably straight, and the lateral pipes are wider than their bottom counterparts. This is because most of the flow exits through the left/right outlets and optimal pipes at low Reynolds numbers are preferably short and wide, as splitting the fluid stream further away from the inlet would require complex bending patterns to connect the outlets, which in turn would increase the transport distance and would thus be detrimental in terms of cost function.

4.3.3 Multiple inlets/multiple outlets duct flow

In this example, the focus is on a duct flow problem with multiple inlet and outlets, whose setup is shown in Fig. 4.3(d). The design domain has two identical inlets on the left and right sides, and four identical outlets on all other sides, hence three reflectional symmetries with respect to the outlet and the two inlet/outlet planes. Parabolic inflow/outflow conditions are formulated in the same way as above, with outflow velocities adjusted for each outlet to have $1/4$ of the fluid flow entering through the inlets. The entire cavity is discretized using 5M mesh elements. The initial design in Fig. 4.10 consists of spherical occlusions occupying about 27% of the cavity, after which the volume of fluid is progressively decreased, starting at 73% of the cavity, down until it reaches a 5% target within the desired tolerance. The

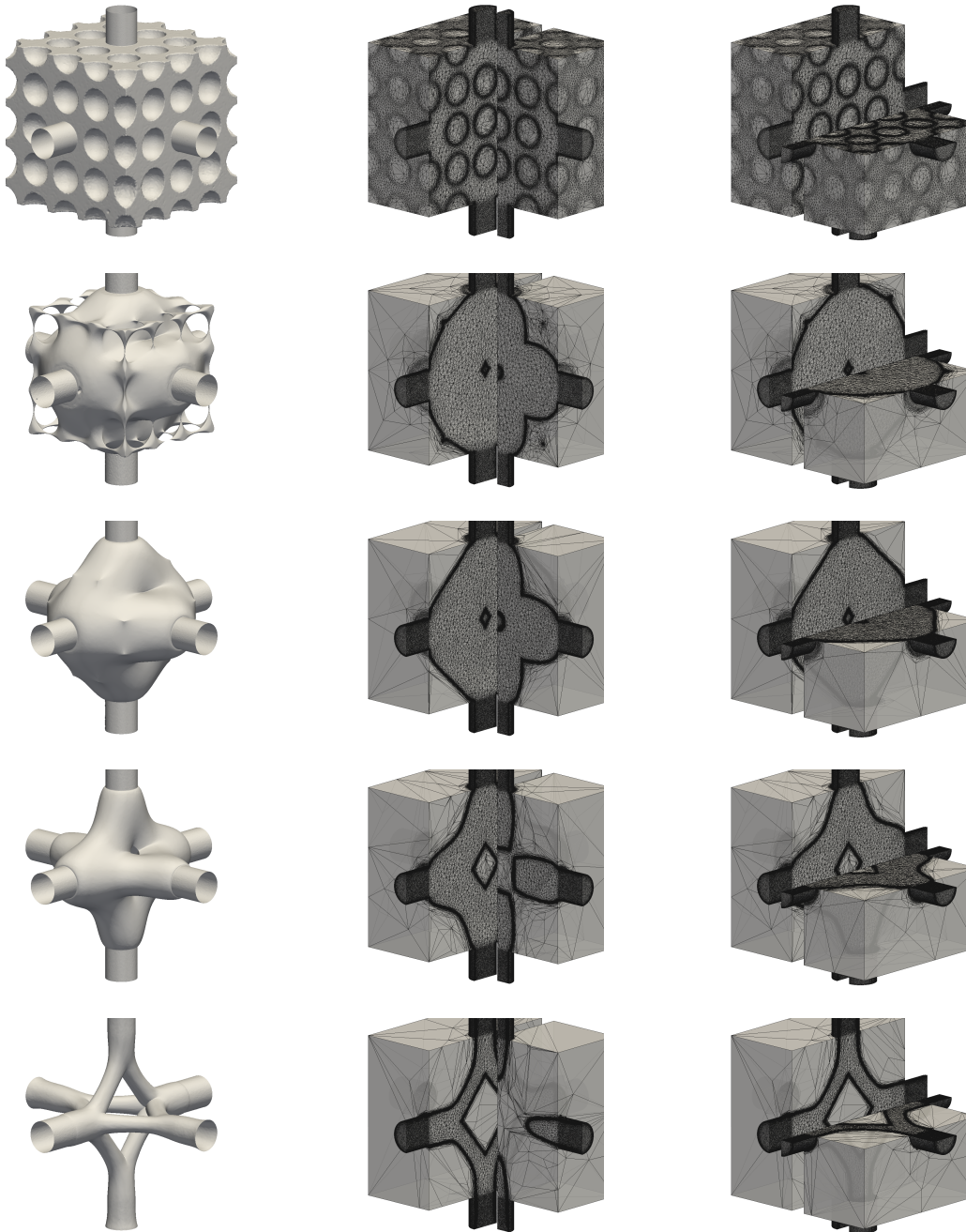


Figure 4.10: Optimization of the multiple inlet/multiple outlet duct flow presented in Fig. 4.3(d). The zero iso-value of the level set function and associated anisotropic adapted meshes are sampled at intermediate iterations 1, 201, 283, 400 and 550 (from top to bottom) using the parameters given in Tab. 4.2. The associated volumes of fluid are 72.8%, 45.9%, 34.8%, 18.9% and 4.9%, respectively.

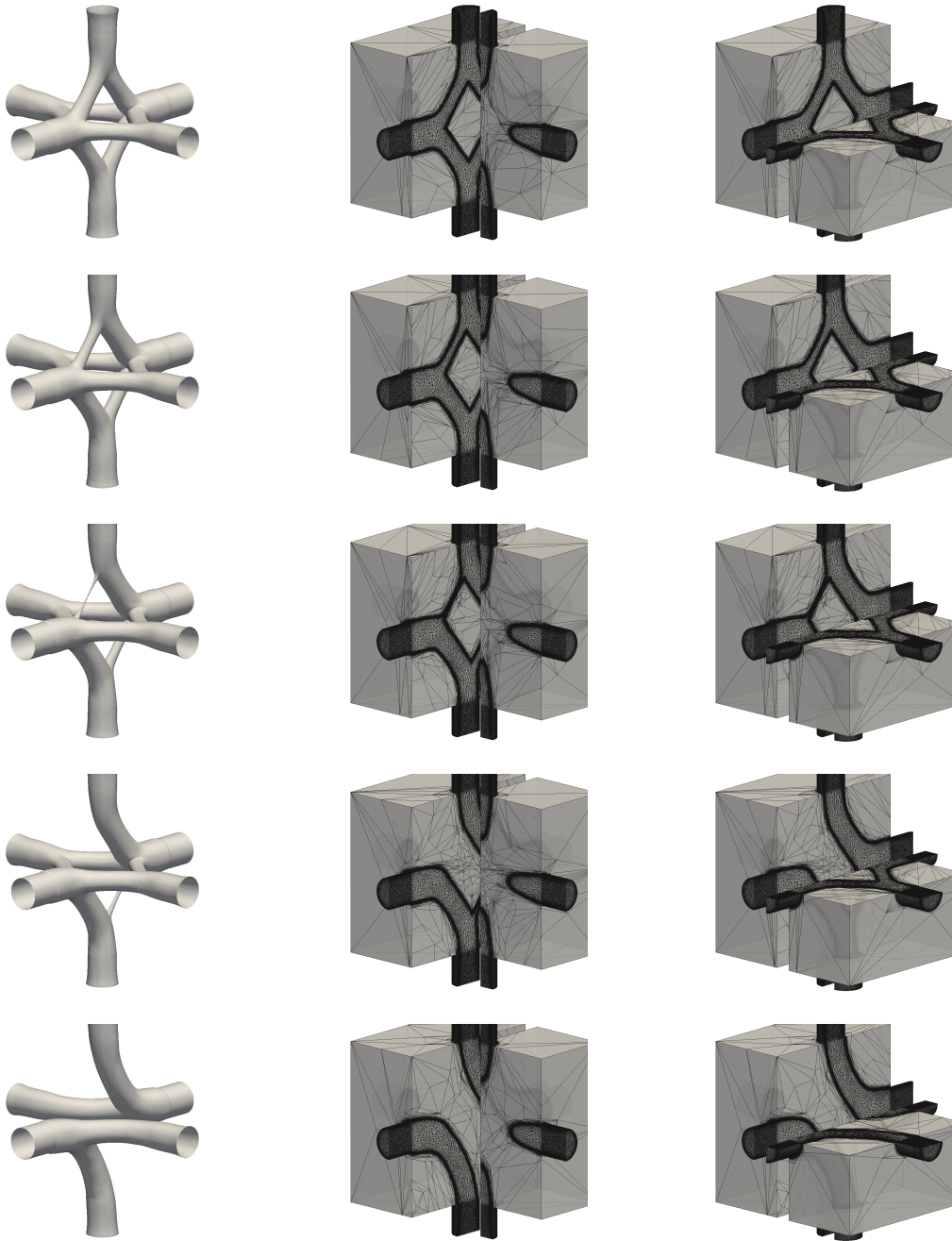
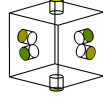


Figure 4.11: Optimization of the multiple inlet/multiple outlet duct flow presented in Fig. 4.3(d). The zero iso-value of the level set function and associated anisotropic adapted meshes are sampled at intermediate iterations 700, 800, 830, 850 and 1000 (from top to bottom) using the parameters given in Tab. 4.2. The associated volume of fluid of all samples matches the target (5%) within the desired tolerance.



$\Omega = [0; 1] \times [0; 1] \times [0; 1]$	Design domain
$d = 3$	Problem dimensionality
$V_{target} = 0.05$	Target volume of fluid
$V_{\varphi,0} = 0.73$	Initial volume of fluid
$Re = 2$	Reynolds number
$u_{i1} = 0.2$	Inlet 1 centerline velocity
$u_{i2} = 0.2$	Inlet 2 centerline velocity
$e_i = 0.2$	Inlet diameter
$l_i = 0.2$	Inlet leads length
$\mathbf{x}_{i1} = (-0.2, 0.5, 0.5)$	Inlet 1 center coordinates
$\mathbf{x}_{i2} = (1.2, 0.5, 0.5)$	Inlet 2 center coordinates
$u_{o1} = 0.1$	Outlet 1 centerline velocity
$u_{o2} = 0.1$	Outlet 2 centerline velocity
$u_{o3} = 0.1$	Outlet 3 centerline velocity
$u_{o4} = 0.1$	Outlet 4 centerline velocity
$e_o = 0.2$	Outlet diameter
$l_o = 0.2$	Outlet leads length
$\mathbf{x}_{o1} = (0.5, 0.5, -0.2)$	Outlet 1 center coordinates
$\mathbf{x}_{o2} = (0.5, 0.5, 1.2)$	Outlet 2 center coordinates
$\mathbf{x}_{o3} = (0.5, -0.2, 0.5)$	Outlet 3 center coordinates
$\mathbf{x}_{o4} = (0.5, 1.2, 0.5)$	Outlet 4 center coordinates
$N_n = 1M$	Nb. mesh nodes
$N_{el} = 5M$	Nb. mesh elements

Table 4.4: Numerical parameters for the multiple inlet/multiple outlets duct flow problem.

optimization documented in Fig. 4.10 occurs within two different steps, all involving crisp interfaces represented on extremely stretched mesh elements: first, the design looks to be converging to a series of 8 straight pipes connecting each inlet to all four outlets, a duct arrangement that has the same reflectional symmetries as the design domain. This agrees well with the optimal documented in [97] while resembling conceptually the 2-D results from [98]. Nonetheless, this turns to be only a local minimizer, as we show in Fig. 4.11 that the optimization carries on under constant volume of fluid, and progressively wipes off 4 out of the 8 pipes, for the optimal duct to ultimately consist of 4 straight but wider pipes connecting each inlet to two outlets two-by-two perpendicular to one another (the whole arrangement being

symmetric with respect to one of the bisector planes). This stresses the importance of performing full-scale optimization, as the cost function of the asymmetric design is noticeably lower (by almost 30%), and relying on simple problem symmetries to reduce the cost can thus yield suboptimal results; see [97] where only 1/8 of the cavity is simulated.

4.3.4 Discussion

This last section is dedicated to discussing the numerical cost of the presented approach. Figure 4.12(a) presents detailed timing results obtained by averaging (and normalizing to achieve unit average time per iteration) dedicated update steps performed on 64 cores (150 steps in 2-D, 50 steps in 3-D). In 2-D, the cost of an iteration is dominated by that of computing the state solution (about 10 Navier–Stokes iterations representing 50% of the total cost, which can be scaled down substantially in the context of steady-state problems using an iterative Newton-like method), and otherwise by that of adapting the mesh (about 30% of the total cost). Using the same number of processors, the cost of a 3-D iteration is larger than its 2-D counterpart by roughly three orders of magnitude, the cost of which is essentially that of the two passes of mesh adaptation (about a cumulative 75% of the total cost, although the cost of the first pass is twice as large as that of the second pass, since (i) the volume constraint is not applied at each design step, only when the difference between the actual and target volumes exceeds the 5% tolerance, and (ii) less elements and nodes need to be moved and migrated across processors. Meanwhile, the cost of both geometrically reinitializing the signed distance function level set and of optimizing the volume constraint offset is very affordable, as it represents less than 4% in total, with 4-5 dichotomy iterations needed to reach the desired accuracy. The timing results reported in Figs. 4.12(c-e) show that the same conclusions carry over when applying the method to the other multiple inlet/outlet duct flows tackled herein . The only difference is in the cost of the volume constraint step, as the frequency at which consecutive corrections are applied indirectly depends on the number of design steps taken to reach the target volume. This gives hope that the observed trends may carry over to any other problem of same dimensionality, tackled with comparable parameters.

The associated absolute run times per iteration shown in Fig 4.13 are seen to be very consistent, in the sense that they change little from case to case. In return, the total run times reported in Tab. 4.5 are entirely driven by the number of design steps needed to converge. Here, the reported cost is essentially that of recovering the proper volume of fluid, as fulfilling the proper volume constraint from the outset requires a larger number of smaller solid inclusions, which would either dramatically increase the surface of the interfaces that needs be captured (and thus the number of mesh elements needed to maintain the numerical accuracy), or risk clogging the

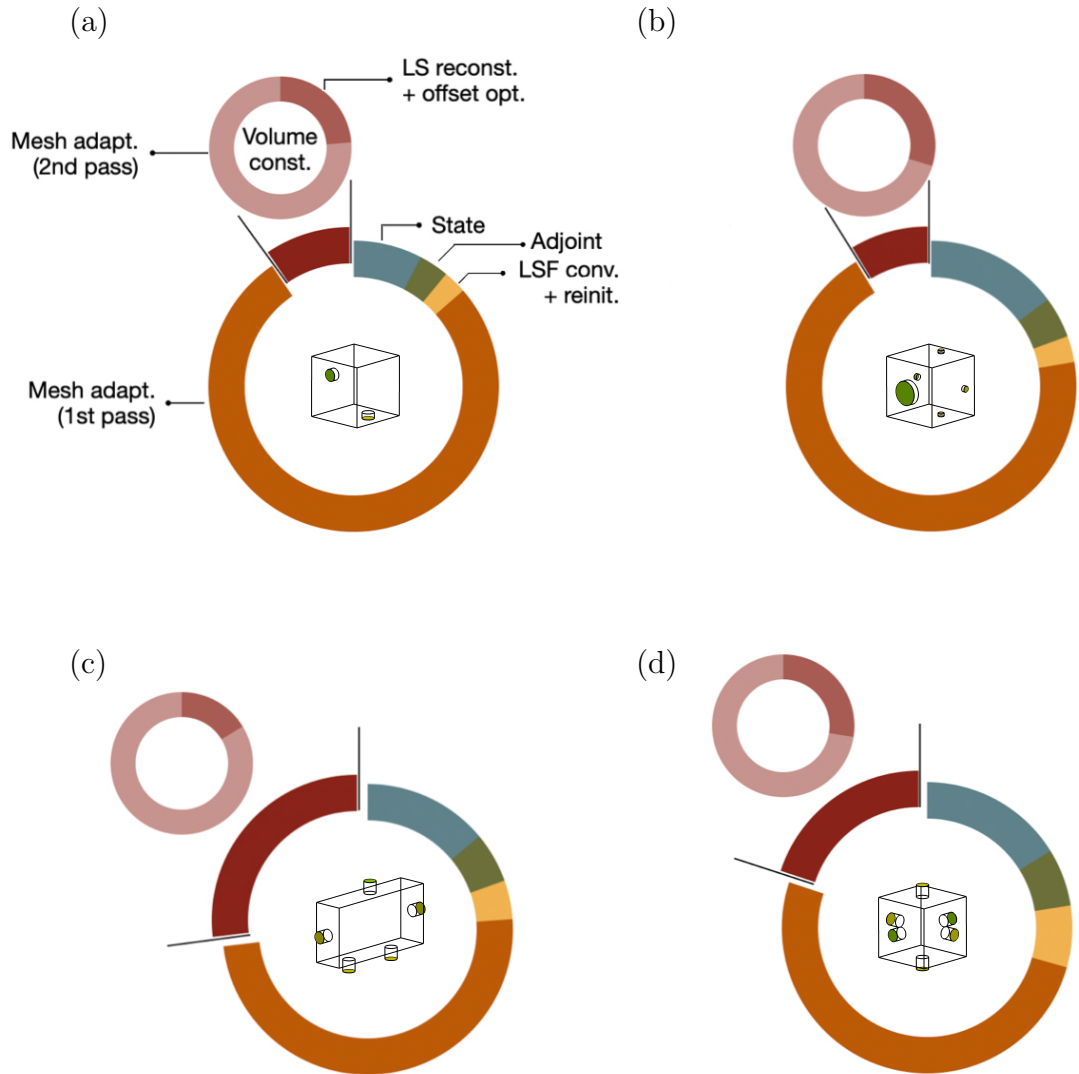


Figure 4.12: (a) Computational cost of the implemented algorithm, as obtained averaging 50 update steps of the 3-D single inlet/single duct flow presented in Fig. 4.3(a). (b) Same as (a) for the single inlet/multiple outlet duct flow presented in Fig. 4.3(b), (c) single inlet/multiple outlet duct flow presented in Fig. 4.3(c), and (d) multiple inlet/multiple outlet duct flow presented in Fig. 4.3(d). All simulation parameters are those provided in Tabs. 4.1-4.4. The LS and LSF labels stand for level set (LS) and filtered level set (LSF), respectively.

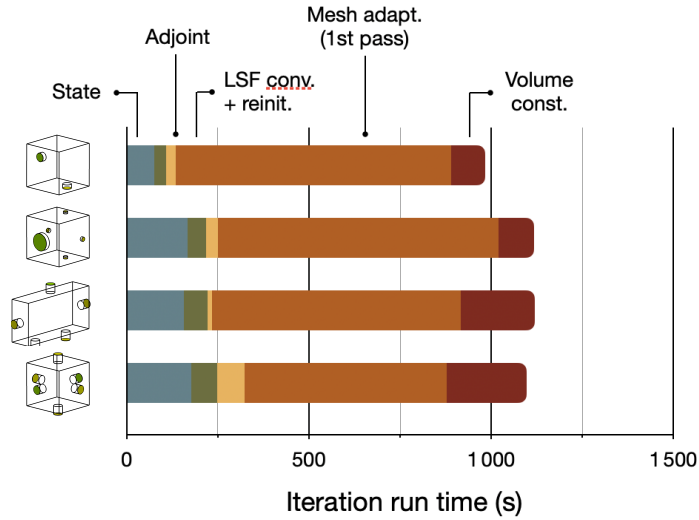


Figure 4.13: Average run time per iteration for the various cases documented in Fig. 4.12.

fluid path due to insufficient mesh refinement. Because the single inlet/multiple outlet duct flow presented in Fig. 4.3(d) all rely on cylindrical, not spherical inclusions, their run time benefits from a lower initial volume of fluid (in the range between 35 and 50%, while all other case start above 75%), which speeds up the process or meeting the desired target volume. Once this has been done, all cases converge within about 200 iterations (about 60h of resolution time, a similar run time being achieved when initializing the single inlet/single outlet test case with a quarter torus fitting exactly to the inlet and outlet). The only exception is the multiple inlet/multiple outlet duct flow presented in Fig. 4.3(d), as an extra 300 iterations are needed to bypass the basin of attraction of the symmetric local minimizer and reach the asymmetric global minimizer. The reported run times, while large in a vacuum, are actually much lower than those that required to converge on a fixed uniform grid with similar mesh refinement. To give a taste, discretizing the single inlet/single outlet case with a uniform element size of 5×10^{-3} would require about 70M elements, even though the interface value achieved here is one order of magnitude smaller. It is also worth emphasizing in this regards that we did not seek to optimize efficiency, neither by adjusting the initial design (we actually used numerous inclusions on purpose to showcase the ability of the method to support complex topological changes), nor by fine tuning the descent factor (the only requirement being that the displacement achieved at each step must be below the cut-off thickness of the level set for the evolved interface to remain accurately tracked).

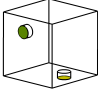
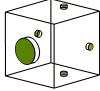
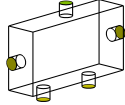
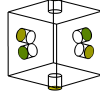
				
64	>	>	>	Nb. cores
290h	340h	150h	330h	Run time
1000	1000	500	1000	Nb. design steps
800	800	200	500	Nb. steps to target volume

Table 4.5: Run times for the various cases documented in Fig. 4.12.

4.4 Résumé du chapitre en français

Ce chapitre a décrit la parallélisation des outils numériques et mis en évidence l'originalité du solveur de remaillage parallèle. Bien que les cas tests étudiés aient présenté certaines symétries dans leur configuration initiale, cette symétrie n'a pas été prise en compte, d'abord pour augmenter la complexité du problème, et ensuite parce que notre expérience a montré que des problèmes posés symétriquement peuvent conduire à des résultats non symétriques, comme cela a été démontré dans le dernier problème abordé. La motivation pour l'optimisation à grande échelle résidait dans la nécessité de résoudre des problèmes géométriquement complexes et tridimensionnels, notamment pour des applications industrielles. Une discussion à la fin a été consacrée à la partition du maillage et au coût numérique.

Chapter 5

Topology Optimization Framework : Design of Conjugate Heat Transfer Systems

Contents

5.1	Introduction	83
5.2	Governing Equations	84
5.3	Adjoint Based Sensitivity Analysis	86
5.4	Multi-Objective Optimization	89
5.5	Numerical Resolution	90
5.5.1	Heat Equation	91
5.5.2	Adjoint Heat Equation	91
5.5.3	Adjoint Navier–Stokes	92
5.6	Numerical Benchmark	93
5.6.1	Preliminaries	93
5.6.2	Two-dimensional single pipe with heated walls	95
5.6.3	Three-dimensional single pipe with heated walls	104
5.7	Résumé du chapitre en français	108

5.1 Introduction

The focus of this chapter is on conjugate convective heat transfer systems, in which temperature variations occur within the fluid and solid material due to thermal interactions dominated by conduction in the solid and convection in the fluid. This is a matter of great engineering interest, as many industries have embraced the ability of topology optimization to improve the performances and cut the production costs of thermal devices like heat exchangers (to regulate process temperatures and ensure that machinery, chemicals, water, gas, drugs or food remain within safe operating conditions), finned surfaces, microelectronic equipment and heat sinks, and deliver more compact designs with less mass, less frictional losses and better thermal efficiency. In this context, the early related literature can be broadly classified into two categories: pure heat conduction problems maximizing heat evacuation from singular tree-like optimal structures of high conduction material, and pure fluid flow problems minimizing the power dissipated inside the domain (alternatively minimizing drag or maximizing the outlet flow uniformity) from complex channel layouts in the diffusion and convection dominated regimes; see [99, 16] for recent reviews and references therein. Since then, the topology optimization of coupled thermal-fluid problems (that combine both aspects, and thus require dual objective function strategies to increase heat transfer while keeping dissipation as low as possible) has become an active field of research. Although variants of the level set method have received attention recently [100, 101, 13], the vast majority of available studies implement a density-based monolithic approach [102, 103, 104, 105, 106, 107, 108, 109, 110] to overcome the fact that the fluid-solid interface is constantly changing over the optimization process, which makes using either a constant heat transfer coefficient or some specific surrogate model to model the heat transfer between the fluid and its surrounding ineffective. A variety of models have been used, ranging from oversimplified (dismissing the thermal conductivity differences between the solid and fluid regions [106] or numerically imposing a constant solid temperature [105]), to highly realistic (full coupling of flow and heat transfer under dual objective function strategies [102]). This chapter can be viewed as an extension to Chaps. 3 and 4, as heat transfer will be modeled by coupling the Energy Equation with the same Navier–Stokes equations of that same chapter. This will require the computation of a new adjoint system, which forms be the core investigation of the subsequent study. Multi-objective Optimization will be introduced, and the IVM and VMS explained in Chap. 2 will also be utilized for numerical implementation. The advected level set method and anisotropic mesh adaptation, previously discussed in the study will remain common and will not be further elaborated here. Lastly, numerical experiments showcasing the potential of the adopted approach to increase the recoverable thermal power while minimizing the dissipated power in two dimensional and three-dimensional systems will be presented; with particular attention paid to highlighting

the improved accuracy during all stages of the optimization.

5.2 Governing Equations

In the following, recall from Sec. 2.2 that Ω is a fixed, open bounded domain in \mathbb{R}^d (with d the space dimension), with boundary $\partial\Omega$ oriented with inward-pointing normal vector \mathbf{n} . Throughout this chapter, $\Omega = \Omega_f \cup \Omega_s$ remains the disjoint reunion of a fluid domain Ω_f and a solid domain Ω_s , separated by an interface $\Gamma = \Omega_f \cap \Omega_s$. The boundary $\partial\Omega_f$ of the fluid domain is split into interface, inlet Γ_i (defined as the combined boundary of all surfaces where fluid enters the domain), and outlet Γ_o (the combined boundary of all surfaces where fluid leaves the domain). The boundary $\partial\Omega_s$ of the solid domain is split into interface, isothermal Γ_{iso} (the combined boundary of all surfaces where temperature is prescribed), and adiabatic (the combined boundary of all surfaces where heat is exchanged with no gain or loss).

On the thermal side, distinct physical phenomena govern the fluid and solid regions, where both forced convection and diffusion occur within the fluid regions, while only the latter manifests within the solid regions. Additionally, these regions are characterized by different thermal properties. Numerically, the system of PDEs representing these phenomena can be expressed as:

$$\rho_f c_{p_f} \mathbf{u} \cdot \nabla T_f = \nabla \cdot (k_f \nabla T_f) \quad \text{in } \Omega_f \quad (5.1)$$

$$\nabla \cdot (k_s \nabla T_s) = 0 \quad \text{in } \Omega_s \quad (5.2)$$

where c_{p_f} and k_f are respectively the thermal heat capacity and thermal conductivity of the fluid, k_s is the thermal conductivity of the solid, and \mathbf{u} is the result of the Navier–Stokes equations. They are associated with the following boundary conditions :

$$T_f = T_i \quad \text{on } \Gamma_i \quad (5.3)$$

$$T_s = T_h \quad \text{on } \Gamma_{iso} \quad (5.4)$$

$$\nabla T_s \cdot \mathbf{n} = 0 \quad \text{on } \Gamma_{ad} \quad (5.5)$$

$$\nabla T_f \cdot \mathbf{n} = 0 \quad \text{on } \Gamma_o \quad (5.6)$$

$$k \nabla T \cdot \mathbf{n} = \eta (T - T^*) \quad \text{on } \Gamma \quad (5.7)$$

consisting of a prescribed temperature at the inlet and heated walls of the domain, a zero heat flux at the outlet, together with a (Robin) convective heat flux condition at the interface. T^* in Eq. (5.7) is a reference temperature and η is a heat transfer coefficient driving the budget of heat-flux and temperature variance between the fluid and solid domains (as it is widely recognized that neither isothermal nor isoflux boundary conditions can realistically mimic actual heat transfer in practical

applications, especially when the thermal diffusivity of the solid and the fluid are of the same order of magnitude [111]).

In practice, the heat transfer coefficient η ensuring that the fluid and solid exchange the proper amount of heat remains an unknown. Computing said coefficient is no small task, as it often requires solving an inverse problem to assimilate relevant experimental data, which in turn requires such data to be available. Such a lack of availability is generally acknowledged to be a limiting issue for practical applications, especially for topology optimization where varying the shape, amount, and distribution of the solid domain is integral to the optimization process itself. The immersed volume method (see Sec. 2.5) underlying this research combines both the fluid and solid phases into a single fluid with variable material properties. It thus solves the convection diffusion heat equation:

$$\rho c_p \mathbf{u} \cdot \nabla T = \nabla \cdot (k \nabla T) \quad \text{in } \Omega \quad (5.8)$$

identical to (5.1), but with variable thermal conductivity, adequately interpolated over a small layer around the interface, and otherwise equal to their fluid and solid values. In practice, we compute the composite thermal conductivity as the harmonic mean of the solid and fluid values, i.e.,

$$\frac{1}{k} = \frac{1}{k_f} H_\epsilon(\varphi) + \frac{1}{k_s} (1 - H_\epsilon(\varphi)) \quad (5.9)$$

where H_ϵ is the smoothed Heaviside function on the fluid domain defined in (3.4). This ensures continuity of the heat flux across the interface, as obtained from a steady, no source, one dimensional analysis of the heat flux when the conductivity varies stepwise from one medium to the next (see [112] for detailed derivation and analysis, and [113] for proof of the gain in numerical accuracy with respect to the classical arithmetic mean model).

This allows dropping altogether the interface thermal condition (and thus alleviates the need for a heat transfer coefficient), hence the associated boundary conditions:

$$T = T_i \quad \text{on } \Gamma_i \quad (5.10)$$

$$T = T_w \quad \text{on } \Gamma_{iso} \quad (5.11)$$

$$\nabla T \cdot \mathbf{n} = 0 \quad \text{on } \Gamma_{ad} \cup \Gamma_o \quad (5.12)$$

Provided the velocity is zero in the solid domain, the convective term vanishes in (5.8), that reduces to the pure conduction equation for the solid, together with prescribed temperature and zero heat flux conditions at the solid isothermal and adiabatic walls, respectively.

5.3 Adjoint Based Sensitivity Analysis

Mathematically, the problem is fully modeled after the coupled steady incompressible Navier–Stokes and Heat equations, hence:

$$\rho \mathbf{u} \cdot \nabla \mathbf{u} = -\nabla p + \nabla \cdot (2\mu \boldsymbol{\varepsilon}(\mathbf{u})) \quad \text{in } \Omega \quad (5.13)$$

$$\nabla \cdot \mathbf{u} = 0 \quad \text{in } \Omega \quad (5.14)$$

$$\rho c_p \mathbf{u} \cdot \nabla T = \nabla \cdot (k \nabla T) \quad \text{in } \Omega \quad (5.15)$$

with open flow boundary conditions:

$$\begin{aligned} T = T_i & \quad \text{on } \Gamma_i & \quad \mathbf{u} = \mathbf{u}_i & \quad \text{on } \Gamma_i \\ \nabla T \cdot \mathbf{n} = 0 & \quad \text{on } \Gamma_o & \quad \mathbf{u} = \mathbf{u}_o & \quad \text{on } \Gamma_o \\ T = T_w & \quad \text{on } \Gamma_w^i & \quad \mathbf{u} = \mathbf{0} & \quad \text{on } \Gamma_w^i \cup \Gamma_w^a \\ \nabla T \cdot \mathbf{n} = 0 & \quad \text{on } \Gamma_w^a \end{aligned} \quad (5.16)$$

consisting of a prescribed velocity and temperature at the inlet, and a prescribed velocity and zero heat flux at the outlet (with outflow velocity adjusted for the total amount of mass flow exiting through the outlet to match exactly that entering through the inlet). The problem of minimizing the cost function subject to the above mentioned state equations is tackled using the same continuous adjoint method as in Sec. 2.4. Thus, we form the Lagrangian:

$$\begin{aligned} \mathcal{L} = \int_{\Gamma_i \cup \Gamma_o} J_s \, ds - \int_{\Omega_f} \tilde{p} \nabla \cdot \mathbf{u} \, dv - \int_{\Omega_f} \tilde{\mathbf{u}} \cdot (\rho \mathbf{u} \cdot \nabla \mathbf{u} + \nabla p - \nabla \cdot (2\mu \boldsymbol{\varepsilon}(\mathbf{u}))) \, dv \\ - \int_{\Omega_f} \tilde{T} \cdot (\rho c_p \mathbf{u} \cdot \nabla T - \nabla \cdot (k \nabla T)) \, dv \end{aligned} \quad (5.17)$$

featuring the adjoint pressure \tilde{p} as the Lagrange multiplier for the continuity equation (5.14), the adjoint velocity $\tilde{\mathbf{u}}$ as the Lagrange multiplier for the momentum equations (5.13), and the adjoint temperature \tilde{T} as the Lagrange multiplier for the heat equation (5.15). One then seeks to decompose the variation of \mathcal{L} due to a change in the interface position into individual variations with respect to the adjoint, state and design variables. The variation with respect to the adjoint variables:

$$\begin{aligned} \delta_{(\tilde{\mathbf{u}}, \tilde{p}, \tilde{T})} \mathcal{L} = - \int_{\Omega_f} \delta \tilde{p} \nabla \cdot \mathbf{u} \, dv - \int_{\Omega_f} \delta \tilde{\mathbf{u}} \cdot (\rho \mathbf{u} \cdot \nabla \mathbf{u} + \nabla p - \nabla \cdot (2\mu \boldsymbol{\varepsilon}(\mathbf{u}))) \, dv \\ - \int_{\Omega_f} \delta \tilde{T} \cdot (\rho c_p \mathbf{u} \cdot \nabla T - \nabla \cdot (k \nabla T)) \, dv \end{aligned} \quad (5.18)$$

is trivially zero as long as (\mathbf{u}, p, T) is solution to the above coupled equations (5.14)-(5.15), in which case $\mathcal{L} = J$. After integrating by parts, the variation with respect to the state variables is:

$$\begin{aligned}
 \delta_{(\mathbf{u}, p, T)} \mathcal{L} &= \int_{\Omega_f} (\nabla \cdot \tilde{\mathbf{u}}) \delta p \, dv + \int_{\Omega_f} (\rho c_p \mathbf{u} \cdot \nabla \tilde{T} + \nabla \cdot (k \nabla \tilde{T})) \delta T \, dv \\
 &\quad + \int_{\Omega_f} (-\rho \mathbf{u} \cdot \nabla \tilde{\mathbf{u}} + \rho \nabla \mathbf{u}^T \cdot \tilde{\mathbf{u}} - \nabla \tilde{p} - \nabla \cdot (2\mu \boldsymbol{\varepsilon}(\tilde{\mathbf{u}})) - \rho c_p T \nabla \tilde{T}) \cdot \delta \mathbf{u} \, dv \\
 &\quad + \int_{\Gamma_i \cup \Gamma_o} \partial_{\mathbf{u}} J_s \cdot \delta \mathbf{u} \, ds + \int_{\partial \Omega_f} (\tilde{p} \mathbf{n} + 2\mu \boldsymbol{\varepsilon}(\tilde{\mathbf{u}}) \cdot \mathbf{n} + \rho(\mathbf{u} \cdot \mathbf{n}) \tilde{\mathbf{u}} + \rho c_p T \tilde{T} \mathbf{n}) \cdot \delta \mathbf{u} \, ds \\
 &\quad - \int_{\Gamma_i \cup \Gamma_o} \partial_p J_{\Gamma} \mathbf{n} \cdot (-\delta p \mathbf{n} + 2\mu \boldsymbol{\varepsilon}(\delta \mathbf{u}) \cdot \mathbf{n}) \, ds - \int_{\partial \Omega_f} \tilde{\mathbf{u}} \cdot (-\delta p \mathbf{n} + 2\mu \boldsymbol{\varepsilon}(\delta \mathbf{u}) \cdot \mathbf{n}) \, ds \\
 &\quad + \int_{\Gamma_i \cup \Gamma_o} \partial_T J_s \delta T \, ds + \int_{\partial \Omega_f} (k \nabla \tilde{T} \cdot \mathbf{n} + \rho c_p (\mathbf{u} \cdot \mathbf{n}) \tilde{T}) \delta T \, ds - \int_{\partial \Omega_f} \tilde{T} (k \nabla \delta T \cdot \mathbf{n}) \, ds
 \end{aligned} \tag{5.19}$$

on behalf of the viscous stress being purely tangential in incompressible flows. At this stage, adjoint equations and boundary conditions are designed to ensure $\delta_{(\mathbf{u}, p, T)} \mathcal{L} = 0$, which requires the domain and boundary integrals to vanish individually in (5.19). We thus obtain the linear, homogeneous problem:

$$-\rho \mathbf{u} \cdot \nabla \tilde{\mathbf{u}} + \rho \nabla \mathbf{u}^T \cdot \tilde{\mathbf{u}} = \nabla \tilde{p} + \nabla \cdot (2\mu \boldsymbol{\varepsilon}(\tilde{\mathbf{u}})) + \rho c_p T \nabla \tilde{T} \quad \text{in } \Omega \tag{5.20}$$

$$\nabla \cdot \tilde{\mathbf{u}} = 0 \quad \text{in } \Omega \tag{5.21}$$

$$-\rho c_p \mathbf{u} \cdot \nabla \tilde{T} = \nabla \cdot (k \nabla \tilde{T}) \quad \text{in } \Omega \tag{5.22}$$

driven by the following boundary conditions:

$$\tilde{\mathbf{u}} = -\partial_p J_{\Gamma} \mathbf{n} \quad \text{on } \Gamma_i \tag{5.23}$$

$$\tilde{T} = 0 \quad \text{on } \Gamma_i \tag{5.24}$$

$$\tilde{\mathbf{u}} = -\partial_p J_{\Gamma} \mathbf{n} \quad \text{on } \Gamma_o \tag{5.25}$$

$$k \nabla \tilde{T} \cdot \mathbf{n} + \rho c_p (\mathbf{u} \cdot \mathbf{n}) \tilde{T} = -\partial_T J_{\Gamma} \quad \text{on } \Gamma_o \tag{5.26}$$

$$\tilde{\mathbf{u}} = \mathbf{0} \quad \text{on } \Gamma_w^i \cup \Gamma_w^a \tag{5.27}$$

$$\tilde{T} = 0 \quad \text{on } \Gamma_w^i \tag{5.28}$$

$$\nabla \tilde{T} \cdot \mathbf{n} = 0 \quad \text{on } \Gamma_w^a \tag{5.29}$$

The key difference between the state and adjoint equations lies in the minus sign in front of the convective term of Eqs. (5.20)-(5.22), to reflect that adjoint information is convected upstream, not downstream, due to the non-normality of the linearized evolution operator [61]. Expressing the interface perturbations after [62] as:

$$\delta \mathbf{u} = \beta \nabla \mathbf{u} \cdot \mathbf{n}, \quad \delta T = \beta \nabla T \cdot \mathbf{n} \tag{5.30}$$

the variation with respect to the design variable is ultimately computed as:

$$\begin{aligned} \delta_\beta J_s \equiv \delta_\beta \mathcal{L} = & \beta \int_\Gamma (\tilde{p}\mathbf{n} + 2\mu\boldsymbol{\varepsilon}(\tilde{\mathbf{u}}) \cdot \mathbf{n} + \rho c_p T \tilde{T}\mathbf{n}) \cdot (\nabla \mathbf{u} \cdot \mathbf{n}) \, ds \\ & + \beta \int_\Gamma k(\nabla \tilde{T} \cdot \mathbf{n})(\nabla T \cdot \mathbf{n}) \, ds - \beta \int_\Gamma \tilde{T} (k\nabla(\nabla T \cdot \mathbf{n}) \cdot \mathbf{n}) \, ds \end{aligned} \quad (5.31)$$

which reduces to:

$$\begin{aligned} \delta_\beta J_s = & \beta \int_\Gamma \mu(\nabla \tilde{\mathbf{u}} \cdot \mathbf{n}) \cdot (\nabla \mathbf{u} \cdot \mathbf{n}) \, ds + \beta \int_\Gamma k(\nabla \tilde{T}_f \cdot \mathbf{n})(\nabla T \cdot \mathbf{n}) \, ds \\ & - \beta \int_\Gamma \tilde{T} (k\nabla(\nabla T \cdot \mathbf{n}) \cdot \mathbf{n}) \, ds \end{aligned} \quad (5.32)$$

due to the incompressibility of the state and adjoint solutions [60]. The simplest steepest-descent algorithm implemented herein therefore moves down the cost function, in the direction of the steepest slope using:

$$\beta = -\mu(\nabla \tilde{\mathbf{u}} \cdot \mathbf{n}) \cdot (\nabla \mathbf{u} \cdot \mathbf{n}) - k(\nabla \tilde{T} \cdot \mathbf{n})(\nabla T \cdot \mathbf{n}) + \tilde{T}(k\nabla(\nabla T \cdot \mathbf{n}) \cdot \mathbf{n}) \quad (5.33)$$

up to a positive multiplicative factor to control the step taken in the gradient direction. Since $\nabla(\mathbf{n} \cdot \mathbf{n}) = 0$ due to the normal vector having unit norm, it can be shown that:

$$\nabla(\nabla T \cdot \mathbf{n}) \cdot \mathbf{n} = (\nabla(\nabla T) \cdot \mathbf{n}) \cdot \mathbf{n} + (\nabla \wedge \mathbf{n}) \cdot (\mathbf{n} \wedge \nabla T) \quad (5.34)$$

and thus:

$$\nabla(\nabla T \cdot \mathbf{n}) \cdot \mathbf{n} = (\nabla \wedge \mathbf{n}) \cdot (\mathbf{n} \wedge \nabla T) \quad (5.35)$$

because the second derivatives vanish due to the use of P1 linear finite element approximations. Also, since the normal vector in a level set framework is computed as $\mathbf{n} = \nabla \phi / \|\nabla \phi\|$, we have:

$$\nabla \left(\frac{\phi}{\|\nabla \phi\|} \right) = \mathbf{n} - \frac{\phi}{\|\nabla \phi\|^3} H(\phi) \cdot \nabla \phi \quad (5.36)$$

where H is the Hessian of ϕ . Since $\phi = 0$ by design on the interface, we thus have:

$$\nabla \wedge \mathbf{n} = \nabla \wedge \nabla \left(\frac{\phi}{\|\nabla \phi\|} \right) = \mathbf{0} \quad (5.37)$$

It follows that:

$$\nabla(\nabla T \cdot \mathbf{n}) \cdot \mathbf{n} \equiv 0 \quad (5.38)$$

and Eq. (5.33) reduces to:

$$\beta = -\mu(\nabla \tilde{\mathbf{u}} \cdot \mathbf{n}) \cdot (\nabla \mathbf{u} \cdot \mathbf{n}) - k(\nabla \tilde{T} \cdot \mathbf{n})(\nabla T \cdot \mathbf{n}) \quad (5.39)$$

That goes through all the process from Sec. 3.2.2 to 3.2.3 to localize the computation around the interface, eliminate singularities, and ensure the maximum possible deformation within the thickness of the adapted mesh.

5.4 Multi-Objective Optimization

A classical objective in topology optimization of conjugate heat transfer is to maximize heat transfer in the domain without increasing the mechanical pumping power that need be spent to overcome friction and move the fluid through the device (nor blocking the fluid flow). This is done in some studies by maximizing heat transfer under prescribed pressure drop values [106, 109], and in others by minimizing pressure drop under prescribed heat transfer performance [114]. We rather use here multi-criteria optimization and minimize the linear weighted sum of a hydraulic cost function J_ν and a thermal cost function J_Θ . This yields:

$$J_s = (1 - \omega)J_\nu + \omega J_\Theta \quad (5.40)$$

where $\omega \in [0; 1]$ is the so-called thermal weigh, a scalar-valued factor weighing the priority given to each objective function ($\omega = 0$ in the pure hydraulic limit, and $\omega = 1$ in the pure thermal limit). In practice, a single point concurrently minimizing both objectives usually does not exist. The solution to such a problem thus aims at identifying the Pareto front [115], i.e., the subset of designs that best manage trade-offs between conflicting criteria, in the sense that further optimizing one cost function decreases the performance of the other one (after which the final design is selected from the Pareto optimal subset by a human decision maker based on subjective preferences).

The bi-objective optimization problems addressed in this chapter aim towards minimizing the linear weighted sum (5.40) of two criteria inspired from [60] and [116], namely the hydraulic cost function J_ν measuring the net inward flux of total pressure through the boundaries (to minimize) and the thermal cost function J_Θ measuring the recoverable thermal power from the domain through the inlet and outlet flow boundary conditions (to maximize, the minimization applies to $-J_\Theta$). Since the orientation of the normal \mathbf{n} yields $\mathbf{u} \cdot \mathbf{n}|_{\Gamma_i} > 0$ and $\mathbf{u} \cdot \mathbf{n}|_{\Gamma_o} < 0$, this is expressed in the form of (2.11) as

$$J_\nu = p_{tot}(\mathbf{u} \cdot \mathbf{n}) = (p + \frac{1}{2}\rho(\mathbf{u} \cdot \mathbf{u}))(\mathbf{u} \cdot \mathbf{n}) \quad \text{and} \quad J_\Theta = \rho c_p T(\mathbf{u} \cdot \mathbf{n}) \quad (5.41)$$

By substituting J_ν and J_Θ of Eq. (5.40) by their respective values of Eq. 5.41, and adding the minus sign before J_Θ (for maximization), we can reconstitute the general cost function:

$$J_s = (1 - \omega)(p + \frac{1}{2}\rho(\mathbf{u} \cdot \mathbf{u}))(\mathbf{u} \cdot \mathbf{n}) - \omega \rho c_p T(\mathbf{u} \cdot \mathbf{n}) \quad (5.42)$$

Finally, we can specify the derivatives of the cost function with respect to the state

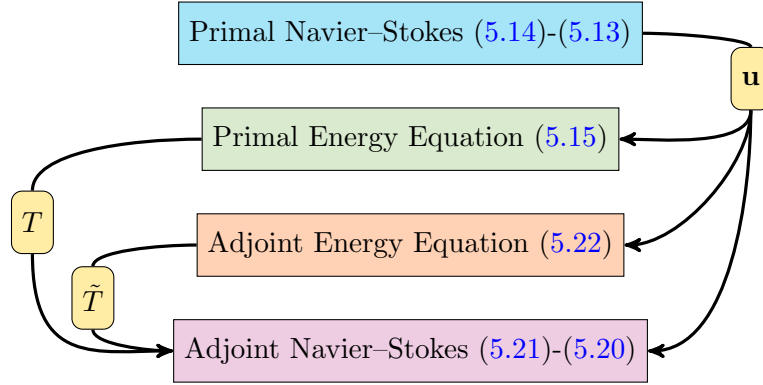


Figure 5.1: Schematic of the inputs/outputs of the computational models and their coupling.

variables $(p; \mathbf{u}; T)$, that are given by:

$$\partial_p J_s = (1 - \omega)(\mathbf{u} \cdot \mathbf{n}) \quad (5.43)$$

$$\partial_{\mathbf{u}} J_s = (1 - \omega)p_{tot}\mathbf{n} + (1 - \omega)\rho(\mathbf{u} \cdot \mathbf{n})\mathbf{u} - \omega\rho c_p T \mathbf{n} \quad (5.44)$$

$$\partial_T J_s = -\omega\rho c_p(\mathbf{u} \cdot \mathbf{n}) \quad (5.45)$$

5.5 Numerical Resolution

The resulting velocity of the Navier–Stokes equations (5.14)–(5.13) serves as an input velocity to equation (5.8). They are thus the first to be solved, and their computation follows the explanation in Sec. 2.8. The momentum equation of the adjoint system (5.20) contains a term in \tilde{T} . Since the linear adjoint thermal equation (5.22) has no terms in neither $\tilde{\mathbf{u}}$ nor \tilde{p} , we start by solving it first, then consider $\rho c_p T \nabla \tilde{T}$ as a constant source term in the momentum equation. In addition, the computation of the adjoint equations (5.20) and (5.22) requires converged velocity and temperature solutions of the steady state primal equations (5.14)–(5.15). Thus, the coupling of the state and adjoint equations is summarized in Fig. 5.1

5.5.1 Heat Equation

The coarse scale variational problem for the heat equation reads

$$\int_{\Omega} (\rho c_p \mathbf{u} \cdot \nabla T) s \, dv + \int_{\Omega} k \nabla T \cdot \nabla s \, dv - \sum_{k=1}^{N_e} \int_{\Omega_k} \tau_4 r_4 \rho c_p \mathbf{u} \cdot \nabla s \, dv - \sum_{k=1}^{N_e} \int_{\Omega_k} \tau_5 r_4 \rho c_p \mathbf{u}_{\parallel} \cdot \nabla s \, dv = 0 \quad (5.46)$$

where \mathbf{u}_{\parallel} is the (normalized) velocity projected along the direction of the temperature gradient defined as

$$\mathbf{u}_{\parallel} = \frac{\mathbf{u} \cdot \nabla T}{\|\nabla T\|^2} \nabla T \quad (5.47)$$

r_4 is the heat equation residual

$$-r_4 = \rho c_p \mathbf{u} \cdot \nabla T \quad (5.48)$$

and $\tau_{4,5}$ are mesh-dependent stabilization parameters acting both in the direction of the solution and of its gradient, that proceed from the stabilization of the ubiquitous convection-diffusion-reaction equation [77, 78], whose definition is given in [117, 118]. Equation (5.46) is solved with implicit treatment of the convection term and conduction terms (as the convection velocity is taken as a given) and explicit treatment of the stabilization coefficients.

5.5.2 Adjoint Heat Equation

Since the adjoint heat equation (5.22) is formally identical to its state counterpart (see Eq. (5.8), save for the change in the sign of the convection velocity), its coarse scale variational problem deduces straightforwardly as:

$$\begin{aligned} & - \int_{\Omega} (\rho c_p \mathbf{u} \cdot \nabla T) s \, dv + \int_{\Omega} k \nabla T \cdot \nabla s \, dv + \sum_{k=1}^{N_e} \int_{\Omega_k} \tau_4 r_4 \rho c_p \mathbf{u} \cdot \nabla s \, dv \\ & + \sum_{k=1}^{N_e} \int_{\Omega_k} \tau_5 r_4 \rho c_p \mathbf{u}_{\parallel} \cdot \nabla s \, dv - \int_{\Gamma_o} \rho (\mathbf{u} \cdot \mathbf{n}) \tilde{T} s \, ds = \int_{\Gamma_o} \partial_T J_s s \, ds \end{aligned} \quad (5.49)$$

and features the same residual r_4 and stabilization coefficients $\tau_{4,5}$ as in Sec. 2.8. Note, Eq. (5.49) also includes boundary terms evaluated at the outlet, which is because the integration by part of the conductive term unveils a boundary term:

$$\int_{\partial\Omega} (k \nabla T \cdot \mathbf{n}) s \, ds = - \int_{\Gamma_o} \left(\rho (\mathbf{u} \cdot \mathbf{n}) \tilde{T} + \partial_T J_s \right) s \, ds \quad (5.50)$$

due to the adjoint outflow thermal condition (5.26). In practice, though, preliminary tests have assessed that the adjoint thermal power term $\rho c_p(\mathbf{u} \cdot \mathbf{n})\tilde{T}$ consistently dominates by at least four orders of magnitude over the heat flux term $k\nabla\tilde{T} \cdot \mathbf{n}$. We thus end up simplifying the numerical implementation using the approximate condition:

$$\tilde{T} = -\omega \quad \text{on } \Gamma_o \quad (5.51)$$

and solve the scale variational problem (without boundary term):

$$\begin{aligned} & -\int_{\Omega} (\rho c_p \mathbf{u} \cdot \nabla T) s \, dv + \int_{\Omega} k \nabla T \cdot \nabla s \, dv \\ & + \sum_{k=1}^{N_e} \int_{\Omega_k} \tau_4 r_4 \rho c_p \mathbf{u} \cdot \nabla s \, dv + \sum_{k=1}^{N_e} \int_{\Omega_k} \tau_5 r_4 \rho c_p \mathbf{u}_{\parallel} \cdot \nabla s \, dv = 0 \end{aligned} \quad (5.52)$$

with implicit treatment of the convection term and conduction terms (as the convection velocity is taken as a given) and explicit treatment of the stabilization coefficients.

5.5.3 Adjoint Navier–Stokes

For the adjoint Navier–Stokes equation, we follow the exact same philosophy of Sec. 2.8.2, adding the discretization of the additional source term. The application of the stabilized formulation (as described there) yields the following coarse scale variational problem:

$$\begin{aligned} & \int_{\Omega} (-\rho \mathbf{u} \cdot \nabla \tilde{\mathbf{u}} + \rho \nabla \mathbf{u}^T \cdot \tilde{\mathbf{u}}) \cdot \mathbf{w} \, dv + \int_{\Omega} 2\mu \boldsymbol{\varepsilon}(\tilde{\mathbf{u}}) : \boldsymbol{\varepsilon}(\mathbf{w}) \, dv + \int_{\Omega} \tilde{p}(\nabla \cdot \mathbf{w}) \, dv \\ & - \int_{\Omega} \rho c_p T \nabla \tilde{T} \cdot \mathbf{w} \, dv + \int_{\Omega} (\nabla \cdot \tilde{\mathbf{u}}) q \, dv - \sum_{k=1}^{N_e} \int_{\Omega_k} \tilde{\tau}_1 \tilde{\mathbf{r}}_1 \cdot (-\rho \mathbf{u} \cdot \nabla \mathbf{w}) \, dv \\ & - \sum_{k=1}^{N_e} \int_{\Omega_k} \tilde{\tau}_1 \tilde{\mathbf{r}}_1 \cdot \nabla q \, dv - \sum_{k=1}^{N_e} \int_{\Omega_k} \tilde{\tau}_2 \tilde{r}_2 (\nabla \cdot \mathbf{w}) \, dv = 0 \end{aligned} \quad (5.53)$$

where the the stabilization coefficients $\tilde{\tau}_{1,2}$ and the associated momentum and continuity residuals ($\tilde{\mathbf{r}}_1, \tilde{r}_2$) are the same as those in Sec. 2.8.2. This implicitly amounts to neglecting the additional stabilization stemming from the $\rho \nabla \mathbf{u}^T \cdot \tilde{\mathbf{u}}$ term describing the production of adjoint perturbations, that has been found to have no effect on the numerical results, as the problems considered herein are in the convection (not reaction) dominated limit.

$h_{\perp} = 0.0001$	Min. interface normal mesh size
$\Delta t = 0.1$	CFD Numerical time step
$E = 0.005$	Level set cut off thickness
$ \delta\varphi = [0.0005; 0.001]$	Initial volume recovery offset
$r_s = 0.0125$	Transition radius
$\alpha_s = 2.1$	Sharpness parameter
$(\epsilon_{s1}, \epsilon_{s2}) = (0.0005, 0.005)$	Regularization parameters

Table 5.1: Algorithmic parameters.

5.6 Numerical Benchmark

5.6.1 Preliminaries

This section assesses the efficiency of the numerical framework through a series of topology optimization problems showcasing the accuracy to which the optimal interfaces are captured in the simulation model. Several cases are considered in 2-D and 3-D, for which we aim at maximizing heat transfer in the domain while minimizing the total pressure losses in the fluid channels.

In all cases, a reference design domain is chosen under the form of a cubic or cuboid (parallelepipedic) cavity, with cylindrical inlet and outlet at which parabolic profiles normal to the boundary are prescribed, as defined by

$$\mathbf{u}_{i,o} = u_{i,o} \left(1 - \frac{4r^2}{e_{i,o}^2} \right) \mathbf{n} \quad (5.54)$$

with r the distance to the inlet/outlet center, e_i (resp. e_o) the inlet diameter (resp. the outlet diameter) and u_i (resp. u_o) the inlet centerline velocity (resp. the outlet centerline velocity, adjusted for the mass flow exiting through the outlet to match exactly that entering through the inlet). For each case, the control parameters are the Reynolds (built here on inlet diameter and maximum inlet velocity) and Prandtl numbers.

The remainder of the practical implementation details are as follows:

- All design domains are initialized with solid inclusions coming in various shapes and sizes. From experience, the flow topology optimization problems tackled in the following are essentially insensitive to the initial design provided a sufficient large number of inclusions is used (additional mechanisms for seeding solid inclusions could be added to the proposed framework, but however lie outside the scope of this study).

- The admissible error on the target volume is set to 1% in 2-D, and 5% in 3-D.
- The fluid is systematically conveyed into and out of the design domain using leads of length l_i (the same at all inlets) and l_o (the same at all outlets) appended normal to the boundary. This is for numerical consistence, as the exact problem formulation in the literature may vary depending on the case, and it is not always clear whether such leads should be included in the design domain (which they are here, although they are not considered in the volume constraint, neither in definition of the target volume nor in the computation of the volume of fluid).
- The singular subsets excluded from the displacement normalization step are the sharp intersections between the leads and the boundary of the cavities. Note, this is not a consequence of explicitly representing the leads, as the exact same procedure has been found suitable without such appendage. In practice, since all inlets and cylindrical outlets are cylindrical, each smooth filter ζ therefore transitions from 0 to 1 over a circle of radius $2r_s$ (in 2-D) or a torus of minor radius $2r_s$ and major radius equal to the inlet/outlet radius (in 3-D).
- The leads are excluded from the displacement normalization step, for which we simply add to the max argument of (3.5) a binary filter returning a value of 0 at all nodes located inside the pipes. This is again to avoid slowing down the convergence rate of the iterative optimization process, as the maximum displacement is otherwise located in the leads (because the easiest way to minimize the dissipated power is to suppress the flow by having the solid entirely clogging the leads).
- Without seeking to optimize the performance, all optimization runs have been found to converge within a few hundreds iterations, which is essentially the number of steps used to fulfill the fluid volume constraint (more details in the following) while ensuring that the displacement achieved at each iteration remains below the level set cut-off thickness.
- All 3-D meshes (resp. 2-D meshes) have been checked to have an element-to-node ratio close to 5 (resp. close to 2), as should be for denses mesh made up of tetrahedral (resp. triangular) elements. In order to ease the comparison with the available literature, the mesh information is thus documented in the following in terms of its equivalent number of elements, defined as $N_{el} = 5N_n$ (resp. $N_{el} = 2N_n$).

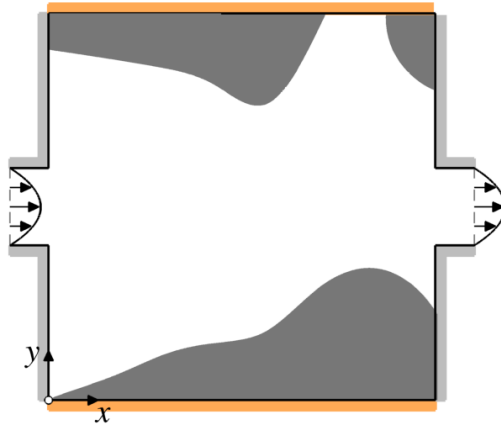


Figure 5.2: Set-up of the two-dimensional single pipe problem with heated walls. The orange and light gray shade denote hot isothermal and adiabatic walls, respectively.

5.6.2 Two-dimensional single pipe with heated walls

The first case study is a two-dimensional conjugate heat transfer problem that has received substantial attention in the recent literature [116, 110, 12, 119]. The design domain shown in Fig. 5.2 is a square cavity of unit height. It has a single inlet on the left side and a single outlet on the right side lined up in front of each other, and is discretized with 50000 elements. A cold fluid is flowing from the inlet, and is heated by the top and bottom walls, subject to a fixed (hot) temperature. All other walls (cavity and leads) are insulated from the surroundings with zero heat absorbed or released (i.e., adiabatic). The solid is set to be 10 times more diffusive than the fluid, which allows using fluid to insulate thermally inner regions from the cold inlet temperature. The aim is to determine the optimal design that connects the inlet to the outlets subject to the constraint that the fluid must occupy 40% percent of the cavity (twice as much as the straight parallel pipe fitting exactly to the inlet and outlet). All other problem parameters, including Reynolds and Prandtl numbers, are given in Tab. 5.2. Note, because the inlet and outlet diameters are the same, mass conservation demands the same velocity condition to be prescribed at the inlet and outlet. We do not share the view expressed in [110] that this is ill-posed, in the sense that it does force the algorithm to identify acceptable trade-offs between both hydraulic and thermal for heat and mass transfer optimization without yielding broken flow paths, dead ends or non-physical artifacts, which is the desired goal. Moreover, the argument that the optimization is limited by the fact that the sole variables left to optimization are the pressure (not total pressure)

$\Omega = [0; 1] \times [0; 1]$	Design domain
$d = 2$	Problem dimensionality
$V_{target} = 0.4$	Target volume of fluid
$V_{\varphi,0} = 0.4$	Initial volume of fluid
$Re = 4.5$	Reynolds number
$Pr = 5$	Prandtl number (fluid)
$k_s/k_f = 10$	Solid to fluid thermal diffusivity ratio
$T_w = 10$	Hot wall temperature
$u_i = 1$	Inlet centerline velocity
$T_i = 0$	Inlet cold temperature
$e = 0.2$	Inlet diameter
$l_i = 0.1$	Inlet leads length
$\mathbf{x}_i = (-0.1, 0.5)$	Inlet center coordinates
$u_o = 1$	Outlet centerline velocity
$e_o = 0.2$	Outlet diameter
$l_o = 0.1$	Outlet lead length
$\mathbf{x}_o = (1.1, 0.5)$	Outlet 1 center coordinates
$N_n = 25000$	Nb. mesh nodes
$N_{el} = 50000$	Nb. mesh elements

Table 5.2: Numerical parameters for the two-dimensional single pipe problem with heated walls.

drop between the inlet and outlet, and the outlet temperature (which removes the need to explore, e.g., converging or narrowing channels designs aimed at increasing the fluid velocity), while true in this particular setting, does not hold if multiple inlets/outlets or different inlet/outlet diameters are used.

We show in Fig. 5.3 distinct optimal designs computed by increasing progressively the thermal weigh, to which we come back below for further discussion. At this stage, the point of interest is that all related optimization runs go through several complex stages all accurately represented on anisotropic adapted meshes made up of extremely stretched elements on either side of the interface. This is evidenced by the selected samples shown in Figs. 5.4-5.5, where the main difference compared to the hydraulic cases of Sec. 3.4 is the finer element size used to discretize the inner solid domain (here the same as in the inner fluid domain) to accurately resolve heat conduction. This is all the more important given that the increased non-linearity of the optimization problem at large thermal weights (where there is almost no contribution from the hydraulic cost function) yields strongly anisotropic material distributions, that require adequately capturing the formation and destruction of

very fine cross-flow fluid structures whose diameter can be below 1/20 the inlet diameter.

For low thermal weights, the optimal design is a single, straight pipe connecting the inlet to the outlet, as evidenced in Fig. 5.4(a). This is because the contribution of the thermal cost function is negligible, so the only objective is to minimize the fluid power dissipation, hence short and wide pipes. In return, the optimal pipe is as wide as allowed by the volume constraint, with increased cross section halfway though (compared to the inlet and outlet) to minimize shear. Increasing ω adds more priority to increase the recoverable thermal power, which opens the possibility to depart from the straight pipe even at the cost of some increase in the hydraulic objective. In this regards, our results highlight the existence of two distinct branches of solution, referred to as symmetric and asymmetric.

Symmetric designs feature a solid core forming at the center of the cavity, hence dividing the lead into a lower and an upper pipe, as shown in Fig. 5.4(b). This increases both the dissipated power and the recoverable thermal power, as it lengthens the distance over which the fluid travels, but moves both pipes towards the hot walls, and heats up the fluid without any temperature losses associated to heat flux conduction through the solid (as the solid thermal conductivity is 10 times that of the fluid). The asymmetric designs presented in Fig. 5.5(a) conversely feature a single pipe bending into either the lower or the upper half of the domain, which is a different trade-off involving both less recoverable thermal power and less dissipated power, as the fluid is heated up at only one out of the two hot wall, but travels in a wider pipe.

Increasing the thermal weight forces the fluid along the hot walls to expand the exchange surface. Beyond a certain threshold, the symmetric solid core splits vertically into an increasing number of subcores, as a network of fluid strips forms to act as a large thermal resistance breaking the horizontal temperature gradient to reduce the core heat conduction; see Fig. 5.4(c). Meanwhile, in Fig. 5.5(b), the asymmetric bent pipe gives way in to the more complex Z-shaped pipe successively forcing the flow along the top and bottom walls (yet another trade-off that increases both the recoverable thermal power and the dissipated power, as the heat exchange surface doubles, but the fluid travels in a thinner and longer pipe.), whose solid layout eventually fragments vertically near the Z edges to make the most of the low conductivity of the fluid; see Fig. 5.5(c).

Upon comparing the above design to those in Ref. [116] (the closest study to our work in the available literature), the following remarks can be made:

- anisotropic adapted meshes dramatically improve the accuracy of all geometric representations, as most results in the recent available literature exhibit obvious staircase effects in all curved regions.
- the solid and fragmented core solutions are generally consistent, although they

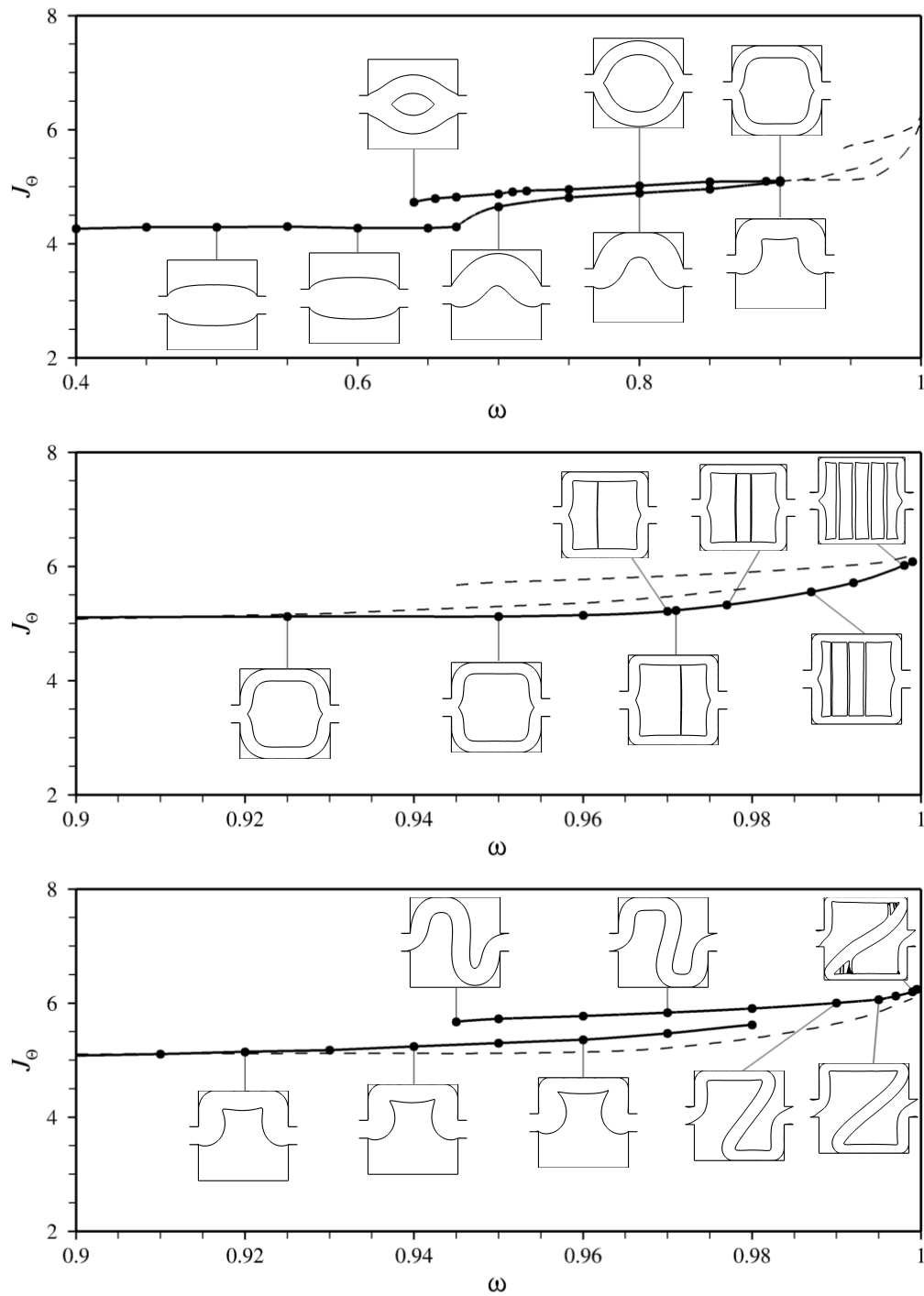


Figure 5.3: Optimal designs sorted by weighting ω for the two-dimensional single pipe device with heated walls presented in Fig. 5.2. (a) Low and intermediated thermal weights. The dashed lines denote the results obtained at large thermal weights, further presented by the close-ups in (b-c) for (b) symmetric and (c) asymmetric designs.

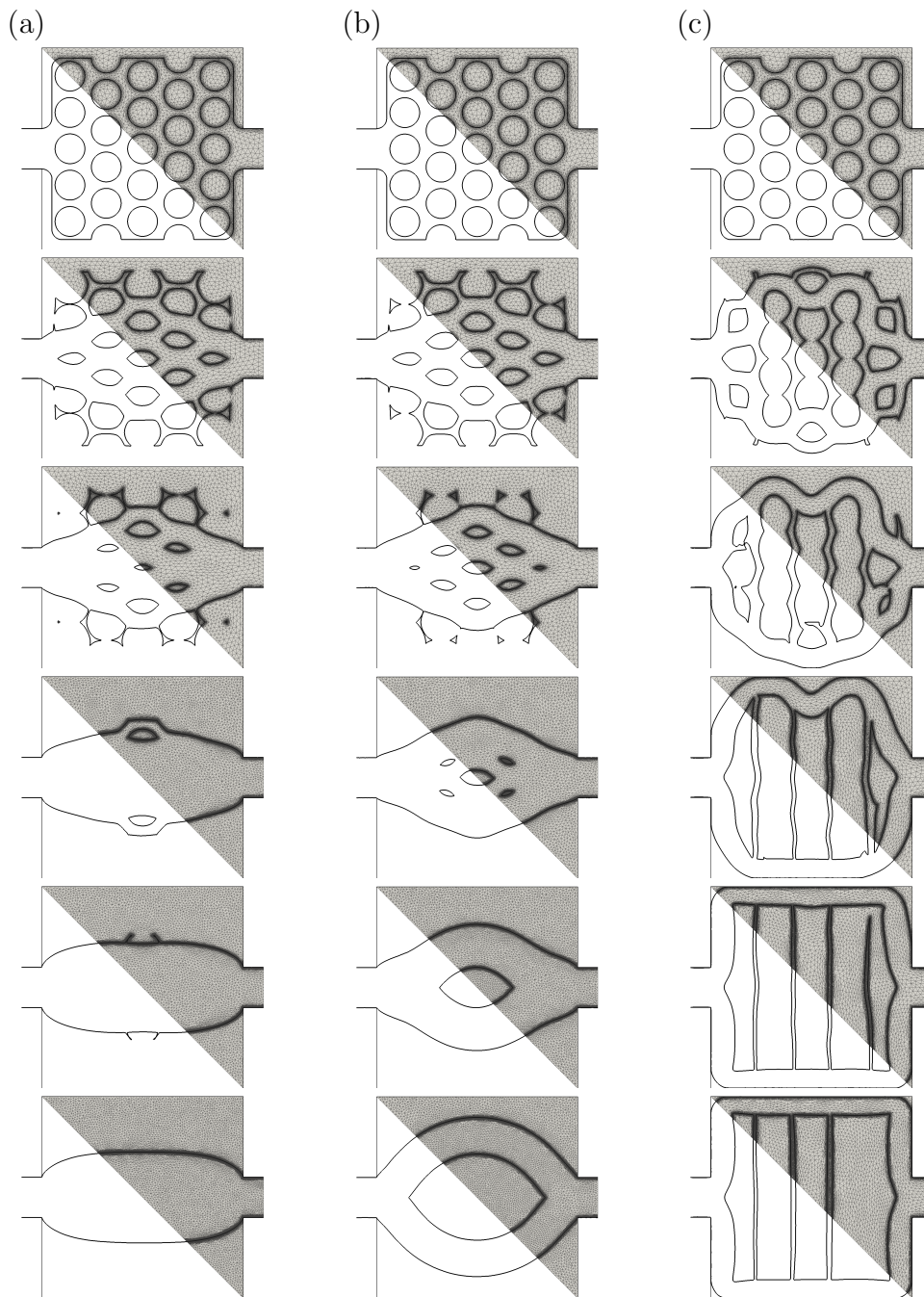


Figure 5.4: Multi-objective optimization of the two-dimensional single pipe device with heated walls presented in Fig. 5.2. From top to bottom: the zero iso-value of the level set function and associated anisotropic adapted meshes are sampled over the course of optimization using the parameters given in Tab. 5.2. (a) Straight pipe solution with $\omega = 0.4$. (b) Solid core solution with $\omega = 0.7$. (c) Fragmented core solution with $\omega = 0.987$.

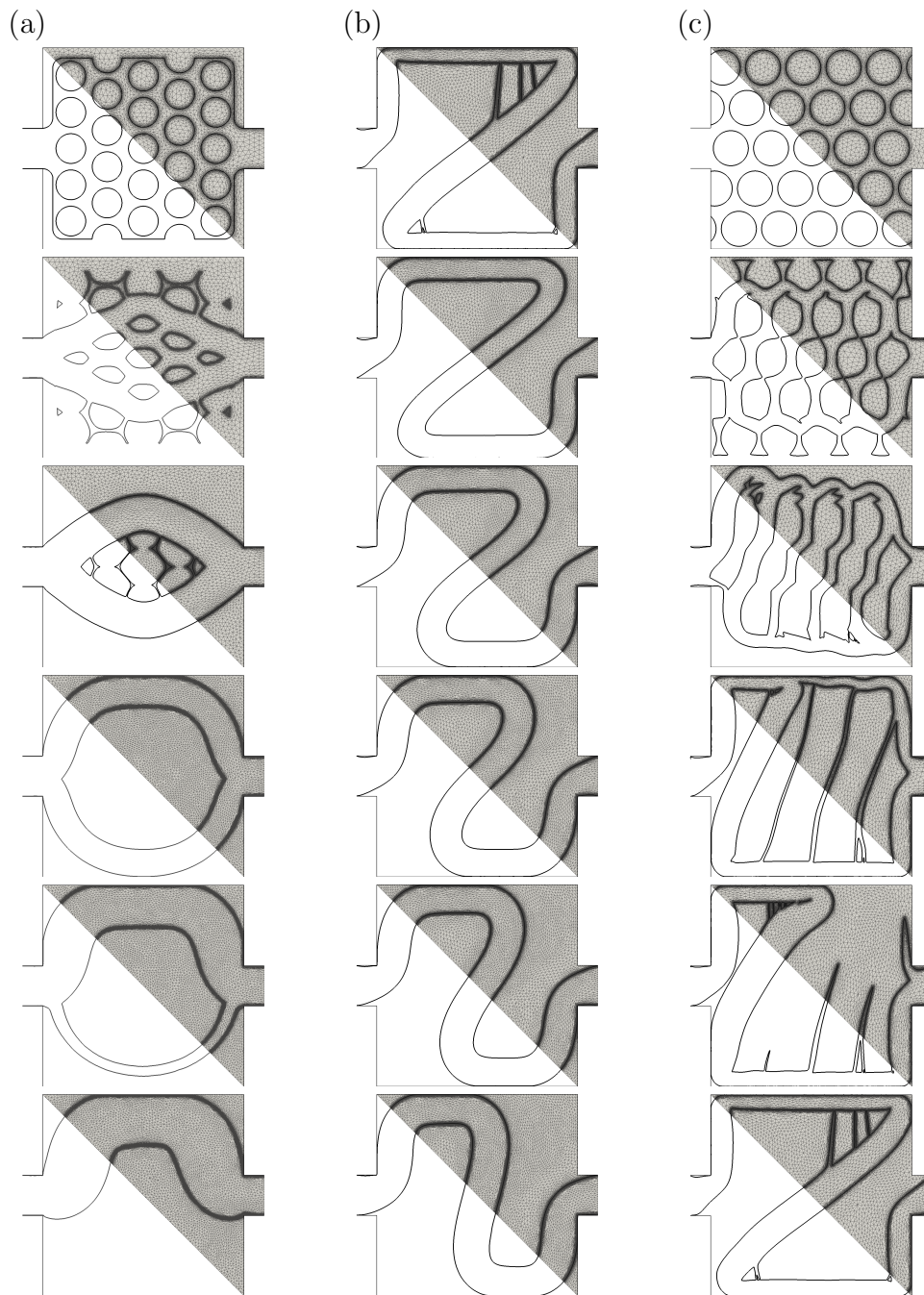


Figure 5.5: Multi-objective optimization of the two-dimensional single pipe device with heated walls presented in Fig. 5.2. From top to bottom: the zero iso-value of the level set function and associated anisotropic adapted meshes are sampled over the course of optimization using the parameters given in Tab. 5.2. (a) Bent pipe solution with $\omega = 0.85$. (b) Z pipe solution with $\omega = 0.97$. (c) Fragmented Z pipe solution with $\omega = 0.998$.

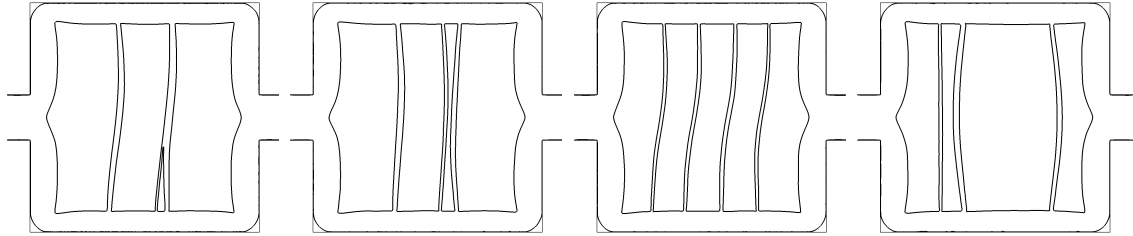


Figure 5.6: Fragmented core solutions computed under various initial designs under thermal weigh $\omega = 0.987$.

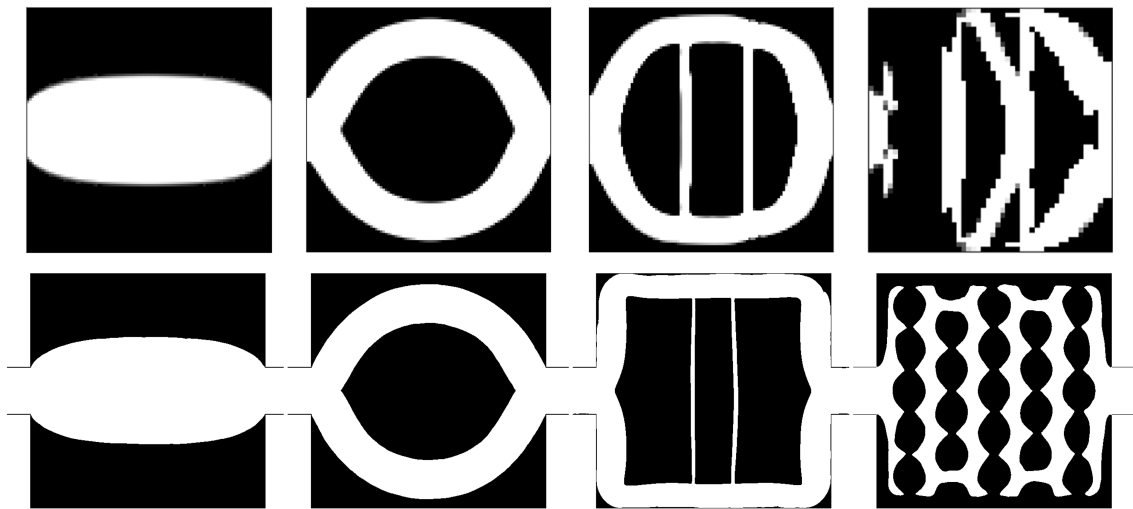


Figure 5.7: Comparison of similar architectures encountered in [116] (on the top) and in the current study (on the bottom). Optimal designs were taken at different thermal weights, for intence on the top, and from left to right, $\omega = 0, 0.6, 0.8, \text{ and } 1.0$, where for the current study (also from left to right) $\omega = 0, 0.8, 0.97, \text{ and } 1.0$

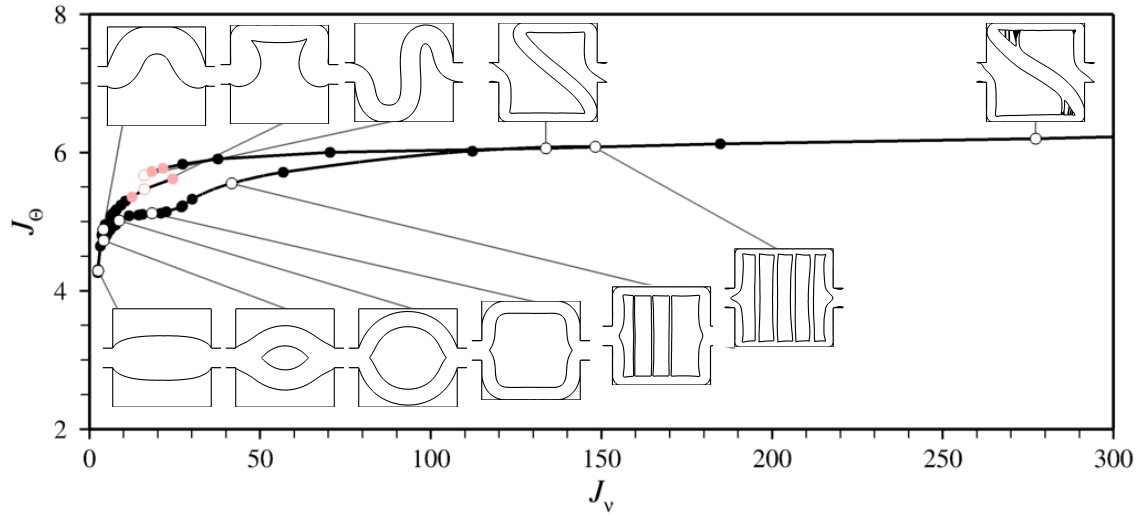


Figure 5.8: Pareto frontier for bi-objective topology optimization of the single pipe device with heated walls. The red symbols are the near-optimal design for which both the dissipated power and the recoverable thermal power approach their single objective optimization value.

show up in [116] at surprisingly much lower values of ω (an issue already raised in [110]) and with lesser horizontal symmetry at large thermal weights (which may be because the authors in the aforementioned study do not impose a specific target volume of fluid, but only an upper bound).

- asymmetric designs are noticeably absent from [116, 110] and from other studies tackling variations of this problem. Again the explanation may lie in the constraint on the maximum volume of fluid, in the sense that for a given asymmetric design minimizing the cost function under a certain thermal weigh, a more efficient symmetric design may exist at a smaller volume of fluid. Asymmetric designs are reported in [12], for which the authors allude to the use of unstructured meshes, but we believe they are rather the consequence of different flow regimes, as the aforementioned study considers a much higher Reynolds number of 400 and a much lower Prandtl number of 0.05, and the present use of unstructured meshes does not alters the solutions symmetry.
- similar formation fluid strips to act like a heat insulation material at large ω is documented in [116]. While it is a robust mechanism, in the sense that even a non-fragmented solid cores and Z pipes computed at a slightly smaller thermal weigh end up breaking up, we have found the way the solid layout splits to be very sensitivity to the optimization path. This is evidenced in Fig. 5.6 showing a series of fragmented core designs generated by varying the

initial design under constant thermal weigh. The number of subcores and the subcores arrangements doe vary, but they yield identical cost functions (and thermal cost functions) within 1%, which suggests that fragmented solutions are actually flat minimizers.

- non-physical designs (e.g., broken flow paths, dead ends and total fluid flow blockage, all highly undesirable from manufacturing point of view) have been obtained at much higher values of $\omega > 0.999$, which is when the contribution of the hydraulic cost function becomes negligible. This may have to do with the modeling of the solid material, as a porous media does allow solutions with no fluid connection between the inlet and outlet flows, while the IVM rigorously forces the solid velocity to zero.

Additional testing has been performed in the attempt to clarify the connection between the various branches of solutions (although not the intended scope of this study). The main findings are threefold: first, the straight pipe solution exists up to $\omega \sim 0.7$, after which its centerline shifts increasingly in the upper domain (or lower domain, by vertical reflectional symmetry) and the solution evolves continuously into the bent pipe solution. Second, the solid core solution branches off the straight pipe at about $\omega \sim 0.64$ (this has been estimated using a branch-tracking technique in which the design is initialized with a solid core solution computed at a slightly larger thermal weigh), then evolves continuously into the fragmented core solution. Finally, the connection between the bent and Z pipe solutions remains uncertain: both solutions have been found to coexist over a range of thermal weights from 0.94 to 0.98, where they yield almost identical cost functions. Meanwhile, we could not manage to have a bent pipe continuously turn into a Z, regardless of the value of ω and the number of update steps (up to several ten thousands). This raises the possibility that the Z pipe solution may branch off subcritically from the bent pipe solution, leading to hysteresis (testing this hypothesis is uneasy due to the difficulty of consistently generating Z pipe solutions unless a branch-tracking technique is used, which is why the optimization run documented in Fig. 5.5(b) does not start from the classical design with solid occlusions).

Finally, Fig. 5.8 recasts the obtained results into the Pareto frontier of the multi-objective optimization problem. Interestingly, it turns out that the Pareto-efficient subset consists exclusively of straight, bent and Z pipes (although the fragmented core solutions equally dominate at very high influences of the thermal objective function). Interestingly, the close-to-convex shape of the Pareto front means that a few solutions provide an acceptable trade-off by having both single cost functions close to their single objective optimization. This corresponds here to the bent pipe at ω 0.97 and the Z pipe at $\omega = 0.95$, for which the recoverable thermal power is below its single objective maximum by less than 10% (the dissipated power is 7

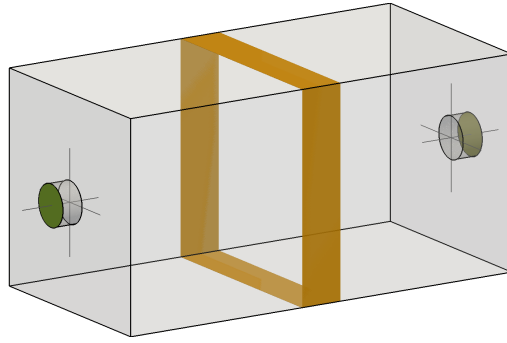


Figure 5.9: Set-up of the three-dimensional single pipe problem with heated walls: one single hot stripe. The orange and light gray shade denote hot isothermal and adiabatic walls, respectively.

times as large as its single objective minimum, which is not small strictly speaking, but very reasonable given that the worst performance is actually by a factor of 100).

5.6.3 Three-dimensional single pipe with heated walls

The second and last family of test cases stands as a three-dimensional counterpart of the two-dimensional conjugate heat transfer problem considered in Sec. 5.6.2. The setting inspired from [13] is depicted in Fig. 5.9, with detailed problem parameters given in Tab. 5.3. The design domain is a cuboid cavity of unit height and aspect ratio 2:1:1, with a single inlet on the left and a single outlet on the right, again lined up in front of each other. A cold fluid is flowing from the inlet, and is heated by the cavity walls, with the difference that only a finite stripe at the middle of the cavity walls is maintained at a constant (hot) temperature, and all remaining walls (cavity and leads) are considered adiabatic. In what follows, the thermal weight is set to $\omega = 0.95$ to add more priority to increase the recoverable thermal power. Note, although the configuration has two reflectional symmetries, we do not reduce the computational cost by modeling only a quarter of the domain together with symmetry boundary conditions, which is feasible [97] but would not allow assessing the method in the context of large scale systems. The entire domain is thus discretized with 5000000 mesh elements, and we let symmetry eventually arise as a result of the optimization process.

The initialization shown in Fig. 5.10 corresponds to a fluid box filled with islands of solid spherical inclusions occupying about 10% of the cavity. The fluid thus fills initially 90% of the cavity, which violates the volume constraint set to 20%. This is because enforcing the proper volume would require using many more smaller inclusions, which in turn would either dramatically increase the surface of the interfaces that needs be captured (and thus the number of mesh elements needed to maintain

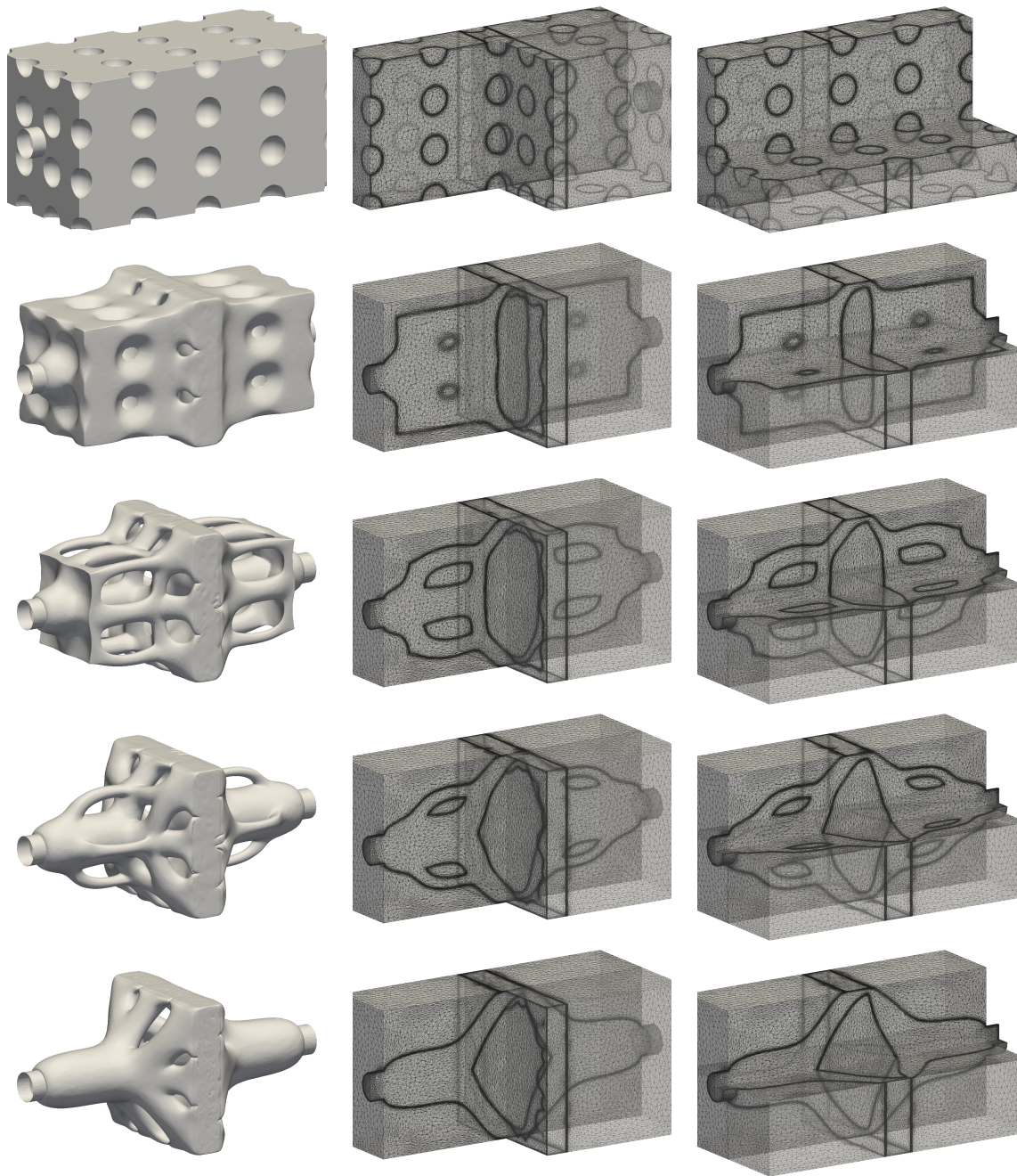


Figure 5.10: Multi-objective optimization of the three-dimensional single pipe device with heated walls (one single hot stripe) presented in Fig. 5.9. The zero iso-value of the level set function and associated anisotropic adapted meshes are sampled over the course of optimization using the parameters given in Tab. 5.3. The associated volume of fluid (from top to below) is as follows: 90%, 42.9%, 20.6%, 20.5% and 20.4%, respectively.

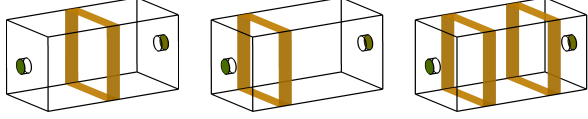
		
$\Omega = [0; 2] \times [0; 1] \times [0; 1]$	>>	>> Design domain
$d = 3$	>>	>> Problem dimensionality
$V_{target} = 0.4$	>>	>> Target volume of fluid
$V_{\varphi,0} = 1.8$	>>	>> Initial volume of fluid
$Re = 12$	>>	>> Reynolds number
$Pr = 83.5$	>>	>> Prandtl number
$k_s/k_f = 10$	>>	>> Thermal conductivity ratio
$T_w = 10$	>>	>> Hot stripe temperature
$\Delta x_h = 0.2$	>>	>> Hot stripe width
$x_{h1} = 1$	0.5	>> Hot stripe 1 center coordinate
-	-	$x_{h2} = 1.5$ Hot stripe 2 center coordinate
$u_i = 1$	>>	>> Inlet centerline velocity
$T_i = 0$	>>	>> Inlet cold temperature
$e = 0.2$	>>	>> Inlet diameter
$l_i = 0.1$	>>	>> Inlet leads length
$\mathbf{x}_i = (-0.1, 0.5, 0.5)$	>>	>> Inlet center coordinates
$u_o = 1$	>>	>> Outlet centerline velocity
$e_o = 0.2$	>>	>> Outlet diameter
$l_o = 0.1$	>>	>> Outlet lead length
$\mathbf{x}_o = (2.1, 0.5, 0.5)$	>>	>> Outlet 1 center coordinates
$N_n = 1000000$	>>	>> Nb. mesh nodes
$N_{el} = 5000000$	>>	>> Nb. mesh elements

Table 5.3: Numerical parameters for the three-dimensional single pipe problem with heated walls.

the numerical accuracy), or risk clogging the fluid path due to insufficient mesh refinement. In all optimization runs documented below, there is thus an initial transient during which the cost function has little physical meaning, as the constraint value is decreased up to the point where it reaches the target within the desired tolerance. Once the constraint is satisfied, the cost function adjusts until a feasible minimum is found. Again, the method is found to handle well the various topological changes occurring over the course of optimization, and all anisotropic adapted meshes exhibit extremely stretched elements regardless of the interface complexity, that allow sharply representing the fluid and solid domains (also, the edges of the hot stripe) and accurately computing the solutions during all stages of opti-

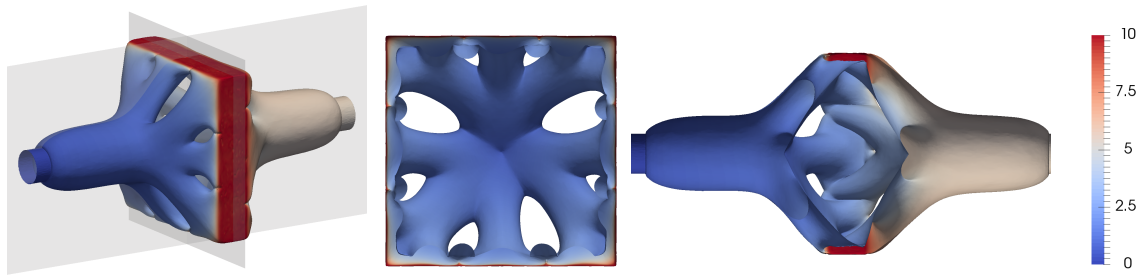


Figure 5.11: Optimal design of the three-dimensional single pipe device with heated walls (one single hot stripe) presented in Fig. 5.9, together with stream-wise and cross-wise cuts at positions shown by the gray planes. The colors hue corresponds to the temperature profile.

mization. In the optimal solution shown in Fig. 5.10, the fluid flows in and out of the cavity through single, straight pipes. This is because the hot stripe is far from the inlet/outlet sections, so there is a good proportion of the cavity where the thermal cost function contributes little to nothing, and the best trade-off is to minimize power dissipation. Similarly to what could be observed in the 2-D test case, a solid core forms in the stripe region, that divides the inlet/outlet pipes into a near-perfect symmetrical network of 8 pipes. The latter force the fluid along the hot walls and eventually merging into a thin, square annulus shaped to the hot stripe to maximize the fluid heat up. As illustrated in Fig. 5.11, the optimal features thin inclusions of fluid attached to the main pipes. This is essentially reminiscent of the two-dimensional fragmentation mechanism observed at such large thermal weigh, where fluid is used to insulate thermically the inner pipes from the cold inlet temperature. The present optimal design is overall close to that documented in [13], but the pipe arrangements differ in the hot region, most likely the authors in the aforementioned reference optimize the thermal recoverable power by imposing an upper bound threshold for the pressure drop (which yields to a different trade-off).

Two other cases have been considered to assess the capability of designing more complex shapes by giving more importance to the thermal cost function. The associated setups depicted in Fig. 5.12 differ by the number and position of hot stripes, namely the first case (case 1) has one stripe shifted upstream against the inlet, and the second one (case 2) has two stripes against the inlet and outlet arranged symmetrically with respect to the middle of the cavity; see Tab. 5.3 for provision of other detailed problem parameters and Figs. 5.13-5.14 for illustration of the corresponding optimization runs using anisotropic adapted meshes. For case 1, the main features of the baseline optimal discussed herein-above carry over, with the difference that the solid core moves upstream to follow in the footsteps of the hot stripe, hence the inlet lead immediately splits into a similar network of 8 pipes. For case 2, the presence of two separated hot spots yields a different optimal, with the 8 pipes reconfiguring

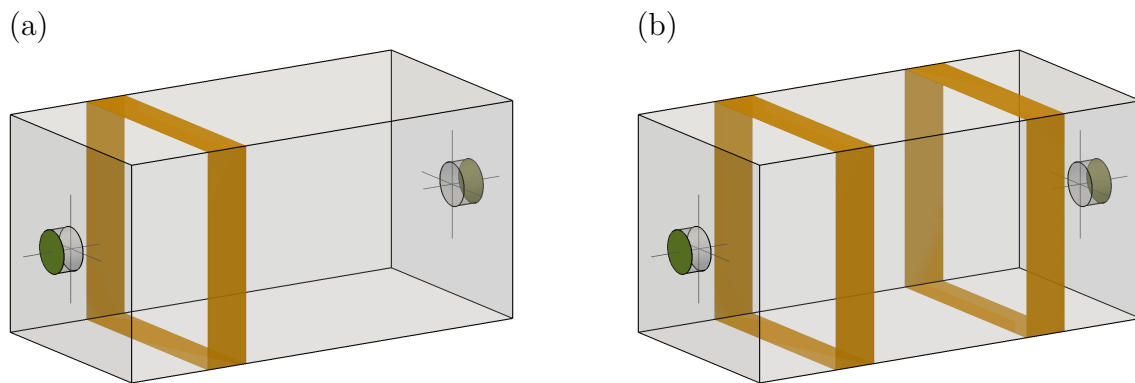


Figure 5.12: Set-up of the three-dimensional single pipe problem with heated walls: one single upstream hot stripe vs. two hot stripes. The orange and light gray shade denote hot isothermal and adiabatic walls, respectively.

into 4 wider pipes to transport fluid the shortest way downstream and avoid the cost of bending. These pipes then widen to form four quasi triangular prisms shaped to the downstream stripe (to maximize the fluid heat up) before merging to connect to the outlet. In both cases, the optimal designs shown in Fig. 5.15 exhibit the same thin inclusions of fluid attached to the main pipes to benefit from the insulating low-conductivity of the fluid.

5.7 Résumé du chapitre en français

Ce chapitre a abordé l'optimisation de la topologie des systèmes de transfert de chaleur conjugué. Les équations de Navier-Stokes incompressibles ont été couplées à l'équation stationnaire d'énergie en convection-diffusion. Les modifications des équations d'état ont entraîné des mises à jour dans le système adjoint, où à la fois une équation de chaleur et un terme source pour les équations de Navier-Stokes sont apparus du côté adjoint. Le couplage numérique et les formulations variationnelles à grande échelle ont été détaillés pour les équations nouvellement ajoutées. L'optimisation multi-objective a été introduite, et l'équilibre entre la réduction de la perte de charge et l'amélioration du transfert de chaleur a été largement discuté. Le problème du tuyau chauffé en 2D et 3D a également été largement étudié.

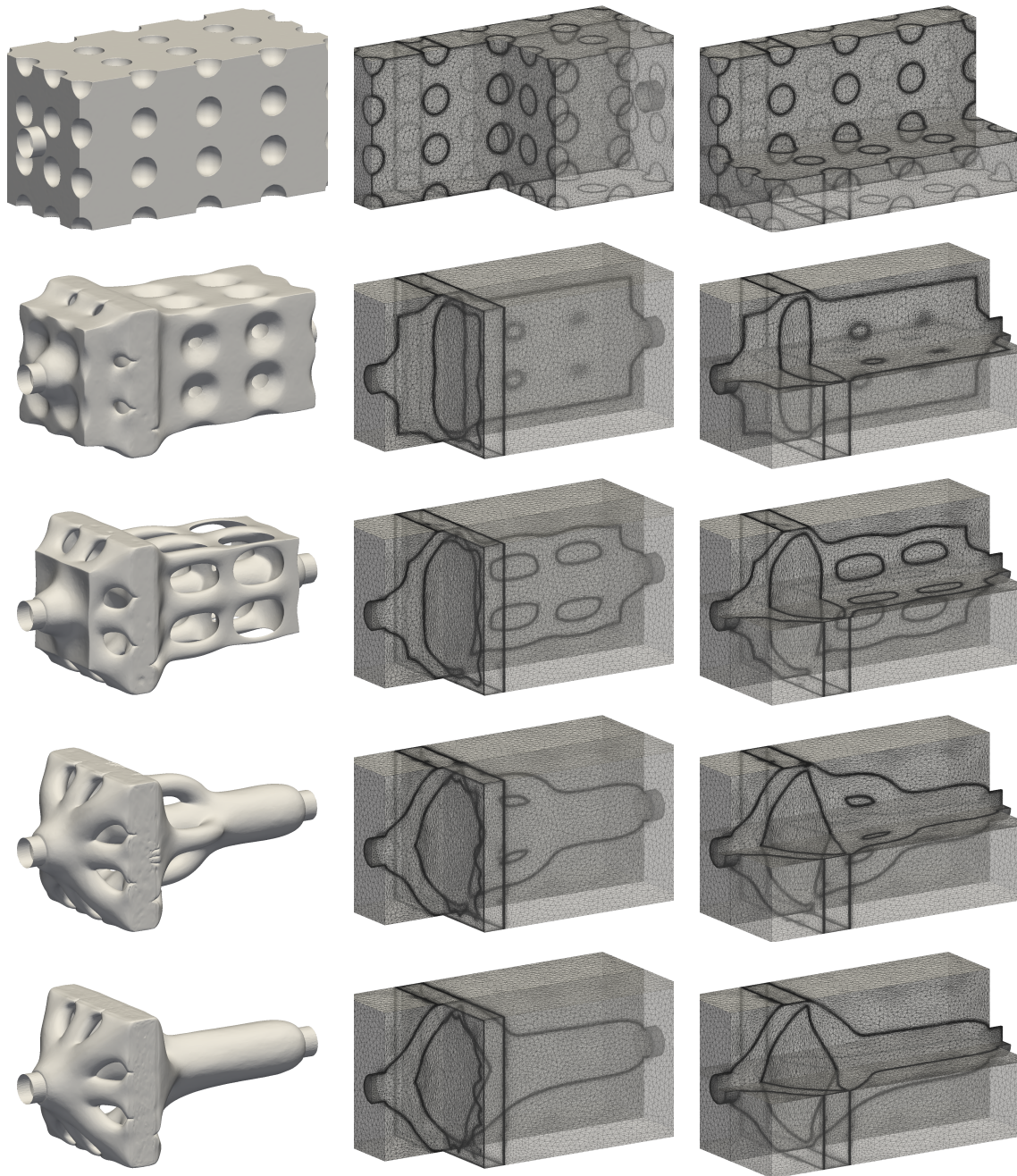


Figure 5.13: Multi-objective optimization of the three-dimensional single pipe device with heated walls (one single upstream hot stripe) presented in Fig. 5.12(a). The zero iso-value of the level set function and associated anisotropic adapted meshes are sampled over the course of optimization using the parameters given in Tab. 5.3. The associated volume of fluid (from top to below) is as follows: 90%, 43.0%, 20.4%, 20.5% and 20.4%, respectively.

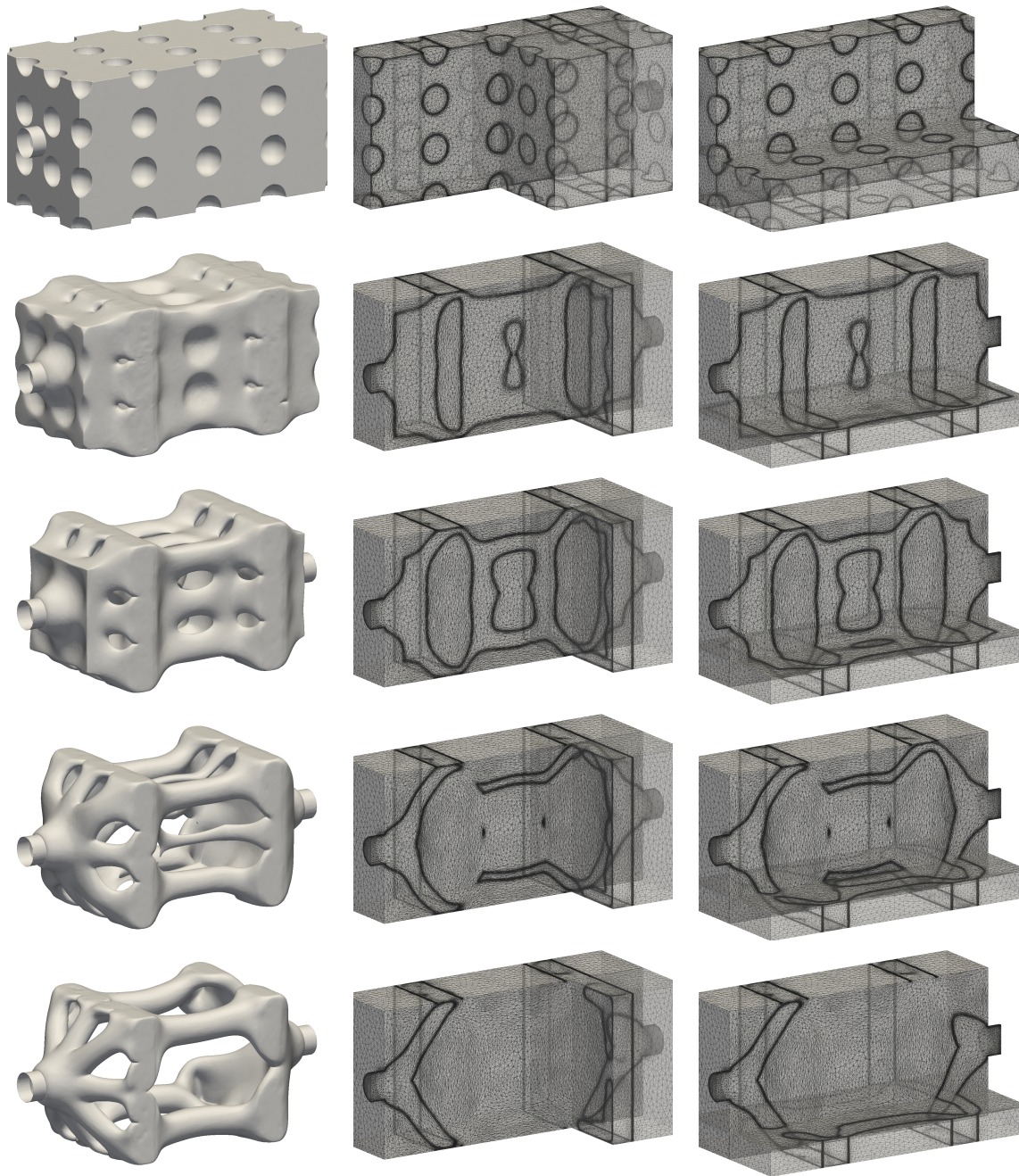


Figure 5.14: Multi-objective optimization of the three-dimensional single pipe device with heated walls (two hot stripes) presented in Fig. 5.12(b). The zero iso-value of the level set function and associated anisotropic adapted meshes are sampled over the course of optimization using the parameters given in Tab. 5.3. The associated volume of fluid (from top to below) is as follows: 90%, 54.4%, 31.9%, 20.6% and 20.3%, respectively.

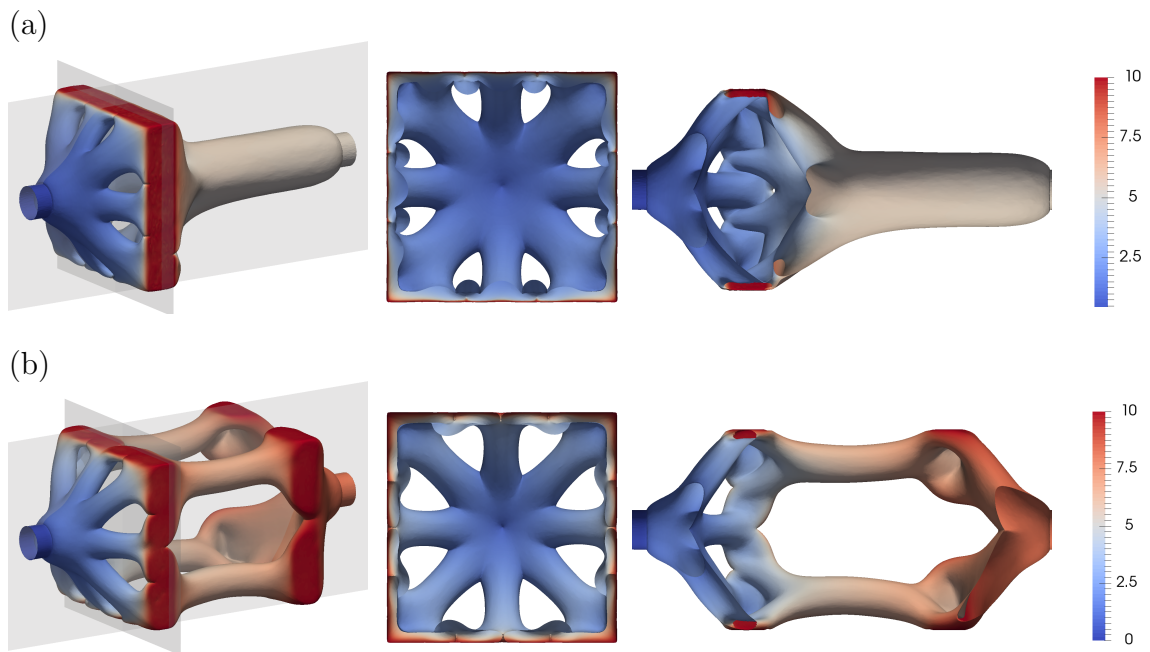


Figure 5.15: (a) Optimal design of the three-dimensional single pipe device with heated walls (one single upstream hot stripe) presented in Fig. 5.12(a), together with stream-wise and cross-wise cuts at positions shown by the gray planes. (b) Same as (a) for the device with heated walls (two hot stripes) presented in Fig. 5.12(b). The colors hue corresponds to the temperature profile.

Chapter 6

Industrial Application

Contents

6.1	Introduction	113
6.2	PFHE Simplified Header	114
6.3	PFHE Modified geometry	114
6.4	Collector Optimization	121
6.5	Résumé du chapitre en français	124

6.1 Introduction

In the preceding chapters, all the numerical applications were derived from academic benchmarks commonly addressed in the topology optimization community. The primary aim was to establish the reliability of our framework and demonstrate how anisotropic mesh adaptation allows improving the numerical representation of the various shapes. Having successfully showcased the capabilities of the method, especially in handling large-scale problems, we are now ready to address the industrial application that served as the principal motivation behind these advancements.

In summary, the main objective of the industrial application is to optimize the upstream and downstream parts of a Plate and Fins Heat Exchanger (PFHE) using topology optimization. The first major goal is to reduce the operational cost of the exchanger by minimizing pressure drop in regions that have minimal impact on the overall thermal performance of the system. For readers interested in further details, Appendix B provides a comprehensive description of the PFHE in question, elucidating the technical aspects of the exchangers that guided our decision in modeling the exchanger.

The PFHE actually in service is shown in Figs. 6.1. The modeling of a distributor



Figure 6.1: PFHE actually in service shown from different perspectives.

(whether for experiments or numeric computation), presents restrictive complexity. To streamline the optimization process, two simplifications will be made:

- A single-phase fluid (the liquid phase) will be considered.
- The gravity will be neglected.

By implementing these simplifications, the optimization process can be more efficiently conducted while still capturing essential aspects of the distributor's behavior.

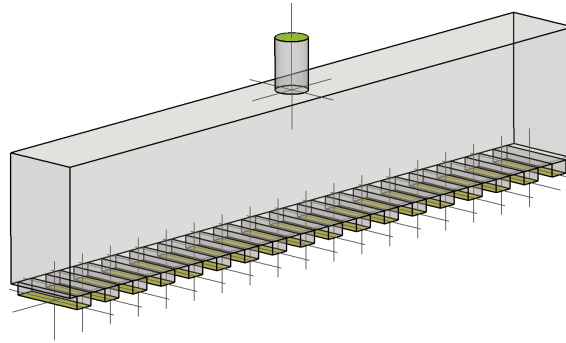


Figure 6.2: Problem set-up for the simplified PFHE distributor.

6.2 PFHE Simplified Header

First, a simplified case was considered, where the focus is on the distributor over plate-shaped outlets. We leave aside here the question of flow distribution and heat transfer, and assess the ability of our numerical framework to minimize the total pressure drop in a design domain comprising a large number of outlet orifices. The design domain is a cuboid of height 0.5 and aspect ratio $2.7 : 0.5 : 0.3$ shown in Fig. 6.2, that has one cylindrical inlet at the top, and 18 rectangular outlets at the bottom, each of which is the entry section into one of the 18 plates and has $1/18$ of the fluid flow entering through the inlet. In return, there is no need to model either the fins or the hot fluid, since the latter flows orthogonally between the plates. Parabolic velocity profiles are prescribed at the inlets and the outlets, with the outflow distribution in each outlet section defined as the Cartesian product of parabolic variations along the two lines of symmetry, which stands as a first approximation of the series-based, theoretical velocity profile of flow through a channel of rectangular cross-section [120]. The entire domain is meshed with 5M elements, with the remaining parameters given in Tab. 6.1. Due to the cavity low aspect ratio in the third dimension, the initial design is initialized with cylindrical solid occlusions occupying about 65% of the cavity, and the volume of fluid is progressively decreased until it reaches the target within the desired tolerance. This yields the optimal duct shown in Fig. 6.3, that delivers most of the fluid in the center area of the cavity before distributing it to the plates via the comb-like structure at the bottom.

6.3 PFHE Modified geometry

In this section, we consider another design in which the plates are replaced by a series of eight consecutive T-junctions, which is more representative of the distributor geometries indeed tackled by the industrial partner. The base geometry for

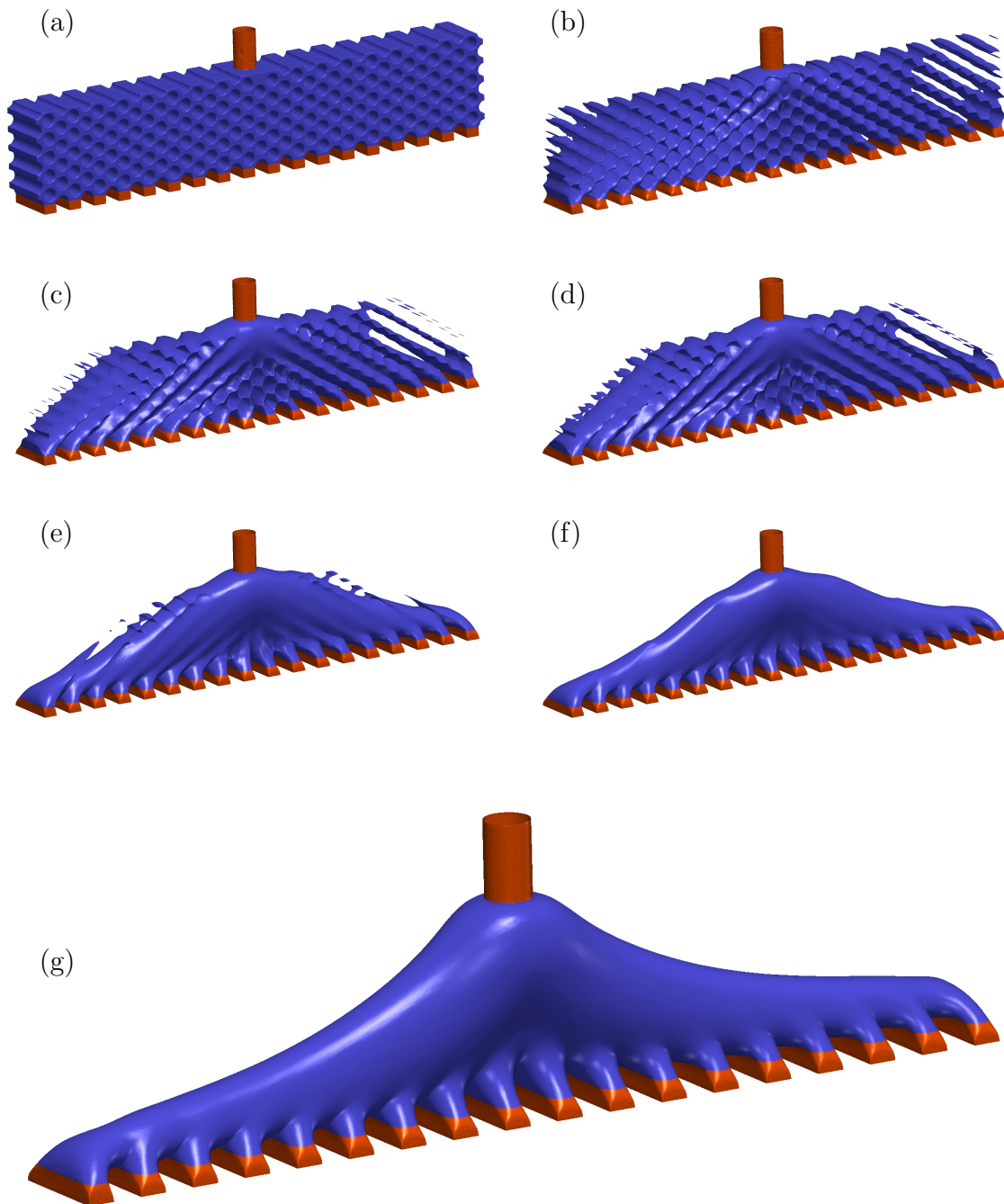
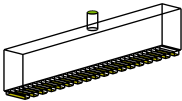


Figure 6.3: Optimization of the plate fin heat exchanger distributor presented in Fig. 6.2. The zero iso-value of the level set function is sampled at intermediate iterations 1, 70, 100, 110, 140, 160 and 400 (from top to bottom, left to right) using the parameters given in Tab. 6.1. The associated volumes of fluid are 50%, 28.8%, 26.3%, 25.5%, 23.1%, 21.4% and 17.6%, respectively. The red color highlights the leads, here representing the inlets and outlets of the system.



$\Omega = [0; 2.7] \times [0; 0.7] \times [0; 0.3]$	Design domain
$d = 3$	Problem dimensionality
$V_{target} = 0.10$	Target volume of fluid
$V_{\varphi,0} = 0.20$	Initial volume of fluid
$Re = 4$	Reynolds number
$u_{i1} = 0.4$	Inlet centerline velocity
$e_i = 0.12$	Inlet diameter
$l_i = 0.2$	Inlet leads length
$\mathbf{x}_{i1} = (1.35, 0.7, 0.15)$	Inlet center coordinates
$u_{ok} = 0.00591$	Outlet k centerline velocity
$e_o = (0.075; 0.3)$	Outlet width
$l_o = 0.05$	Outlet leads length
$\mathbf{x}_{ok} = (0.075 + 0.15k, 0.35, 0.15)$	Outlet k center coordinates
$N_n = 1M$	Nb. mesh nodes
$N_{el} = 5M$	Nb. mesh elements

Table 6.1: Numerical parameters for the plate fin heat exchanger distributor problem.

distributor design improvement is represented in Fig. 6.4. The design domain is a cuboid with height 0.89 and aspect ratio 2.8 : 0.89 : 0.65. The feeding tube takes charge of conducting the fluid until it reaches the header and thus could be regarded as an inlet. It is long enough to allow the incoming fluid to fully develop into a Poiseuille flow, which justifies prescribing a parabolic velocity profile at the numerical inlet. The eight channels represent the exchanger core. They are responsible for redirecting the fluid out of the header, and are therefore considered as the numerical outlets. Each outlet has a circular cross-section of diameter 0.05, which yields an aspect ratio of 1:6 with the inlet, or 1 : 18 with the domain depth. Two different inlet positions are considered in the following, either on the left or the top sides to assess the effect on the efficiency of the pressure drop reduction; see the corresponding sketches in Fig. 6.5. In both cases the main characteristics of the header remain unchanged, including the header dimensions and inlet flow rate, see Tab. 6.2 for exhaustive provision of the case parameters.

The target volume of fluid for this case is set to 0.13 (8%). Since the inlet and outlets are set to be in the same plane, we choose initial designs made up of cylindrical solid occlusions, as it has been shown in Sec. 4.3 that this can significantly increase the convergence rate with little impact on the global optimum. The oc-

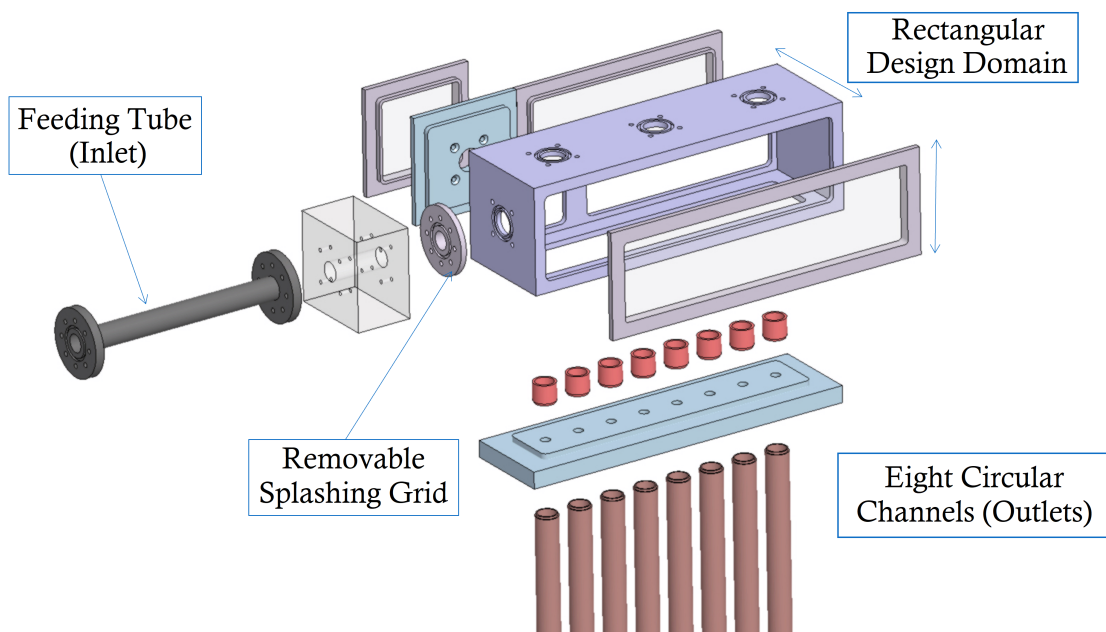


Figure 6.4: Base Geometry for Topology Optimization [121]

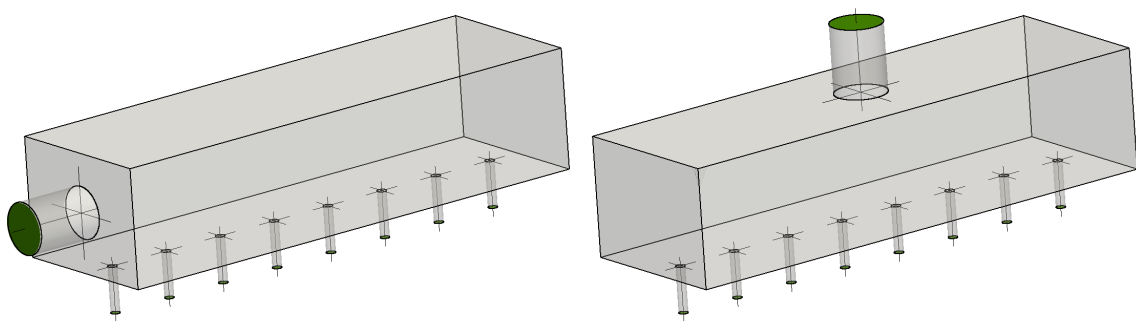


Figure 6.5: Problem setup for the manifold with (a) inlet to the left and (b) inlet at the top center of the manifold


		
$\Omega = [0; 2.8] \times [0; 0.89] \times [0; 0.65]$		» Design domain
$d = 3$		» Problem dimensionality
$V_{target} = 0.13$		» Target volume of fluid
$V_{\varphi,0} = 0.92$		» Initial volume of fluid
$Re = 4$		» Reynolds number
$u_i = 1$		» Inlet centerline velocity
$e_i = 0.283$		» Inlet diameter
$l_i = 0.375$		» Inlet leads length
$\mathbf{x}_i = (0, 0.445, 0.325)$	$\mathbf{x}_i = (1.4, 0.445, 0.65)$	Inlet center coordinates
$u_o = 4.00445$		» Outlet centerline velocity
$e_o = 0.05$		» Outlet diameter
$l_o = 0.25$		» Outlet leads length
$\mathbf{x}_{ok} = (0.275 + 0.55k, 0.35, 0)$		» Outlet k center coordinates
$N_n = 1M$		» Nb. mesh nodes
$N_{el} = 5M$		» Nb. mesh elements

Table 6.2: Numerical parameters for the two possible configurations of the distributor of the heat exchanger.

clusions initially represent about 57% of the design domain for both configurations. Only minor modifications are made to adapt the different inlet positions, which results in slightly different positions of the occlusions to avoid clogging the fluid path, but the number of occlusions and their size remains the same.

The design evolution over the course of optimization is shown in Figs. 6.6 and 6.7. For both cases, the target volume is reached after 500 iterations, and convergence is achieved after another 200 iterations. For the first case with the left-sided inlet, it can be seen in the bottom picture of Fig. 6.6, the optimal shape forms at first a large and straight duct emerging from the inlet, which is consistent with the trends observed in the previous chapters. For the second case with the top-sided inlet, the flow coming from the feeder splits into the eight channels while forming a comb-like structure similar to that observed on the PFHE with plates. Quantitatively, the optimal cost functions (using the inlet diameter and maximum inlet velocity as reference scales) are 1.16 for the left-sided inlet, and 2.41 for the top-sided inlet, which selects the first configuration as the optimal one to reduce the total pressure drop.

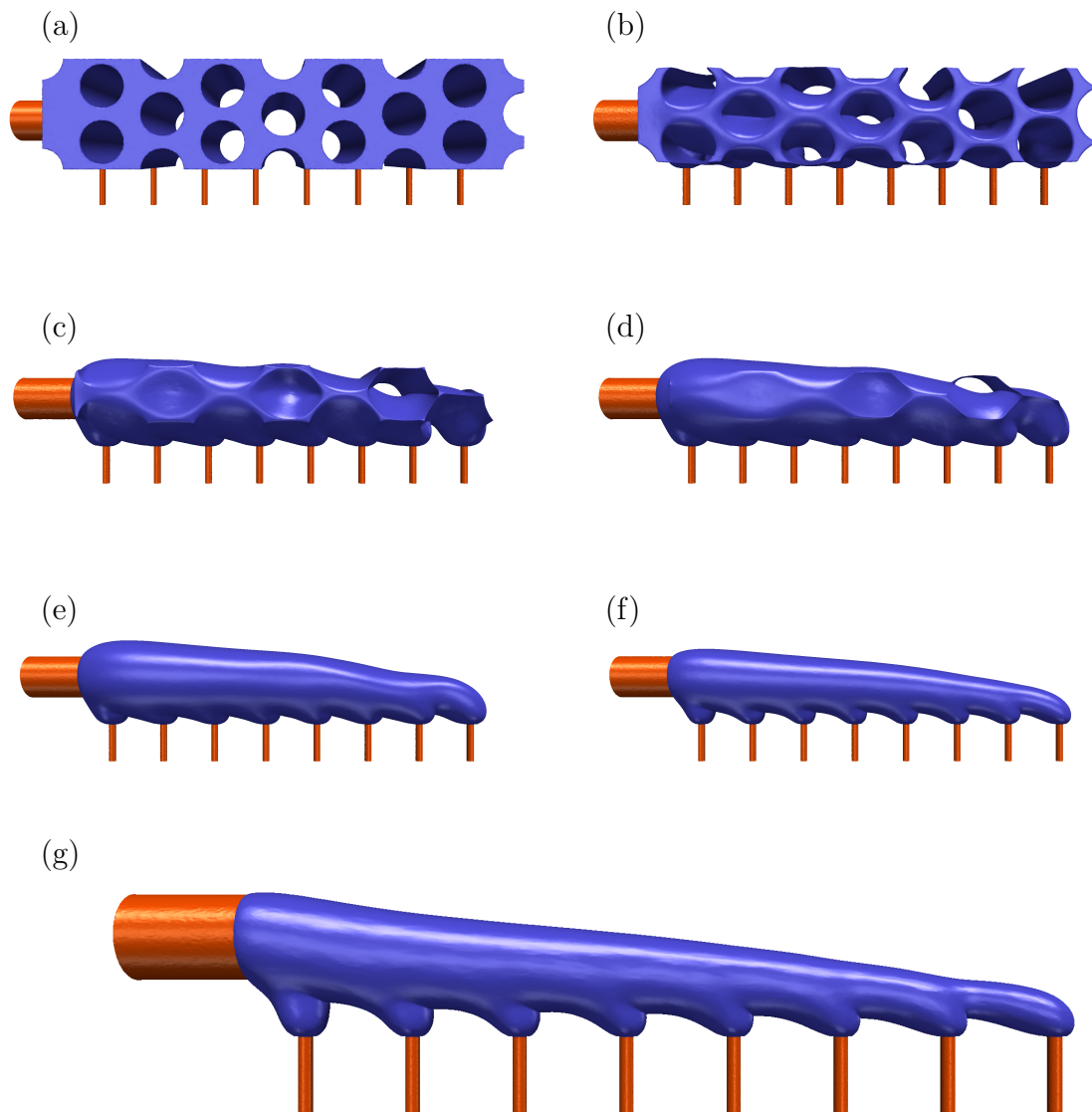


Figure 6.6: Optimization of the first configuration of the exchanger's manifold (with the inlet positioned on the center left of the box) presented in Fig 6.4(a). The zero iso-value of the level set function is sampled at intermediate iterations 1, 70, 180, 230, 320, 440 and 700 (from top to bottom, and from left to right) using the parameters given in Tab 6.2. The associated volumes of fluid are 57.0%, 49.0%, 23.5% and 8%, respectively. The red color highlights the leads, here representing the inlets and outlets of the system.

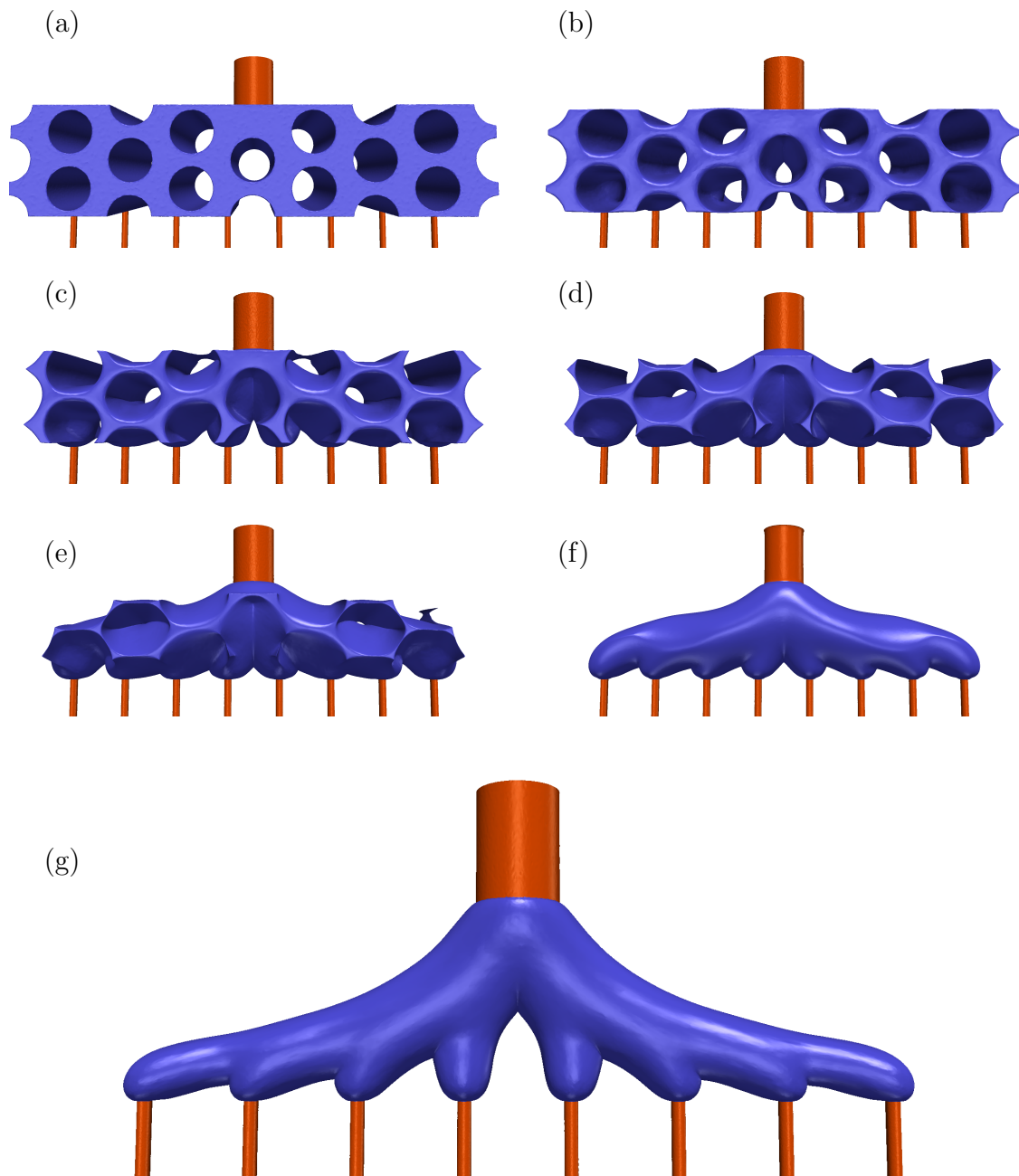


Figure 6.7: Optimization of the first configuration of the exchanger's manifold (with the inlet positioned on the top center of the box) presented in Fig 6.4(b). The zero iso-value of the level set function is sampled at intermediate iterations 1, 50, 120, 180, 230, 380 and 700 (from top to bottom, and from left to right) using the parameters given in Tab 6.2. The associated volumes of fluid are 56.8%, 53.8%, 47.0%, 40.8%, 35.0%, 20.5% and 8%, respectively. The red color highlights the leads, here representing the inlets and outlets of the system.

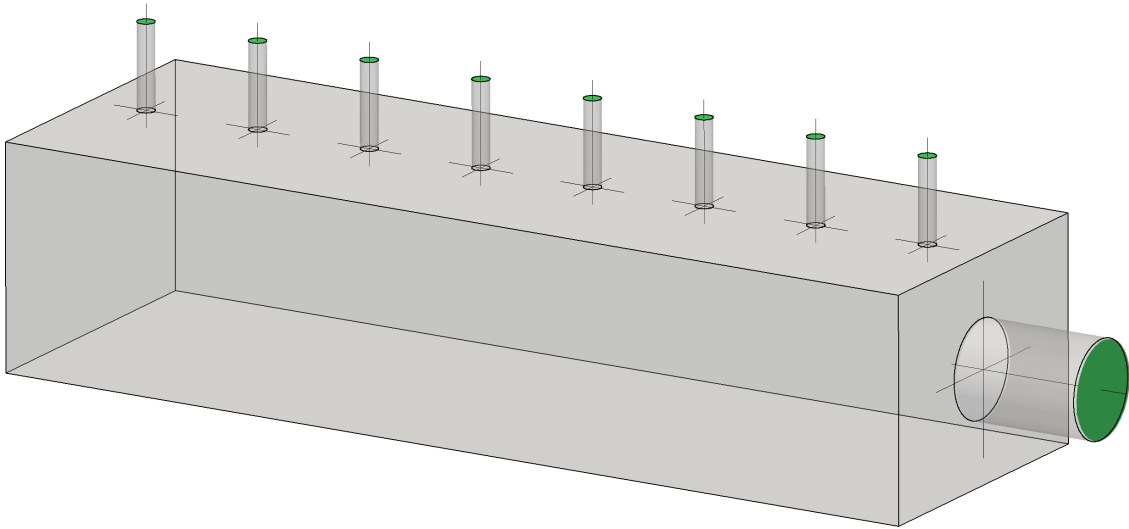
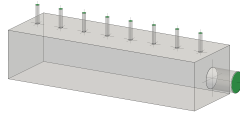


Figure 6.8: Problem setup for the collector.

6.4 Collector Optimization

The same approach has been used to optimize the collector, i.e., the downstream part of the exchanger, for which the corresponding domain is exactly identical to that of the distributor, except that the role of the inlet and outlets are reversed, hence 8 inlets and 1 outlet. However, the outlet is fixed to the right side to accommodate industrial design constraints. The same target volume of fluid is used (0.13, equivalently 8% of the design domain). Perfect distribution in the header is assumed, hence the flow is modeled to enter the collector through eight identical paraboloids, with the total flow imposed also as a paraboloid profile on the cylindrical outlet position of the right side of the collector. All other problem parameters are given in Tab. 6.3.

The design evolution over the course of optimization is shown in Figs. 6.9. The flow from each inlet channel merges in a large, horizontal duct conveying the fluid straight towards the outlet. We can notice that the optimized shape of the collector in Fig. 6.9(g) closely resembles Fig. 6.6(g) where the inlet of the distributor mirrors the outlet of the collector, the design domains being exactly identical. This similarity can be attributed to the low Reynolds Number prevailing in both applications, which drives the problem toward a Stokes flow regime. Notably, the Stokes equations, characterized by their diffusive nature, are reversible equations, in contrast to the irreversible nature of the Navier–Stokes equations, mainly due to their advection term. This phenomenon tends to diminish gradually as the Reynolds Number increases, taking the modelization a step further towards the PFHE opti-



$\Omega = [0; 2.8] \times [0; 0.89] \times [0; 0.65]$	Design domain
$d = 3$	Problem dimensionality
$V_{target} = 0.13$	Target volume of fluid
$V_{\varphi,0} = 0.92$	Initial volume of fluid
$Re = 4$	Reynolds number
$u_i = 4.00445$	Inlet centerline velocity
$e_i = 0.05$	Inlet diameter
$l_i = 0.25$	Inlet leads length
$\mathbf{x}_{ik} = (0.275 + 0.55k, 0.35, 0)$	Inlet center coordinates
$u_o = 1$	Outlet centerline velocity
$e_o = 0.283$	Outlet diameter
$l_o = 0.375$	Outlet leads length
$\mathbf{x}_o = (2.8, 0.445, 0.325)$	Outlet k center coordinates
$N_n = 1M$	Nb. mesh nodes
$N_{el} = 5M$	Nb. mesh elements

Table 6.3: Numerical parameters for the collector of the heat exchanger.

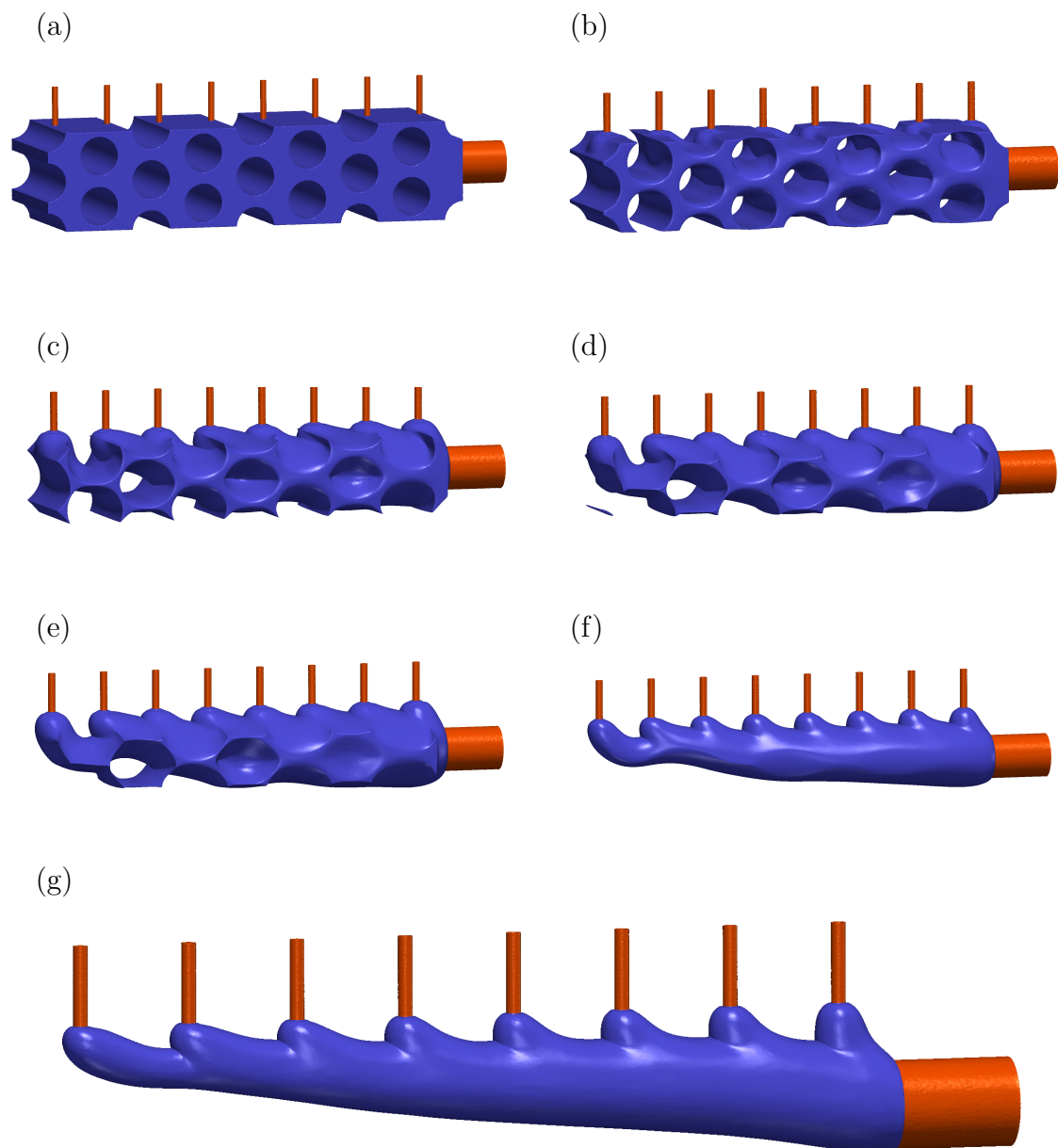


Figure 6.9: Optimization of the exchanger's collector presented in Fig 6.4(a). The zero iso-value of the level set function is sampled at intermediate iterations 1, 80, 250 and 700 (from top to bottom, and from left to right) using the parameters given in Tab 6.3. The associated volumes of fluid are 57.0%, 49.2%, 32.5% and 8%, respectively. The red color highlights the leads, here representing the inlets and outlets of the system.

mization.

6.5 Résumé du chapitre en français

Ce chapitre a rassemblé les outils développés et a suivi la méthodologie prescrite pour concevoir les parties amont et aval d'un échangeur de chaleur à plaques ailettes. Il a d'abord fourni un aperçu général sur le projet et ses exigences avant de présenter une série de conceptions optimales possibles pour les distributeurs et les collecteurs, allant de formulations simples du problèmes à des formulations de plus en plus complexes.

Chapter 7

Conclusions and Perspectives

Contents

7.1 Conclusion	126
7.2 Perspectives	128

7.1 Conclusion

This thesis was devoted to the development of a topology optimization framework for thermofluidic systems governed by the incompressible Navier-Stokes and Heat equations. The framework used the Level-Set method for interface capture and an anisotropic mesh adaptation technique to maximize the precision while maintaining an affordable computational cost. Sensitivity analysis was carried out using the continuous adjoint method, while the advected level-set approach was employed for interface update. Throughout the applied chapters, several numerical benchmarks were conducted to validate the robustness and reliability of the proposed methodology. These benchmarks served as building blocks before addressing the main industrial application that was the primary motivation for this research study. To provide a concise summary of the manuscript, let us now recapitulate the different topics covered in each of the seven chapters.

We started in Chapter 2 by giving a detailed description of the numerical models employed in the general optimization algorithm of flows governed by the incompressible Navier–Stokes equations and driven by Objective Functions formulated on the design domain’s boundaries. The State Equations were introduced, and the derivation of the adjoint system for sensitivity analysis through the Lagrangian approach was detailed. The Level-Set method for interface capture was utilized, and its position was updated by the advected level method that was selected for its particularities of built-in reinitialization and domain filtering, reducing significantly the computational cost. The IVM was then introduced to penalize the solid regions while solving the governing equations in the computational domain as a whole. In the course of computational methods, the VMS method was selected to prevent numerical instabilities, and the coarse-scale variational formulation was derived for the primal and adjoint equations, as it was for the Interface Update Scheme. Finally, some numerical considerations were detailed for practical reasons linked to topology optimization. These include geometrical constraints (to avoid the two extreme cases of the solid domain clogging the entire design domain or disappearing altogether) and sensibility filtering and normalization (to ensure maximal displacement per iteration of the interface). Anisotropic mesh adaptation was the main novelty of this study, since it had never been implemented before in the context of topology implementation. The main idea was to generate a uniform mesh in a prescribed Riemannian metric space, but anisotropic and well adapted in the Euclidean space. We thus compute, for each node, the corresponding Metric based on an a posteriori error estimation and a stretching factor. We finally generate the new mesh and interpolate linearly the computed fields on the newly generated mesh. The chapter was concluded with a practical example of mesh adaptation over a filtered level-set, since it was the adaptation criterion of the current study.

Chapter 3 was the core of this thesis, where the previously described numerical

methods were combined into a well-structured algorithm for topology optimization of incompressible laminar flows. Several optimization problems were addressed: the design of a pipe bend, a four terminal device, and a double pipe. The presented results showcased the superiority of the method when compared to its precedents by eliminating staircase effects and gray-scale regions while maintaining a relatively low computational cost. A discussion covering computational efficiency and mesh dependency was also elaborated.

The motivation for large-scale optimization laid in the need to address geometrically complex and three-dimensional problems, namely for industrial applications. The parallelization of the framework was described in Chapter 4, underlying the originality of the parallel remeshing solver. Even though the benchmarked cases presented some symmetries in their initial setup, this symmetry was not taken into consideration, first to increase the complexity of the problem and second because our experience showed that symmetrical problem formulation may lead to unsymmetrical results, as was shown in the last tackled problem. A discussion at the end was dedicated to mesh partitioning and numerical cost.

Chapter 5 tackled the topology optimization of conjugate heat transfer systems. The incompressible Navier–Stokes equations were coupled to the steady-state convection-diffusion energy equation. The modifications of the state equations led to updates in the adjoint system, where both a heat equation and a source term for the Navier–Stokes equations appeared on the adjoint side. Numerical coupling and coarse scale variational formulations were detailed for the newly added equations. Multi-objective optimization was introduced, and the balance between pressure drop reduction and heat transfer enhancement was extensively discussed. The heated pipe problem in 2d and 3d was also largely investigated.

Finally, Chapter 6 gathered the developed tools and followed the prescribed methodology to design the upstream and downstream parts of a PFHE. It first provided a general overview of the general project and its requirements. It then showed a series of possible optimized designs for distributors and collectors, ranging from simpler to more complex problem formulations.

In conclusion, by developing a topology optimization framework for heat exchangers in aircraft cabin cooling systems, this research aimed to contribute to reducing the environmental impact of the heat exchanger while improving thermal performance. The proposed methodology holds the potential to provide valuable insights and guidelines for future design processes, leading to more efficient and reliable heat exchanger configurations in the pursuit of a sustainable aviation industry.

7.2 Perspectives

This thesis provided a significant tool for topology optimization, pushing the boundaries in terms of precision and affordability. However it also highlighted many challenges, and raised important questions that are worth the investigation in the future. Some of these potential areas of future research will be discussed in the following.

Numerical Cost

An interesting extension to our research would be to analyze the time added by mesh adaptation versus the time deducted by reducing the number of elements. It is also worth it to explore the position of the interface after it is updated and just before applying the adaptation. The idea behind it would be to find a compromise between good accuracy and affordable computational cost. This might allow us to avoid systematic mesh adaptation after every interface update (whether by advection or by simple offset). Mesh adaptation would be then applied at specified checkpoints whose position would depend on several factors (i.e., maximum number of iterations between two mesh adaptations, maximum real displacement measured after updating the interface position, the stage of the optimization algorithm, ...).

Flow Regimes

To extend our field of study, we can also upgrade the available framework to deal with unsteady flows. Ideally, this done by averaging the quantities of interest over time. The sensitivity would then be computed integrating backwards in time an unsteady adjoint problem from knowledge of the entire history of the state solution [122]. Although numerically accurate, this necessitates an massive computational cost. A pragmatic approach to improve feasibility would then be to average the state velocity over time. Subsequently, this temporally-averaged velocity is introduced into the steady-state adjoint system as a mean state velocity. This will yields an adjoint mean velocity that can be used to compute a physically relevant approximation of the sensitivity, as discussed for instance in [122, 123]. This approach offers a twofold advantage: it significantly reduces computational expenses and facilitates the handling of unsteady problems without substantial modifications to the actual framework. This would pave the path for a systematic increment in the Reynolds number: first within the laminar regime, then subsequently advancing into turbulent regimes using frozen viscosity techniques [124] in the frame of Reynolds-Averaged Navier–Stokes (RANS) modeling.

Multiphase Flow Optimization

It would also be interesting to upgrade the optimization algorithm, in order to tackle real bi-fluidic applications. The optimization procedure heavily relies on how we model the physical problem in a multi-phase context. Models that numerically represent the interface separating the two fluids can be very critical on the adjoint side. Indeed, in addition to the adjoint formulation related to the interface transport equation, these problems often lead to unsteady state solutions, adding complexity and making it nearly impossible to compute the sensitivity using the adjoint method. Therefore, opting for a less intricate model, especially in cases where homogeneous fluids are considered, can offer significant advantages when working with the adjoint method. This could be done by introducing a volume fraction α representative of the mixture of the homogeneous fluids. A scalar transport equation (similar to the energy equation) can then be introduced to update the flow mixture:

$$\rho \mathbf{u} \cdot \nabla \mathbf{u} = -\nabla p + \nabla \cdot (2\mu \boldsymbol{\varepsilon}(\mathbf{u})) \quad \text{in } \Omega \quad (7.1)$$

$$\nabla \cdot (\rho \mathbf{u}) = 0 \quad \text{in } \Omega \quad (7.2)$$

$$\rho \mathbf{u} \cdot \nabla \alpha = \nabla \cdot (\rho D \nabla \alpha) \quad \text{in } \Omega \quad (7.3)$$

where D is the mass diffusivity. Ultimately, a subsequent adjoint can be derived, noting that the resulting system closely resembles the primal system discussed in Chap. 5. The primary distinction lies in that the fluid properties vary spatially within the fluid region. A cost function suitable for this kind of applications could be:

$$J_{bi-fluidic} = \int_{\Gamma_o} \frac{1}{2} (\alpha_d - \alpha)^2 (\mathbf{u} \cdot \mathbf{n}) d\Gamma_o \quad (7.4)$$

where α_d is a user-specified desired volume fraction. This objective function is computed on the outlets of the system and is representative of the fluids' distribution. A possibility of combining it with pressure drop minimization can also be considered.

Applications

A last suggestion would be to deal with less complex but more encountered case studies that are heat sink devices. The objective then would be directed towards the optimization of spatial distribution of temperatures within the solid regions of the system. To address this objective, a variety of cost functions can be employed, such as in [125] or [126]:

$$J_{\theta 1} = \int_{\Omega} \gamma (T_{ref} - T) d\Omega \quad (7.5)$$

where γ serves as a binary indicator for the presence of solid material, and T_{ref} is a reference temperature. As observed, Eq. (7.5) is a volumetric cost function. Thus,

they induce some modifications to the volumetric adjoint equations. To simplify the approach, and make it more convenient with the proposed methodology, an alternative is proposed: minimizing the thermal resistance of the system. This scalar quantity is specifically evaluated on the heated surfaces, giving rise to the subsequent surface integral as in [127]:

$$J_{\theta 2} = \int_{\Gamma_{heated}} \frac{T - T_{in}}{Q} d\Gamma_{heated} \quad (7.6)$$

where Q is the heat flux applied on the heated surfaces. This optimization criterion could also be combined with pressure drop minimization to find a compromise between the operational cost of a system and its thermal performance.

Appendix A

Brief Overview of Temisth

The company TEMISTh, who funded this PhD, was established in 2012 by five researchers from the IUSTI laboratory (CNRS UMR 7343), with the aim of transferring academic knowledge and expertise to the industry. It then positioned itself as a design and engineering firm dedicated to industrial thermal systems.

Today, TEMISTh's comprehensive offering of customized design and component modification enables the acceleration of innovative energy system development phases. The company's technical skills and expertise are based on three main themes:

- Sizing and optimization of compact heat exchangers
- CFD analysis of fluid flows and heat transfers
- CAD design for additive manufacturing

With this foundation of expertise and its technical resources, the company reduces the duration of thermal, fluidic, and mechanical sizing, as well as costs and prototyping time. The expertise of experts and the numerical/experimental resources provided by research centers from all over Europe, complement these optimization cycles. As a player in the development of thermal systems, TEMISTh relies on the maturity of new techniques such as additive manufacturing (high-precision 3D printing) and direct industrialization to create unique components that meet increasingly important energy efficiency constraints, including thermo-fluidic performance, compactness, weight, ease of installation, and price. On the short term, the company has ambitions for applications such as:

- Design and Manufacturing of compact heat exchangers for eco-friendly applications : Brayton cycle power plant operating with supercritical CO₂, thermal management for hydrogen refueling stations.

- Design of heat sinks and cold plates for power electronics and electric equipment.
- Characterization of regenerative circuits involving boiling fluids.

In the medium term, the company aims to establish itself in application areas such as concentrated solar power and thermosiphon loops. The targeted markets are therefore in the energy sector, including transportation, aerospace, electronics, solar, etc. To achieve this program, TEMISTh aims to develop a multi-scale optimization methodology for heat exchange structures. The development of a precise and innovative sizing tool for thermal components integrated into a global energy system is at the heart of the company's program. The development of the Topology Optimization Framework gave TEMISTh a distinct advantage in the sizing of new prototypes essential to the development of its activities.

Appendix B

Generalities about Heat Exchangers

B.1 Definition

A heat exchanger is a component of a system that allows for thermal transfer between two fluids (bi-fluid exchanger) at different temperatures and typically separated by a solid, rigid, and highly conductive material wall [128]. There are also direct contact exchangers (mono-fluid), where the exchange surface is eliminated [129], which are reserved for specific applications such as cooling towers, solid-gas recuperative exchangers, gas-liquid contactors for heating water from gas effluents, air humidifiers, etc. These components are found in numerous industrial sectors and processes, including several industry sectors (chemical, petrochemical, steel making, food processing, energy production, etc.), transportation (automotive, rail, aerospace, marine), as well as in the residential and commercial sectors (heating, air conditioning, air treatment, etc.). For example, in a common car, there can be between 5 and 6 different heat exchangers [130].

Due to their widespread presence, the functionalities of heat exchangers are extremely diverse. Moreover, a single heat exchanger can perform multiple functions within a system. This is the case, for example, of reactor-exchangers, where plates through which the reactive fluid flows are alternated with cooling or heating plates [131].

B.2 Classification of Heat Exchangers

Given the wide range of applications, it can be challenging to make effective decisions when designing heat exchangers for specific problems. However, several criteria can guide the selection process and narrow down the choice of suitable technological solutions.

The selection of a heat exchanger for a particular application relies on various parameters, such as the temperature and pressure ranges of the operating fluids,

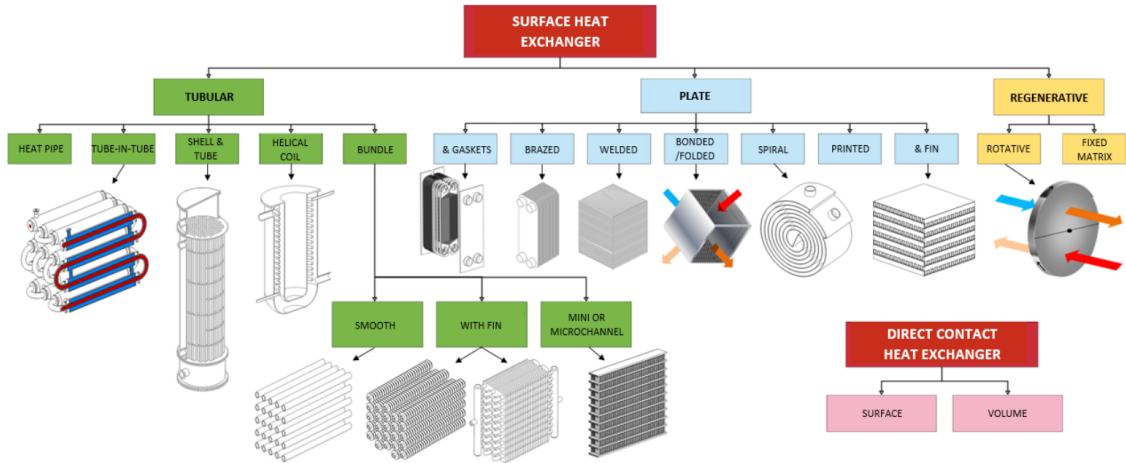


Figure B.1: Classification of Heat Exchangers with respect to their Architecture [134].

their physical and chemical properties (i.e., corrosion and fouling tendencies), space constraints, maintenance accessibility, ect. Inspired by the selection criteria, heat exchangers can be classified based on the following:

- The architecture of the heat exchanger,
- The flow arrangement,
- The number of times a fluid exchanges with the other (number of passes),
- The nature and properties of the fluids involved,
- The dominant heat transfer mechanism(s),

B.2.1 Architecture

At the architectural level, heat exchangers can be classified into three main families: tubular, plate-based, and regenerative. These families can further be divided into several subcategories, as summarized in Fig. B.1. These three families account for more than two-thirds of the global heat exchanger market [132]. Shell and Tube heat exchangers hold the top position with a market size of 9.5 billion euros, and this number is expected to grow by 5.4 % by the end of 2027 [133]. This is mainly due to their high adaptability in terms of pressure and temperature resistance, material diversity, and good thermohydraulic performance.

Plate-based exchangers are also highly regarded in various energy sectors, including air conditioning, heating, and cogeneration. The popularity of plate exchangers has increased due to their compactness, ease of mass production, high

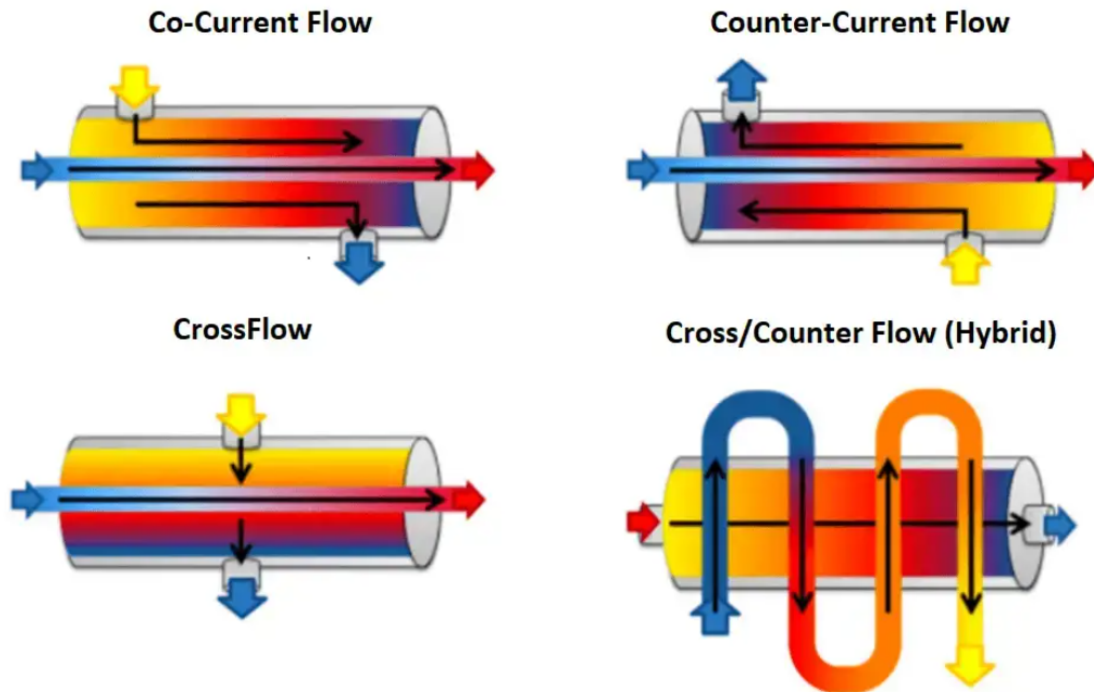


Figure B.2: Schematic representation of several types of flow arrangement [136].

efficiency, and significant surface area-to-volume ratio (reaching up to 700 or even $1000 \text{ m}^2/\text{m}^3$) [135]. The design of the plates has gradually evolved, with the introduction of fins and chevrons being the two main improvements, enabling greater heat transfer capacity and improved resistance to high levels of pressure and temperature.

B.2.1.1 Flow Arrangement

In terms of flow arrangement, a heat exchanger can be classified into three main types: co-current flow (also known as parallel flow), counter-current flow (also known as counter flow), cross-flow, and hybrid flow (including all its variations). The choice of flow arrangement is an important criterion in heat exchanger design as it directly impacts its performance.

The counter-current flow [136] configuration offers the best thermal performance, as it allows for maximum heat transfer and potentially high efficiency. It maintains a continuous temperature difference between the two fluids along the entire length of the heat exchanger, promoting efficient heat transfer from the hotter fluid to the cooler fluid.

On the other hand, the parallel flow [137] configuration is less common because it limits the total power exchanged. It results in a reduced temperature difference

between the two fluids over the length of the exchanger, leading to a lower overall heat transfer rate. However, it may be more suitable for certain applications that require a specific temperature approach.

The choice of flow direction depends on the requirements of the application and, as shown in Fig. B.2, these configurations can be combined to meet the specific needs of certain problems.

B.2.2 Fluids Involved

The diversity of fluids, along with the wide range of nominal capacities in installations, has resulted in a significant variety of technologies based on tubular or plate heat exchanger designs. In refrigeration systems, the fluids used for the compression cycle are often refrigerants or organic fluids derived from hydrocarbons. Common examples include hydrofluorocarbons (HFCs) like *R134a*, *R410a*, or *R407C*, and hydrochlorofluorocarbons (HCFCs) like *R22* [138]. Hydrocarbons such as isobutane and propane, as well as inorganic compounds like ammonia, carbon dioxide, and water, are reserved for specific applications or are currently being studied for potential industrial integration (for instance, supercritical *CO2*) [139].

The selection of a fluid depends on several factors. Physical properties such as specific heat, thermal conductivity, and more are taken into consideration, as well as the fluid's ability to withstand extreme operating conditions (i.e., critical temperatures and pressures). The enthalpy of phase change also plays a crucial role in the choice of fluid. Other criteria to consider include health risks (such as toxicity for ammonia), fire hazards, and self-ignition (more prevalent in hydrocarbons), and environmental risks (significant for HCFCs).

B.3 Multiphase Heat Exchangers

When the fluids involved only exchange sensible heat (without a phase transition), it is called a single-phase heat exchanger. If one or both of the fluids undergo a phase change during their passage through the exchanger, it is then referred to as a Multiphase Heat Exchanger (MpHE) [140]:

- **Evaporator:** In the case where a subcooled liquid fluid absorbs energy from the hot secondary fluid to vaporize either completely or partially.
- **Condenser:** In the case where a saturated or superheated vapor fluid releases energy to the secondary cooling fluid to condense either completely or partially.

Like single-phase heat exchangers, evaporators and condensers are widely used in industrial processes. For bi-fluid heat exchangers, there are essentially three main types of applications:

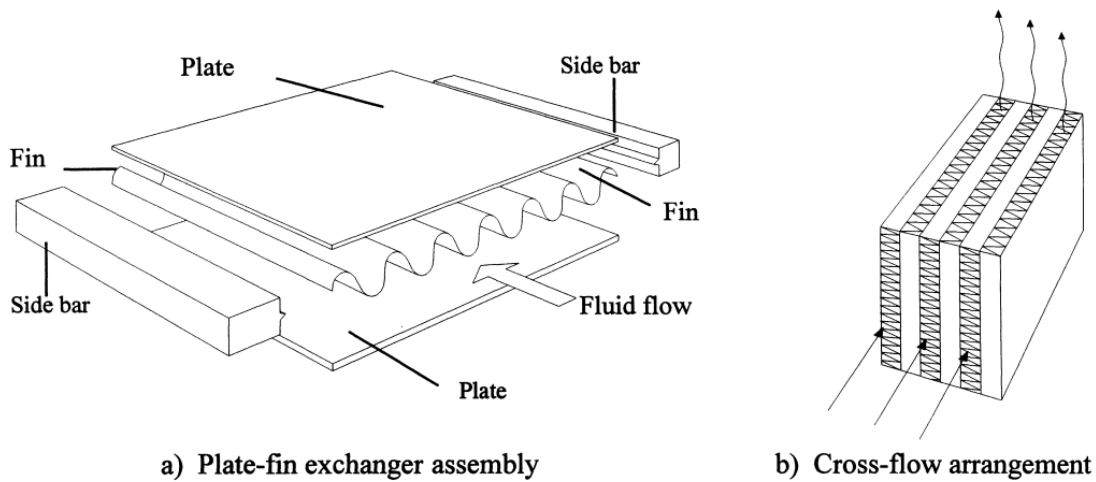


Figure B.3: Typical assembly and cross-flow arrangement of plate-fin PFHE: (a) plate-fin exchanger assembly; (b) cross-flow arrangement [143].

- Mechanical and electrical power generation through a thermodynamic cycle such as a steam Rankine cycle. In this case, the steam produced in the steam generator/evaporator is expanded in a turbine, which generates mechanical work to drive a generator for electricity production. The fluid exiting the turbine passes through a condenser that is directly or indirectly cooled by ambient air or a cooling fluid [141]. This principle is also the basis of operation for nuclear power plants, traditional thermal power plants, and solar power plants.
- Cold production in a closed cycle (i.e., Vapor Cycle System), where vapor production at a temperature lower than the ambient temperature allows for the absorption of thermal energy from the source to be cooled. This operating principle applies to almost all current refrigeration or air conditioning equipment. The thermal capacities of these units vary greatly, ranging from a few hundred watts for a household refrigerator to several tens of megawatts in a refrigeration system powered by a chilled water network for the air conditioning of an urban area.
- Thermal distillation [142], most commonly used for separating compounds in liquid phases. It is applied in various sectors and processes such as food and beverage production (alcohol production), cryogenics (air gas purification), petrochemicals (separation of hydrocarbons or organic compounds), etc.

The fins are inserted between the plates to compensate for the high thermal resistance, particularly when one of the fluids is a gas [144].

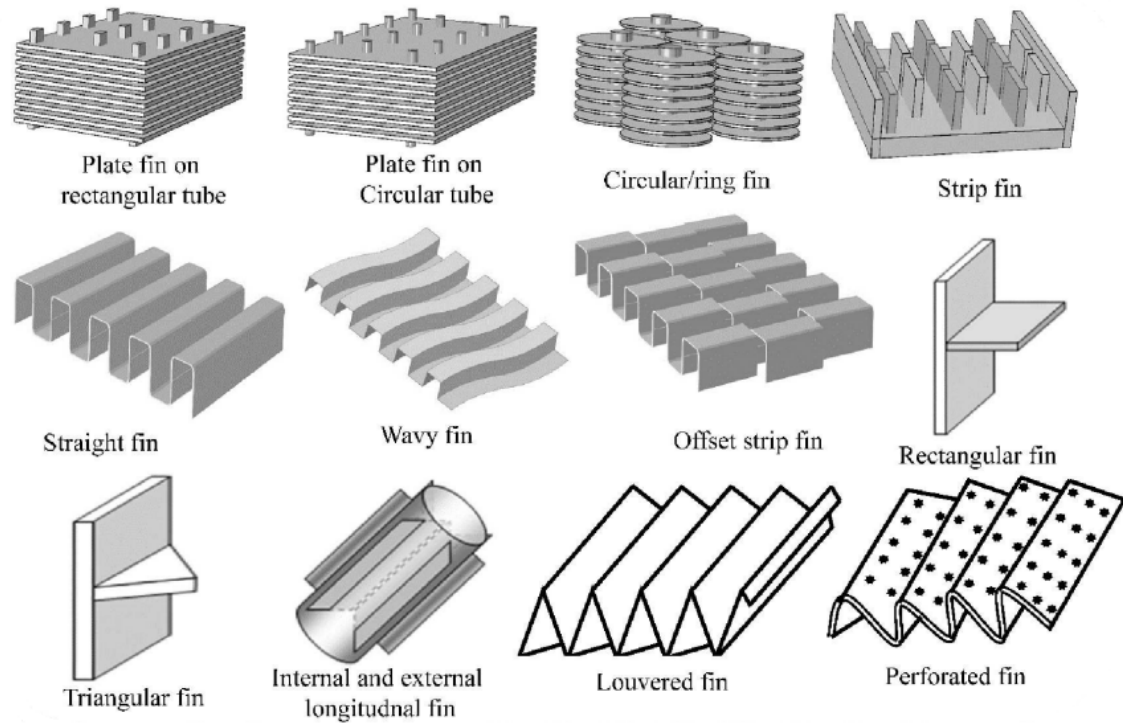


Figure B.4: Schematic diagrams of different geometries of fin surfaces encountered in PFHEs [146].

B.4 Plate and Fin Heat Exchangers

A Plate-Fin Heat Exchanger (PFHE) is composed of stacked flat plates and fin structures that are brazed together in a controlled atmosphere furnace [145]. Fig. B.3 illustrates typical plate-fin configurations. Flat plates separate louvered or corrugated fins. Crossflow, counterflow, or parallel flow arrangements can be obtained readily by properly arranging the fins on each side of the plate. This type of extended surface heat exchanger can have a variety of fin geometries, as shown in Fig. B.4. Each geometry has a different impact on heat transfer and pressure drop, allowing for a balance between the two ¹.

PFHEs have specific characteristics [128]. Their surface densities range from 850 to 1500 m^2/m^3 , which is more than five times larger than that of a Shell and Tube heat exchanger for comparison -on the fins side, it can reach 6000 m^2/m^3 . This makes them very recommended in aerospace industries where the criteria of compactness is unavoidable. Furthermore, a single PFHE can accommodate multiple

¹Due to the complexity associated with selecting appropriate fin geometry, size, and density, it was addressed in a stand-alone study undertaken as part of the Panther project.

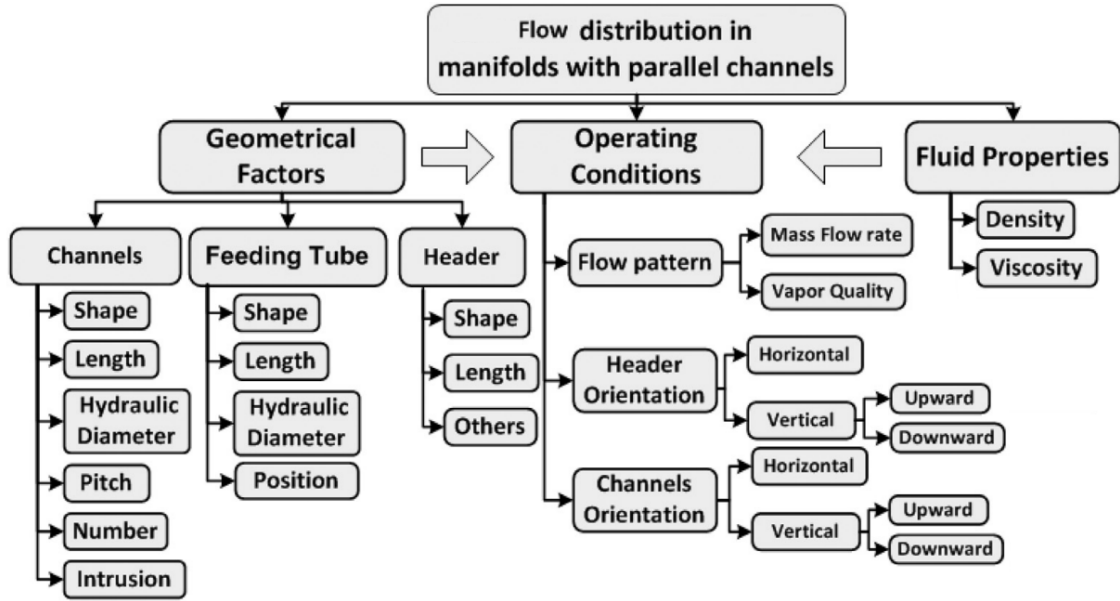


Figure B.5: Impact factors on flow distribution over multi-channel heat exchangers [147].

fluid streams for different processes. The plate design enables the fluids to remain separate while interacting at specific intermediate regions within the exchanger.

PFHEs are particularly suitable for low temperature differences, ideally less than $1\text{ }^{\circ}\text{C}$. The fin thickness varies from 0.05 to 0.25 mm , and the fin height corresponds to the spacing between the plates, typically ranging from 2 to 25 mm . Typical fin densities range from 120 to 700 fins/m . The temperature limitations depend largely on the construction material, ranging from $-270\text{ }^{\circ}\text{C}$ (i.e., low cryogenic operations) to $800\text{ }^{\circ}\text{C}$. In the case of aluminum brazing, as considered in our study, the PFHE can operate at temperatures up to $200\text{ }^{\circ}\text{C}$ and pressures up to 10 bars .

B.5 Flow Distribution

The issue of uneven flow distribution in the parallel channels of compact heat exchanger headers has been extensively investigated in the literature for several decades due to its detrimental effect on heat transfer efficiency. This concern becomes even more critical when the fluid enters the header in a liquid-vapor state [148]. Achieving a homogeneous distribution of the liquid phase is particularly crucial since underfed liquid channels result in complete vaporization of the liquid shortly after exiting the header, leading to "dry out", leading to a significant reduction in heat transfer in the near-wall region.

However, achieving an equal distribution of phases in each channel is challenging

due to the influence of numerous parameters, including fluid properties, geometrical aspects, and operating conditions. These parameters vary in their level of significance, and the most impactful factors are summarized in Fig. B.5. The extensive number of influential factors further supports the case for using topology optimization as a design tool for the distributor.

Bibliography

- [1] T. Dehne, P. Lange, D. Schmeling, I. Gores, Micro-jet ventilation – a novel ventilation concept for long-range aircraft cabins, in: *Ventilation 2022*, 2022. [2](#)
- [2] T. Planès, S. Delbecq, V. Pommier-Budinger, E. Bénard, [Modeling and design optimization of an electric environmental control system for commercial passenger aircraft](#), *Aerospace* 10 (3) (2023). doi:[10.3390/aerospace10030260](https://doi.org/10.3390/aerospace10030260). URL <https://www.mdpi.com/2226-4310/10/3/260> iv, [2](#)
- [3] J. Herzog, L. A. Lindenberg, *Electrification of the environmental control system*, 2006. [2](#)
- [4] M. Mohanraj, S. Jayaraj, C. Muraleedharan, [Environment friendly alternatives to halogenated refrigerants—a review](#), *International Journal of Greenhouse Gas Control* 3 (1) (2009) 108–119. doi:<https://doi.org/10.1016/j.ijggc.2008.07.003>. URL <https://www.sciencedirect.com/science/article/pii/S1750583608000674> [2](#)
- [5] X. Wu, S. Hu, S. Mo, Carbon footprint model for evaluating the global warming impact of food transport refrigeration systems, *Journal of Cleaner Production* 54 (2013) 115–124. doi:[10.1016/j.jclepro.2013.04.045](https://doi.org/10.1016/j.jclepro.2013.04.045). [2](#)
- [6] A. G. Devecioğlu, V. Oruç, [Characteristics of some new generation refrigerants with low gwp](#), *Energy Procedia* 75 (2015) 1452–1457, clean, Efficient and Affordable Energy for a Sustainable Future: The 7th International Conference on Applied Energy (ICAE2015). doi:<https://doi.org/10.1016/j.egypro.2015.07.258>. URL <https://www.sciencedirect.com/science/article/pii/S1876610215010267> iv, [3](#)
- [7] X.-B. Duan, F.-F. Li, X.-Q. Qin, Adaptive mesh method for topology optimization of fluid flow, *Appl. Math. Lett.* 44 (2015) 40–44. [4](#), [40](#), [43](#), [65](#)

-
- [8] K. E. Jensen, Topology optimization of stokes flow on dynamic meshes using simple optimizers, *Comp. Fluids* 174 (2018) 66–77. [4](#), [5](#)
- [9] X.-B. Duan, X.-Q. Qin, Optimality criteria coupled adaptive mesh method for optimal shape design of stokes flow, *Math. Methods Appl. Sci.* 39 (2016) 3910–3920. [4](#)
- [10] X.-B. Duan, F.-F. Li, X.-Q. Qin, Topology optimization of incompressible navier–stokes problem by level set based adaptive mesh method, *Comput. Math. Appl.* 72 (2016) 1131–1141. [4](#), [40](#), [43](#), [65](#)
- [11] H. Garcke, C. Hecht, M. Hinze, C. Kahle, Numerical approximation of phase field based shape and topology optimization for fluids, *SIAM J. Sci. Comput.* 37 (2015) A1846–A1871. [4](#)
- [12] F. Feppon, G. Allaire, F. Bordeu, J. Cortial, C. Dapogny, Shape optimization of a coupled thermal fluid–structure problem in a level set mesh evolution framework, *SeMA* 76 (2019) 413–458. [4](#), [95](#), [102](#)
- [13] F. Feppon, G. Allaire, C. Dapogny, P. Jolivet, Topology optimization of thermal fluid–structure systems using body-fitted meshes and parallel computing, *J. Comput. Phys.* 417 (2020) 109574. [4](#), [83](#), [104](#), [107](#)
- [14] F. Feppon, G. Allaire, C. Dapogny, P. Jolivet, Body-fitted topology optimization of 2d and 3d fluid-to-fluid heat exchangers, *Comput. Methods Appl. Mech. Engrg.* 376 (2021) 113638. [4](#)
- [15] F. Alauzet, A. Loseille, A decade of progress on anisotropic mesh adaptation for computational fluid dynamics, *Comput. Aided Des.* 72 (2016) 13–39. [4](#)
- [16] J. Alexandersen, C. S. Andreasen, A review of topology optimisation for fluid-based problems, *Fluids* 5 (2020) 29. [5](#), [83](#)
- [17] J. Sari, F. Cremonesi, M. Khalloufi, F. Cauneau, P. Meliga, Y. Mesri, E. Hachem, Anisotropic adaptive stabilized finite element solver for rans models, *Int. J. Numer. Meth. Fl.* 86 (2018) 717–736. [5](#)
- [18] L. Huang, M. S. Lee, K. Saleh, V. Aute, R. Radermacher, [A computational fluid dynamics and effectiveness-ntu based co-simulation approach for flow mal-distribution analysis in microchannel heat exchanger headers](#), *Applied Thermal Engineering* 65 (1) (2014) 447–457. doi:<https://doi.org/10.1016/j.applthermaleng.2014.01.046>. URL <https://www.sciencedirect.com/science/article/pii/S1359431114000520> [6](#)

-
- [19] X. Peng, D. Li, J. Li, S. Jiang, Q. Gao, [Improvement of flow distribution by new inlet header configuration with splitter plates for plate-fin heat exchanger](#), *Energies* 13 (6) (2020). doi:10.3390/en13061323.
URL <https://www.mdpi.com/1996-1073/13/6/1323> 6
- [20] A. Raul, B. Bhasme, R. Maurya, [A numerical investigation of fluid flow maldistribution in inlet header configuration of plate fin heat exchanger](#), *Energy Procedia* 90 (2016) 267–275, 5th International Conference on Advances in Energy Research (ICAER) 2015. doi:<https://doi.org/10.1016/j.egypro.2016.11.194>.
URL <https://www.sciencedirect.com/science/article/pii/S1876610216314047> 6
- [21] M. Zhu, [Topology Optimization of Frame Structures: Design for Constructability and Stochastic Dynamic Loads](#), Theses, Johns Hopkins University (Aug. 2015).
URL <http://jhir.library.jhu.edu/handle/1774.2/39572> 6
- [22] T. Djourachkovitch, [Conception de Matériaux Micro-Architecturés Innovants : Application à l’Optimisation Topologique Multi-Échelle](#), Theses, Université de Lyon (Sep. 2020).
URL <https://theses.hal.science/tel-03177211> 6
- [23] L. Rakotondrainibe, [Topology Optimization of Connections in Mechanical Systems](#), Theses, Institut Polytechnique de Paris (Dec. 2020).
URL <https://theses.hal.science/tel-03106332> 6
- [24] S. Boyd, L. Vandenberghe, *Convex Optimization*, Cambridge University Press, New York, United States of America, 2004. 6
- [25] G. Allaire, *Conception optimale de structures*, Springer Berlin, Heidelberg, Federal Republic of Germany, 2007. doi:10.1007/978-3-540-36856-4. 6, 10, 11
- [26] S. L. Vatanabe, T. N. Lippi, C. R. de Lima, G. H. Paulino, E. C. Silva, [Topology optimization with manufacturing constraints: A unified projection-based approach](#), *Advances in Engineering Software* 100 (2016) 97–112. doi:<https://doi.org/10.1016/j.advengsoft.2016.07.002>.
URL <https://www.sciencedirect.com/science/article/pii/S0965997816301703> 7
- [27] P. Duysinx, *Optimisation topologique : Du milieu continu à la structure élastique*, Ph.D. thesis, ULiège - Université de Liège (06 February 1996). 7

-
- [28] M. Bendsøe, O. Sigmund, *Topology optimization. Theory, methods, and applications*. 2nd ed., corrected printing, Springer, 2004. doi:[10.1007/978-3-662-05086-6](https://doi.org/10.1007/978-3-662-05086-6). 7, 8
- [29] D. R. Barbary, *Optimisation Topologique des Transferts Thermiques et Massiques dans un Canal Asymétriquement Chauffé*, Theses, Université de la Réunion (Dec. 2017).
URL <https://theses.hal.science/tel-01879640> 7
- [30] K. Deb, *Multiobjective Optimization Using Evolutionary Algorithms*, Wiley, New York, 2001, Ch. 2, pp. 13–49. 7
- [31] M. Uy, J. K. Telford, Optimization by design of experiment techniques, in: 2009 IEEE Aerospace conference, 2009, pp. 1–10. doi:[10.1109/AERO.2009.4839625](https://doi.org/10.1109/AERO.2009.4839625). 7
- [32] L. Wang, Workflow for applying optimization-based design exploration to early-stage architectural design - case study based on evomass, *International Journal of Architectural Computing* 20 (2022) 41–60. doi:[10.1177/147807712211082254](https://doi.org/10.1177/147807712211082254). 7
- [33] G. Marck, *Optimisation Topologique des Transferts de Chaleur et de Masse : Application aux Échangeurs de Chaleur*, Theses, Ecole Nationale Supérieure des Mines de Paris (Dec. 2012).
URL <https://pastel.archives-ouvertes.fr/pastel-00819099> 8
- [34] R. E. Burkard, A. Jameson, G. Strang, P. Deuffhard, J.-L. Lions, V. Capasso, J. Periaux, H. W. Engl (Eds.), *Aerodynamic Shape Optimization Techniques Based on Control Theory*, Springer Berlin Heidelberg, Berlin, Heidelberg, 2000, pp. 151–221. doi:[10.1007/BFb0103920](https://doi.org/10.1007/BFb0103920).
URL <https://doi.org/10.1007/BFb0103920> 8
- [35] E. Papoutsis-Kiachagias, N. Magoulas, J. Mueller, C. Othmer, K. Giannakoglou, *Noise reduction in car aerodynamics using a surrogate objective function and the continuous adjoint method with wall functions*, *Computers & Fluids* 122 (2015) 223–232. doi:<https://doi.org/10.1016/j.compfluid.2015.09.002>.
URL <https://www.sciencedirect.com/science/article/pii/S0045793015003084> 8
- [36] R. Lapuh, Mesh morphing technique used with open-source cfd toolbox in multidisciplinary design optimisation, 2018. 8

-
- [37] H. Kallath, J. S. Lee, F. K. Kholi, M. Y. Ha, J. K. Min, [A multi-objective airfoil shape optimization study using mesh morphing and response surface method](#), *Journal of Mechanical Science and Technology* 35 (2021) 1075–1086. doi:10.1007/s12206-021-0221-0. URL <https://link.springer.com/article/10.1007/s12206-021-0221-0> 8
- [38] G. Karpouzas, E. Papoutsis-Kiachagias, T. Schumacher, E. De Villiers, K. Giannakoglou, C. Othmer, Adjoint optimization for vehicle external aerodynamics 7 (2016) 1–7. 8
- [39] B. S. B. Mohamodhosen, [Topology Optimisation of Electromagnetic Devices](#), Theses, Ecole Centrale de Lille (Dec. 2017). URL <https://theses.hal.science/tel-01818091> 8
- [40] M. Okruta, [Three-Dimensional Topology Optimization of Statically Loaded Porous and Multi-Phase Structures](#), Theses, University of Rhode Island (Sep. 2014). URL <https://digitalcommons.uri.edu/theses/347/> 8, 10, 11
- [41] M. P. Bendsøe, N. Kikuchi, Generating optimal topologies in structural design using a homogenization method, *Comput. Methods Appl. Mech. Engrg.* 71 (1988) 197–224. 8
- [42] K. Suzuki, N. Kikuchi, A homogenization method for shape and topology optimization, *Comput. Methods Appl. Mech. Engrg.* 93 (1991) 291–318. 8
- [43] G. Allaire, E. Bonnetier, G. Francfort, F. Jouve, Shape optimization by the homogenization method, *Numer. Math.* 76 (1997) 27–68. 8
- [44] J. A. Sethian, A. Wiegmann, Structural boundary design via level set and immersed interface methods, *J. Comput. Phys.* 163 (2000) 489–528. 10
- [45] M. Y. Wang, X. Wang, D. Guo, A level set method for structural topology optimization, *Comput. Methods Appl. Mech. Engrg.* 192 (2003) 227–246. 10
- [46] G. Allaire, F. Jouve, A.-M. Toader, Structural optimization using sensitivity analysis and a level-set method, *J. Comput. Phys.* 194 (2004) 363–393. 10
- [47] N. P. Van Dijk, K. Maute, M. Langelaar, F. Van Keulen, Level-set methods for structural topology optimization: a review, *Struct. Multidiscipl. Optim.* 48 (2013) 437–472. 10

-
- [48] R. Tawk, [Topology Optimization of Heat and Mass Transfer in bi-Fluid Laminar Flow : Application to Heat Exchangers](#), Theses, Université Paris sciences et lettres (Jun. 2018).
URL <https://pastel.archives-ouvertes.fr/tel-02274990> 10
- [49] P. Hajela, E. Lee, C.-Y. Lin, [Genetic Algorithms in Structural Topology Optimization](#), Springer Netherlands, Dordrecht, 1993, pp. 117–133. doi: [10.1007/978-94-011-1804-0_10](https://doi.org/10.1007/978-94-011-1804-0_10).
URL https://doi.org/10.1007/978-94-011-1804-0_10 10, 11
- [50] T. Jiang, P. Papalambros, A first order method of moving asymptotes for structural optimization, WIT Press 14 (1995) 9. doi: [10.2495/OP950101](https://doi.org/10.2495/OP950101). 10, 11
- [51] N. Kim, T. Dong, D. Weinberg, J. Dalidd, Generalized optimality criteria method for topology optimization, Applied Sciences 11 (2021) 3175. doi: [10.3390/app11073175](https://doi.org/10.3390/app11073175). 10, 11
- [52] J. Guan, W. Zhang, Improved topological optimization method based on particle swarm optimization algorithm, IEEE Access 10 (2022) 52067–52074. doi: [10.1109/ACCESS.2022.3174602](https://doi.org/10.1109/ACCESS.2022.3174602). 10, 11
- [53] P. Dunning, A. Kim, [Introducing the sequential linear programming level-set method for topology optimization](#), Structural and Multidisciplinary Optimization 51 (2015) 631–643. doi: [10.1007/s00158-014-1174-z](https://doi.org/10.1007/s00158-014-1174-z).
URL <https://link.springer.com/article/10.1007/s00158-014-1174-z> 10, 11
- [54] K. Long, X. Wang, H. Liu, [Stress-constrained topology optimization of continuum structures subjected to harmonic force excitation using sequential quadratic programming](#), Structural and Multidisciplinary Optimization 59 (2019) 1747–1759. doi: [10.1007/s00158-018-2159-0](https://doi.org/10.1007/s00158-018-2159-0).
URL <https://link.springer.com/article/10.1007/s00158-018-2159-0> 10, 11
- [55] H. R. Najafabadi, T. G. Goto, M. S. Falheiro, T. C. Martins, A. Barari, M. S. G. Tsuzuki, [Smart topology optimization using adaptive neighborhood simulated annealing](#), Applied Sciences 11 (11) (2021). doi: [10.3390/app11115257](https://doi.org/10.3390/app11115257).
URL <https://www.mdpi.com/2076-3417/11/11/5257> 10, 11
- [56] G. K. Kenway, C. A. Mader, P. He, J. R. Martins, [Effective adjoint approaches for computational fluid dynamics](#), Progress in Aerospace Sciences 110 (2019)

100542. doi:<https://doi.org/10.1016/j.paerosci.2019.05.002>.
URL <https://www.sciencedirect.com/science/article/pii/S0376042119300120> 10
- [57] J. Siva, A. Jameson, Studies of the continuous and discrete adjoint approaches to viscous automatic aerodynamic shape optimization (08 2001). doi:[10.2514/6.2001-2530](https://doi.org/10.2514/6.2001-2530). 11
- [58] S. Nadarajah, A. Jameson, Studies of the continuous and discrete adjoint approaches to viscous automatic aerodynamic shape optimization, Stanford University, Aerospace Computing Laboratory, 15th AIAA Computational Fluid Dynamics Conference, Anaheim, California, 2001. iv, 11
- [59] S. Nadarajah, A. Jameson, A comparison of the continuous and discrete adjoint approach to automatic aerodynamic optimization (11 2014). doi:[10.2514/6.2000-667](https://doi.org/10.2514/6.2000-667). 11
- [60] C. Othmer, A continuous adjoint formulation for the computation of topological and surface sensitivities of ducted flows, *Int. J. Numer. Meth. Fl.* 58 (2008) 861–877. 16, 18, 88, 89
- [61] J.-M. Chomaz, Global instabilities in spatially developing flows: Non-normality and nonlinearity, *Annu. Rev. Fluid Mech.* 37 (2005) 357–392. 18, 87
- [62] O. Soto, R. Löhner, On the computation of flow sensitivities from boundary integrals, AIAA-2004-0112 (2004). 18, 87
- [63] L. Ville, L. Silva, T. Coupez, Convected level set method for the numerical simulation of fluid buckling, *Int. J. Numer. Meth. Fl.* 66 (2011) 324–344. 20
- [64] T. Coupez, L. Silva, E. Hachem, Implicit boundary and adaptive anisotropic meshing, in: S. Perotto, L. Formaggia (Eds.), *New challenges in grid generation and adaptivity for scientific computing*, Springer, 2015, pp. 1–18. 20
- [65] A. Bonito, J.-L. Guermond, S. Lee, Numerical simulations of bouncing jets, *Int. J. Numer. Meth. Fl.* 80 (2016) 53–75. 20
- [66] T. Coupez, Metric construction by length distribution tensor and edge based error for anisotropic adaptive meshing, *J. Comput. Phys.* 230 (2011) 2391–2405. 21, 22, 23
- [67] G. Jannoun, E. Hachem, J. Veysset, T. Coupez, Anisotropic meshing with time-stepping control for unsteady convection-dominated problems, *Appl. Math. Model.* 39 (7) (2015) 1899–1916. 21, 23

-
- [68] T. Coupez, Génération de maillage et adaptation de maillage par optimisation locale, *Rev. Eur. Elem. Finis* 9 (4) (2000) 403–423. [21](#), [24](#), [60](#)
- [69] M. Khalloufi, Y. Mesri, R. Valette, E. Massoni, E. Hachem, High fidelity anisotropic adaptive variational multiscale method for multiphase flows with surface tension, *Comput. Methods Appl. Mech. Engrg.* 307 (2016) 44–67. [24](#)
- [70] T. Coupez, G. Jannoun, J. Veysset, E. Hachem, Edge-based anisotropic mesh adaptation for CFD applications, in: X. Jiao, J.-C. Weill (Eds.), *Procs. of the 21st International Meshing Roundtable*, Springer, 2013, pp. 567–583. [26](#), [59](#)
- [71] P. Meliga, J.-M. Chomaz, D. Sipp, Unsteadiness in the wake of disks and spheres: Instability, receptivity and control using direct and adjoint global stability analyses, *J. Fluid Struct.* 25 (2009) 601–616. [26](#)
- [72] E. Hachem, B. Rivaux, T. Kloczko, H. Digonnet, T. Coupez, Stabilized finite element method for incompressible flows with high Reynolds number, *J. Comput. Phys.* 229 (23) (2010) 8643–8665. [27](#)
- [73] R. Codina, Stabilized finite element approximation of transient incompressible flows using orthogonal subscales, *Comput. Methods Appl. Mech. Engrg.* 191 (2002) 4295–4321. [27](#), [28](#)
- [74] E. Hachem, S. Feghali, R. Codina, T. Coupez, Immersed stress method for fluid-structure interaction using anisotropic mesh adaptation, *Int. J. Numer. Meth. Eng.* 94 (2013) 805–825. [27](#)
- [75] T. Tezduyar, Y. Osawa, Finite element stabilization parameters computed from element matrices and vectors, *Comput. Methods Appl. Mech. Engrg.* 190 (3–4) (2000) 411–430. [28](#)
- [76] R. Codina, Stabilization of incompressibility and convection through orthogonal sub-scales in finite element methods, *Comput. Methods Appl. Mech. Engrg.* 190 (2000) 1579–1599. [28](#)
- [77] R. Codina, Comparison of some finite element methods for solving the diffusion-convection-reaction equation, *Comput. Methods Appl. Mech. Engrg.* 156 (1998) 185–210. [29](#), [91](#)
- [78] S. Badia, R. Codina, Analysis of a stabilized finite element approximation of the transient convection-diffusion equation using an ALE framework, *SIAM J. Numer. Anal.* 44 (2006) 2159–2197. [29](#), [91](#)
- [79] T. Borrvall, J. Petersson, Topology optimization of fluids in Stokes flow, *Int. J. Numer. Meth. Fl.* 41 (2003) 77–107. [v](#), [40](#), [41](#), [43](#), [44](#), [49](#), [55](#), [65](#)

- [80] X.-B. Duan, Y.-C. Ma, R. Zhang, Shape-topology optimization for Navier–Stokes problem using variational level set method, *J. Comput. Appl. Math.* 222 (2008) 487–499. [40](#), [65](#)
- [81] A. Gersborg-Hansen, O. Sigmund, R. B. Haber, Topology optimization of channel flow problems, *Struct. Multidiscipl. Optim.* 30 (2005) 181–192. [40](#), [65](#)
- [82] M. Abdelwahed, M. Hassine, M. Masmoudi, Optimal shape design for fluid flow using topological perturbation technique, *J. Math. Anal.* 356 (2009) 548–563. [vii](#), [40](#), [44](#), [65](#), [67](#), [73](#), [74](#)
- [83] L. H. Olesen, F. Okkels, H. Bruus, A high-level programming-language implementation of topology optimization applied to steady-state Navier–Stokes flow, *Int. J. Numer. Meth. Eng.* 65 (2006) 975–1001. [41](#), [43](#)
- [84] J. K. Guest, J. H. Prévost, Topology optimization of creeping fluid flows using a Darcy–Stokes finite element, *Int. J. Numer. Meth. Eng.* 66 (2006) 461–484. [44](#)
- [85] P. E. Papadopoulos, I. P. A. and Farrell, T. M. Surowiec, Computing multiple solutions of topology optimization problems, *SIAM J. Sci. Comput.* 43 (2021) A1555–A1582. [44](#), [46](#), [73](#)
- [86] O. Sigmund, K. Petersson, Numerical instabilities in topology optimization: a survey on procedures dealing with checkerboards, mesh-dependencies and local minima, *Struct. Opt.* 16 (1998) 68–75. [55](#)
- [87] T. Borrvall, J. Petersson, Large-scale topology optimization in 3d using parallel computing, *Comput. Methods Appl. Mech. Engrg.* 190 (2001) 6201–6229. [58](#)
- [88] A. Evgrafov, C. J. Rupp, K. Maute, M. L. Dunn, Large-scale parallel topology optimization using a dual-primal substructuring solver, *Struct. Multidiscipl. Optim.* 36 (2008) 329–345. [58](#)
- [89] N. Aage, B. S. Lazarov, Parallel framework for topology optimization using the method of moving asymptotes, *Struct. Multidiscipl. Optim.* 47 (2013) 493–505. [58](#)
- [90] N. Aage, B. S. Lazarov, Topology optimization using PETSc: An easy-to-use, fully parallel, open source topology optimization framework, *Struct. Multidiscipl. Optim.* 51 (2015) 565–572. [58](#)

-
- [91] J. Alexandersen, O. Sigmund, N. Aage, Large scale three-dimensional topology optimisation of heat sinks cooled by natural convection, *Int. J. Heat Mass Transfer* 100 (2016) 876–891. [58](#)
- [92] S. Balay, S. Abhyankar, M. F. Adams, J. Brown, P. Brune, K. Buschelman, L. Dalcin, A. Dener, V. Eijkhout, W. Gropp, et al., PETSc users manual (rev. 3.13), Technical report ANL-95/11-Rev. 3.13, Argonne National Lab. (2020). [60](#)
- [93] Y. Mesri, H. Digonnet, H. Guillard, Mesh partitioning for parallel computational fluid dynamics applications on a grid, in: *Procs. of the 4th International Symposium on. Finite Volumes for Complex Applications*, 2005, pp. 631–642. [60](#), [62](#)
- [94] H. Digonnet, L. Silva, T. Coupez, Cimlib: a fully parallel application for numerical simulations based on components assembly, in: *Procs. of the 9th International Conference on Numerical Methods in Industrial Forming Processes*, 2007, pp. 269–274. [60](#)
- [95] H. Digonnet, L. Silva, T. Coupez, Massively parallel computation on anisotropic meshes, in: *Procs. of the 6th International Conference on Adaptive Modeling and Simulation*, 2013, pp. 199–211. [60](#)
- [96] Y. Mesri, H. Digonnet, T. Coupez, Advanced parallel computing in material forming with CIMLib, *Eur. J. Comput. Mech.* 18 (2009) 669–694. [61](#)
- [97] C. H. Villanueva, K. Maute, CutFEM topology optimization of 3D laminar incompressible flow problems, *Comput. Methods Appl. Mech. Engrg.* 320 (2017) 444–473. [64](#), [65](#), [73](#), [77](#), [78](#), [104](#)
- [98] G. Pingen, M. Waidmann, A. Evgrafov, K. Maute, A parametric level-set approach for topology optimization of flow domains, *Struct. Multidiscipl. Optim.* 41 (2010) 117–131. [77](#)
- [99] T. Dbouk, A review about the engineering design of optimal heat transfer systems using topology optimization, *Appl. Therm. Eng.* 112 (2017) 841–854. [83](#)
- [100] K. Yaji, T. Yamada, S. Kubo, K. Izui, S. Nishiwaki, A topology optimization method for a coupled thermal–fluid problem using level set boundary expressions, *Int. J. Heat Mass Transfer* 81 (2015) 878–888. [83](#)
- [101] P. Coffin, K. Maute, Level set topology optimization of cooling and heating devices using a simplified convection model, *Struct. Multidiscipl. Optim.* 53 (2016) 985–1003. [83](#)

-
- [102] E. M. Dede, Multiphysics topology optimization of heat transfer and fluid flow systems, in: *Procs. of the COMSOL Users Conference*, 2009. [83](#)
- [103] G. H. Yoon, Topological design of heat dissipating structure with forced convective heat transfer, *J. Mech. Sci. Technol.* 24 (2010) 1225–1233. [83](#)
- [104] G. Marck, Optimisation topologique des transferts de chaleur et de masse: application aux échangeurs de chaleur, Ph.D. thesis, Ecole Nationale Supérieure des Mines de Paris (2012). [83](#)
- [105] E. A. Kontoleontos, E. M. Papoutsis-Kiachagias, A. S. Zymaris, D. I. Papadimitriou, K. C. Giannakoglou, Adjoint-based constrained topology optimization for viscous flows, including heat transfer, *Eng. Optim.* 45 (2013) 941–961. [83](#)
- [106] T. Matsumori, T. Kondoh, A. Kawamoto, T. Nomura, Topology optimization for fluid–thermal interaction problems under constant input power, *Struct. Multidiscipl. Optim.* 47 (2013) 571–581. [83](#), [89](#)
- [107] J. Alexandersen, N. Aage, C. Andreasen, O. Sigmund, Topology optimisation for natural convection problems, *Int. J. Numer. Meth. Fl.* 76 (2014) 699–721. [83](#)
- [108] X. Qian, E. M. Dede, Topology optimization of a coupled thermal-fluid system under a tangential thermal gradient constraint, *Struct. Multidiscipl. Optim.* 54 (2016) 531–551. [83](#)
- [109] F. Dugast, Y. Favennec, C. Josset, Y. Fan, L. Luo, Topology optimization of thermal fluid flows with an adjoint Lattice Boltzmann method, *J. Comput. Phys.* 365 (2018) 376–404. [83](#), [89](#)
- [110] V. Subramaniam, T. Dbouk, J.-L. Harion, Topology optimization of conjugate heat transfer systems: A competition between heat transfer enhancement and pressure drop reduction, *Int. J. Heat Fluid Flow* 75 (2019) 165–184. [83](#), [95](#), [102](#)
- [111] C. Flageul, S. Benhamadouche, É. Lamballais, D. Laurence, DNS of turbulent channel flow with conjugate heat transfer: Effect of thermal boundary conditions on the second moments and budgets, *Int. J. Heat Fluid Flow* 55 (2015) 34–44. [85](#)
- [112] S. V. Patankar, *Numerical heat transfer and fluid flow*, Taylor & Francis, 1980. [85](#)

-
- [113] S. V. Patankar, A numerical method for conduction in composite materials, flow in irregular geometries and conjugate heat transfer, in: *Procs. of the 6th International Heat Transfer Conference*, 1978, pp. 297–302. [85](#)
- [114] S. Zeng, B. Kanargi, P. S. Lee, Experimental and numerical investigation of a mini channel forced air heat sink designed by topology optimization, *Int. J. Heat Mass Transfer* 121 (2018) 663–679. [89](#)
- [115] T. W. Athan, P. Y. Papalambros, A note on weighted criteria methods for compromise solutions in multi-objective optimization, *Eng. Optim.* 27 (1996) 155–176. [89](#)
- [116] G. Marck, M. Nemer, J.-L. Harion, Topology optimization of heat and mass transfer problems: laminar flow, *Numer. Heat Tr. B-Fund.* 63 (2013) 508–539. [viii](#), [89](#), [95](#), [97](#), [101](#), [102](#)
- [117] A. Brooks, T. J. R. Hughes, Streamline upwind/Petrov–Galerkin formulations for convection dominated flows with particular emphasis on the incompressible Navier–Stokes equations, *Comput. Methods Appl. Mech. Engrg.* 32 (1982) 199–259. [91](#)
- [118] A. C. Galeão, E. G. D. Do Carmo, A consistent approximate upwind Petrov–Galerkin method for convection-dominated problems, *Comput. Methods Appl. Mech. Engrg.* 68 (1988) 83–95. [91](#)
- [119] G. Gargantini, Design of bi-fluid heat exchangers using topology optimization, Ph.D. thesis, Master Thesis Politecnico di Milano (2020). [95](#)
- [120] J. Boussinesq, Mémoire sur l’influence des frottements dans les mouvements réguliers des fluides, *Journal de mathématiques pures et appliquées* 13 (1868) 377–424. [114](#)
- [121] V. K. I. of Fluid Dynamics (2023). [x](#), [117](#)
- [122] P. Meliga, E. Boujo, G. Pujals, F. Gallaire, [Sensitivity of aerodynamic forces in laminar and turbulent flow past a square cylinder](#), *Physics of Fluids* 26 (10) (2014) 104101. [doi:10.1063/1.4896941](#).
URL <https://doi.org/10.1063/1.4896941> [128](#)
- [123] P. Meliga, [Computing the sensitivity of drag and lift in flow past a circular cylinder: Time-stepping versus self-consistent analysis](#), *Phys. Rev. Fluids* 2 (2017) 073905. [doi:10.1103/PhysRevFluids.2.073905](#).
URL <https://link.aps.org/doi/10.1103/PhysRevFluids.2.073905> [128](#)

-
- [124] J. Peter, R. Dwight, Numerical sensitivity analysis for aerodynamic optimization: A survey of approaches, *Computers & Fluids* 39 (2010) 373–391. doi:[10.1016/j.compfluid.2009.09.013](https://doi.org/10.1016/j.compfluid.2009.09.013). 128
- [125] F. Dugast, Y. Favenec, C. Josset, Y. Fan, L. Luo, [Topology optimization of thermal fluid flows with an adjoint lattice boltzmann method](#), *Journal of Computational Physics* 365 (2018) 376–404. doi:<https://doi.org/10.1016/j.jcp.2018.03.040>. URL <https://www.sciencedirect.com/science/article/pii/S0021999118302067> 129
- [126] T. Matsumori, T. Kondoh, A. Kawamoto, T. Nomura, Topology optimization for fluid–thermal interaction problems under constant input power, *Structural and Multidisciplinary Optimization* 47 (04 2013). doi:[10.1007/s00158-013-0887-8](https://doi.org/10.1007/s00158-013-0887-8). 129
- [127] J. H. Haertel, K. Engelbrecht, B. S. Lazarov, O. Sigmund, [Topology optimization of a pseudo 3d thermofluid heat sink model](#), *International Journal of Heat and Mass Transfer* 121 (2018) 1073–1088. doi:<https://doi.org/10.1016/j.ijheatmasstransfer.2018.01.078>. URL <https://www.sciencedirect.com/science/article/pii/S0017931017337146> 130
- [128] T. Kuppan, [Heat Exchanger Design Handbook](#), Marcel Dekker - New York Basel, 2000. URL <http://www.dekker.com> 133, 138
- [129] B. Zohuri, [Heat Exchanger Types and Classifications](#), Springer International Publishing, 2017, Ch. 2, pp. 19–56. doi:[10.1007/978-3-319-29835-1_2](https://doi.org/10.1007/978-3-319-29835-1_2). 133
- [130] E. A. Association, [Applications – Power train – Heat exchangers](#), European Aluminium Association, Brussels, Belgium, 2011, Ch. 1, p. 3. URL <https://european-aluminium.eu/wp-content/uploads/2022/11/aam-applications-power-train-7-heat-exchangers.pdf> 133
- [131] J. E. Hesselgreaves, R. Law, D. A. Reay, [Chapter 1 - introduction](#), in: J. E. Hesselgreaves, R. Law, D. A. Reay (Eds.), *Compact Heat Exchangers* (Second Edition), second edition Edition, Butterworth-Heinemann, 2017, pp. 1–33. doi:<https://doi.org/10.1016/B978-0-08-100305-3.00001-X>. URL <https://www.sciencedirect.com/science/article/pii/B978008100305300001X> 133
- [132] technavio, [Heat exchanger market by product, end-user, and geography - forecast and analysis 2023-2027](#), accessed on July 12, 2023 (07 2023).

- URL <https://www.technavio.com/report/heat-exchanger-market-industry-share-analysis> 134
- [133] Markets, Markets, Shell and tube heat exchanger market by material (steel, nickel and nickel alloys, titanium, tantalum), application (chemicals, petrochemicals, hvac and refrigeration, food and beverages, power generation, pulp and paper), and region - global forecast to 2027, accessed on July 12, 2023 (2023).
URL <https://www.marketsandmarkets.com/Market-Reports/shell-tube-heat-exchangers-market-92257371.html> 134
- [134] GRETh, Heat Exchangers Technologies, GRETh, LA MOTTE SERVOLEX, France, 2019, Ch. 1, p. 17.
URL <https://greth.fr/e-book-tome-1/> x, 134
- [135] S. Kakaç, H. Liu, A. Pramuanjaroenkij, Heat Exchangers: Selection, Rating, and Thermal Design, Third Edition, Taylor and Francis, 2012.
URL <https://books.google.fr/books?id=sJXpvP6xLZsC> 135
- [136] E. Staff, Why counter-current heat exchangers are better than co-current?, accessed on July 12, 2023 (2023).
URL <https://instrumentationtools.com/counter-current-and-co-current-heat-exchangers/> x, 135
- [137] F. John, N. Lorraine, Mean temperature difference in cross-flow heat exchange applied to multipass air-cooled fin-tube units with a finite number of rows, University of Pretoria (1972) 091401. 135
- [138] A. G. Devecioğlu, V. Oruç, Characteristics of some new generation refrigerants with low gwp, Energy Procedia 75 (2015) 1452–1457, clean, Efficient and Affordable Energy for a Sustainable Future: The 7th International Conference on Applied Energy (ICAE2015).
doi:<https://doi.org/10.1016/j.egypro.2015.07.258>.
URL <https://www.sciencedirect.com/science/article/pii/S1876610215010267> 136
- [139] G. Musgrove, S. Sullivan, D. Shiferaw, P. Fourspring, L. Chordia, 8 - heat exchangers, in: K. Brun, P. Friedman, R. Dennis (Eds.), Fundamentals and Applications of Supercritical Carbon Dioxide (sCO_2) Based Power Cycles, Woodhead Publishing, 2017, pp. 217–244.
doi:<https://doi.org/10.1016/B978-0-08-100804-1.00008-6>.
URL <https://www.sciencedirect.com/science/article/pii/B9780081008041000086> 136

- [140] M. O. B. Costa, L. Beckedorff, K. V. de Paiva, J. L. G. Oliveira, [Multiphase flows in plate and shell heat exchangers](#), *Journal of Fluids Engineering* 144 (9) (2022) 091401. [arXiv:https://asmedigitalcollection.asme.org/fluidsengineering/article-pdf/144/9/091401/6863662/fe\144\09\091401.pdf](#), [doi:10.1115/1.4053902](#).
URL [https://doi.org/10.1115/1.4053902](#) 136
- [141] C. Fu, R. Anantharaman, T. Gundersen, [Optimal integration of compression heat with regenerative steam rankine cycles](#), in: M. R. Eden, J. D. Sirola, G. P. Towler (Eds.), *Proceedings of the 8th International Conference on Foundations of Computer-Aided Process Design*, Vol. 34 of *Computer Aided Chemical Engineering*, Elsevier, 2014, pp. 519–524. [doi:https://doi.org/10.1016/B978-0-444-63433-7.50071-7](#).
URL [https://www.sciencedirect.com/science/article/pii/B9780444634337500717](#) 137
- [142] P. Fellows, [Chapter 12 - evaporation and distillation](#), in: P. Fellows (Ed.), *Food Processing Technology (Fifth Edition)*, fifth edition Edition, Woodhead Publishing Series in Food Science, Technology and Nutrition, Woodhead Publishing, 2022, pp. 389–413. [doi:https://doi.org/10.1016/B978-0-323-85737-6.00016-9](#).
URL [https://www.sciencedirect.com/science/article/pii/B9780323857376000169](#) 137
- [143] M. Picon-Nuñez, G. Polley, E. Torres-Reyes, A. Gallegos-Muñoz, [Surface selection and design of plate–fin heat exchangers](#), *Applied Thermal Engineering* 19 (9) (1999) 917–931. [doi:https://doi.org/10.1016/S1359-4311\(98\)00098-2](#).
URL [https://www.sciencedirect.com/science/article/pii/S1359431198000982](#) x, 137
- [144] R. Perry, D. Green, [Chemical engineers' handbook. second edition \(perry, john h., ed.\)](#), *Journal of Chemical Education* 19 (9) (1942) 449. [arXiv:https://doi.org/10.1021/ed019p449.2](#), [doi:10.1021/ed019p449.2](#).
URL [https://doi.org/10.1021/ed019p449.2](#) 137
- [145] M. Stewart, O. T. Lewis, [Chapter 2 - heat exchanger configurations](#), in: M. Stewart, O. T. Lewis (Eds.), *Heat Exchanger Equipment Field Manual*, Gulf Professional Publishing, Boston, 2013, pp. 93–251. [doi:https://doi.org/10.1016/B978-0-12-397016-9.00002-6](#).
URL [https://www.sciencedirect.com/science/article/pii/B9780123970169000026](#) 138

- [146] J. Singh, A. Montesinos-Castellanos, K. D. P. Nigam, [Process intensification for compact and micro heat exchangers through innovative technologies: A review](#), *Industrial and Engineering Chemistry Research* 58 (2019) 6. doi: [10.1021/acs.iecr.9b02082](https://doi.org/10.1021/acs.iecr.9b02082).
URL <https://doi.org/10.1021/acs.iecr.9b02082> x, 138
- [147] E. Dario, L. Tadrist, J. Passos, [Review on two-phase flow distribution in parallel channels with macro and micro hydraulic diameters: Main results, analyses, trends](#), *Applied Thermal Engineering* 59 (1) (2013) 316–335. doi: <https://doi.org/10.1016/j.applthermaleng.2013.04.060>.
URL <https://www.sciencedirect.com/science/article/pii/S1359431113003311> xi, 139
- [148] J. Choi, V. Payne, P. Domanski, [Effects of non-uniform refrigerant and air flow distributions on finned tube evaporator performance](#) (01 2003). 139

RÉSUMÉ

Cette thèse aborde l'optimisation topologique des systèmes multiphysiques en utilisant la méthode Level-Set pour le suivi d'interface et la méthode adjointe continue pour le calcul de la sensibilité. Elle commence par aborder les problèmes d'écoulements laminaires incompressibles, puis s'étend aux systèmes de transfert de chaleur conjugué. Le cadre d'optimisation combine une méthode de volume immergé pour résoudre des formulations d'éléments finis stabilisées intégrées dans le cadre de la méthode de Variational Multiscale (VMS) avec des fonctions distances représentant l'interface fluide-solide, utilisées comme estimateur d'erreur a posteriori pour minimiser l'erreur d'interpolation sous contrainte d'un nombre prescrit de nœuds dans le maillage. Les étapes de résolution et de remaillage sont toutes deux effectuées dans un cadre massivement parallèle, permettant l'optimisation de systèmes complexes. En particulier, une stratégie de parallélisation originale est utilisée pour l'adaptation du maillage, qui combine le remaillage local effectué séquentiellement et indépendamment sur chaque sous-domaine avec des interfaces bloquées et une répartition contrainte pour déplacer de manière optimale les interfaces entre les sous-domaines (les deux sont itérés jusqu'à obtenir un maillage et une partition satisfaisants). Des résultats numériques sont fournis pour plusieurs problèmes bidimensionnels et tridimensionnels de minimisation de perte de charges et/ou d'amélioration du transfert de chaleur, impliquant des degrés de liberté de l'état variables, allant de plusieurs milliers (dans les problèmes en 2D) à plusieurs dizaines de millions (dans les problèmes en 3D). Les conceptions optimales concordent bien avec les résultats de référence de la littérature tout en offrant une précision supérieure par rapport aux études antérieures résolues sur des maillages isotropes. Le potentiel de la méthode pour les problèmes d'ingénierie d'intérêt pratique est finalement exposé en optimisant les parties de distribution et de collection transportant le fluide froid à l'intérieur des plaques d'un échangeur de chaleur à plaques et à ailettes.

MOTS CLÉS

Mechanique des Fluides, Optimisation Topologique, Adjoint Continu, Ligne de Niveau, Maillage Anisotropique Adaptatif, Transfert Thermique Conjugué, Systèmes Complexes, Parallélisation, Echangeur de Chaleur, Distributeur.

ABSTRACT

This PhD considers the Optimization of Multi-Physics systems using the Level-Set Method for surface tracking and the Continuous Adjoint Method for sensitivity computation. It starts by addressing laminar incompressible flow problems, then expands to conjugate heat transfer systems. The optimization framework combines an immersed volume method for solving stabilized finite element formulations cast in the Variational Multiscale (VMS) framework with level set representations of the fluid-solid interfaces, used as a posteriori error estimator to minimize the interpolation error under the constraint of a prescribed number of nodes in the mesh. Both the resolution and remeshing steps are performed in a massively parallel framework, allowing for the optimization of large-scale systems. In particular, an original parallelization strategy is used for mesh adaptation that combines local remeshing performed sequentially and independently on each subdomain with blocked interfaces and constrained repartitioning to optimally move the interfaces between subdomains in an optimal way (both iterated until a satisfying mesh and partition are obtained). Numerical results are provided for several two- and three-dimensional problems of power dissipation minimization and/or heat transfer enhancement, involving varying state degrees of freedom, going from several thousands (in 2d problems) to several dozen million (in 3d problems). The optimal designs agree well with reference results from the literature while providing superior accuracy over prior studies solved on isotropic meshes. The potential of the method for engineering problems of practical interest is eventually exposed by optimizing the distributor and collector sections conveying the cold fluid within the plates of a plate and fin heat exchanger.

KEYWORDS

Fluid Mechanics, Topology Optimization, Continuous Adjoint, Level-Set Method, Anisotropic Mesh Adaptation, Conjugate Heat Transfer, Large-Scale Systems, Parallelization, Heat Exchanger, Manifold.